UNIVERSITÀ DEGLI STUDI DI PALERMO

Dottorato in Scienze Fisiche
Dipartimento di Fisica e Chimica – Emilio Segrè
Settore Astronomia ed Astrofisica (FIS/05)

Accretion onto Neutron Stars: spectral and timing investigation of Low Mass X-ray Binaries

IL DOTTORE
SIMONA MICHELA MAZZOLA

IL COORDINATORE
Prof. GIOACCHINO MASSIMO PALMA

IL TUTOR
Prof. ROSARIO IARIA

EVENTUALE CO TUTOR
Prof.ssa TIZIANA DI SALVO

CICLO XXXIII
ANNO CONSEGUIMENTO TITOLO - 2021

Al mio adorato Nonno,
in memoria del suo amore imperituro,
per essere sempre rimasto al mio fianco.

Un punto piccoletto,
superbo e iracondo,
"Dopo di me" gridava
"verrà la fine del mondo!".

Le parole protestarono:
"Ma che grilli ha pel capo?
Si crede un Punto-e-basta,
e non è che un Punto-e-a-capo".

Tutto solo a mezza pagina
lo piantarono in asso
e il mondo continuò
una riga più in basso.

Gianni Rodari, *Il Dittatore*

Abstract

The X-ray astronomy is a relatively recent research field. It was born in the early 1960s and received a great boost from the discovery of the first extra-solar X-ray source (Scorpius X-1, Giacconi et al. 1962). The first dedicated X-ray satellite, the *Uhuru* observatory (Giacconi et al. 1971b), was launched in 1970 and it allowed to discover and study hundreds of Galactic sources and many important extra-Galactic ones in just three years of mission. The *Uhuru* Catalogue, which the last issued version is the 4U catalogue, was the first comprehensive X-ray sources archive, containing 339 objects and covering the whole sky in the 2–6 keV band (Forman et al. 1978). The primary target of investigation of *Uhuru*, and of all the following missions, are the X-ray binaries, i.e. binary systems in which a compact object (a white dwarf, a neutron star or a black hole) accretes matter lost from a companion star, which is generally in main sequence. The emission of these systems falls mainly in the X-band due to the accretion processes, in which the kinetic energy of the accreting matter is converted into radiation. The X-ray binary systems are classified, in general, as High Mass X-Ray Binary (HMXB) and Low Mass X-Ray Binary (LMXB) depending on the mass of the companion star.

Topic of this thesis is the study of the timing and spectral properties of several LMXBs hosting weakly magnetised neutron stars (NSs) through the data analysis of observations collected by some of the most important X-ray missions.

The NS-LMXBs are composed of a NS and a late-type companion star (CS) which, generally, has a very small mass ($M_{CS} \lesssim 0.5 M_{\odot}$). In this case, the accretion occurs via *Roche lobe overflow* and the formation of an accretion disc around the compact object, in which the plasma follows Keplerian orbits.

Depending on the value of the inclination angle between the line of sight and the perpendicular to the orbital plane of the system, *eclipses* and/or *dips* can be observed in the light curves of these sources. In the first case ($75^{\circ} \leq \theta \leq 90^{\circ}$) the shielding effect is due to the periodic transit of CS

between the radiation source and the observer; in the second one ($60^\circ \leq \theta \leq 80^\circ$) the localised decrease of the count/rate is due to the presence of a bulge of accreting matter in the outermost region of the disc instead. Since both dips and eclipses occur at the same orbital period of the system, through a dedicated analysis of their occurrence, the orbital period of the system can be estimated and its secular evolution described.

Another powerful investigation method to study the LMXBs is the broadband spectral analysis of their emission. In the continuum of the X-ray spectra of these sources, in general, a soft thermal component (due to the blackbody emission from the NS and/or the accretion disc) and a hard component, due to the Comptonisation of soft photons from a hot electron corona, can be identified. Furthermore, the spectra of these sources show often a reflection component, originated from direct Compton scattering of the Comptonised photons, outgoing the hot corona, with the cold electrons in the top layers of the inner accretion disc. The presence of the reflection is mainly indicated by the detection of a strong broad (FWHM up to 1 keV) emission line from Fe atoms between 6.4 and 6.97 keV (Fe-K region), often observed in the spectra of NS-LMXBs. Besides, means of the lines diagnostic it is also possible to test the effects of the strong gravity exerted by NS on the inner region of the disc, where they are (probably) produced.

In the first part of this thesis the theoretical background of the subject is discussed: in Chapter 1 the basics of the physics of the accretion processes and the general characteristics of the X-ray binaries are summarised; in Chapter 2 the theory of the secular evolution of the LMXBs is described, meanwhile in Chapter 3 the spectral properties of these sources with the current explaining models are reviewed.

In the second part, the analysis carried out on a sample of these sources and the obtained results are reported.

In Chapter 4 the orbital timing analysis of the source X 1822-371, an eclipsing compact binary system with a period close to 5.57 hr, is presented. The *XMM-Newton* observation taken in 2017 allowed to update the orbital ephemeris and verify whether the orbital period derivative has been stable over the last 40 yr. To do so, two new values obtained from *RXTE* and *XMM-Newton* observations are added to the X-ray eclipse arrival times from 1977 to 2008. Fitting the delays of the eclipse arrival times with a quadratic model enabled to update the estimation of the orbital period of the source; the spin-period of the NS and its first derivative were also evaluated. An alternative scenario, in which a gravitational coupling between the orbit and the change in the oblateness of the companion star could explain the quadratic trend of the delays, was also investigated .

In Chapter 5 it is shown the broadband spectral analysis of the source 4U 1702-429, a NS-LMXB

showing type-I bursts. A 0.3-60 keV spectrum obtained combining *XMM-Newton* and *INTEGRAL* observations and three 0.1-100 keV spectra extracted from *BeppoSAX* observations were analysed. The *XMM-Newton/INTEGRAL* spectrum is well-fitted using a model composed of a disc blackbody plus a Comptonised component and a smeared reflection component. The same spectral model was used for the *BeppoSAX* spectra, finding that the addition of a smeared reflection component is statistically significant. The best-fit values of the parameters are compatible to each other for the *BeppoSAX* spectra. Meanwhile, the relative reflection fraction and the ionisation parameter are incompatible between the *XMM-Newton/INTEGRAL* and the *BeppoSAX* observations and the characteristics of the Comptonising corona suggest that the source was observed in a soft state in the former observation and in a hard state in the latter.

In Chapter 6 it is presented the study of a *NuSTAR* observation of the Z-source Scorpius X-1, the brightest persistent low-mass X-ray binary known so far. The data from the normal and flaring branches were separated in order to investigate the evolution of the source along the Z-track. The 3-60 keV *NuSTAR* spectra were fitted using the same models for both the branches. Two description were adopted for the continuum: a blackbody plus a thermal Comptonisation which seed photons originating in the accretion disc, and a disc-blackbody plus a Comptonisation with a blackbody-shaped spectrum of the incoming seed photons. The two models provide the same physical scenario for the source in both the branches. Furthermore, two lines related to the Kα and Kβ transitions of the He-like Fe XXV ions were detected at 6.6 keV and 7.8 keV, respectively. A hard tail modelled by a power law was also required.

In Chapter 7 the project developed in collaboration with the *INTEGRAL* Science Data Centre (ISDC, Department of Astronomy, University of Geneva, Switzerland) is presented. It consists in a decade-long based analysis of the spectral changes of a large sample of persistent NS-LMXB, monitored by *INTEGRAL* during its lifetime. The *INTEGRAL* data span over eighteen years and usually comprise several mega-seconds of observations of nearly-uninterrupted 200-300 ks-long pointings of many persistent NS-LMXBs over the 3-500 keV energy range. The stated aim is a unified description for all these sources, through the identification of the different spectral states a source cyclically exhibits and the characterisation of these states thanks to spectral model fits on the corresponding broad-band spectra, obtained by stacking available mega-seconds of data for each state. In this thesis, the semi-automatic processing chain set up is discussed and the preliminary results are shown. The study of the broad-band spectrum of the source GX 17+2, performed applying the developed step-by-step analysis method, is presented.

Contents

Part I

Physics of the Low Mass X-ray Binaries

Chapter 1

Physics of Accretion

1.1 Accretion onto a compact object

In a binary system, two stars orbit around each other under the influence of their mutual gravitational attraction, moving in elliptical orbits around their common centre of mass. In general, the brightest star is called *primary*, while the other one is the *companion* star. In an X-ray binary (XRB) system, the primary star is a compact object (a white dwarf, a neutrons or a black hole) and the companion star (CS) is, generally, a main sequence star. The observed emission in the X-ray band is due to the fall of the matter lost by CS onto the compact object, which determines the conversion of the the mechanical energy of the matter into radiation.

Accretion of matter onto compact objects is an efficient mechanism to explain the X-ray emission of the brightest sources known so far. Nuclear processes are indeed inadequate for this role: it is clear making an estimate of the energy released in the two cases, as radiation energy mainly. For an object of mass $M_* \sim 1.4\ M_\odot$ and radius $R_* \sim 10$ km, the potential gravitational energy released by the accretion of a mass m on the surface is

$$\Delta E_{ACC} = \frac{G\ M_*\ m}{R_*} \sim 10^{20}\,\mathrm{erg\ g^{-1}}\ \text{(per accreted gram)}, \tag{1.1}$$

where G is the gravitational constant. Meanwhile, the maximum energy achievable from the nuclear fusion reactions is obtained considering a mass m_H of hydrogen burnt into helium:

$$\Delta E_{NUCL} = 0.007\ m_\mathrm{H}\ c^2 \simeq 6 \times 10^{18}\,\mathrm{erg\ g^{-1}}$$

with c the speed of light. By a simple comparison it is $\Delta E_{NUCL} = \frac{1}{20}\ \Delta E_{ACC}$.

From the Equation 1.1 it can be seen that the efficiency of the accretion mechanism depends on the *compactness* M_*/R_* of the object and it is read $\eta = \frac{GM_*}{R_* c^2}$; for the typical value of $M_{\rm NS}$ and $R_{\rm NS}$ of a neutron star $\eta \simeq 0.15$ (Frank et al. 2002).

1.1.1 The Eddington limit

For a fixed value of compactness, the luminosity of the source depends on the *mass accretion rate* $\dot{M}$, i.e. the amount of mass accreted in the time unit. Since the accretion luminosity is defined as

$$L_{\rm acc} = \frac{GM_*\dot{M}}{R_*},$$

under certain circumstances, it is possible to obtain a threshold on the luminosity related to the mass of the object and, therefore, a corresponding limit value for $\dot{M}$. The mass accretion rate is thought to be ruled by the interaction between the radiation from the central object and the accretion flow of matter coming from the companion. Basically, the proton-electron pairs in the plasma flow, which should fall onto the compact object, are pushed in the opposite direction, because the emitted radiation transfers to them an impulse through photon scattering. Under the assumption of steady state and spherical accretion of matter, if the accreting matter is mainly fully ionised hydrogen, the electromagnetic radiation interact with electrons by Thomson scattering. Indeed, the Thomson cross section is $\sigma_T = \frac{8}{3}\pi\frac{e^4}{m_{\rm cp}^2 c^4}$, where $m_{\rm cp}$ is the mass of the charged particle, then the cross-section of the protons is a factor 10^{-6} smaller than the electrons one and it is negligible here. Hence, the resulting force on the electrons is

$$F_N = \frac{\sigma_T S}{c}$$

in which S is the flow of energy per unit area per unit of time, called *Poynting vector*. However, due to the electrostatic attraction between electrons and protons, the particles pairs will be subjected to the gravitational force also:

$$F_g = \frac{G\ M_*\ (m_e + m_p)}{r^2} \simeq \frac{G\ M_*\ m_p}{r^2},$$

where r is the distance to the centre of the compact object. Thereby, if L is the luminosity of the source, the flux of energy is

$$S = \frac{L}{4\pi r^2} \tag{1.2}$$

and there will be a maximum value of L for which the radiation pressure is balanced by the gravitational force exerted on the protons. This value is known as *Eddington luminosity*:

$$L_{\rm Edd} = \frac{4\pi\ M_*\ G\ m_p\ c}{\sigma_T} \simeq 1.3 \times 10^{38}\ \frac{M_*}{M_\odot}\ {\rm erg\ s^{-1}}. \tag{1.3}$$

For $L > L_{\rm Edd}$ the radiation pressure becomes greater than the gravitational force and the accretion process can be blocked. This means that, if the luminosity is entirely due to accretion, it may go out.

The Eddington luminosity suggests that there is also a maximum value on the mass that the accreting object can reach. Thus, the Eddington limit implies a limit on the mass accretion rate $\dot{M}$, that can be obtained considering $L_{acc} = L_{Edd}$:

$$\dot{M}_{Edd} = \frac{4\pi\ R_*\ m_p\ c}{\sigma_T}. \tag{1.4}$$

Typical values of $\dot{M}$ are about $10^{16} - 10^{17}$ g s^{-1}, then, for a NS $L_{acc} = 1.26 \times 10^{38} M_{\rm NS}/M_\odot$ erg s^{-1}.

1.2 The Roche potential

Given two stars of mass M_1 and M_2 orbiting one another, it can be always defined an effective gravitational potential associated to the system. Considering a Cartesian reference frame centred on M_1 and rotating with M_2, with both the stars on the x-axis at an orbital separation a, it has to be taken into account that the centre of mass of the system will rotate also and a term due to centrifugal effects will be present. Under the assumption of point-like objects following circular orbits, the effective gravitational potential is the so-called *Roche potential*:

$$\Phi(x, y, z) = \frac{GM_1}{R_1} + \frac{GM_2}{R_2} + \frac{1}{2}\Omega^2 R_3^2, \tag{1.5}$$

where $R_1 = \sqrt{x^2 + y^2 + z^2}$ and $R_2 = \sqrt{(x-a)^2 + y^2 + z^2}$ are the distances of M_1 and M_2 from the origin of the reference frame, respectively, $R_3 = \sqrt{(x - x_c)^2 + y^2}$ (with $x_c = a\ M_2/(M_1 + M_2)$

abscissa of the centre of mass) is the distance of the rotation axis of the binary system with respect to the origin of the reference frame and Ω is the angular velocity of the system, related to the orbital separation as $\Omega = \sqrt{2G(M_1 + M_2)/a^3}$. The equipotential surfaces described envelope the two stars,

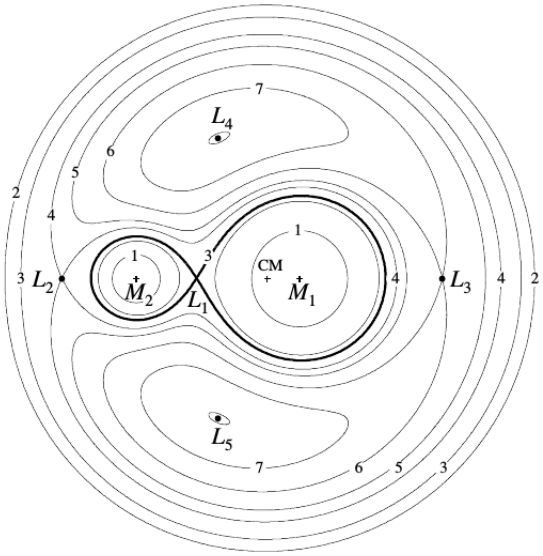

Figure 1.1: 2-dimensional representation of the Roche equipotential surfaces (labelled from 1 to 7) around a binary system. The five Lagrangian points and the position of the centre of mass are shown also (Frank et al. 2002).

and close to them they are closed and roughly spherical, forming the so-called *Roche lobes*. The point at which the two lobes are joined is the *inner Lagrangian point* L_1, one of the points in which the total resultant force is null. Two other Lagrangian points (L_2 and L_3) are located on the same x-axis of L_1 and two more (L_4 and L_5) on the orbital plane (see Figure 1.1). The inner Lagrangian point is an unstable equilibrium point and it plays a fundamental role in the mass transfer from CS to the compact object. Indeed, if at some stage of its evolution the companion increases its radius filling its Roche lobe, the pressure gradient will push the gas through L_1 into the Roche lobe of the primary, and the so-called *Roche lobe overflow* takes place. On the other hand, at some evolutionary phase, the companion can eject a substantial quantity of its mass through the Roche lobe in form of stellar wind, which can be gravitationally captured by the compact object (*stellar wind accretion*).

The geometry of the Roche lobes is not simple: since they are not actually spherical, an average radius is required to characterise them. This radius will be dependent on the orbital separation a and the mass ratio of the system $q = M_2/M_1$, where M_1 and M_2 are the masses of the compact

object and the companion, respectively. A good approximation is given by the radius of a sphere having the same volume as the lobe. It was estimated from Equation 1.5 for each possible value of q by Eggleton (1983) using numerical calculation, in the form

$$\frac{R_{L_2}}{a} = \frac{0.49\ q^{2/3}}{0.6\ q^{-2/3} + \ln\left(1 + q^{-1/3}\right)};$$

the value R_{L_1} is obtained replacing q with q^{-1}.

However, a simpler form was derived by Paczyński (1971) for $0.1 \leq q \leq 0.8$:

$$\frac{R_{L_2}}{a} = 0.462 \left(\frac{M_2}{M_1 + M_2}\right)^{1/3}; \tag{1.6}$$

R_{L_1} is obviously inferred replacing $\dfrac{M_2}{M_1 + M_2}$ with $\dfrac{M_1}{M_1 + M_2}$.

1.3 Classification of the X-Ray Binaries

The most luminous Galactic sources are XRBs hosting a NS or a BH which accretes matter from a companion. They are generally divided in two main classes, depending on the mass of the CS: the High Mass X-ray Binaries (HMXBs) in which the donor is a massive O-B star in main sequence, and the Low Mass X-Ray Binaries (LMXBs) in which the companion is a late-type cold star (Verbunt 1993). Another classification is based on the ratio of X-ray to optical luminosity (Bradt & McClintock 1983):

$$L_{\mathrm{X/opt}} = \frac{L_{\mathrm{X}}(2 - 10\ \mathrm{keV})}{L_{\mathrm{opt}}(3000 - 7000\ \text{Å})}$$

and it is $L_{\mathrm{X/opt}} \leq 10$ for an HMXB system, while $L_{\mathrm{X/opt}} \gg 10$ for a LMXB system. This classification is also in agreement with the previous one based on the mass of the donor, because an early type massive star shows a predominant optical luminosity; meanwhile, in a LMXB only the accretion disc contributes to the optical luminosity and then the X-ray emission is predominant. In general, the HMXBs are young systems ($< 10^7$ yrs) in which the accretion is driven by stellar wind. The hosted compact object can be a BH or a NS with a strong magnetic field ($\sim 10^{12}$ G) and the accretion timescale is about 10^5 yrs. On the other hand, the LMXBs are old systems ($> 10^9$ yrs) in which the accretion occur via Roche lobe overflow and the formation of an accretion disc around the compact object, which is a BH or a weakly magnetised NS ($10^8 - 10^9$ G); the accretion timescale is about $10^7 - 10^9$ yrs (Frank et al. 2002; Tauris & van den Heuvel

2006).

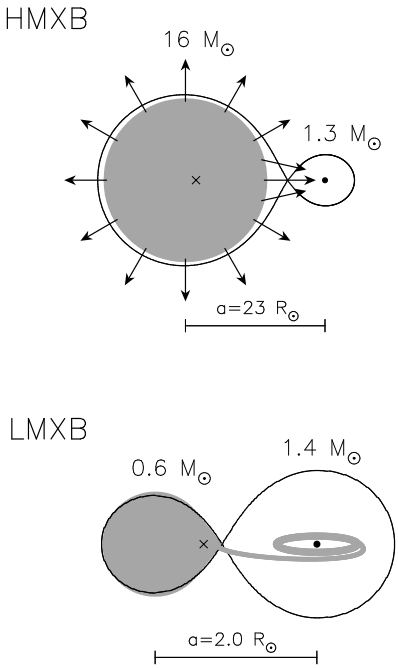

Figure 1.2: Examples of typical HMXB (top) and LMXB (bottom) hosting a NS. In the HMXB, NS is fed by a strong high-velocity stellar wind, while in a LMXB it is surrounded by an accretion disc fed by Roche-lobe overflow (Tauris & van den Heuvel 2006).

The strong magnetic fields of NSs can interact with the accretion flow, which is mainly composed of charged particles. Considering a dipolar magnetic field, the magnetic pressure will be larger close to the NS and, at certain radius, it will become larger than the ram pressure of the infalling matter, forcing the particle to move along the magnetic fields line. This radius represents the limit of the magnetosphere and, for a spherical accretion geometry, it is defined as the *Alfvèn radius*

$$R_{\rm A} = \frac{B^4\ R_{\rm NS}^{12}}{8\ G\ M_{\rm NS}\ \dot{m}}$$

where B is the magnetic field strength, $\dot{m}$ is the mass accretion rate in units of $\dot{M}_{\rm Edd}$ and $M_{\rm NS}$ and $R_{\rm NS}$ are mass and radius of the NS, respectively. The radius of the region in which the plasma is magnetic pressure dominated is the so-called *magnetospheric radius* $R_{\rm m} = \phi\ R_{\rm A}$, with $0.1 \leq \phi \leq 0.5$ depending on the distortion introduced in the magnetosphere by the interaction with the accretion disc (see e.g. Ghosh & Lamb 1979, 1991; Burderi et al. 2000, 2001, 2002).

For HMXBs, in which $B \sim 10^{12}$ G, $R_{\rm A} \sim 100 \times R_{\rm NS}$ and then the accretion will take place mainly at the magnetic poles. If the NS rotation axis does not coincide with the magnetic axis, a periodical modulation in the X-ray light-curve of the source will be observed at the same rotation period of the NS, when the magnetic axis intercepts the line of sight of the observer. The sources which show this behaviour are called *X-Ray pulsars* and they were discovered in the early 1970 thanks to the *Uhuru* satellite (Cen X-3, Giacconi et al. 1971a). For LMXBs, $B \sim 10^8$ G and then $R_{\rm A} \sim R_{\rm NS}$, hence the accretion flow would follow Keplerian orbits up to the NS surface and no X-ray pulsations would be expected from these sources. However, in 1998 the first X-ray pulsation from a LMXB system was detected (SAX J1808.4–3658, Wijnands & van der Klis 1998) and today

about 20 LMXB X-ray pulsars are known.

1.3.1 Low Mass X-ray binary systems

The LMXB systems hosting NS (hereafter NS-LMXBs) are the subject of this thesis; the formation mechanism and the secular evolution of these sources will be discussed in Chapter 2, while the characteristic of their spectral emission will be illustrated in Chapter 3.

The NS-LMXBs are sub-classified in *eclipsing* and *dipping* sources. Indeed, depending on the value of the inclination angle i of the line of sight with respect to the perpendicular to the orbital plane of the system, some typical features can be distinguished in their light-curves.

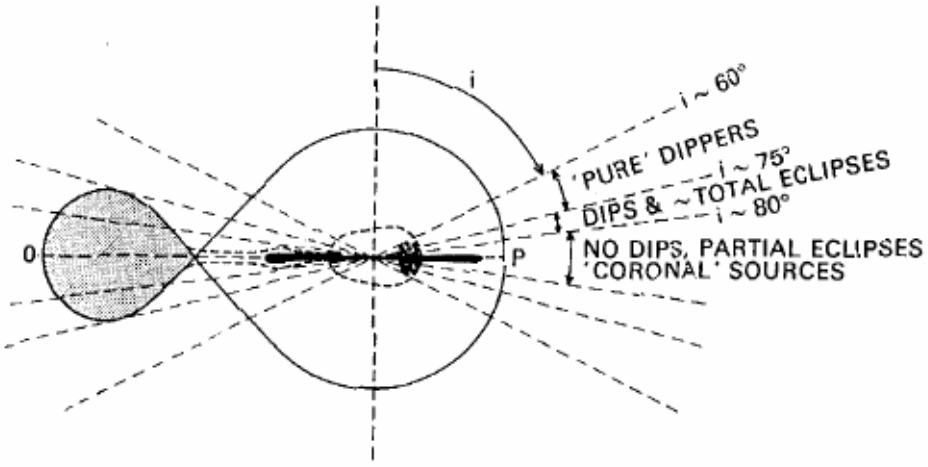

Figure 1.3: Axial cross-section of a NS-LMXB source with a schematic representation of the inclination angle classification (Frank et al. 2002).

For $75° \leq i \leq 90°$ eclipses are observed for the shielding effect due to the periodic transit of CS between the central radiation source and the observer. Since the CS is an opaque screen for the radiation, the eclipse is observable in the whole X-ray band. For $60° \leq i \leq 80°$, instead, localised decreasing of the count/rate, called *dips*, can be observed due to the presence of a bulge in the outermost region of the disc, where the steam of accreting matter coming from CS impacts the disc surface. The shielding effects, in this case, is due to photoelectric absorption, which depends on the temperature of the plasma and the energy of the incident photons and it is more efficient in the soft X-ray. Since dips and eclipses occur at the same orbital period of the system, through a timing analysis of their occurrence, the orbital period and all the other orbital parameters can be

estimated, defining the secular evolution of the system, (see Chapters 2 and 4).

As mentioned above, in NS-LMXB systems the matter lost by the companion star (mainly composed of ionised hydrogen) spills from the inner Lagrangian point in the NS Roche lobe and creates an accretion disc around the compact object. In some of these systems, the hydrogen accreted on the NS surface forms a thin layer, which grows until when, due to the strong gravitational field of the star, it reaches a density such that to trigger a violent thermonuclear explosion. It spreads over the entire NS surface, increasing its temperature by a few tens of millions of degrees. The burning of the hydrogen results in a rapid increase of the X-ray emission, followed by a slower exponential decay, which indicates the progressive cooling of the surface layer affected by the ignition. These phenomena are known as *Type-I bursts* and they can last few seconds up to few minutes. Their profile, indeed, shows a rise time (reaching the emission peak) ranging from 0.3 s to 10 s and a decay time between 5 s and 100 s. The sources showing Type-I bursts represent a sub-class of NS-LMXBs known as *X-ray bursters* (see Lewin et al. 1993; Lewin & van der Klis 2006, for a review).

The observation of Type-I bursts from a source is a signature of the presence of an accreting NS in the system. Actually, the burst mechanism requires a surface on which the hydrogen can be accumulated, and this excludes that the compact object is a BH. Moreover, it is observed that

$$\frac{\langle L_{\rm B}\rangle}{L_{\rm X}} \sim \frac{\Delta E_{NUCL}}{\Delta E_{ACC}} \lesssim \frac{0.009\ c^2 R_{\rm NS}}{G M_{\rm NS}}$$

where $\langle L_{\rm B}\rangle$ is the average burst luminosity, $L_{\rm X}$ is the persistent luminosity of the source, $M_{\rm NS}$ and $R_{\rm NS}$ are the NS mass and radius, respectively, and $0.009\ c^2$ erg g^{-1} is the maximum value assumed by $\Delta E_{\rm NUCL}$, which is obtained from the complete burning of hydrogen into heavy elements (Frank et al. 2002). This relation would not be satisfied if the accreting object were a white dwarf, for which $\Delta E_{\rm NUCL} > \Delta E_{\rm ACC}$. Furthermore, the observed burst spectra are blackbody-like:

$$F = \frac{A}{4D^2} F_{\rm bb}(T),$$

in which A is the emission area, D is the distance to the source and $F_{\rm bb}(T)$ is the blackbody flux with temperature T observed during the burst. In order to obtain an estimation of A, a spherical surface of radius R and a distance $D \sim 8.5$ kpc are supposed (because, from observations, the most of the X-ray bursters are located close to the Galactic centre). From the spectral fits, $R \sim 10$ km, which is the typical value for a NS radius. In conclusion, a model in which bursts are the

result of a thermonuclear fusion reaction on the surface of an accreting NS is in agreement with the observations.

1.4 Emitted spectrum of an accreting NS

What has been said to date allows to make few comments about the spectral range in which an accreting NS emits. Three temperatures related to its spectrum can be defined (Frank et al. 2002):

- the *radiation temperature*, which characterises the continuum (non-thermal) spectrum emitted by a body and it is defined as
$$T_{\rm rad} = \frac{h\nu}{k_{\rm B}},$$
where h is the Planck constant, ν is the frequency of the emitted photons and $k_{\rm B}$ is the Boltzmann constant;

- the *blackbody temperature*, i.e. the temperature the source would have if the given power were radiated as a blackbody spectrum:
$$T_{bb} = \left(\frac{L_{\rm acc}}{4\pi(R_{\rm NS})^2\sigma}\right)^{1/4},$$
in which $L_{\rm acc}$ is the accretion luminosity, σ is the Stefan-Boltzmann constant and $R_{\rm NS}$ the NS radius;

- the *thermalisation temperature*, defined as the temperature the accreting matter would reach if all its potential energy were converted into thermal energy, assuming that there are no other sources of photons. Hence, for each proton-electron pair there is a released potential energy equal to
$$E_p = \frac{G\ M_{\rm NS}\ (m_p + m_e)}{(R_{\rm NS})^2} \simeq \frac{G\ M_{\rm NS}\ m_p}{(R_{\rm NS})^2},$$
where $M_{\rm NS}$, m_p and m_e are the NS, proton and electron masses, respectively; and an associated thermal energy $E_{\rm th} = 2\ \frac{3}{2}\ k_{\rm B}\ T$. Balancing the two energies, it is obtained
$$T_{\rm th} = \frac{G\ M_{\rm NS}\ m_p}{3\ R_{NS}\ k_B}.$$

If the accretion flow is optically thick, the emitted radiation will reach thermodynamic equilibrium with the matter before reaching the observer and therefore $T_{\rm rad} \sim T_{\rm bb}$. On the other hand, if the

accreting matter has a low density, there will be few collisions and the distribution of the outgoing photons will not be thermalised, then $T_{\rm rad} \sim T_{\rm th}$. In general, assuming a constant and uniform temperature for the radiating material, it has to be $T_{\rm bb} \lesssim T_{\rm rad} \lesssim T_{\rm th}$. For a NS of mass $M_{\rm NS} \sim M_{\odot}$ and radius $R_{\rm NS} \sim 10$ km, $T_{\rm th} \sim 5.5 \times 10^{11}$ K; or, in terms of energy: $k_{\rm B}T_{\rm th} \sim 50$ MeV. Meanwhile, taken $L_{\rm acc} \simeq L_{\rm Edd} \simeq 10^{38}$ erg s^{-1}, $T_{\rm bb}$ will be $\sim 10^7$ K, or equivalently $k_{\rm B}T_{bb} \sim 1$ keV. Therefore, it can be concluded that the energies of the emitted photons due to accretion process can vary in the range 1 keV $\lesssim\ h\nu\ \lesssim 50$ MeV.

1.5 The accretion disc

In the Roche lobe overflow regime, the accreting matter loss by CS has a non-zero angular momentum, because the inner Lagrangian point, through which the matter spills from the CS Roche lobe to that one of the compact object, rotates also around the centre of mass of the system. Then, the velocity of the accreting matter has both radial and tangential component. The combined effects of the tangential velocity and the non-zero viscosity of the accreting matter are the reasons for which it follows a spiralling orbit around the object forming an accretion disc, in which the plasma is subjected to viscous forces whose nature is still under investigations (see e.g. Balbus & Hawley 1991, and references therein).

In this section, the steady thin accretion disc approximation and its implication will be described; the main types of disc instabilities will be presented also.

1.5.1 Steady thin discs

In the so-called *steady thin disc approximation* (Pringle & Rees 1972) the accretion disc is seen as a two-dimensional gas flow, because the accretion material is confined very close to the orbital plane of the system. Assuming cylindrical polar coordinates $(R,\ \phi,\ z)$, the matter lies very close to the plane $z = 0$.

Each disc element follows a Keplerian orbit with an angular velocity Ω obtained matching centrifugal and gravitational forces for a mass element m:

$$\Omega = \left(\frac{GM_{NS}}{R^3}\right)^{1/2}, \tag{1.7}$$

where M_{NS} is the mass of the neutron star and R is the distance of m from the NS surface, and a

circular velocity

$$v_\phi = R\ \Omega(R). \tag{1.8}$$

At $R = R_*$, given $G = 6.67 \times 10^{-8}$ cm^3 g^{-1} s^{-2}, $M_{NS} = 1.4\ M_\odot = 1.4 \cdot 2 \times 10^{33}$ gr and $R_*^3 = 10^{18}$ cm, it is

$$\Omega = \left(\frac{6.67 \times 10^{-8} \cdot 1.4 \cdot 2 \times 10^{33}}{10^{18}} \right)^{1/2} \simeq 4 \times 10^3 \,\mathrm{rad\ s^{-1}}$$

and $v_\phi \simeq 4 \times 10^3\ R_* \simeq 4 \times 10^9$ cm, then $\dfrac{v_\phi}{c} \sim 0.1$. Each mass element has to possess also a radial velocity v_R, dependent on R and time, which is assumed much smaller than v_ϕ and to be negative near the NS surface, in order to allow the accretion.

Assuming the disc thickness to be zero and $\Sigma(R,t)$ the disc surface density, the surface of an annulus with radius between R and $R + \Delta R$ is

$$A = \pi(R + \Delta R)^2 - \pi R^2 = \pi R^2 + 2\pi R \Delta R + \pi \Delta R^2 - \pi R^2,$$

then, neglecting the term of second order in ΔR, it is found $A \simeq 2\pi R \Delta R$. Thus, the mass confined in the annulus is $M_R = 2\pi R\ \Delta R\ \Sigma(R,t)$, with a total angular momentum

$$J = M_R R^2 \Omega = 2\pi\ R^3 \Delta R\ \Sigma(R,t)\Omega\ .$$

A single annulus receives a flux of material from the neighbouring annuli: the incoming material from the inner part of the disc is

$$\Sigma(R,t)\ v_R(R,t)\ 2\pi R, \tag{1.9}$$

where $v_R > 0$ because the material is moving to outer region. On the other hand, the material coming from the outer part is

$$\Sigma(R,t)\ v_R(R,t)\ 2\pi R - \Sigma(R+\Delta R,t)\ v_R(R+\Delta R,t)\ 2\pi(R+\Delta R), \tag{1.10}$$

in this case $v_R < 0$ because the flux is towards the inner region.

Rewriting Equation 1.10 such as

$$2\pi\left[\Sigma(R+\Delta R,t)\ v_R(R+\Delta R,t)\ (R+\Delta R) - \Sigma(R,t)\ v_R(R,t)\ R\right] \tag{1.11}$$

it can be noticed that, if divided and multiplied by ΔR, it is the variation rate for the function

$f = R\Sigma v_R$. Then, if ΔR approaches to 0, Equation 1.11 is equal to

$$2\pi\Delta R\frac{\partial}{\partial R}(R\Sigma v_R)$$

Matching with the mass variation in the annulus:

$$-2\pi\Delta R\frac{\partial}{\partial R}(R\Sigma v_R) = \frac{\partial M}{\partial t} = \frac{\partial}{\partial t}(2\pi R\Delta R\Sigma) = 2\pi R\Delta R\frac{\partial \Sigma}{\partial t}$$

and simplifying, it can be found

$$R\frac{\partial \Sigma}{\partial t} + \frac{\partial}{\partial R}(R\Sigma v_R) = 0, \tag{1.12}$$

that is the *mass conservation equation.*

Taking into consideration the transport of momentum due to the torque $G_\nu(R,t)$, the variation of total angular momentum of the annulus reads

$$\begin{aligned}&\frac{\partial}{\partial t}(MR^2\Omega) = \frac{\partial}{\partial t}(2\pi R^3\Delta R\Sigma(R,t)\Omega) = \\ &= v_R(R,t)2\pi R^3\Sigma(R,t)\Omega(R) - v_R(R+\Delta R,t)2\pi(R+\Delta R)^3\Sigma(R+\Delta R,t)\Omega(R+\Delta R) + \frac{\partial G_\nu}{\partial R}\Delta R\end{aligned}$$

Rewriting the last expression such as

$$-2\pi\left[v_R(R+\Delta R,t)(R+\Delta R)^3\Sigma(R+\Delta R,t)\Omega(R+\Delta R) - v_R(R,t)R^3\Sigma(R,t)\Omega(R)\right] + \frac{\partial G_\nu}{\partial R}\Delta R$$

and dividing and multiplying by ΔR, it can be obtained

$$\begin{aligned}&\frac{\partial}{\partial t}(R\Sigma(R,t)R^2\Omega(R) = \\ &= \frac{v_R(R+\Delta R,t)(R+\Delta R)^3\Sigma(R+\Delta R,t)\Omega(R+\Delta R) - v_R(R,t)R^3\Sigma(R,t)\Omega(R)}{\Delta R} + \frac{1}{2\pi}\frac{\partial G_\nu}{\partial R}\end{aligned}$$

Finally, for $\Delta R \longrightarrow 0$, it is *the conservation equation for angular momentum*:

$$R\frac{\partial}{\partial t}(\Sigma R^2\Omega) + \frac{\partial}{\partial R}(R\Sigma v_R R^2\Omega) = \frac{1}{2\pi}\frac{\partial G_\nu}{\partial R}, \tag{1.13}$$

where $G_\nu(R,t) = 2\pi R\nu\Omega(R,t)R^2\Omega^{'}$ is the torque (Frank et al. 2002), with $\Omega^{'} = \dfrac{\partial\Omega}{\partial R}$ and ν is the plasma viscosity.

If a steady state condition $\dfrac{\partial\Omega}{\partial t} = 0$ is assumed, using Equation 1.12, Equation 1.13 can be

simplified as

$$R\Sigma v_R \frac{\partial}{\partial R}(R^2\Omega) = \frac{1}{2\pi}\frac{\partial G_\nu}{\partial R}, \tag{1.14}$$

from which

$$R\Sigma v_R = \frac{1}{2\pi}\frac{\partial G_\nu}{\partial R}\frac{1}{R^2\Omega'}. \tag{1.15}$$

Substituting Equation 1.15 in Equation 1.12, it is

$$R\frac{\partial \Sigma}{\partial t} = -\frac{\partial}{\partial R}\left(\frac{1}{2\pi(R^2\Omega)'}\frac{\partial G_\nu}{\partial R}\right) \tag{1.16}$$

Since $G_\nu(R,t) = 2\pi R\nu\Omega(R,t)R^2\Omega'$, drawing Ω from Equation 1.7 it follows:

$$R\frac{\partial \Sigma}{\partial t} = -\frac{\partial}{\partial R}\left[\frac{1}{2\pi\frac{\partial}{\partial R}\left(R^2\left(\frac{GM}{R^3}\right)^{1/2}\right)}\frac{\partial}{\partial R}(2\pi R\nu\Sigma R^2\Omega')\right]$$

but

$$\frac{\partial}{\partial R}\left[R^2\left(\frac{GM}{R^3}\right)^{1/2}\right] = (GM)^{1/2}\frac{\partial}{\partial R}(R^{1/2}) = \frac{1}{2}(GM)^{\frac{1}{2}}R^{-1/2}$$
$$\Omega' = \frac{\partial}{\partial R}\left(\frac{GM}{R^3}\right)^{1/2} = -\frac{3}{2}(GM)^{1/2}R^{-5/2}$$

and, substituting these two equations in 1.16, finally, the *time evolution equation for surface density of a keplerian disc* is found:

$$\frac{\partial \Sigma}{\partial t} = \frac{3}{R}\frac{\partial}{\partial R}\left(R^{1/2}\frac{\partial}{\partial R}(\nu\Sigma R^{1/2})\right). \tag{1.17}$$

Moreover, combining Equation 1.12 with Equation 1.17 and integrate for R, the *radial velocity of a mass element in the disc* is obtained:

$$v_R = -\frac{3R^{-1/2}}{\Sigma}\frac{\partial}{\partial R}(\nu\Sigma R^{1/2}). \tag{1.18}$$

The time evolution of the surface density $\Sigma(R,t)$ of a ring with mass m in a Keplerian orbit at $R = R_0$ is shown in Figure 1.4. It can be assumed that at the initial time $t = 0$ all the mass m in the ring is concentrated in $R = R_0$. If the ring is released, since the specific angular momentum is $l = R^2\Omega \propto R^{1/2}$, it will lose quickly angular momentum because a small fraction of m, moving towards the outer parts of the disc, takes it away. Therefore, the greatest part of the matter moves

inwards ($R < R_0$) and, if $\tau \gg 1$, a small part of the matter has carried out the greatest part of the initial angular momentum (Papaloizou & Pringle 1977; Lin & Papaloizou 1979).

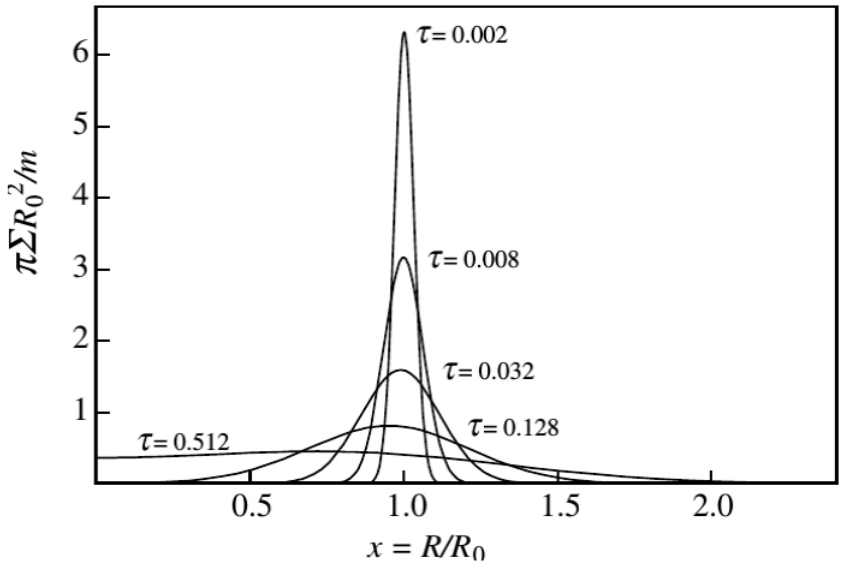

Figure 1.4: Surface density Σ of a ring with mass m in a Keplerian orbit at $R = R_0$ as a function of $x = R/R_0$ and the dimensionless time variable $\tau = 12\nu t {R_0}^{-2}$ (Pringle & Rees 1972)

The time required for the formation of an accretion disc in a LMXB system can be estimated from τ. The viscous time scale, which describes the changes of the radial structure of the disc, is defined as (Frank et al. 2002)

$$t_{visc} \simeq \frac{R^2}{\nu} \tag{1.19}$$

whence $\nu = \frac{t}{t_{visc}} R^2$. Substituting in the expression for τ:

$$\tau = 12\ \nu\ t\ {R_0}^{-2} = 12\ \frac{t}{t_{visc}} \left(\frac{R}{R_0}\right)^2 \tag{1.20}$$

and for $R = R_0$:

$$t = \frac{\tau}{12}\ t_{visc}. \tag{1.21}$$

with $t_{visc} = 3 \times 10^5 \alpha^{-4/5} \dot{M}_{16}^{-3/10} m_1^{1/4} R_{10}^{5/4}\ s$ (α-*disc solution*, from Shakura & Sunyaev 1973, see below). R_{10} is in this case the circularisation radius R_0, i.e. the radius at which the flow of matter coming from CS forms the first ring of the accretion disc around NS. Assuming that the mass ratio

of the system is $q = \frac{M_{CS}}{M_{NS}} \geq 0.5$, the circularisation radius is $R_0 = 0.6\ P_{day}^{2/3}\ R_\odot\ cm$, with P_{day} the orbital period in units of days and $R_\odot$ the radius of the Sun (Frank et al. 2002).

Using typical values $P \sim 7\ h$, $\alpha \sim 0.1$, $\dot{M}_{16} \sim 1$ and $m_1 \sim 1.4$ (that is the mass of NS in units of solar mass $M_\odot$), so

$$R_0 \simeq 1.8 \cdot 10^{10}\ cm \tag{1.22}$$

$$t_{visc} \simeq 2 \cdot 10^6 \cdot 1.8^{5/4} s \simeq 4 \cdot 10^6 s. \tag{1.23}$$

Finally, using a value of τ at which the disc is already formed ($\tau = 0.512$ from Figure 1.4), it is obtained

$$t \sim 2 \cdot 10^5 s \sim 50\ h.$$

Hence, for a LMXB system the accretion disc is formed in a little over two days only.

To examine the steady-state structure of the disc, $\dfrac{\partial}{\partial t} = 0$ is set in the conservation equations (Equation (1.12) and (1.13)), then

$$\frac{\partial}{\partial R}(R\Sigma(R,t)v_R) = 0, \tag{1.24}$$

$$R\Sigma v_R R^2 \Omega = \frac{G_\nu}{2\pi} + \frac{\mathcal{A}}{2\pi} \tag{1.25}$$

where $\mathcal{A}$ is a constant related to the angular momentum flow.

From Equation 1.24 it can be find that the mass of an annulus is constant with respect to R and this implies that the inflow of matter from the neighbouring annuli does not change and it is stable through each point of the ring, so the accretion rate results:

$$\dot{M} = 2\pi R\Sigma(-v_R)\ g/s, \tag{1.26}$$

where $v_R < 0$ is the inward velocity. Equation 1.25 is obtained integrating Equation 1.13 for R and gets

$$-\Sigma\nu\Omega' = \Sigma\Omega(-v_R) + \frac{\mathcal{A}}{2\pi R^3}. \tag{1.27}$$

To determine $\mathcal{A}$, the disc is assumed close to the NS surface ($R = R_*$). In order to not get its broke-up speed, the star angular velocity has to be $\Omega_* < \Omega_k(R)$, where $\Omega_k(R)$ is the Keplerian angular velocity (1.7). Thus, we can image a layer of radius $R = b$ between the NS and the accretion disc, the so-called *boundary layer*, where Ω decreases from Ω_k to Ω_*. If $b \ll R_*$, for $R = R_* + b$

the boundary condition is $\Omega^{'} = 0$, indeed the boundary layer has no structure and $G_\nu(R,t) = 0$. Therefore, using Equation 1.27 and imposing the boundary condition $\Omega^{'} = 0$, it can be obtained

$$\mathcal{A} = 2\pi R_*^3 \Sigma v_R \Omega(R_* + b)|_{R_*+b}.$$

with $\Omega(R_* + b)|_{R_*+b} = \left(\frac{GM}{R_*^3}\right)^{1/2}(1 + O(b/R_*))$. For $b \ll R_*$, then $O(b/R_*) \sim 0$ and using 1.26, $\mathcal{A}$ can be read as

$$\mathcal{A} = \dot{M}(GMR_*)^{1/2}, \tag{1.28}$$

that represents the angular momentum (in units of time) transferred from the disc to the NS.

Now, combining Equations 1.27, 1.28, 1.26 and $\Omega_k(R)$, it can be found that

$$\nu\Sigma = \frac{\dot{M}}{3\pi}\left[1 - \left(\frac{R_*}{R}\right)^{1/2}\right] \tag{1.29}$$

These results can be used to obtain an expression for *viscous dissipation per unit disc face area* that is independent on ν:

$$D(R) = \frac{3GM\dot{M}}{8\pi R^3}\left[1 - \left(\frac{R_*}{R}\right)^{1/2}\right]. \tag{1.30}$$

This suggests that the energy flux through a face area of a steady thin disc does not depend on the plasma viscosity.

The factor $\left[1 - \left(\frac{R_*}{R}\right)^{1/2}\right]$ in Equation 1.30 is the correction $O(b/R_*)$ to the Keplerian velocity in presence of viscous forces. If this correction were zero, there would not be any viscous dissipative effects. In particular, $D(R_*) = 0$ then there are no viscous effects on the NS surface. Moreover, $D(R)$ is an energy flux and, integrating for the surface area of a ring with a radius between R_1 and R_2, its luminosity results

$$L(R_1, R_2) = 2\int_{R_1}^{R_2} D(R) 2\pi R dR. \tag{1.31}$$

If $R_1 = R_*$ and R_2 goes to an infinite distance we obtain the total disc luminosity:

$$L_{DISC} = \frac{GM\dot{M}}{2R_*} = \frac{1}{2}L_{ACC}. \tag{1.32}$$

Interesting information about viscous dissipation can be deduced from Equation 1.30: if an annulus with radius between R_0 and $R_0 + dR$ is considered, the dissipation through its face surfaces

is

$$2 \cdot 2\pi R dR D(R) = \frac{3GM\dot{M}}{2R^2}\left[1 - \left(\frac{R_*}{R}\right)^{1/2}\right] dR, \tag{1.33}$$

in which $\frac{GM\dot{M}}{2R^2}$ is the gravitation energy loss by the accreting material between R_0 and $R_0 + dR$ and $\frac{GM\dot{M}}{2R^2}\left[1 - \frac{3}{2}\left(\frac{R_*}{R}\right)^{1/2}\right] dR$ is the energy released for $R < R_0$.

For $1 - \frac{3}{2}\left(\frac{R_*}{R}\right)^{1/2} < 0$, i.e. $R > \frac{9}{4}R_*$, the energy released because of the viscosity is grater than the emission due to the loss of gravitational energy, which for $R \gg R_*$ is almost negligible. Instead, this is the greatest contribution for $R_* < R < \frac{9}{4}R_*$ where the gravitational force is the strongest.

Finally, it needs to be stressed that the viscosity redistributes the released energy but have no effects on the total emission (Equation 1.33 is indeed independent from the viscosity).

Since the disc has to be geometrically thin in this approximation, no flow of matter in z-direction is assumed and then the *hydrostatic equilibrium equation* for the disc reads:

$$\frac{1}{\rho}\frac{\partial P}{\partial z} = \frac{\partial}{\partial z}\left[\frac{GM}{(R^2 + z^2)^{1/2}}\right]. \tag{1.34}$$

In the geometrical thin disc approximation $z \ll R$, and this one becomes

$$\frac{1}{\rho}\frac{\partial P}{\partial z} = -\frac{GMz}{R^3}; \tag{1.35}$$

furthermore $\frac{\partial P}{\partial z} \sim \frac{P}{H}$, with $H \ll R$ *scale-height* in the z-direction. As $P \propto \rho c_s^2$ (where c_s is the speed of sound) and $z \sim H$, then

$$H = c_s R\left(\frac{R}{GM}\right)^{1/2}; \tag{1.36}$$

$$c_s \ll \left(\frac{R}{GM}\right)^{1/2}. \tag{1.37}$$

Since th local Keplerian velocity of a disc mass element at a radius R is $v_K = \left(\frac{GM}{R}\right)^{1/2}$, hence $v_K \gg c_s$, i.e. the circular matter velocity is *highly supersonic* and it is predominant. If the radial

component of the Euler equation is took into account:

$$v_R \frac{\partial v_R}{\partial R} - \frac{v_\phi^2}{R} + \frac{1}{\rho}\frac{\partial P}{\partial R} + \frac{GM}{R^2} = 0 \tag{1.38}$$

and, because of $\frac{GM}{R^2} \gg \frac{c_s}{R}$ (from Equation 1.36) and $\frac{1}{\rho}\frac{\partial P}{\partial R} \sim \frac{1}{\rho}\frac{P}{R} \sim \frac{c_s^2}{R}$ (at zero-order), the pressure term can be negligible with respect to the gravitational one. Then, the interactions between the particles of the plasma disc are negligible.

Furthermore, if Equation 1.26 and 1.29 are combined, it can be obtained that

$$v_R = -\frac{3\nu}{2R}\left[1 - \left(\frac{R_*}{R}\right)^{1/2}\right]^{-1} . \tag{1.39}$$

Generally, $R_* \ll R$ and $\nu \sim \alpha c_s H$ (with $\alpha \lesssim 1$ *disc viscosity parameter*), so $v_R \ll c_s$ because $\frac{H}{R} \ll 1$. Hence, the radial velocity of a disc mass element at radius R is *highly subsonic* (see Frank et al. 2002, for more details).

Therefore, Equation 1.38 becomes $\frac{v_\phi}{R} \simeq \frac{GM}{R^2}$, from which $v_\phi \simeq \left(\frac{GM}{R}\right)^{1/2}$; in the end, the circular velocity is Keplerian.

All of which suggests that, if a temperature variation occurs in an annulus of the disc, the information will be transferred just radially, because v_ϕ is highly supersonic, and the disc readapts its temperature after a timescale τ_ν depending on the plasma viscosity. Thence, to define its temperature, the disc must be in stationary conditions (i.e. there must be thermodynamic equilibrium between radiation and matter), otherwise its structure and thermodynamics can be analysed by numerical simulations only.

To analyse the local structure of the disc, the temperature and pressure gradient in the disc are assumed to be in the z-direction, then at a fixed radius R, the vertical structure of the disc can be considered as an one-dimensional stellar structure and reads:

$$\frac{1}{\rho}\frac{\partial P}{\partial R} = -\frac{GM}{R^2} . \tag{1.40}$$

Assuming the disc composed of an ideal gas, its temperature is constant in z-direction and equal to the plane disc temperature T_c. The total pressure can be wrote as the sum of gas pressure and

radiation pressure (the first and the second term in Equation 1.41, respectively):

$$P = \frac{\rho k_B T_c}{\mu m_p} + \frac{4\sigma}{3c} T_c^4, \tag{1.41}$$

with k_B Boltzmann constant, $T_c = T_c(R)$ and σ the Stefan-Boltzmann constant. For the previous assumptions, since ρ is independent to z, using Equation 1.35 it can be found:

$$\frac{1}{\rho} c_s^2 \frac{\partial \rho}{\partial z} = -\frac{GMz}{R^3}. \tag{1.42}$$

Solving this equation, the disc density in vertical isothermal approximation is inferred (see Frank et al. 2002, for more details):

$$\rho = \rho_c(R) e^{-\frac{z^2}{2H^2}}. \tag{1.43}$$

Moreover, the disc is assumed optically thick (i.e. the optical depth $\tau \gg 1$), because the presence of a radiation flux suggests that photons and matter are thermalised. Therefore, a blackbody emission can be observed for a fixed radius R, but this implies an effective temperature gradient in z-direction, thus the flux of energy through a surface with $z = constant$ is (see Frank et al. 2002, and reference therein)

$$F(z) = -\frac{16\sigma T^3}{3\kappa_R \rho} \frac{\partial T}{\partial z}.$$

Defining $\tau = \rho H \kappa_R$ (with κ_R *Rosseland mean opacity*) and using $\dfrac{\partial T}{\partial z} \sim \dfrac{T}{H}$, it becomes

$$F(z) \simeq \frac{4\sigma T^4}{3\tau}. \tag{1.44}$$

The flux of radiant energy is also equal to the energy loss due to viscous dissipation, and using Equation 1.30, the *steady disc equation* can be write:

$$\frac{4\sigma}{3\tau} T_c^4 = \frac{3}{8} \frac{GM\dot{M}}{\pi R^3} \left[1 - \left(\frac{R_*}{R} \right)^{1/2} \right]. \tag{1.45}$$

1.5.2 Standard model for a steady accretion disc

Proposed by Pringle & Rees (1972) and theorised by Shakura & Sunyaev (1973), this model allows to solve Equation 1.45. It assumes valid the so-called α-*prescription* for viscosity: $\nu = \alpha c_s H$, and it presumes the Rosseland mean opacity is well-approximated by *Kramer's law*:

$\kappa_R = 5 \cdot 10^{24} \rho T_c^{-7/2}\ cm^2/g$. Neglecting numerical factors and writing the solution for $R_{10} = R/10^{10}$, $m_1 = M/M_\odot$ and $\dot{M} = \dot{M}_{16}/10^{16}$, it can be obtained:

$$\begin{cases} H = 1.7 \cdot 10^8 \alpha^{-1/10} \dot{M}_{16}^{3/20} m_1^{-3/8} R_{10}^{9/8} f^{3/5}\ cm; \\ \rho = 3.1 \cdot 10^{-8} \alpha^{-7/10} \dot{M}_{16}^{11/20} m_1^{5/8} R_{10}^{-15/8} f^{11/5}\ g\ cm^{-3}; \\ T_c = 1.4 \cdot 10^4 \alpha^{-1/5} \dot{M}_{16} m_1^{1/4} R_{10}^{-3/4} f^{6/5}\ K; \\ v_R = 2.7 \cdot 10^4 \alpha^{4/5} \dot{M}_{16}^{3/10} m_1^{-1/4} R_{10}^{-1/4} f^{-14/5}\ cm/s, \end{cases} \tag{1.46}$$

where $f = \left[1 - \left(\frac{R_*}{R}\right)^{1/2}\right]^{1/4}$ is the relativistic correction. α has always an exponent < 1, and this suggests that it has no influence on the magnitude of these quantities, but on the other hand, its real value can not found comparing theoretical results with observations.

From these solutions:

$$\frac{H}{R} = 1.7 \cdot 10^{-2} \alpha^{-1/10} \dot{M}_{16}^{3/20} m_1^{-3/8} R_{10}^{1/8} f^{3/5}. \tag{1.47}$$

For $R \gg R_*$, $H/R \propto \alpha^{-1/10} R^{1/8}$, thus the disc will be concave if H/R will increase with R (i.e. α grows slower than $R^{5/4}$). For values of parameters which satisfy Equation 1.47, a typical result is $H/R \simeq 0.02$ (Frank et al. 2002).

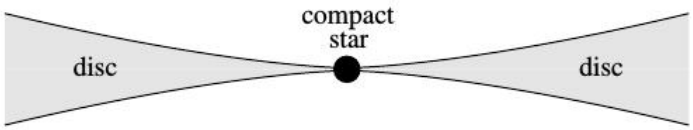

Figure 1.5: Representation (not to scale) of a section of a concave thin accreting disc with $\alpha =$ *constant*.

Moreover, from Equation 1.46 the opacity results

$$\kappa_R = \tau/\sigma = 36 \dot{M}_{16}^{-1/2} m_1^{1/4} R_{10}^{3/4} f^{-2}, \tag{1.48}$$

but for $T \gtrsim 10^4\ K$ the dominant process is the electron scattering, which implies an opacity given by

$$\kappa_{es} \simeq \sigma_T / m_p \simeq 0.4\ cm^2/g, \tag{1.49}$$

where σ_T is the *Thomson cross section* and m_p is the mass of a proton. Then, the Kramer opacity

κ_R is dominant for

$$R \gtrsim 2.5 \cdot 10^7 \dot{M}_{16}^{2/3} m_1^{1/3} f^{8/3} \; cm. \tag{1.50}$$

Similarly, the pressures to whom the plasma in the disc is subjected can be also evaluated: the radiation pressure

$$P_r = \frac{\sigma T^4}{3c} = \frac{a}{3} T^4$$

with $a = 7.6 \cdot 10^{-15}$ *erg/cm radiation constant*, and the gas pressure

$$P_g = nkT = \rho R_g T$$

where $R_g = k_B \cdot N_A = 8.31 \cdot 10^7$ *erg mol*$^-$1 *K*$^-$1 is the *molar gas constant*. Substituting $T = T_c$ and ρ from Equation 1.46, for $m_1 = 1.4$ it is read

$$\frac{P_r}{P_g} = 2.8 \cdot 10^{-3} \alpha^{1/10} \dot{M}_{16}^{7/20} R_{10}^{-3/8} f^{7/5}. \tag{1.51}$$

Then, if it results greater than 1, the plasma in the disc is not considered as an ideal gas. For a value of R less than Equation 1.50, instead, κ_{es} is the dominant opacity and $P_r/P_g \ll 1$, therefore the assumptions made above are still valid.

1.5.3 The disc instability

The model proposed by Shakura & Sunyaev (1973) take into account a simple hypothesis: it supposes that the gravitational potential energy turns into heat by the viscous stress action and the $\alpha-$prescription gives us a phenomenological description of this one without investigating the origin. Moreover, their solution requires that the mass accretion rate is constant, and this is not easy to happen. In most of the cases, it is not constant and the disc is not steady, but it is affected by two principal types of instabilities: the first is due to the ionisation of the hydrogen and the other one to the radiation pressure.

The *hydrogen ionisation instability* (Frank et al. 2002; Cannizzo & Reiff 1992) occurs at low luminosity and it is related to the thermal and viscous instability of the flow in the disc. An α-disc is in a stable state and it is mainly composed of neutral hydrogen (lower branch in Figure 1.6). Take into consideration an annulus at a radius R: a very small increase of the mass causes an increase of the density and of the (outgoing) mass accretion rate, after which the system returns to its initial condition of equilibrium. If the mass enhancement exceeds a certain critical value, the increase

of the opacity is so relevant to results in a rise of temperature, because the interaction between photons and matter gets stronger. This entails the ionisation of the hydrogen, because the emitted photons are re-absorbed and the temperature further increases, until the hydrogen is fully ionised (jump to the upper branch in Figure 1.6). At this point, some of the photons escape because the free-free process cross section reduces (it is $k_{ff} \propto 10^{23}\rho T^{-7/2}$) and the annulus slowly cools down. At the same time, the ionisation of the hydrogen causes also an increasing in the outgoing flow of material, that becomes greater than the ingoing one, and the annulus empties. Therefore, the density and opacity drop and the photons run away. Subsequently, the temperature falls down, until the hydrogen recombines and the accreting mass entering the annulus exceeds the outgoing one and the disc builds up again (fall to the lower branch in Figure 1.6). Hence, the process can restart if the system is perturbed again.

The hydrogen ionisation limit cycle is a local instability that occurs at fixed radius (Figure 1.6), but the variations in the single annulus can propagate to the other ones by means of the heat propagation and the mass transfer, having global consequences. Thus, the entire disc can exhibit a limit cycle instability between an α-disc condition and a quiescent state in which the hydrogen is fully ionised (Done et al. 2007).

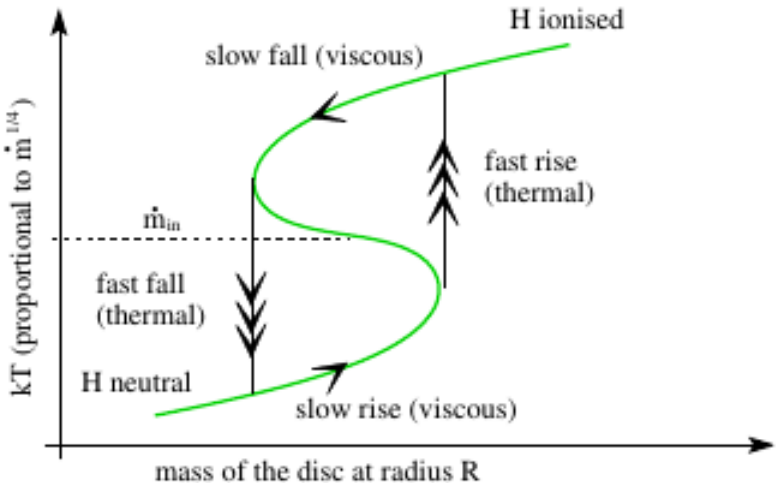

Figure 1.6: The local effects of the hydrogen ionisation limit cycle instability for the variation of the mass accretion rate at a given radius R (Done et al. 2007).

There are systems, however, in which the radiation from the disc is so strong to avoid the hydrogen recombination. This means that the disc is maintained at a high temperature and that causes an important escape of material, not balanced from the accretion flow from the companion

star and in some cases the disc can be wiped out. Then, the temperature and the X-rays emission go down rapidly and the outer temperature of the disc can decrease below the hydrogen ionisation threshold, with a consequent inward cooling wave. In general, anyway, the discs have a convex profile and the presence of a sort of corona, due to an outflow from the disc, can shade the outer parts of the disc from the radiation oncoming from the inner regions (White & Holt 1982).

The *radiation pressure instability* or *Lightman-Eardley instability* (Lightman & Eardley 1974) can occur, instead, at high temperature and mass accretion rate (i.e. in the inner regions), when the disc is no longer gas pressure dominated. A rise in temperature causes an increase of pressure and, subsequently, in the viscosity and in the heat released, because there is a growth in mass of the annulus. If this increase exceeds the critical value, the disc is no longer in a stable state. For the same reason shown above, it determines an increase of the density such as the emitted photons are almost totally absorbed and the temperature and viscosity rise up, until the radiation pressure exceeds the gas pressure (jump to the upper branch in Figure 1.7). Because there is no stable solution for so high $\dot{M}$ in the Shakura and Sunyaev equations, in this scenario the destruction of the disc is attended without a drop of the opacity (Done et al. 2007). Nevertheless, the radial

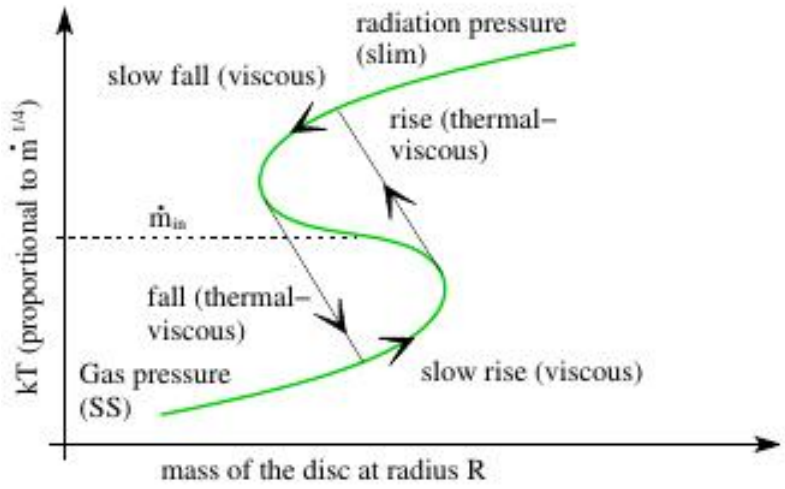

Figure 1.7: The local effects of radiation pressure instability for a variable mass accretion rate at a given radius R (Done et al. 2007).

advection of material flow acts as cooling mechanism, because the outflow of matter entails a fall of density and temperature, and of the viscosity, consequently (fall down in Figure 1.7). Thus, the system returns to its initial conditions and it creates a thermal-viscous limit cycle. Also in this case, it is a local instability that can propagate to the radiation dominated regions of the disc only.

How shown above, the Lightman-Eardley instability affects X-ray binary systems with high $\dot{M}$ value but it is negligible for the other ones. For the source 4U 1702-429 (a LMXB hosting a weakly magnetised NS, see e.g. Iaria et al. 2016; Mazzola et al. 2019a), for example, in the hypothesis of conservative mass transfer, the mass accretion rate can be evaluated as

$$\dot{M} = \frac{LR_{NS}}{GM_{NS}} \simeq 3 \cdot 10^{16}\ gr/s \tag{1.52}$$

in which $R_{NS} = 10^6$ cm is NS radius, $M_{NS} = 1.4 \cdot 2 \cdot 10^{33}$ gr is NS mass, $G = 6.67 \cdot 10^{-8}\ cm^3 g^{-1} s^{-2}$ is the universal gravitational constant and $L = 4\pi D^2 F$ is the observed luminosity of the source, estimated about $L \simeq 6.15 \cdot 10^{36}$ erg/s for a distance to the source of $D = 5,5 \cdot 318 \cdot 10^{21}$ cm (Iaria et al. 2016) and an inferred non-absorbed bolometric flux of $F \sim 1.6 \cdot 10^{-9}\ erg\ cm^{-2} s^{-1}$.

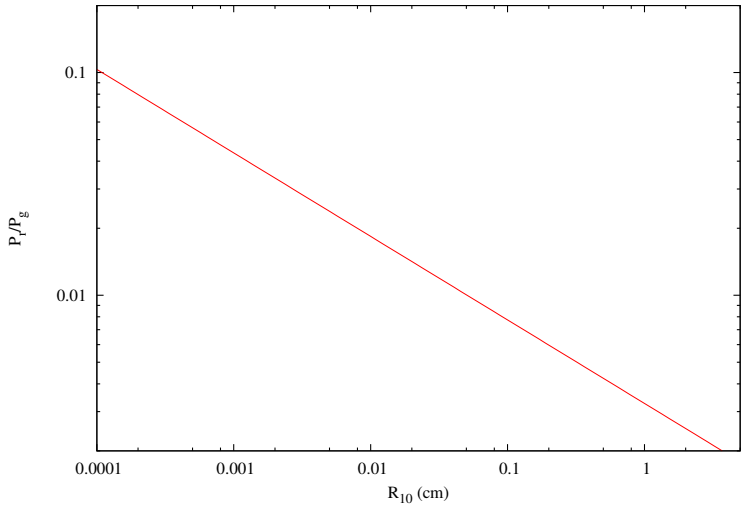

Figure 1.8: Trend of the P_r/P_g ratio in function of the disc radius R_{10} (in unit of $10^{10}\ cm$) for $f \sim 1$, $\dot{M} \simeq 3 \cdot 10^{16} gr/s$ and $\alpha = 0.1$. The logarithmic scale give us the the power of the term R_{10} in Equation 1.51.

Plotting the Equation 1.51 for $f \sim 1$ and fixed $\dot{M}$, the P_r/P_g ratio can be evaluated for different values of α, which are typically in the range [0.1 - 0.5]. In Figure 1.8 is shown the trend for $\alpha = 0.1$, which should give the maximum possible values for the ratio and we can observe that $P_r/P_g \ll 1$ at each radius. Hence, the accretion disc is always gas pressure dominated and not affected by radiation pressure instability.

Chapter 2

Secular evolution of a LMXB system

2.1 Formation of a LMXB

There are two main hypotheses about the formation of a LMXB system. In the first scenario, the companion star is tidally captured by a compact object due to its strong gravitational field and it remains bounded, forming the binary system (Fabian et al. 1975; Bhattacharya & van den Heuvel 1991; Verbunt & Lewin 2006; Voss & Gilfanov 2007; Michaely & Perets 2016). This process, however, is possible only in extremely crowded regions, as the globular clusters, but in the Galactic plane, where many of LMXBs are located, it is not easy to happen.

The alternative scenario considers the LMXB as the result of the evolution of a detached binary system composed of two massive stars in main sequence (sketched in Figure 2.1, Tauris & van den Heuvel 2006, and reference therein). In this case, the most massive of the two stars (the primary) evolves more rapidly with respect to the companion, burning hydrogen into helium in its core. When the hydrogen is exhausted, the primary star leaves the main sequence and expands up to fill its Roche lobe. Hence, it starts to loose matter via Roche lobe overflow, which will be accreted onto the companion. Since the companion is unable to accrete all the material released by the primary, a common envelope surrounding the two stars is formed, triggering a loss of angular momentum from the system. The companion star spirals-in, closer to the primary, and the lost angular momentum is transferred to the common envelope in the form of energy, until the cocoon has stored enough energy to be expelled from the system. At this point, the remaining helium core of the primary can evolve into a NS exploding as a supernova or via accretion-induced collapse. The former case is the crucial moment of the formation of the system, indeed this one will remain bounded only if the mass lost from the system through the explosion is not too much (Kalogera et al. 1998; Kalogera

& Webbink 1998; Kalogera 1998). In the latter, the companion star (left the main sequence) will fed the helium core via Roche lobe overflow, and it will evolve into a massive white dwarf. As a consequence of the mass accretion, the white dwarf can exceed the Chandrasekhar mass limit, collapsing into a NS avoiding the supernova explosion (Whelan & Iben 1973; Bruenn 1973).

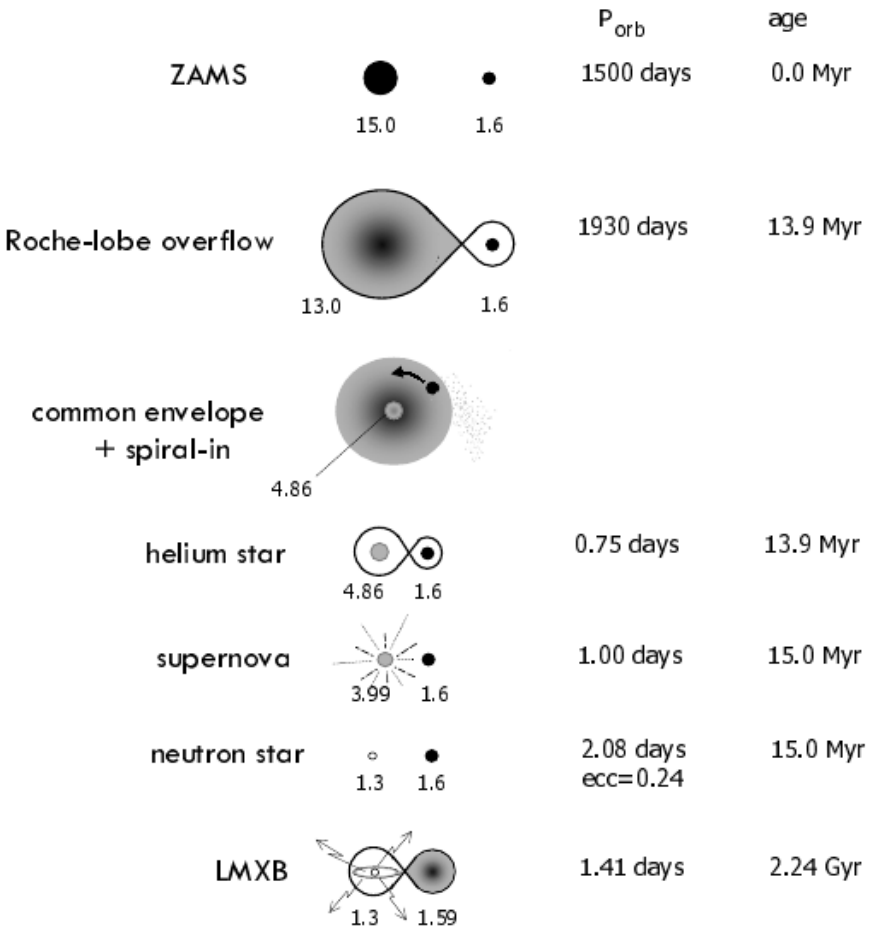

Figure 2.1: Schematic evolution of a massive binary into a LMXB via common envelope phase, followed by the supernova explosion of the helium core of the most massive star. Parameters are given for a scenario leading to the formation of the observed binary millisecond pulsar PSR 1855+09. The stellar masses are reported in solar units (Tauris & van den Heuvel 2006).

2.2 Dynamics of a LMXB

In order to understand the dynamical evolution of a LMXB source, it can be thought as a two (point-like) body system of masses M_1 and M_2. It is convenient to define an equivalent system in which a mass equal to

$$\mu = \frac{M_1 M_2}{M_1 + M_2},$$

called *reduced mass* of the system, rotates around the origin of the reference frame, where a mass $\mathcal{M} = M_1 + M_2$ is located.

The Lagrangian of the equivalent system is

$$\mathcal{L} = \frac{1}{2}\ \mu\ (\dot{r}^2 + r^2\dot{\theta}^2) - V_{\rm Eff}(r) \tag{2.1}$$

where r is the distance of μ to the origin of the reference frame and θ is the angle swept during the motion.

$V_{\rm Eff}$ is the effective potential generated by the mass $\mathcal{M}$ to which μ is subjected and it can be written as

$$V_{\rm Eff} = \frac{1}{2}\frac{l^2}{\mu\ r^2} - \frac{G\ M_1 M_2}{r}$$

with $l = \mu r^2\dot{\theta}^2$ angular momentum of the equivalent system.

The kinetic term in Equation 2.1 is composed of a translatory and a rotational contribution and this suggests that the orbital motion takes place on a plane following an orbit described by a conic section. By mathematical definition, a conic is the set of those points whose distances d to some particular point, called a *focus*, and some particular line, called a *directrix*, are in a fixed ratio, called *eccentricity* (e):

$$r = \frac{e\ d}{1 + e\ \cos\theta} \tag{2.2}$$

The eccentricity is a non-negative real number that uniquely characterises the shape of the conic:

- if $e\ <\ 1\ \Longrightarrow$ ellipse;
- if $e\ =\ 0\ \Longrightarrow$ circle;
- if $e\ =\ 1\ \Longrightarrow$ parabola;
- if $e\ >\ 1\ \Longrightarrow$ hyperbola.

Then, if $0\ \leq\ e < 1$ the orbit will be closed, while for $e \geq 1$ the orbit will be open.

From the first Kepler's law it is known that the orbits in a binary stars system are elliptical. However, in the presence of tidal interaction (as for extended bodies) the eccentricity is reduced over the time and the orbits become circular, due to mechanic energy loss. This phenomenon is called circularising of the orbits and, in the presence of strong gravitational fields and relatively small orbital separation, it takes place in a short time scale (see e.g. Har 2007)

2.3 Stellar timescales

Looking at the stars in the binary system as extended objects, three characteristic timescales can be defined related to the individual evolution of the CS.

Nuclear timescale

The *nuclear timescale* represents the average lifetime of a star, i.e. the time required for the star to leave the main sequence. It is related to the mass of the object and its luminosity, in particular, it can be thought as the time required for the energy E_n produced by proton-proton (p-p) chain reaction in the stellar core to be dissipated:

$$\tau_n \;=\; \frac{E_n}{L}.$$

Since the p-p chain is the main responsible of the energy production, this quantity depends on the number of protons N_p in the core. In general, for a star moving off the main sequence, the relation between the burning core and star mass can be written as $M_{\rm core} = 0.1\ M_*$ (Longair 2011), then assuming the core as composed almost entirely of protons $M_{\rm core} = N_p m_p$, where $m_p = 1.66\ \times 10^{-24}$ g is the proton mass, and then

$$N_p = 0.1\ \frac{M_*}{m_p}.$$

Because of the energy produced in a p-p chain reaction (i.e. the nuclear fusion a hydrogen nucleus into a helium one) is $E_{n_{pp}} = 0.007\ m_p\ c^2$, with c speed of light, the total energy will be

$$E_n = 0.0007 \cdot M_* c^2\,,$$

that is independent from the proton mass. Replacing it in τ_n and using the solar units, it is

$$\tau_n \simeq 10^{10}\ \frac{M_*}{M_\odot}\ \left(\frac{L}{L_\odot}\right)^{-1} \text{yrs.} \tag{2.3}$$

This result, however, is strongly dependent on the mass of the star, indeed (Salaris & Cassisi 2005)

$$\begin{aligned}
\frac{L}{L_\odot} &= 0.23 \left(\frac{M_*}{M_\odot}\right)^{2.3} && M_* < 0.43\ M_\odot;\\
\frac{L}{L_\odot} &= \left(\frac{M_*}{M_\odot}\right)^{4} && 0.43\ M_\odot < M_* < 2\ M_\odot;\\
\frac{L}{L_\odot} &= 1.5 \left(\frac{M_*}{M_\odot}\right)^{3.5} && 2\ M_\odot < M_* < 20\ M_\odot;\\
\frac{L}{L_\odot} &= 3.2 \times 10^3\ \frac{M_*}{M_\odot} && M_* > \ 20\ M_\odot.
\end{aligned}$$

For a CS of $M_{\rm CS} \sim 0.4\ M_\odot$, then, $\tau_n \simeq 16 \times 10^{10}$ yrs, that is longer than the estimated age of the Milky Way ($\sim 14 \times 10^9$ yrs). This suggests that in a LMXB, leaving the main sequence may not be the reason for which the CS fills its Roche lobe, otherwise the accretion process would not be observable. Thus, a different mechanism has to occur for the Roche lobe approaches the CS, causing the Roche lobe overflow of the gas composing its atmosphere. This is possible if the Roche lobe radius is reduced, and then if the orbital separation between the compact object and the companion decreases. As will be discussed in the following sections, it happens when some mechanism of loss of the total angular momentum of the system takes place.

Kelvin-Helmholtz timescale

In analogy with the nuclear timescale, the *Kelvin-Helmholtz* or *thermal timescale* can be defined as the time required to dissipate the thermal energy E_{th} of the star

$$\tau_{th} = \frac{E_{th}}{L}$$

and it represents the time the system needs to restore the thermal equilibrium conditions after a perturbation. If the star is in equilibrium (i.e. balancing between gravitational and radiative pressure), the thermal energy is produced by the particle motion in the stellar plasma, and then $E_{th} \sim E_k$, where E_k is the kinetic energy of the plasma particles. Considering the system composed by the star and a surface mass element m, it is gravitationally bounded and, for the Virial theorem, $\langle E_k \rangle = \ \frac{1}{2}\ \langle E_p \rangle$, where $\langle E_k \rangle$ and $\langle E_p \rangle$ are the average kinetic and potential energy. This last one

can be written using the Gauss theorem as

$$\langle E_p \rangle = \int_{R_*}^{0} \frac{G\ M(r)}{r}\ dm,$$

with r the radius of the virtual surface to integrate and $M(r)$ is the mass enclosed by the same surface. Assuming an uniform density ρ over the star volume, it is $dm = 4\pi r^2 dr$ and then $\langle E_p \rangle = \frac{3}{5}\frac{G\ M_*^2}{R_*}$. Using a more realistic density profile:

$$\langle E_p \rangle = \ 2\ \frac{G\ M_*^2}{R_*}$$

and then, using Solar quantities (Kippenhahn et al. 2012)

$$\tau_{th} = \ \frac{1}{2}\frac{\langle E_p \rangle}{L} = \frac{G\ M_*^2}{2R_* L} \sim 10^7\ \frac{M_*}{M_\odot}\left(\frac{L}{L_\odot}\right)^{-1}\left(\frac{R_*}{R_\odot}\right)^{-1}. \tag{2.4}$$

For the value of $\frac{L}{L_\odot}$ reported by Salaris & Cassisi (2005), if $M_* = M_{\rm CS} \sim 0.4$, $\tau_{th} \simeq 8.6 \times 10^8$ yrs. Hence, in a LMXB the thermal time scale is compatible with the age of the system.

Dynamic timescale

The dynamic timescale is a measure of the time on which a star would expand or contract if the balance between pressure gradients and gravity was suddenly disrupted

$$\tau_d = \ \frac{D_*}{v_s}$$

in which D_* is the star diameter and $v_s = \sqrt{\frac{P_g}{\rho}}$ is the sound speed at which the perturbation propagates within the star. P_g is the gravitational pressure and can be written as

$$P_g = 2\ \frac{G\ M_*}{R_*^2\ A_*}$$

with A_* the total area of the star. Thus, assuming $\rho = \dfrac{M_*}{\frac{4}{3}\pi R_*^3}$, it is

$$v_s = \sqrt{\frac{2}{3}\ \frac{G\ M_*}{R_*}}$$

and

$$\tau_d = 2\ \frac{R^{3/2}}{(G\ M_*)^{\frac{1}{2}}} \simeq\ 3.9\times 10^3 \left(\frac{R_*}{R_\odot}\right)^{-3/2} \left(\frac{M_*}{M_\odot}\right)^{3/2}\ \text{s.} \tag{2.5}$$

For $M_* >\ 0.1\ M_\odot$, $\frac{R_*}{R_\odot} \sim \frac{M_*}{M_\odot}$ and $\tau_d \simeq 1.1 \frac{M_*}{M_\odot}$ hr. That is $\tau_d \ll \tau_n, \tau_{th}$, then it can be said that the star reaches the hydrostatic equilibrium almost instantaneously after losing matter.

2.4 Mass transfer

Mathematical tool: the logarithmic derivative

Given the function u of the variable t, its logarithmic derivative is defined as

$$\frac{d}{dt}\left[\ln u(t)\right] =\ \frac{1}{u}\ \frac{du}{dt}\ =\ \frac{\dot{u}}{u}\,.$$

If $u = a^\alpha\ b^\beta\ c^\gamma$ with $\alpha, \beta, \gamma =$ constant, then

$$\ln u = \ln\left(a^\alpha\ b^\beta\ c^\gamma\right) = \alpha\ \ln a + \beta\ \ln b + \gamma\ \ln c$$

and

$$\frac{d}{dt}\left(\ln u\right) = \frac{d}{dt}\left(\alpha\ \ln a + \beta\ \ln b + \gamma\ \ln c\right) = \alpha\ \frac{\dot{a}}{a} + \beta\ \frac{\dot{b}}{b} + \gamma\ \frac{\dot{c}}{c}.$$

This will be useful in the explanation of the mass transfer scenarios.

2.4.1 Total angular momentum

To discuss the evolution of a LMXB system, a fundamental quantity has to be defined: the *total angular momentum*. From the third Kepler's law, it is known that the orbital period P of the system is related to the orbital separation a as

$$P^2 = \frac{4\ \pi^2}{G\ (M_1 + M_2)}\ a^3$$

with M_1 and M_2 masses of the compact object and the companion star, respectively. Hence, the angular velocity is

$$\omega^2 = \frac{G\ (M_1 + M_2)}{a^3}.$$

Using the centre of mass as reference pole and the relation of the radii by Paczyński (1971), the

total angular momentum of the system can be written as

$$J_B = \left(M_1 r_1^2 + M_2 r_2^2\right)\omega = \left\{M_1 a^2 \left(\frac{M_2}{M_1+M_2}\right)^2 + M_2 a^2 \left(\frac{M_1}{M_1+M_2}\right)^2\right\}\omega^2 =$$
$$= \frac{a^2\ M_1\ M_2}{M_1+M_2}\ \omega$$

Substituting the expression of ω, it is found

$$J_B \ = \ M_1 M_2 \sqrt{\frac{a\ G}{M_1+M_2}} \tag{2.6}$$

This result is obtained neglecting the contribution of the rotation of each star around its own rotational axis, the so-called *spin angular momentum* $J_S = M_*\ R_*^2\ \omega_*$. Thus, the total angular momentum of the system can be written as

$$J_{\rm tot} = J_B + J_{\rm NS} + J_{\rm CS} \tag{2.7}$$

where J_B is the orbital angular momentum and $J_{\rm NS}$ and $J_{\rm CS}$ are the angular momenta of NS and CS due to the rotation around their own axis.

Deriving the orbital separation a from the third Kepler's law and plugging it in Equation 2.6, it is

$$J_B = \frac{G^{2/3}}{\Omega^{1/3}\ (M_1+M_2)^{1/3}}\ M_1\ M_2 = \ G^{2/3}\ \left(\frac{P}{2\ \pi}\right)^{1/3}\ M_1^{5/3}\ \frac{q}{(1+q)^{1/3}} \tag{2.8}$$

with $q = \frac{M_2}{M_1} = \frac{m_2}{m_1}$ mass ratio in units of $M_\odot$ and P orbital period of the system. If $M_1 \sim 1.4\ M_\odot$ and $q \sim 0.3$, $J_B \simeq 10^{51}\ P_{2h}^{1/3}$ erg s in which the orbital period it is reported in units of 2 hrs.

The spin orbital momentum of the NS can be expressed as

$$J_{\rm NS} = I_{\rm NS}\ \omega_{\rm NS} = \ \xi\ \frac{2}{5}\ M_{\rm NS}\ R_{\rm NS}^2\ \omega_{\rm NS}\ \simeq 10^{45}\ \frac{2\ \pi}{P_S} \simeq 6.28 \times 10^{48}\ P_{S_{-3}}^{-1}\ \text{erg s} \tag{2.9}$$

where ξ is the correction factor which takes into account the deviation of the NS geometry from a sphere and PS_{-3} is the spin period in units of 10^{-3} s; the reported value is estimated for a 1.4 $M_\odot$ NS. It can be noticed that the the smaller P_S, the largest $J_{\rm NS}$ and then there will be a minimum value of the spin period below which the NS is disrupted. Indeed, the star is subjected to the gravitational F_g and centripetal F_c forces, which are opposite on the equatorial plane, and for a certain value of the angular velocity $F_c\ >\ F_g$. Equalising the two forces, the minimum of P_S can

be estimated around 1 ms.

Comparing $J_{\rm NS}$ with J_B, it is about two order of magnitude less than the orbital period of the system, and then it can be neglected.

Analogously, the spin orbital momentum of the CS is

$$J_{\rm CS} = I_{\rm NS}\ \omega_{\rm CS} = \chi\ \frac{2}{5}\ M_{\rm CS}\ R^2_{\rm CS}\ \omega_{\rm CS}$$

with χ geometric correction factor. If it is assumed that the CS fills its Roche lobe, $R^2_{\rm CS} = R_{L_2}$, furthermore, since the CS is subjected to the strong gravitational field of the compact object, its rotational period will be synchronised with the orbital period of the system, and then $\omega_{\rm CS} = \Omega$. Hence, using Equation 1.6 and, again, the third Kepler's law, it is obtained

$$\begin{aligned} J_{\rm CS} = \chi\ \frac{2}{5}\ M_{\rm CS}\ R^2_{L_2}\ \Omega = &\ \chi\ \frac{2}{5}\ M_1^{5/3}\ q^{5/3}\ (0.46224)^2\ G^{2/3} \left(\frac{P}{2\pi}\right)^{1/3} \\ \simeq &\ \chi\ 4.6 \times 10^{50}\ m_1^{5/3}\ q^{5/3}\ P_{2h}^{1/3} \simeq\ 10^{48}\ erg\ s\,, \end{aligned} \tag{2.10}$$

for $m_1 \sim 1.4$ and $q \sim 0.3$. Also in this case $J_B \gg J_{\rm CS}$ and the spin angular momentum of the star is negligible.

2.4.2 Conservative case

In the hypothesis of conservative mass transfer, the total mass of the system is a constant over the time and then the total of the mass lost by the CS is accreted onto the NS:

$$\dot{M}_1 = -\dot{M}_2\,. \tag{2.11}$$

Applying the logarithmic derivative on J_B (Equation 2.6), it is obtained:

$$\begin{aligned} \frac{d}{dt}[\ln J_B] = &\ \frac{d}{dt}\left[\ln M_1 + \ln M_2 + \frac{1}{2}\ \ln G + + \frac{1}{2}\ \ln a - \frac{1}{2}\ \ln(M_1 + M_2)\right] \\ = &\ \frac{\dot{M}_1}{M_1} + \frac{\dot{M}_2}{M_2} + \frac{1}{2}\frac{\dot{a}}{a}\,, \end{aligned}$$

and using the conservative condition (Equation 2.11), it becomes

$$\frac{\dot{J}_B}{J_B} = \frac{1}{2}\ \frac{\dot{a}}{a} + \left(1 - \frac{M_2}{M_1}\right)\frac{\dot{M}_2}{M_2}\,. \tag{2.12}$$

Since the binary system is considered as isolated, it can be assumed that it is not subjected to any external forces and then the total angular momentum is constant over the time: $\dot{J}_B = 0$. Thus, from Equation 2.12 the variation of the orbital separation can be derived

$$\frac{\dot{a}}{a} = -2\left(1 - \frac{M_2}{M_1}\right)\frac{\dot{M}_2}{M_2} \tag{2.13}$$

which is a positive quantity if $M_1 - M_2 > 0$, as for the LMXBs ($\dot{M}_2$, indeed, is considered negative for Equation 2.11). However, if $\dot{a} > 0$, the system expands because the orbital separation is increasing, and this imply that also the Roche lobe radii will be enlarged (see Equation 1.6) and the CS will not fill is Roche lobe anymore, stopping the mass transfer.

The same result is obtained applying a similar method to the variation of the Roche lobe radius of the donor star. Indeed, the logarithmic derivative of R_{L_2} (Equation 1.6) reads

$$\frac{d}{dt}[\ln R_{L_2}] = \frac{d}{dt}\left[\ln(0.462) + \frac{1}{3}\ (\ln M_2 - \ln M_1 + M_2) + \ln a\right]$$

and using Equation 2.13:

$$\frac{\dot{R}_{L_2}}{R_{L_2}} = -2\ \frac{\dot{M}_2}{M_2}\left(\frac{5}{6} - \frac{M_2}{M_1}\right). \tag{2.14}$$

Hence, $\dot{R}_{L_2} > 0$ if $\frac{M_2}{M_1} < \frac{5}{6} \sim 0.8$; therefore, in general, in a LMXB system the Roche lobe radius will increase, which lead to the same conclusion reported above. This suggests that the assumption of a constant angular momentum over the time is not suited to explain the observed accretion via Roche overflow and some mechanisms of loss of the total angular momentum have to be taken into account.

2.4.3 Non-conservative case

There are three main channels through which the loss of total angular momentum can occur: the ejection of matter from the system during the accretion process (see e.g. Burderi et al. 2010; Marino et al. 2017, 2019b), the magnetic braking phenomenon due to the interaction between the stellar wind and the magnetic field of the companion itself (Skumanich 1972; Verbunt & Zwaan 1981; Rappaport et al. 1983; Ma & Li 2009a,b; Van et al. 2019) and the emission of gravitational waves (see e.g. Zimmerman 1980; Thorne 1983). Each of them will be discussed in the following.

Mass loss

One of the hypotheses for the non-conservative mass transfer scenario is that only a fraction β of the mass lost by the companion accretes on the NS:

$$\dot{M}_1 = -\beta \dot{M}_2 \qquad \text{with } 0 \leq \beta \leq 1\,; \tag{2.15}$$

the remaining fraction $1-\beta$ represents the mass fraction expelled from the system, hence

$$\dot{M}_1 + \dot{M}_2 = (1-\beta)\ \dot{M}_2\,. \tag{2.16}$$

The angular momentum per unit of mass or *specific angular momentum* of the lost matter can be written as

$$j_{\dot{m}} = \alpha\ r_2^2\ \omega \tag{2.17}$$

with $r_2 = a\ \frac{M_1}{M_1+M_2}$ the distance to the centre of mass of the system, $\omega = \frac{2\pi}{P_{orb}}$ the angular velocity of the system and α is a numerical parameter which indicates from which point the mass leaves the system.

It is easy to understand that a mass loss involves a loss of total angular momentum, taken away from the escaping mass. Then, the lost angular momentum in the time unit will be

$$\dot{J}_{\dot{M}} = \alpha(1-\beta)\ \dot{M}_2\ r_2^2\ \omega\,. \tag{2.18}$$

Deriving ω from the third Kepler's law and using the definition of r_2 reported above, it can be found

$$r_2^2\ \omega = \sqrt{\frac{G\ a}{M_1+M_2}} M_1\ M_2\ \frac{M_1}{M_2(M_1+M_2)} = J_B\ \frac{M_1}{M_2(M_1+M_2)}$$

and the variation of the total angular momentum reads:

$$\frac{\dot{J}_{\dot{M}}}{J_B} = \alpha(1-\beta)\ \frac{M_1}{M_1+M_2}\ \frac{\dot{M}_2}{M_2}\,. \tag{2.19}$$

Applying the logarithmic derivative on Equation 2.6 again and equalising to Equation 2.19, the variation of the orbital separation can be derived also:

$$\frac{\dot{a}}{a} = \ -2\ \frac{\dot{M}_2}{M_2}\ \left[1 - \beta\frac{M_2}{M_1} - \frac{1}{2}\ (1-\beta)\ \frac{M_1}{M_1+M_2} - \alpha\ (1-\beta)\ \frac{M_1}{M_1+M_2}\right]\,; \tag{2.20}$$

it can be noticed that for $\beta = 1$ the same form of the conservative case (Equation 2.13) is obtained.

It is assumed that the angular momentum loss is due only to the mass loss.

Equation 2.7 can be recast using Equations 2.8, 2.9 and 2.10 as

$$\begin{aligned} J_{\rm tot} &= J_B + J_{\rm NS} + J_{\rm CS} = J_B \left(1 + \frac{J_{\rm NS}}{J_B} + \frac{J_{\rm CS}}{J_B}\right) = \\ &= J_B \left[1 + 1.1 \times 10^{-3}\ I_{\rm NS}\ P_{-3}^{-1}\ m_1^{-5/3}\ q^{-1}\ (1+q)^{1/3}\ P_{2h}^{-1/3} + \chi\ 2.4 \times 10^{-2}\ q^{2/3}\ (1+q)^{1/3}\right] = \\ &= J_B\ \mu\,. \end{aligned} \tag{2.21}$$

Applying the logarithmic derivative for a finite time interval, it becomes

$$\frac{\Delta J_{\rm tot}}{J_{\rm tot}} = \frac{\Delta\mu}{\mu} + \frac{\Delta J_B}{J_B} = \frac{\Delta\mu}{\mu} - \frac{1}{3}\frac{\Delta\Omega}{\Omega} - \frac{1}{3}\ \frac{\Delta(M_1+M_2)}{M_1+M_2} + \frac{\Delta M_1}{M_1} + \frac{\Delta M_2}{M_2}\,.$$

Since $\dot{M}_1 = -\beta\dot{M}_2$ and $M_1 + M_2 = M_2\left(\frac{1+q}{q}\right)$, then

$$\begin{aligned} \Delta(M_1+M_2) &= (1-\beta)\ \dot{M}_2\ \Delta t \\ \frac{\Delta(M_1+M_2)}{M_1+M_2} &= (1-\beta)\ \frac{1+q}{q}\ \frac{\dot{M}_2}{M_2}\ \Delta t \end{aligned}$$

and, finally,

$$\frac{\Delta J_{\rm tot}}{J_{\rm tot}} = \frac{\Delta\mu}{\mu} - \frac{1}{3}\frac{\Delta\Omega}{\Omega} - \frac{1}{3}(1-\beta)\ \frac{1+q}{q}\ \frac{\dot{M}_2}{M_2}\ \Delta t + \frac{\dot{M}_2}{M_2}\ \Delta t - \beta\ q\ \frac{\dot{M}_2}{M_2}\ \Delta t\,. \tag{2.22}$$

Given $\Delta J_{\dot{M}}$ the mass loss term, it can be written as

$$\Delta J_{\dot{M}} = M_{\rm ej}\ l_{\rm ej} = \ \dot{M}_2\ \Delta t\ (1-\beta)\ l_{\rm ej}\ ,$$

with $M_{\rm ej}$ the mass ejected from the system and $l_{\rm ej}$ its specific angular momentum, which depends on the position from which the matter is ejected. On that one, there are two main hypotheses: the mass could be radially ejected from the companion or it could leave the system through the inner Lagrangian point (the so-called *propeller effect* mechanism, more likely related to systems hosting accreting millisecond pulsars, Ghosh & Lamb 1979; Stella et al. 1986; Shu et al. 1994; Lovelace et al. 1995; Campana et al. 1998, 2001, 2018); here, only the former will be discussed.

Assuming that the matter is ejected from the position of the CS, it specific angular momentum

is equal to

$$l_{\rm ej} = d^2\Omega = a^2 \frac{M_1^2}{(M_1+M_2)^2}\Omega \ , \tag{2.23}$$

where $d = a^2 \ \dfrac{M_1^2}{(M_1+M_2)^2}$ is the distance between the CS and the centre of mass of the system. Expressing the orbital separation a in term of the orbital period of the system P via the third Kepler's law and replacing in Equation 2.23, it becomes

$$l_{\rm ej} = G^{2/3} \ M_1^2 \ (M_1+M_2)^{-4/3} \left(\frac{P}{2\ \pi}\right)^{1/3} \ .$$

Rewriting in terms of the mass ratio q, the mass loss term reads

$$\Delta J_{\dot{M}} = \dot{M}_2 \ \Delta t \left(\frac{G\ M_1}{(1+q)^2}\right)^{2/3} \left(\frac{P}{2\pi}\right)^{1/3} \tag{2.24}$$

which, divided by Equation 2.8, provides the variation of the orbital period due to the mass loss:

$$\frac{\Delta J_{\dot{M}}}{J_B} = \ \alpha(1-\beta) \ \frac{1}{1+q} \ \frac{\dot{M}_2}{M_2} \ \Delta t \ , \tag{2.25}$$

with $\alpha = \left(\frac{d}{a-x_{CM}}\right)^2$ (x_{CM}: position of the centre of mass) is the parameter which takes into account the position of the ejection point of the matter.

Magnetic braking

Another way to lose angular momentum in a binary system is through *magnetic braking*. In this scenario, the plasma lost by the donor star interacts with the lines of the magnetic field of the star itself, freezing them, and this causes a tidal friction which transfers part of the CS angular momentum to the matter, that escapes the system. The model for this phenomenon was developed by Verbunt & Zwaan (1981) for stars with $M_* \gtrsim 0.6 M_\odot$ in thermal equilibrium conditions (i.e. G-stars in main sequence) and, following that, the angular momentum of the donor is

$$J_2 = k^2 \ M_2 \ R_2^2 \ \omega_2 \tag{2.26}$$

where k is a dimensionless parameter which takes into account geometrical and structural corrections and it is (Verbunt & Zwaan 1981):

$$k = \begin{cases} 0.277 & \text{Sun} - \text{type stars} \\ 0.378 & \text{M} - \text{type stars } (0.4\ M_{\odot} \leq M_{*} \leq 0.6\ M_{\odot})\,. \end{cases}$$

The angular velocity of the donor can be written using the relation with the equatorial velocity of the star:

$$v_2 = \omega_2\ R_2 = 10^{14} f\ t^{-1/2} \tag{2.27}$$

in which f is a numerical corrective factor that can assume two possible values:

$$f = \begin{cases} 1.78 & \text{(Smith 1979)} \\ 0.73 & \text{(Skumanich 1972)}\,. \end{cases}$$

Replacing ω_2 in Equation 2.26 and differentiating, the magnetic braking term $\dot{J}_{\rm MB}$ can be calculated:

$$\frac{dJ_2}{dt} = -10^{14}\ \frac{1}{2}\ k^2\ M_2\ R_2\ f\ t^{-3/2}\,;$$

deriving $t^{-3/2} = 10^{-42}\ \frac{(\omega_2\ R_2)^3}{f^3}$ from Equation 2.27, it is

$$\dot{J}_{\rm MB} = -\frac{1}{2}\ k^2\ M_2\ f^{-2} \times 10^{-28}\ R_2^4\ \omega^3 = \ \Delta J_{\rm MB}\,. \tag{2.28}$$

If the binary system is locked $\omega_2 = \Omega$ and, if the donor fills its Roche lobe, $R_2 = R_{L_2}$ (Equation 1.6), hence dividing by Equation 2.6 in terms of the mass ratio q, the term of angular momentum loss due to magnetic braking is obtained:

$$\frac{\Delta J_{\rm MB}}{J_B} = -2.24 \times 10^{-30}\ \frac{k^2}{f^2}\ q^{4/3}\ (1+q)^{1/3}\ (G\ M_1\ \Omega)^{2/3}\ \Delta t\,. \tag{2.29}$$

Gravitational waves emission

The magnetic braking is the dominant angular momentum loss mechanism in binaries with orbital period longer than few hours, meanwhile the *gravitational radiation* dominates in close binaries. The gravitational waves are emitted by interacting (accelerated) masses such as the electromagnetic waves are emitted by accelerated charged particles. In the quadrupole approximation, for circularly

orbiting masses M_1 and M_2, the rate at which angular momentum is carried out by gravitational waves can be written as (Burko 2017, and references therein)

$$\frac{\Delta J_{\rm GW}}{J_B} = -\frac{32}{5}\,\frac{G^3}{c^5}\,M_1\,M_2\,\frac{M_1+M_2}{a^4}\,\Delta t\ , \tag{2.30}$$

with c the speed of light. It can be noticed that the efficiency of this contribution depends on the orbital separation a: the closer the system, the more relevant will be the angular momentum loss due to the gravitational waves emission. In particular, it results the dominant effect for $P_{\rm orb} < 2$ hrs, meanwhile for $P_{\rm orb} > 1$ day the predominant mechanism is the magnetic braking (Rappaport et al. 1983).

At this point, putting together all the contribution in Equations 2.25, 2.29 and 2.30, the total variation of the angular momentum of the system is obtained:

$$\frac{\Delta J_b}{J_B} = \frac{\Delta J_{\dot{M}}\ + \Delta J_{\rm MB}\ + \Delta J_{\rm GW}}{J_B}\,. \tag{2.31}$$

Balancing the explicit form of Equation 2.31 (in term of q) and Equation 2.22, assuming $\frac{1}{\mu} \sim 1$, in the end the *secular evolution of the angular velocity* of the system can be inferred

$$\frac{\dot{\Omega}}{\Omega} = 3\ g(\beta,q,\alpha)\ \frac{\dot{M}_2}{M_2} + 3\cdot 6.4\cdot 10^{-17} m_1^{5/3} P_{2h}^{-8/3} \frac{q}{(1+q)^{1/3}}\ [1+T_{\rm MB}] \tag{2.32}$$

where

$$\begin{aligned} g(\beta,q,\alpha) &= 1-\beta q - \frac{1-\beta}{3}\frac{q}{1+q} - \alpha\ \frac{1-\beta}{1+q} \\ T_{\rm MB} &= 8.4\ k_{0.1}^2\ \frac{P_{2h}^2}{m_1}\ f^{-1}\ q^{1/3}\ (1+q)^{2/3} \qquad \text{magnetic braking term.} \end{aligned} \tag{2.33}$$

2.5 Dynamical evolution

In order to understand the secular evolution of the system, it needed to find a prediction for the mass-loss rate of the donor star which takes into account the loss of angular momentum due to magnetic braking and gravitational radiation.

It is assumed that the companion star fills its Roche lobe $R_2 = R_{L_2}$ but also that $\dot{R}_2 = \dot{R}_{L_2}$, then

$$\frac{\dot{R}_2}{R_2} = \frac{\dot{R}_{L_2}}{R_{L_2}}\,. \tag{2.34}$$

Using the relation provided by Paczyński (1971) and the third Kepler's law, it is

$$R_{L_2} = 0.462 \left(\frac{G\ M_2}{\Omega^2}\right)$$

that, applying the logarithmic derivative over a time interval Δt, becomes

$$\frac{\dot{R}_{L_2}}{R_{L_2}} = \frac{1}{3}\frac{\dot{M}_2}{M_2} - \frac{2}{3}\frac{\dot{\Omega}}{\Omega}\,. \tag{2.35}$$

If the CS is in main sequence, the mass-radius relation can be written in the simple general form (Neece 1984):

$$R_2 \propto M_2^n\,. \tag{2.36}$$

Furthermore, the variation of the angular velocity Ω is related to the variation of the orbital period P

$$\frac{\dot{\Omega}}{\Omega} = -\frac{\dot{P}}{P}\,. \tag{2.37}$$

Using the logarithmic derivative on Equation 2.36 and plugging it in Equation 2.35, taking into account Equation 2.37, the evolution of the orbital period on dynamical evolution time scale of the companion is obtained:

$$\frac{\dot{P}}{P} = -\frac{3n-1}{2}\frac{\dot{M}_2}{M_2}\,; \tag{2.38}$$

it can be noticed that the period derivative $\dot{P} > 0$ if the mass-radius index is $n < \frac{1}{3}$.

Rewriting the relation with P in units of 2 hrs, $\dot{P}$ in units of 10^{12} s s^{-1}, M_2 in units of solar masses and $\dot{M}$ in units of $10^{-8}\ M_\odot$ yr^{-1}, it becomes

$$\frac{\dot{P}_{12}}{P_{2h}} = 2.28\ \frac{3n-1}{2}\ \frac{-\dot{m}_{-8}}{m_2} = \ 2.28\ \frac{3n-1}{2}\ q^{-1}m_1^{-1}(-\dot{m}_{-8}) \tag{2.39}$$

where q is the mass ratio of the system and m_1 the mass of the compact object in units of solar masses.

Equalising Equation 2.39 to the secular equation (2.32), the mass transfer rate from CS can be inferred:

$$\dot{m}_{-8} = \left[2.8\ \left(\frac{1-3n}{2}\right) - 6.8\ g(\beta,q,\alpha)\right]^{-1} 1.37\ q^2(1+q)^{-1/3}m_1^{8/3}P_{2h}^{8/3}\ [1+T_{\rm MB}] \tag{2.40}$$

with $g(\beta,q,\alpha)$ and $T_{\rm MB}$ defined as Equation 2.33.

In the hypothesis of conservative mass transfer, $g(\beta, q, \alpha) = 1 - q$ and then the secular mass accretion rate can be re-written as (see e.g. Burderi et al. 2010; Gambino et al. 2016)

$$\dot{m}_{-8} = 0.6\ (3q - 1.5n - 2.5)^{-1}\ q^2(1+q)^{-1/3} m_1^{8/3} P_{2h}^{8/3}\ [1 + T_{\rm MB}] \tag{2.41}$$

from which it is easy to see that, if $T_{\rm MB} = 0$, the contribution to the angular momentum loss due to gravitational radiation is strongly dependent on the orbital period: the larger P_{2h}, the less will be this contribution.

Searching for the orbital period

The orbital period of the system is actually an observable quantity. As mentioned in Chapter 1, the NS-LMXB light-curves can show eclipses or dips due to the shielding effect of the companion or a bulge of matter in the outer rim of the accretion disc, depending on the value of the inclination angle the system is observed with. Since dips and eclipses occur at the same orbital period of

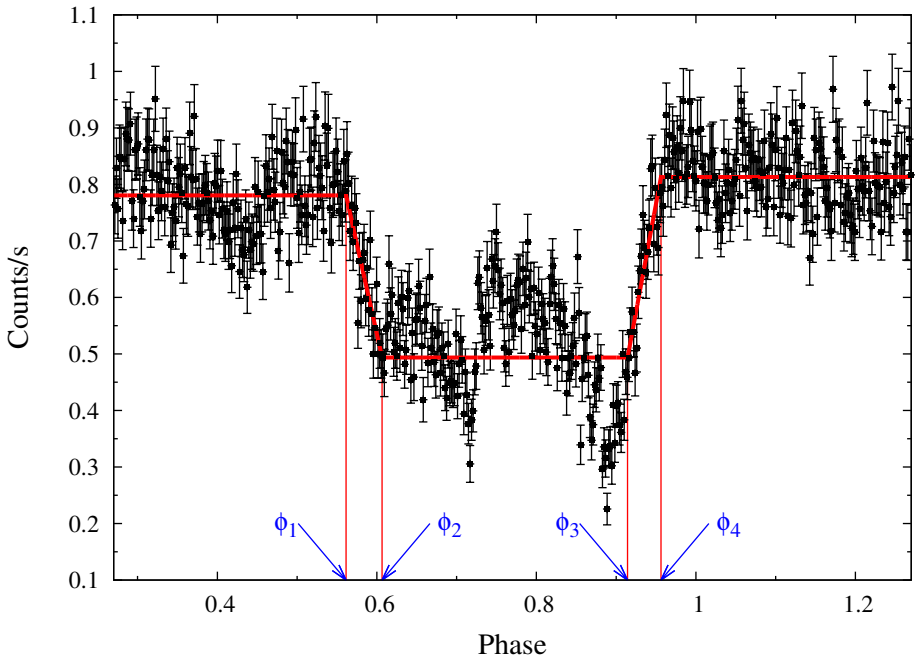

Figure 2.2: Folded light curve of two joined Chandra observations of the source 4U 1323-619 showing the dip. The red line is a step-and-ramp function that better fits the dip. The blue arrows highlight the phases of ingress (ϕ_1 and ϕ_2) and egress (ϕ_3 and ϕ_4) of the dip (Gambino et al. 2016).

the system, through a timing analysis of their occurrence this period can be estimated and the

orbital ephemerides are calculated. In order to improve the statistics of the data, the *epoch folding* method is often applied, which consists in dividing the light curve in time intervals of same duration, coincident with a trial expected period, and folding it. In this way, the profile of a single eclipse (or dip) with high statistics is displayed in the light-curve, through which analysis it is possible to infer the arrival time of the features (see e.g. Burderi et al. 2006, 2007; di Salvo et al. 2008; Burderi et al. 2009, 2010; Iaria et al. 2011, 2014, 2015a; Gambino et al. 2016, 2017; Iaria et al. 2018; Sanna et al. 2018).

If the trial period is the real orbital period of the system P_{orb}, the occurrence times of the analysed features should follow the relation

$$T_{arrival} = T_0 + NP_{trial} \tag{2.42}$$

where T_0 is the reference epoch at which the feature occurs and N is the number of orbital cycles of the source. However, if $P_{trial} \neq P_{orb}$, N is not an integer number and its decimal part represents the delay with respect to the expected arrival times of the dip/eclipse. Fitting the delay in function of the orbital cycles, the correct form of the ephemerides and the correction to the trial period are inferred and, hence, the correct value of the orbital period of the system is found.

Chapter 3

Spectral properties of a LMXB system

3.1 Spectral components

The X-ray spectra of LMXBs hosting NS are the result of several processes and today their picture is not still complete. Two main components can be distinguished, in general, in the continuum: a soft thermal one at the lowest energies, associated to the blackbody emission from the NS and/or the accretion disc, and a hard component at the highest energies due to the Comptonisation of soft photons from a hot electron corona located in the innermost region of the system. Furthermore, the spectra of these sources show often a reflection component originating from the interaction of photons leaving the Comptonising cloud and scattered by the surface of the disc. Some discrete features such as emission/absorption lines and absorption edges can be also detected.

In the following, the characteristics of each components and the physical mechanism involved in their origin are discussed.

3.1.1 The soft thermal component

The direct soft emission observed from these sources, related to the accretion processes, is represented by the blackbody emission from NS and/or the multi-coloured blackbody from the accretion disc. For the optically thick disc (in z-direction) assumption discussed in chapter 1, each disc element can be considered as a blackbody emitting with temperature $T(R)$ such that $\sigma T(R)^4 = D(R)$. Using Equation 1.45, it can be defined as

$$T(R) = \left\{ \frac{3}{8} \frac{GM\dot{M}}{\pi R^3 \sigma} \left[1 - \left(\frac{R_*}{R} \right)^{1/2} \right] \right\}^{1/4} . \tag{3.1}$$

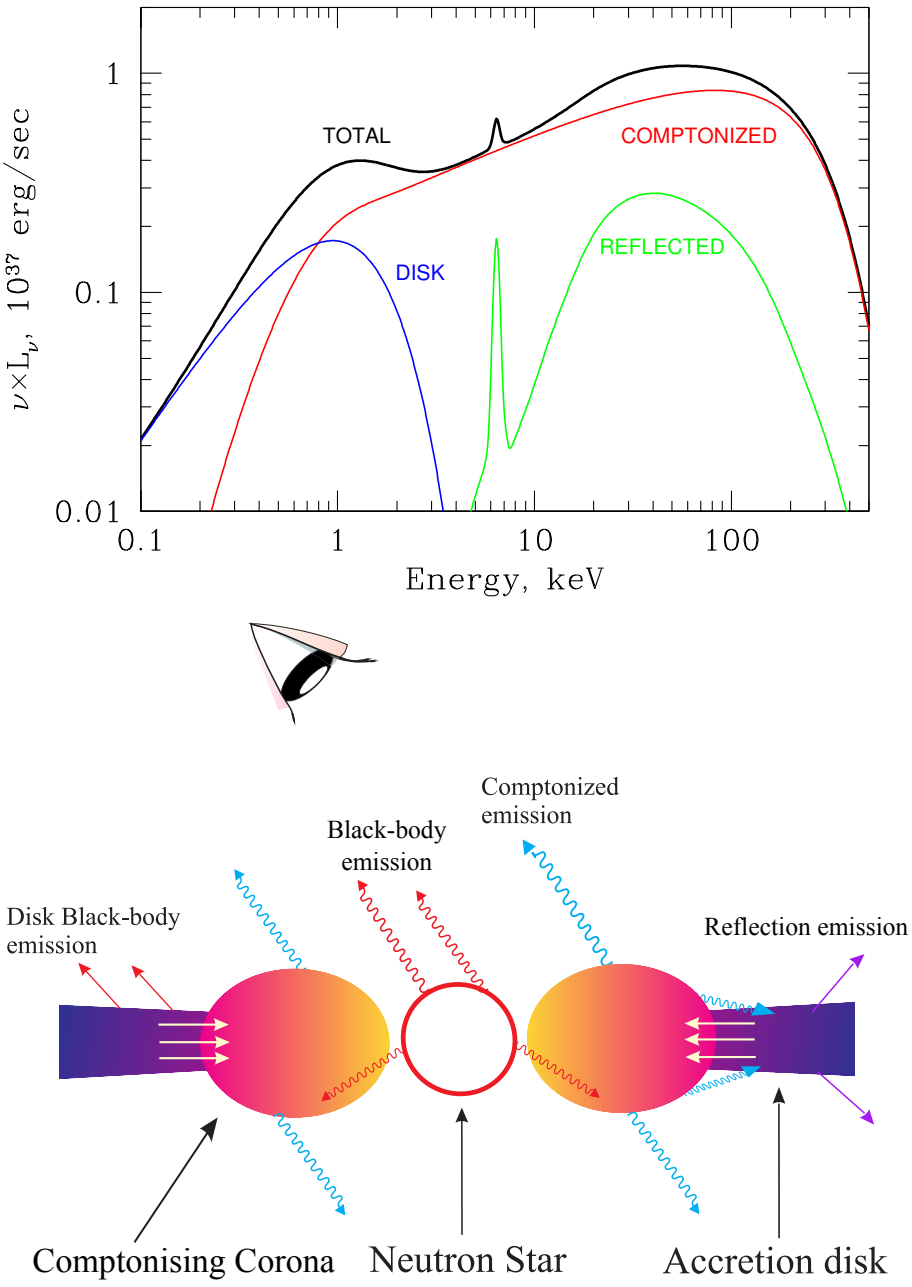

Figure 3.1: On the top: main spectral component for LMXBs (Gilfanov 2010). On the bottom: suggested geometry of a source. Disc and NS soft photons are upscattered in the Comptonising corona located between the accretion disc and NS surface. Some fraction of these photons (red trajectories) is seen directly by the observer (adapted from Seifina et al. 2015).

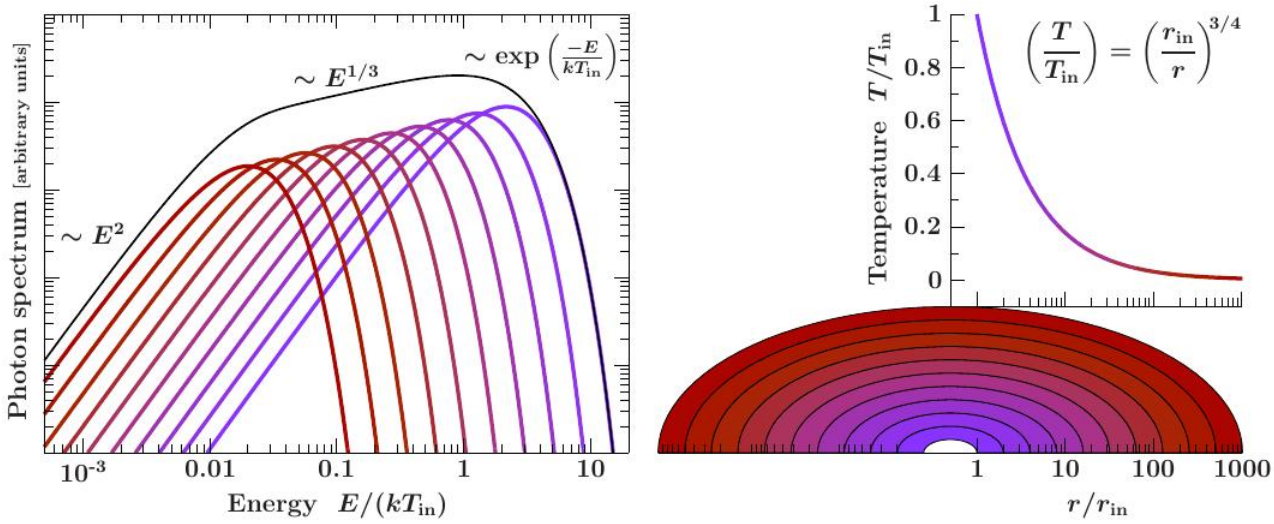

Figure 3.2: Multi-colour blackbody spectrum (black curve on the right panel), which approximates the superimposition of the blackbody emission from each ring in the optically thick accretion disc (Hanke 2011; Egron 2013).

For $R \gg R_*$, $T(R) = T_* \left(\frac{R}{R_*}\right)^{-3/4}$ where

$$T_* = \left(\frac{3GM\dot{M}}{8\pi R_*^3 \sigma}\right)^{1/4} \simeq 10^7 m_1^{1/4} \dot{M}^{1/4} R_6^{3/4} K, \tag{3.2}$$

written using $\dot{M}_{16} = \dot{M}/10^{16}$, $m_1 = M/M_\odot$ and $R_6 = R/10^6$. Neglecting the effects of disc atmosphere, which opacity can strongly depend on radiation frequency υ, the emitted spectrum of each surface element can be approximated with

$$I_\upsilon = B_\upsilon(T(R)) = \frac{2h\upsilon^3}{c^2\left(e^{h\upsilon/k_B T(R)} - 1\right)} \text{ erg s}^{-1} \text{ cm}^{-2} \text{ Hz}^{-1} \text{ sr}^{-1}. \tag{3.3}$$

Then, the radiation flux for an observer at distance D, whose line-of-sight has an inclination angle θ respect to the disc plane, for a fixed υ is

$$F_\upsilon = \int_{R_*}^{R_{out}} \frac{I_\upsilon 2\pi cos\theta R dR}{D^2},$$

where R_{out} is the outer radius of the disc and $\frac{2\pi cos\theta RdR}{D^2}$ is the solid angle subtended by the ring with radius between R and $R+dR$. Substituting I_υ from Equation 3.3, it becomes

$$F_\upsilon = \frac{4\pi h\upsilon^3 cos\theta}{c^2 D^2} \int_{R_*}^{R_{out}} \frac{RdR}{e^{h\upsilon/k_B T(R)} - 1} \tag{3.4}$$

and it is independent from the plasma viscosity, as a consequence of the steady disc assumption and the blackbody approximation. From Equation 3.4, it can be deduced that

- for $\upsilon \ll k_B T(R_{out})/h$, B_υ tends to the *Rayleigh-Jeans Law*[1] so $F_\upsilon \propto \upsilon^2$;
- for $\upsilon \gg k_B T_*/h$, B_υ is in a *Wien Law*[2] form then F_υ is an exponential law dominated by the hottest part of the disc;
- for intermediate υ, defining $x = h\upsilon/k_b T(R) \simeq (h\upsilon/k_b T_*)(R/R_*)^{3/4}$, then

  $$F_\upsilon \propto \upsilon^{1/3} \int_0^{+\infty} \frac{x^{5/3}}{e^x - 1} dx \propto \upsilon^{1/3}$$

  that is the typical *stretched-out blackbody* associated to an accreting disc.

The Standard model (described in chapter 1), however, can not be applied when the plasma in the disc is not efficiently cooled. It is the case of the advection-dominated accretion flows (ADAF, Ichimaru 1977; Narayan & Yi 1994, 1995), in which the thermal energy produced by viscous dissipation is not locally radiated but it is advected radially inwards. It can occur in two cases: at very high mass accretion rate $\dot{M} > \dot{M}_{\rm Edd}$, when the radiation is trapped in the accreting flow due to the high optical depth, and at very low accretion regime, when the plasma becomes optically thin and the cooling time exceeds the accretion time (see e.g. Abramowicz et al. 1995, 1998; Chen et al. 1995). The ADAF model is the basis of the so-called truncated disc model, in which the inner thick accretion disc is absent and it is replaced by the thin ADAF because of the presence of a strong magnetic field (see e.g. Barret et al. 2000, for a detailed discussion). Furthermore, ADAF-like models was proposed to take into account also the effects of the radial convection efficiency(Narayan et al. 2000), possible outflows (Fukue 2004a,b) and the presence of a strong magnetic field (Abbassi et al. 2008).

[1] Rayleigh-Jeans Law: $I_\upsilon = \frac{2k_B T\upsilon^2}{c^2}$

[2] Wien Law: $I_\upsilon = \frac{2h\upsilon^3}{c^2} e^{-h\upsilon/k_B T_*}$

3.1.2 The hard component

The hard component of the spectra is mainly due to the *Comptonisation*, a modification of the spectrum of a cold photons distribution as results of the interaction with a hot electron cloud having an optical depth sufficient for the Compton scattering being the predominant process. The Compton scattering is a process that involves a photon scattered by a free electron. Assuming both as particles, because the interaction occurs it should be $h\nu \gtrsim m_e c^2$, i.e. the energy of incident photon should be greater or equal than the energy at rest of the electron. In this hypothesis, the collision is inelastic and there are non-classical effects that modify energy and direction of propagation of the particles.

If the electron is initially at rest, after the scattering it is subjected to a recoil and has a gain in kinetic energy, while the final energy of the photon is less than the initial one. This process is called *direct Compton scattering* (Figure 3.3) . Using the conservation of the energy and momentum for

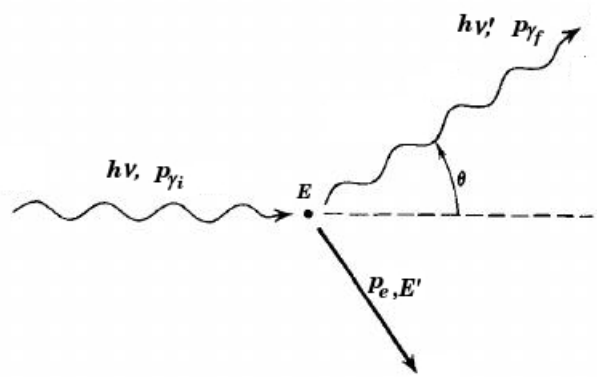

Figure 3.3: Schematic representation of direct Compton scattering: an incident photon with an energy $h\nu$ and a momentum p_{γ_i} interacts with an electron at rest with an energy $E = m_e c^2$. After colliding, the electron has a momentum p_e and an energy $E' \neq E$, so these quantities are not the same also for the photon, which has $h\nu'$ and p_{γ_f} and a direction of propagation that forms an angle θ with the initial one.

the particles before and after the interaction, it is obtained (Longair 2011; Rybicki & Lightman 1979)

$$h\nu' = \frac{h\nu}{1 + \frac{h\nu}{m_e c^2}(1 - \cos\theta)}, \tag{3.5}$$

where $h\nu$ and $h\nu'$ are the initial and final photon energy, respectively, and θ is the scattering angle (see Figure 3.3). It can be observed that more $h\nu$ is close to $m_e c^2$, the greater is the energy lost by the photon; furthermore, the loss depends on the angle and it is maximum at $\theta = \pi$, i.e. when the

photon is reflected in the incidence direction.

The angular distribution of the photons after the interaction with electrons is not isotropic and it is defined by the Klein-Nishina formula (Rybicki & Lightman 1979)

$$\frac{d\sigma}{d\Omega} = \frac{3}{16}\left(\frac{\nu'}{\nu}\right)^2\left(\frac{\nu}{\nu'} + \frac{\nu'}{\nu} - \sin^2\theta\right) \tag{3.6}$$

with ν and ν' the initial and final frequency of the photon, respectively.

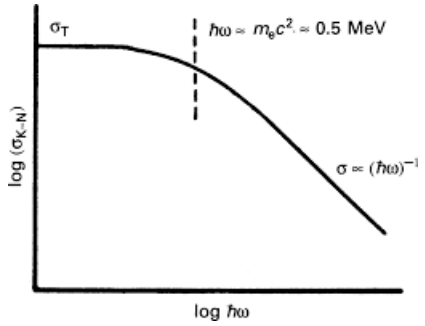

Figure 3.4: A schematic diagram (logaritmic scale) showing the dependence of the Klein–Nishina cross-section upon photon energy

Integrating on the solid angle, the Klein-Nishina total cross-section is (Rybicki & Lightman 1979)

$$\sigma_{KN} = \frac{3}{4}\sigma_T\left[\frac{1+x}{x^3}\left(\frac{2x(1+x)}{1+2x} - \ln(1+2x)\right) + \frac{1}{2x}\ln(1+2x) - \frac{1+3x}{(1+2x)^2}\right] \tag{3.7}$$

where $\sigma_T = \frac{8}{3}\pi\left(\frac{e^2}{m_e c^2}\right)^2 = 6.625 \cdot 10^{-25}$ cm^2 is the Thomson cross-section and $x = \frac{h\nu}{m_e c^2}$, that for small value of $h\nu$ is well approximated by

$$\frac{d\sigma_T}{d\Omega} \sim \frac{3}{8\pi}\sigma_T\left(\frac{1+\cos^2\theta}{2}\right) \tag{3.8}$$

(see Figure 3.4). Since $\sigma_T \propto m_e^{-2}$, then $\sigma_{KN} \propto m_e^{-2}$, so the interactions of photons with protons and ions are negligible because they are less significant of a factor $(m_e/m_p) \sim 10^{-7}$.

In the *inverse Compton scattering*, the electron has an initial velocity v_e (hence a momentum $p_{e_i} \neq 0$) and an amount of its energy is transferred to the photon during the interaction. Ultimately, the photon has a final energy $h\nu'$ greater than the initial (Figure 3.5). In the reference system in which the electron is at rest, an observer sees direct Compton scattering, then the Equation 3.5 can b applied and, operating a frame transformation, last the final energy of the photon is (Longair

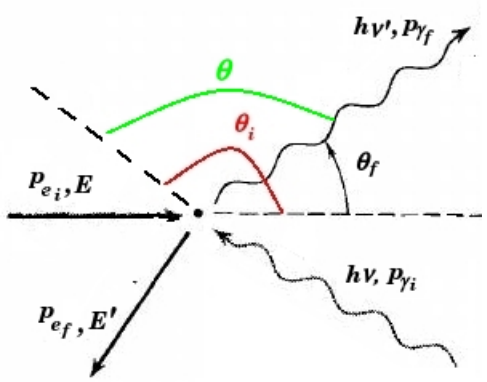

Figure 3.5: Schematic representation of the inverse Compton scattering, in which the incident photon (the wavy arrow) with energy $h\nu$ and momentum p_{γ_i} interacts with a moving electron (the straight arrow) with an energy E and a momentum p_{e_i}. The final energies and momenta are indicated with $h\nu'$ and p_{γ_f} for the photon and E' and p_{e_f} for the electron. The angles indicated represented respectively the angle between the initial direction of propagation of the particles (θ_i in red), the angle between the final and the initial direction of propagation of the photon (θ in green) and the angle between the initial direction propagation of the electron and that final of the photon (θ_f in black).

2011):

$$h\nu' = \frac{(1-\beta\cos\theta)h\nu}{1-\beta\cos\theta_f + \frac{h\nu}{\gamma m_e c^2}(1-\cos\theta)} \tag{3.9}$$

where θ is the angle between the final and the initial direction of propagation of the photon and θ_f is angle between the initial direction of propagation of the electron and the final one of the photon (see Figure 3.5), $\beta = v_e/c$ is the ratio between the velocities of the particles and $\gamma = \sqrt{1-\beta^2}$ is the Lorentz factor.

For an isotropic incident distribution of photons, the power emitted by inverse Compton scattering for a single electron target is (Rybicki & Lightman 1979; Blumenthal & Gould 1970)

$$P_{\text{Compt}} = \frac{4}{3}\sigma_T c\gamma^2\beta^2 U_{ph} \tag{3.10}$$

with U_{ph} the incident energy density. The final energy of the photon is much greater than the initial, although the energy gained is a very small fraction of the initial one of the electron. Thus, the inverse Compton scattering is an efficient method to obtain high energy photons from low energy ones (Di Salvo 2001; Hirayama 2000).

If the incident photons distribution is isotropic, monochromatic with frequency ν_0 and has a

density $N(\nu_0)$, the spectral emissivity is defined as (Longair 2011)

$$I(\nu)d\nu = \frac{3\sigma_T c}{16\gamma^4}\frac{N(\nu_0)}{\nu_0^2}\nu\left[2\nu\ln\left(\frac{\nu}{4\gamma^2\nu_0}\right)+\nu+4\gamma^2\nu_0-\frac{\nu^2}{2\gamma^2\nu_0}\right] \tag{3.11}$$

At low frequencies the term between the square parenthesis in Equation 3.11 is approximately constant, then $I(\nu)\propto\nu$; while for high frequency we have a cut-off in the spectrum at the maximum energy achievable $h\nu_{max}\approx 4\gamma^2 h\nu_0$, that is obtained when the incident photon is back-scattered.

Assuming that the electrons are non-relativistic, in the reference system in which they are at rest the average variation of energy for direct (Equation 3.12) and inverse Compton (Equation 3.13) for a thermalised or quasi-thermalised electron Comptonising cloud is:

$$\frac{\Delta E}{E}\simeq -\frac{h\nu}{m_e c^2}; \tag{3.12}$$

$$\frac{\Delta E}{E}\simeq \frac{4kT_e - h\nu}{m_e c^2}. \tag{3.13}$$

where $4kT_e$ is the thermal energy of the electrons and $m_e c^2$ is their rest energy.

If the plasma has an optical depth $\tau = n_e\sigma_T x$, the average number of collisions is calculated assuming that the photons undergo a random walk before escaping the cloud and it results $N = max(\tau,\tau^2)$ (Longair 2011; Rybicki & Lightman 1979).

The total energy variation is approximated by the *Compton paramater* $y = \frac{4kT_e}{m_e c^2}max(\tau,\tau^2)$, which is an estimation of the significance of the Comptonisation process for the system: if $y\geq 1$ the Comptonised spectrum is called *flat* (or *hard*) and it is predominant above the spectrum of the seed photons, viceversa, if $y<1$ the seed photons spectrum is less affected and the Comptonised spectrum is called *steep* (or *soft*). If the electron cloud is optically thick ($\tau\gg 1$), an emerging spectrum shifted to grater temperature is expected (Ghisellini 2013). However, the number of particles involved in Compton scattering is a conserved quantity, thus the final number of photons is almost unchanged and there is no longer thermal balance. . Then, the outgoing spectrum has not a blackbody shape but it is in the Bose-Einstein form, in which the peak temperature corresponds to the maximum of the electrons in the cloud. If the initial energy of photons $h\nu_0\sim kT_e$, the spectrum is in the Wien form $I(E)\propto E^3 exp\{-E/kT_e\}$ and it is called *saturated Comptonisation spectrum.*

For $\tau<1$ and $h\nu_0<kT_e$ the spectrum is well approximated by a power law $I(E)\propto I_0 E^{-\alpha}$ where α is the so-called photon index, and exhibits a cut-off for $h\nu\sim kT_e$ (*unsaturated Comptonisation*

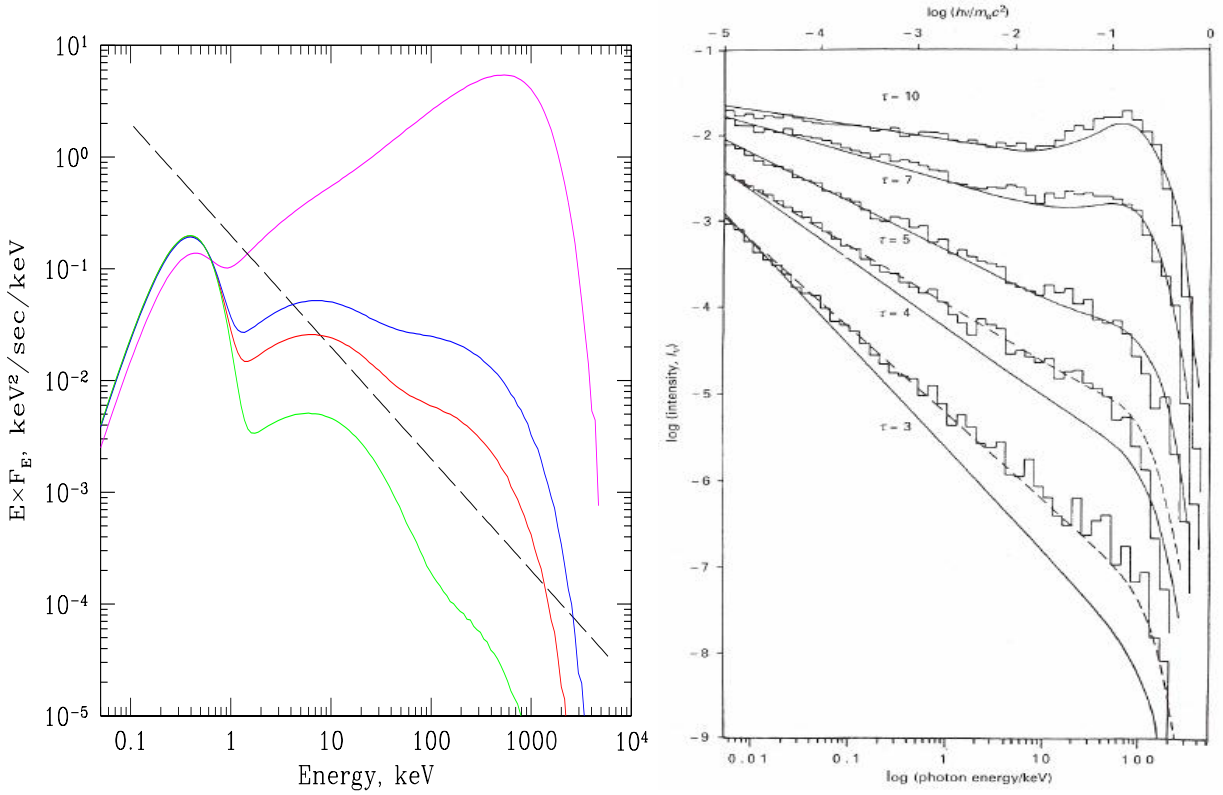

Figure 3.6: On the left: Monte-Carlo simulations assuming spherical geometry of the Comptonization spectrum in the case of large temperature and small optical depth: $kT_{bb} = 100$ eV, $kT_e = 300$ keV, $\tau = 0.01, 0.05, 0.1, 1$ (from the bottom to the top). The left-most peak in all spectra is made of seed photons which left the Comptonisation region without scatterings. The dashed line is a power law with a photon index of $\Gamma = 3$ (Gilfanov 2010). On the rigth: Comptonisation emitted spectrum (in logarithmic scale) of seed photons in a homogeneous thermal non-relativistic plasma for different optical depth (Pozdnyakov et al. 1983).

spectrum). The Comptonisation spectra of seed photons with a blackbody temperature in a thermal non relativistic plasma for different optical depth are shown in Figure 3.6. The spectrum labelled with $\tau = 3$ is referred to the unsaturated Comptonisation , which generates a power law with a cut-off at the electron temperature. The spectrum labelled with $\tau = 10$, instead, is related to the saturated Comptonisation which, for very large optical depth presents the so-called Wien bump at the electron temperature, due to thermalisation of the seed photons with the electron cloud (Pozdnyakov et al. 1983).

The emitted spectrum is obtained from the Kompaneets equation (Rybicki & Lightman 1979)

$$\frac{\partial \eta}{\partial y} = \frac{1}{x^2}\frac{\partial}{\partial x}\left[x^4\left(\frac{\partial \eta}{\partial x} + \eta + \eta^2\right)\right], \tag{3.14}$$

in which η is the photon density, $x = \dfrac{h\nu}{kT_e}$ and $y = \int \frac{kT_e}{m_e c^2}\sigma_T N_e \, dl$ (with N_e the electron density). This equation describes the evolution of the system of photons to an equilibrium state in the hypothesis of non-relativistic electrons and negligible Bremsstrahlung effects (Rybicki & Lightman 1979). The term $\dfrac{\partial \eta}{\partial x}$ describes the Doppler shift due to the stochastic collisions of the photons with the electrons and gives a measure of the diffusion in frequency of the photons, while η and η^2 represent the energy lost by the photons for direct Compton scattering and the energy gain by them for inverse Compton, respectively.

The total spectrum is a combination of different scattering orders, depending on the initial energy of the photons, with a slope dependent on the temperature and the thickness of the plasma (see e.g. Di Salvo 2001; Malzac & Jourdain 1999).

The origin of the hot electron corona responsible of the Comptonisation of the soft spectrum is still matter of debate (see e.g. Degenaar et al. 2018, and references therein). It might originate from the evaporation of the outer layers of the accretion disc due to the irradiation from the NS (Shakura & Sunyaev 1973; Meyer & Meyer-Hofmeister 1994), or from the heating of the disc external atmosphere

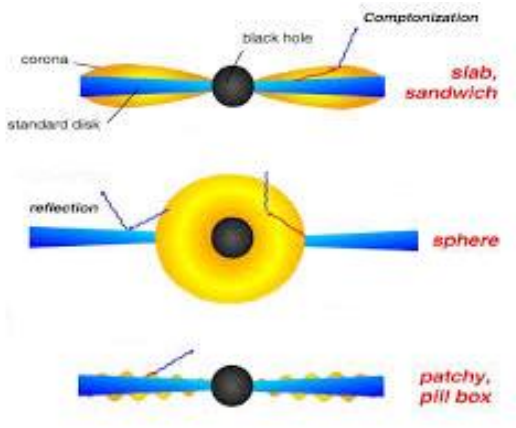

Figure 3.7: Representation of the proposed geometry for the Comptonising corona: slab (on the top), spherical (in the middle) and patchy (at the bottom) (adapted from Müller 2004).

because of the disc emission itself (Thorne & Price 1975; Liang & Price 1977), or even from magnetic reconnection phenomena related to magneto-hydrodynamic instabilities of the plasma in the disc (Balbus & Hawley 1991; Gammie & Balbus 1994; Hawley & Balbus 1997). In the most accredited scenario, in the presence of a low-magnetised NS, the accretion disc can extend closer to the NS surface, where the high radiation flux photo-ionises and heats the inner disc creating the so-called accretion disc corona (ADC model, White & Holt 1982).

The geometry of the corona is also not completely clear (see Figure 3.7). It is thought to be located in the innermost part of the system, covering the NS and the inner accretion disc (spherical geometry, see e.g. Dove et al. 1997, and reference therein), but a slab corona with a plane-parallel geometry above and below the accretion disc is possible as well (see Sunyaev & Titarchuk 1980; Haardt & Maraschi 1991) and even a non-uniform patchy corona composed of blobs distributed all over the disc was hypothesised (Haardt et al. 1994; Reynolds & Nowak 2003).

3.1.3 The reflection component

Some of the radiation outgoing from the electron cloud is reflected by the surface of the accretion disc and gives an important contribution to the total spectrum. The reflection spectrum provides information about the ionisation state of the plasma in the disc and the geometry of the system. At low energies ($E < 1 - 10$ keV), indeed, the spectrum is a function of the ionisation degree of the matter and the abundance of the elements, because the dominant process is the photo-electric absorption (Longair 2011). It is the result of the interaction between soft photons and ISM or the disc matter. It is a bound-free process in which the low-energy incident photon is absorbed by an atom or an ion with the emission of an electron with energy $E_e = h\nu_0 - E_{\rm bound}$, where $h\nu_0$ is the incident photon energy and $E_{\rm bound}$ is the dissociation energy of the electron. Then, the probability for the photo-absorption depends on the energy of the incident photon and on the atomic number Z of the target and the related cross-section for one collision is (Heitler 1954)

$$\sigma_k \propto \frac{Z^5}{(h\nu)^{7/2}}. \tag{3.15}$$

The total absorption cross-section is obtained by adding up σ_k of each process, weighed for the abundances of each element involved. Because of the strong dependence on Z, although heavy elements are less abundant, their contribution is predominant.

The plasma is composed also of ions of heavy elements (such as oxygen, iron, carbon, nitrogen, etc...) which are irradiated by the emission coming from the innermost region of the system. When

an incident photon is absorbed, the ion becomes unstable and one of more external electrons fall in the vacancy left by the other one expelled. If this process is associated with a photon emission, we have *fluorescence* phenomenon; while, if there is an internal energy transfer with an emission of another electron, the *Auger effect* (see Figure 3.8).

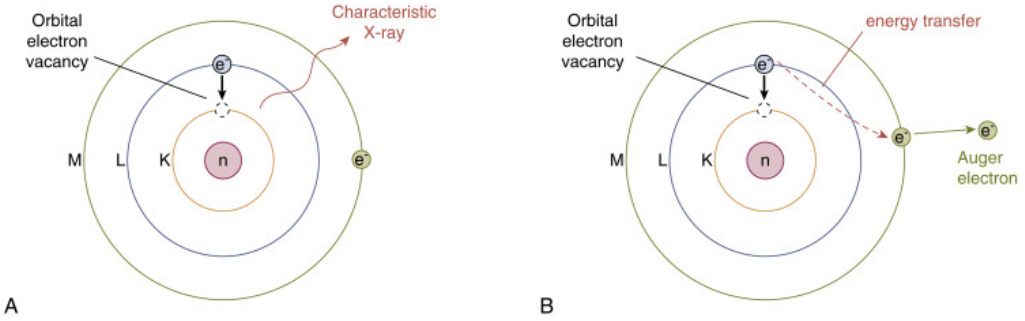

Figure 3.8: Simplified representation of fluorescence (A) and Auger (B) effect.

The decay probability for fluorescence is $\propto Z^4$, while that for Auger effects is almost constant. Therefore the fluorescence gain is more important for heavy element, whereas for small Z the Auger is predominant. The fluorescence is responsible of the emission lines in the spectrum. Among them, the iron emission lines, in particular, are really interesting.

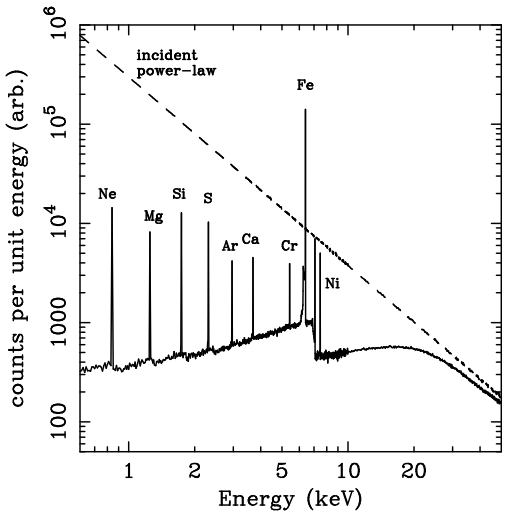

Figure 3.9: Monte Carlo simulation of X-ray reflection from an illuminated disc. The dashed line represent the incident X-ray continuum while the solid line is the reflected spectrum (integrated over all angles) (Reynolds 1999).

Broad emission lines (FWHM up to 1 keV) in the Fe-K region (6.4 - 6.97 keV) are often observed in the spectra of NS-LMXBs with both an inclination angle lower than 60° (e.g. Matranga et al. 2017a; Chiang et al. 2016; Papitto et al. 2013; Sanna et al. 2013; Piraino et al. 2012; Cackett et al. 2009; Di Salvo et al. 2009; Iaria et al. 2009; Shaposhnikov et al. 2009; Pandel et al. 2008; Cackett et al. 2008) and with an inclination angle between 60° and 90° (the so-called dipping and eclipsing sources; e.g. Iaria et al. 2019; Gambino et al. 2019; Ponti et al. 2018; Pintore et al. 2015;

Díaz Trigo et al. 2012, 2009; Iaria et al. 2007; Boirin et al. 2005; Parmar et al. 2002; Sidoli et al. 2001). These broad lines are identified with the Kα radiative transitions of iron at different ionisation states, and most likely originate in the region of the accretion disc close to the compact object, where matter is rapidly rotating and reaches velocities up to a few tenths of the speed of light. From

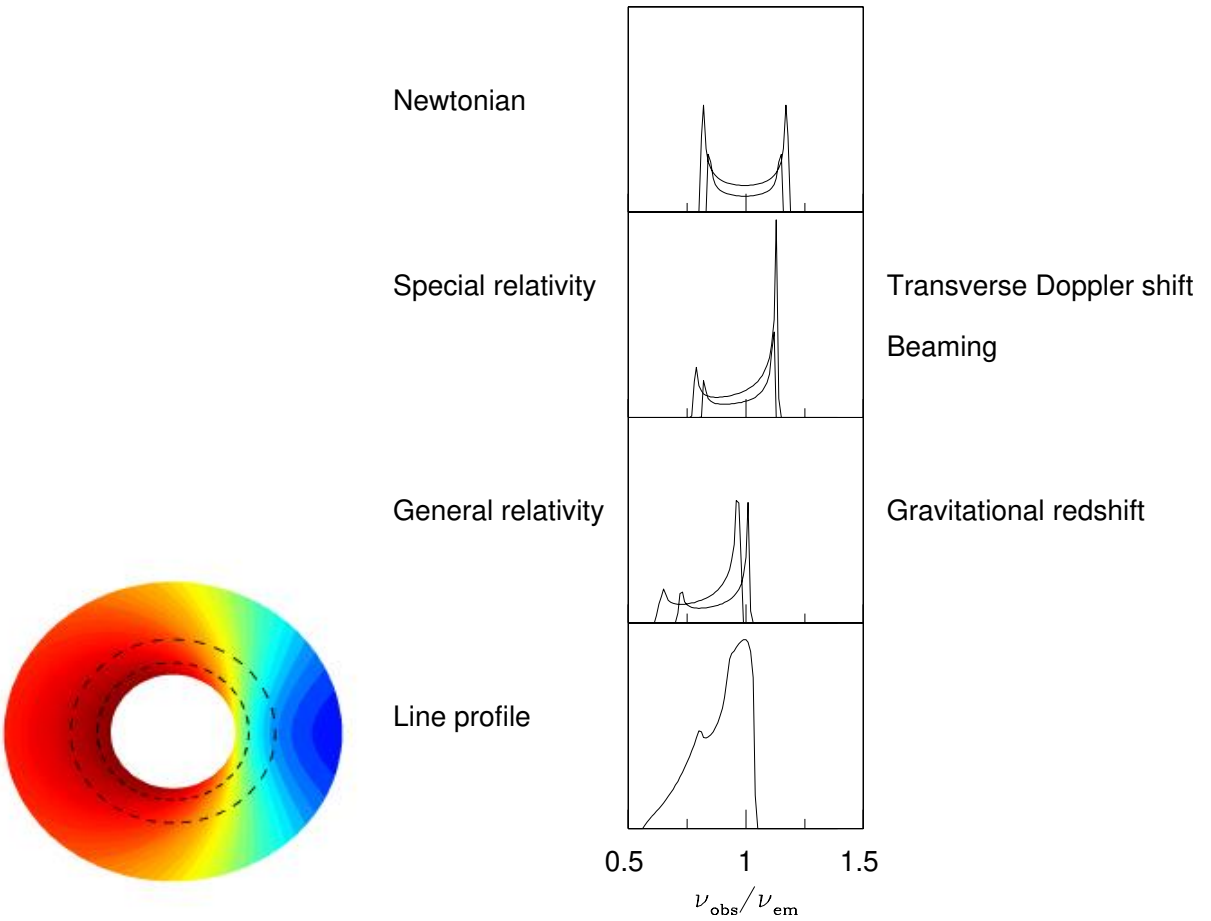

Figure 3.10: Left panel: representation of the accretion disc from the top, with matter approaching (blue) and receding (red). The dashed lines indicate two radii of the disc (Egron 2013). Right panel: evolution of the Fe emission line shape for Doppler and relativistic effects (first three boxes). The total line profile results very broad and skewed (last box). The line is represented in term of observed flux (on y-axis) on the ratio of observed and emitted frequency (on x-axis) (Fabian et al. 2000).

classical issues, indeed, a Gaussian-type line affected by thermal broadening would be expected, due to the Maxwellian distribution of the particle in the plasma. The thermal broadening is $\propto (kT/m_A)^{1/2}$, with kT the temperature of emitting particles and m_A their mass; however, in order

to produce the observed broadening, the temperature should be hundreds of keV. Furthermore, these emission lines results also energetically shifted and show an asymmetric and skewed profile (see e.g. Fabian et al. 1989; Laor 1991). Since they have origin in the inner part of the disc, where the Keplerian velocity of the matter is $v_\phi \sim 0.1c$ (Equation 1.8), each ring produces a double-peaked line as a results of the Doppler effect (first box in Figure 3.10). The peak at high frequencies (blue peak) is affected by the relativistic beaming effect and is enhanced (second box in Figure 3.10). At the same time, the red peak is affected by gravitational redshift because it is "moving away" and is enlarged (third box in Figure 3.10) (Fabian et al. 2000). The final shape is shown in the last box of Figure 3.10. The two lines shown in the same figure are emitted at two different radius of the disc and the broadest corresponds to the inner radius. Being the whole reflection spectrum modified by transverse Doppler shifts, Doppler broadening, relativistic Doppler boosting and gravitational redshift, these lines provide a useful probe to understand the effects of the strong gravitational field of NS on the inner region of the accretion disc.

It should be mentioned that relativistic (plus Compton) broadening is not the unique physical interpretation for the large width of the iron line profile in these systems. For instance, Titarchuk et al. (2003) suggested that the characteristic asymmetric skewed profile of the iron line could originate from an optically thick flow ejected from the disc, outflowing at relativistic speeds. However, for an increase of the observed broadening this model requires a corresponding increase of the equivalent hydrogen column due to the increased number of scatterings, and this correlation seems to be absent for NS-LMXBs (Cackett & Miller 2013). The study of the line profile therefore provides important information on the ionisation state, geometry, and velocity field of the reprocessing plasma in the inner accretion flow.

In addition to the emission lines, some LMXB spectra exhibits the so-called absorption edges, due to the absorption of a photon by a target that reaches its ionisation state. They can be observed when the energy of incident photon is equal to the ionisation limit of the atom, i.e. $h\nu = E_i$ (see e.g. Iaria et al. 2019, and reference therein).

3.2 Spectral variability

The emission of a LMXB source is characterised by two main spectral states, referred to as *soft* and *hard*.

The soft state spectrum (left panel in Figure 3.11 and (b) in Figure 3.12) is characterised by a (predominant) blackbody or disc-blackbody component and a harder saturated Comptonised

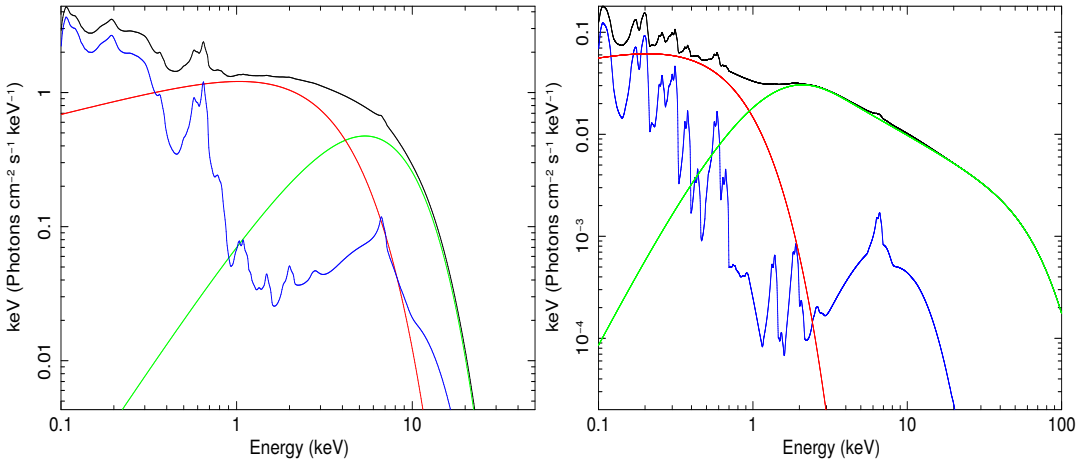

Figure 3.11: Best fitting model in the E×f(E) representation of the soft (left panel: thermal disk emission in red, blackbody thermal emission in red and reflection component in blue) and hard state (right panel: thermal soft disc emission in red, Comptonised component in green and reflection component/iron line in blue) for the proto-type NS-LMXB source 4U 1705-44 (D'Aì et al. 2010)

component represented by a weak power law, probably due to the inverse Compton scattering affecting the seed photons (see e.g. Di Salvo et al. 2009; Done et al. 2007; Di Salvo et al. 2005; Piraino et al. 2007; Barret & Olive 2002). Moreover, strong emission lines are often detected and the observed luminosity is very high (less or equal to 0.1 L_{EDD} with $L_{EDD} \simeq 1.5 \cdot 10^{38}(M/M_{\odot})$ erg/s the Eddington luminosity) (Zdziarski & Gierliński 2004).

Meanwhile, the hard state (HS) spectrum (right panel in Figure 3.11 and (d) in Figure 3.12) can be described by a weak thermal emission, sometimes not significantly detected (see e.g. Ludlam et al. 2016), plus a power law with a high-energy cut-off explained as due to inverse Compton scattering of soft photons in the hot electron corona (see e.g. Di Salvo et al. 2015; D'Aì et al. 2010; Cackett et al. 2010). Some HS spectra have been described in terms of a hybrid model of a broken power-law/thermal Comptonisation component plus two blackbody components (Lin et al. 2007; Armas Padilla et al. 2017). However, the broken power-law model does not carry information about the origin of the seed photons of the Comptonised component, that is, it does not allow one to distinguish between the contribution to the Comptonised component of a blackbody or a disc-blackbody. In this sense, a Comptonisation model is more useful for the identification of the origin of all the spectral components, and in particular the main component responsible for the soft thermal emission. Recently, some HS spectra have been interpreted in terms of a double Comptonised component with seed photons emitted by NS and the accretion

disc (Zhang et al. 2016).

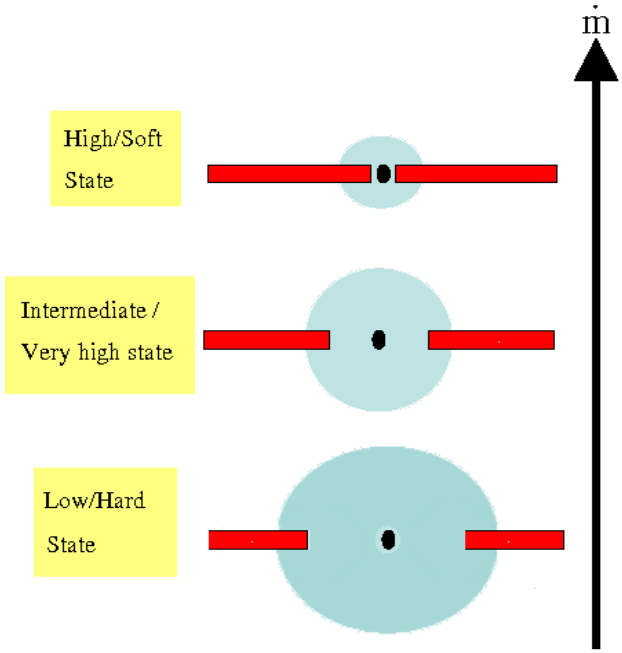

Figure 3.12: Simplified representation of the corona and disc geometry in the three main spectral states (possibly) related to the variation in the mass accretion rate (adapted from Fender 2001).

The reflection is less efficient in HS usually showing a lower degree of ionisation of the accreting matter and the presence of weaker features with respect to SS. The efficiency of the reflection is mainly indicated by the presence of a strong emission line from highly ionised Fe atoms; this probably reflects the greater emissivity of the accretion disc, which is proportional to r^{-betor}, where r is the radius of the disc at which the incident radiation arrives and *betor* is the power-law dependence of emissivity and is usually found to be between 2 (in the case of a dominating central illuminating flux) and 3 (which describes approximately the intrinsic emissivity of a disc). The higher emissivity in SS is the consequence of the disc (generally) being closer to the NS surface than in HS(see e.g. Di Salvo et al. 2015; Egron et al. 2013). In addition to these one, another three kind of spectral states were observed:

- the *ultrasoft* or *pure state*, characterised almost exclusively by a blackbody with a peak at lower energy than in the soft state and by a low luminosity ($L \sim 0.02\ L_{EDD}$, expected more likely for BH-systems, see e.g. Zdziarski et al. 2004);
- the *intermediate state*, a transition state between the soft and the hard states, distinguished by an high-energy tail close to the blackbody peak (due to the disc emission) and by a very low luminosity ($L \lesssim 0.02\ L_{EDD}$, see e.g. Marino et al. 2019a);
- the *no-accretion* or *quiescent state*, typical of those binary systems hosting a highly-magnetised NS, in which a strong propeller effect wipes out most of the accreting

matter (see e.g. Degenaar & Wijnands 2012; Parikh & Wijnands 2017).

The state transitions are possible from the soft to the intermediate state and vice versa, from the intermediate to the hard state and vice versa and from the hard to the quiescent state (Matsuoka & Asai 2013). The transitions are related in general to the variation of the accreting flow (i.e. of $\dot{M}$) which involves variation of the inner radius of the disc (Zdziarski & Gierliński 2004): in general the greater $\dot{M}$, the softer the spectrum.

Contrarily to the BH-LMXBs case (see Belloni 2010; Done et al. 2007, for a review), the NS-LMXBs spectral changes are not well understood. In order to investigate the long-term spectral

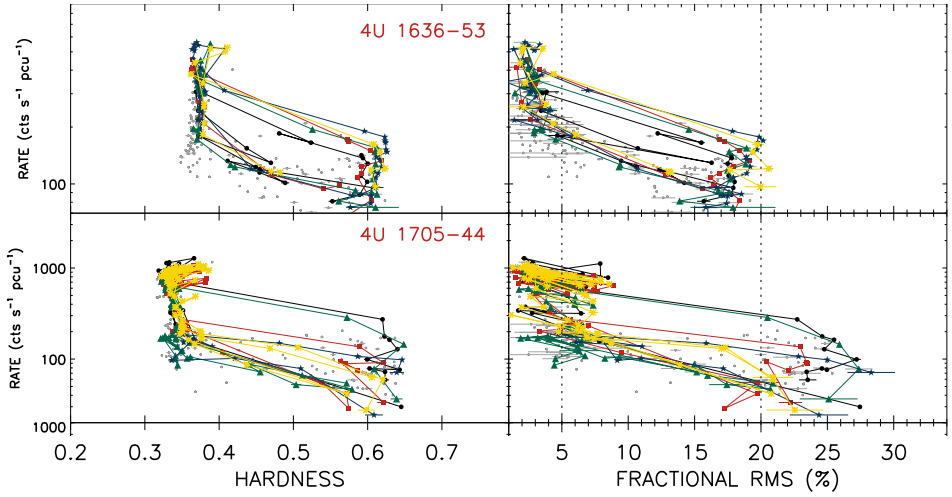

Figure 3.13: Example of hysteresis in the HID (on the right) and RID (on the right) of persistent NS-LMXBs 4U 1636-53 and 4U 1705-44 (only five representative loops are highlighted for clarity Muñoz-Darias et al. 2014).

variability of these sources, Muñoz-Darias et al. (2014) studied a sample of 50 NS-LMXBs monitored by the *Rossi-XTE*, for a total of more of ten thousands observations. They constructed and analysed the power density spectra (PDS, i.e. the distribution of the average power in a certain range of frequencies Belloni et al. (2006)), the rms-intensity diagram (RID, i.e. the relation between the rms amplitude of the variability and the total count/rate Muñoz-Darias et al. (2011)) and the hardness-intensity diagram (HID, i.e the relation between the ratio of the count/rate of the source in two different energy bands and the total count/rate Muñoz-Darias et al. (2014)) for all the sample. They observed a cyclical behaviour from both HID and RID: ten of these source presented hysteresis pattern for the spectral transitions, indeed the systems initially evolve from HS to the SS, to then return to the former following a different luminosity track; intermediate states (IS) can

be identified during the transitions (see Figure 3.13 for example).

A sub-classification of NS-LMXBs is based on the spectral and timing variability of the sources (Hasinger & van der Klis 1989), pointed out by the pattern traced by a single source in its X-ray colour-colour diagram (CD) or HID. Thus, we distinguish the so-called Atoll-class (with luminosity $\sim$ 0.01-0.1 of the Eddington luminosity $L_{\rm Edd}$) and Z-class (luminosity close to $L_{\rm Edd}$) systems.

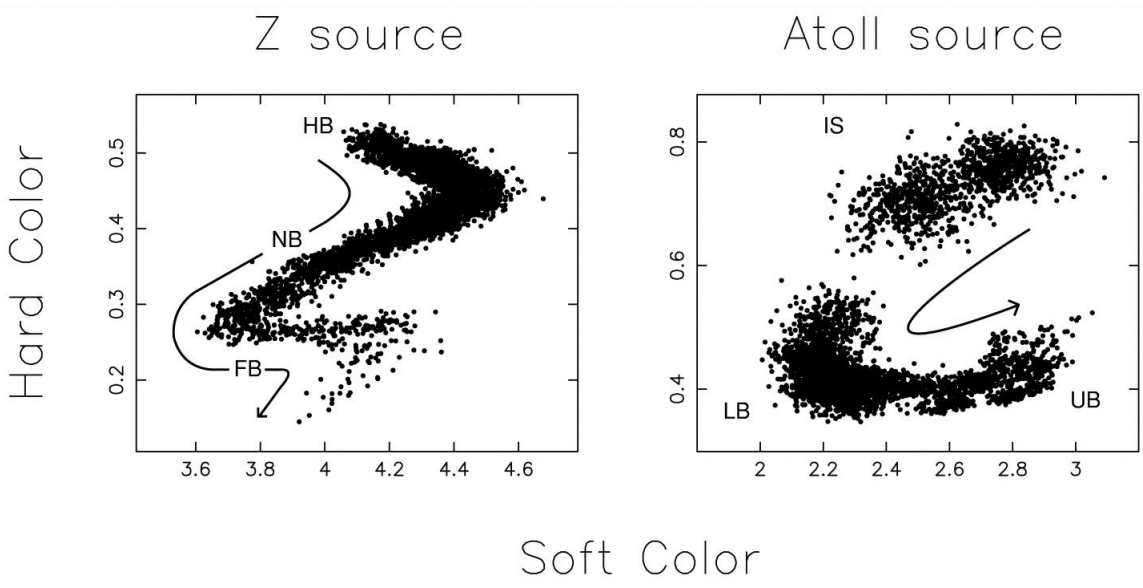

Figure 3.14: Simplified description of the relation of accretion / luminosity to patterns of NS-LMXBs. For the Z sources (on the left) it shows the horizontal (HB), normal (NB) and flaring (FB) branches. Meanwhile, for the atoll sources (on the right) the island state , the lower banana (LB) and the upper banana (UB) can be identified. The expected direction of increasing mass accretion rate $\dot{m}$ is indicated by the arrows (comparison of CDs by Jonker et al. 2000b; van Straaten et al. 2003, with RXTE data).

The CD of the Z-sources shows the typical three branches pattern, in which we identify the horizontal branch (HB) at the top of the track, the normal branch (NB) in the middle and flaring branch (FB) at the bottom (see e.g. Hasinger & van der Klis 1989). The evolution of an individual source along the Z-track occurs in a timescale of few days and it is (probably) driven by the variability in the mass accretion rate $\dot{M}$ (Hasinger et al. 1990). The power spectrum of a Z-source shows quasi periodic oscillations (QPOs), i.e. low-amplitude X-ray modulation with frequencies between 5-1000 Hz. According to one of the standard scenarios, QPOs are due to the interaction between the weak ($< 10^{10}$ G) magnetic field of NS and transient blobs of accreting matter in the innermost region of the accretion disc (see van der Klis 1989, 2006a, for a review). The QPOs

frequencies could be compatible with the beat between the NS spin frequency and the Keplerian frequency of the blobs (Alpar & Shaham 1985) and result in a modulation in the mass accretion rate $\dot{M}$ chargeable to the X-ray intensity variation (Lamb et al. 1985). Since the highest frequency oscillations, the so-called kHz QPOs (see e.g. Strohmayer et al. 1996; van der Klis 2000; Jonker et al. 2000a; van der Klis 2006b), occur near the orbital frequencies of matter in the inner accretion disc, a constraint on the mass and the radius of the NS can be inferred assuming a stable orbital motion around the NS with radius between the NS surface and the innermost stable circular orbit (ISCO= $6GM/c^2$). Under these hypotheses, it is possible to find an upper limit on the observable frequency at the ISCO in the range 1000-1250 Hz, assuming a NS with mass $M_{\rm NS} = 2M_{\odot}$ (Zhang et al. 1997; Miller et al. 1998).

An Atoll source shows, instead, two main different states during its evolution, called island (IS) and banana (BS) state, respectively, moving from one to another in a timescale of weeks. Together with the QPOs, the power spectrum of the source shows a band-limited noise with frequencies up to tens of Hz (high-frequency noise, HNF) in IS, while in BS the power spectrum is dominated by a power-law noise below 1 Hz (very low-frequency noise, VLFN). It is deemed that these features are related to the mass accretion rate variability, which seems to increase from IS to BS (see e.g. van der Klis 1995).

The spectral features of the two classes are those described in the previous section 3.1. It has to be noticed that the Z-sources present also a hard power-law component predominant above 20 keV (e.g. Reig & Kylafis 2016; Paizis et al. 2006; Iaria et al. 2001a; Di Salvo et al. 2001) which strength is usually related with the position of the source in the CD, being highly significant in the HB up to disappear in the FB (see e.g. Di Salvo et al. 2000; D'Aí et al. 2007; Titarchuk et al. 2014; Revnivtsev et al. 2014). The origin of the hard tail is still matter of debate: it may originate by the Comptonisation in a hybrid thermal/non-thermal electron corona (see e.g. Farinelli et al. 2005; Poutanen & Coppi 1998), or in a mildly relativistic bulk motion of matter close to the compact object (e.g. Farinelli et al. 2008; Psaltis 2001).

Comparison with BH-systems (in a nutshell)

Binary systems hosting a neutron star show similar spectral characteristics with respect to black hole systems, and it would be very hard to distinguish between these two kinds of systems looking only at their spectra. In the BH-candidate systems (BHs) the accreting matter may free fall into the compact object because close to the event horizon the gravitational force predominates the pressure forces. On the other hand, in the NS systems (NSs), the free fall of accreting matter is slowed down by the presence of the solid surface emitting a large part of the total flux and therefore radiation pressure forces should be predominant. Generally this means a mass accretion rate higher than for NSs and possibly a hotter Comptonized component (Di Salvo et al. 2006).

In BHs a correlation seems to be present between the softness (or hardness) of the spectrum and the value of the photon index. In particular, the steeper the power law, the softer the spectrum (Steiner et al. 2016); for NSs this correlation does not always seem to be present, as in the case of the source 4U 1702-429 described in Chap. 5 (Mazzola et al. 2019a). Furthermore, as for BHs the spectral variation is led by the variation in the flux of the seed photons in the corona and then in a variation in the flux of the outgoing Comptonised photons (Del Santo et al. 2008). The emission lines observed in the spectra of NSs turn out to be broadened and skewed like the lines detected in BHs spectra, suggesting that in both the cases they are produced in the innermost region of the accretion disc, where the effects of the gravitational field of the compact object is stronger. However, both in HS and SS of NSs, the broadening of the line is not as extreme as in the case of some BH X-ray binaries or AGNs (see e.g. Reis et al. 2009; Fabian et al. 2009).

The reflection component has a similar behaviour in BH and NS systems and turns out to be more evident in the SS than in the HS, at least in the standard X-ray range (2-10 keV), with the presence of stronger features (see e.g Di Salvo et al. (2015); Egron et al. (2013); Di Salvo et al. (2009) for NS systems and Steiner et al. (2016); Zdziarski (2002) for BH systems).

XRBs are also characterised by the emission of radiatively inefficient collimated outflows, known as *jets*, resulting from the synchrotron emission by relativistic particles ejected from the system along the rotation axis, which represent the most relevant mass ejection mechanism of these sources. Jets are characterised by flat spectra in the radio-to-IR band and the interaction between the accretion disc and the central compact object is thought to be at the origin of its production, based on the observation that the mass accretion rate variability drives changes in the jets behaviour (disc-jet coupling model, see e.g. Fender et al. 2004b, 2009). Studying relativistic jets in XRBs allows to investigate the link between the jets production and the different accretion regimes and

find some similarities in the radio/X-ray emission correlation between NS and BH systems (see Migliari & Fender 2006, for a review). For example, both BHs and NSs produce steady jets in their HS (luminosity below a few per cent of the Eddington limit, see e.g. Migliari & Fender 2006; Migliari et al. 2007b, 2010), while transient jets are associated with highly variable and outbursting sources at the highest luminosities (see e.g. Fomalont et al. 2001; Fender et al. 2004a; Migliari et al. 2011). However, important differences can be inferred by the observations: for example, the jets in NSs are less powerful and seem to be not suppressed when the NSs are steadily in their SS (see e.g. Migliari et al. 2004). Moreover, the presence of transient optically thin jets is associated with hard-to-soft state transitions during BH outbursts, but they are not observed in the case of NSs (Miller-Jones et al. 2010, 2011), suggesting that jets powering is dependent on the nature of the compact object (see e.g. Migliari et al. 2011).

Part II

Research Activity

Chapter 4

Updated orbital ephemeris of the ADC source X 1822-371: a stable orbital expansion over 40 years

S. M. Mazzola, R. Iaria, T. Di Salvo, A.F. Gambino, A. Marino, L. Burderi,
A. Sanna, A. Riggio and M. Tailo (2019, A&A, 625, L12)

4.1 Introduction

The low-mass X-ray binary system (LMXB) X 1822-371 is a persistent eclipsing source with an orbital period of 5.57 hr, hosting an accreting X-ray pulsar with a spin frequency close to 1.69 Hz (Jonker & van der Klis 2001) that is increasing with a derivative of $\dot{\nu} = (7.57 \pm 0.06) \times 10^{-12}$ Hz s^{-1} (Bak Nielsen et al. 2017; Iaria et al. 2015b). The mass function of the system is $(2.03 \pm 0.03) \times 10^{-2}$ $M_\odot$ (Jonker & van der Klis 2001), with a lower limit on the companion star mass of 0.33 ± 0.05 $M_\odot$ (Jonker et al. 2003). X 1822-371 belongs to the class of accretion disc corona (ADC) sources (White & Holt 1982), with an inclination angle between 81° and 84° (Heinz & Nowak 2001). The distance to this source was estimated to be between 2-2.5 kpc by Mason & Cordova (1982) using infrared and optical observations. The 0.1-100 keV unabsorbed luminosity is 1.2×10^{36} erg s^{-1} when a distance of 2.5 kpc is adopted (Iaria et al. 2001b). The most recent orbital ephemeris of the source X 1822-371 was reported by Chou et al. (2016), who suggested that the orbital period derivative is $\dot{P}_{\rm orb} = (1.464 \pm 0.041) \times 10^{-10}$ s s^{-1} by adopting quadratic

ephemeris, or $\dot{P}_{\rm orb} = (1.94 \pm 0.27) \times 10^{-10}$ s s^{-1} by adopting cubic ephemeris. The value of $\dot{P}_{\rm orb}$ is three orders of magnitude higher than what is expected from conservative mass transfer driven by magnetic breaking and gravitational radiation and can be explained only by assuming a mass transfer rate higher than three times the Eddington limit for a neutron star (NS) (Burderi et al. 2010; Bayless et al. 2010). Bak Nielsen et al. (2017) suggested that X 1822-371 is a relatively young binary in which the donor is transferring mass on a thermal timescale. The authors suggested that the super-Eddington mass transfer rate generates an outflow of matter from the magnetospheric radius.

A suggestion to explain the evolutionary stage of X 1822-371 comes also from recent numerical studies of the secular evolution of LMXBs including X-ray irradiation of the donor (Tailo et al. 2018). These models show that when the donor has a mass $0.4 \lesssim {\rm M/M_\odot} \lesssim 0.6$, like in this system, the evolution is subdivided into cycles of short mass-transfer phases, during which the donor expands on the thermal timescale of its convective envelope and the orbital period increases significantly, followed by long phases of detachments during which thermal relaxation takes place and the donor recovers full thermal equilibrium. The next stage of mass transfer occurs when the orbital period has decreased again so that the stellar radius fills the Roche lobe again, and a new orbital expansion follows. The maximum $\dot{P}_{\rm orb}$ in the published models is $\sim 6 \times 10^{-11}$ s s^{-1} (see e.g. Tailo et al. 2018), but the specific evolution of X 1822-371 may be obtained by reasonable variations of the input parameters.

In this work, the eclipse arrival times reported by Iaria et al. (2011) were used, with the addition of two new eclipse arrival times obtained from analysing the *RXTE* observation performed in 2011 and the *XMM-Newton* observation performed in 2017; our eclipse arrival times span 41 yr. The statistical significance for the presence of a second derivative of the orbital period and the possibility that the quadratic term mimics a wide sinusoidal modulation were investigated. In the latter case, it was excluded that the sinusoidal modulation could be explained as due to a gravitational coupling of the orbit with changes in the oblateness of the magnetically active companion star, the so-called Applegate mechanism (Applegate 1992).

4.2 Observations and data analysis

The *XMM-Newton* Observatory (Jansen et al. 2001) observed the source X 1822-371 on 2017 March 3 between 01:10:54 UTC and 19:12:27 UTC (ObsId. 0784820101) for a total observing time of 69 ks. The data collected by pn-type CCD detector of the European Photon Imaging

Camera (Epn, Strüder et al. 2001), operating in Timing Mode, were analysed with the aim to estimate the eclipse arrival time. I reprocessed the data using the Science Analysis Software (SAS) v16.1.0, verified the absence of background flaring during the observation, and applied the barycentric correction to the event times.

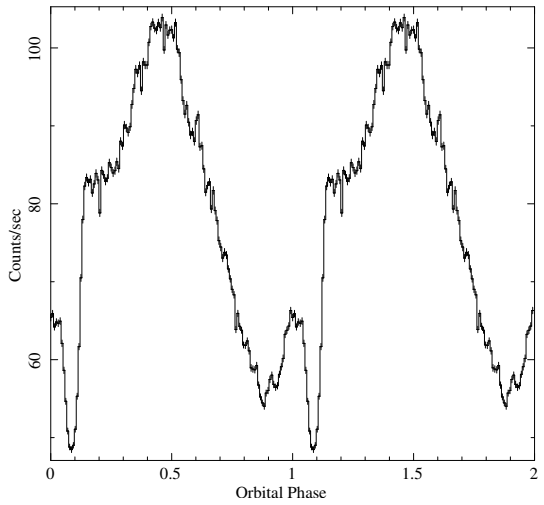

Figure 4.1: *XMM-Newton/Epn* folded orbital light curve obtained by adopting a period of 0.2321107 days. The period is divided into 128 bins. The observed asymmetrical shape is due to the fact that the eclipses are partial (see Burderi et al. 2010, for a detailed discussion) and the central X-ray emission is also partially obscured by a structure in the accretion disc with a variable height above the orbital plane (White & Holt 1982), implying a high inclination angle of observation ($81^\circ - 85^\circ$, Heinz & Nowak 2001; Ji et al. 2011; Iaria et al. 2013)

I extracted the Epn 0.3-10 keV light curve considering only PATTERN$\leq$4 and FLAG=0 events from a region that included the brightest columns of the detector (RAWX between 30 and 45), while for the background I extracted the events from a region far away from the source (RAWX between 5 and 10). Three partial eclipses were present at 14 ks, 34 ks, and 54 ks from the start time in the Epn background-subtracted light curve. The observation covers almost 3.4 orbital periods of the system. I folded the background-subtracted light curve, adopting a reference epoch $T_{\rm fold}$ = 57818.4237 MJD (corresponding to a time close to the mid-time of the observation) and a reference period of $P_{\rm fold}$ = 0.2321107 days. The folded light curve is shown in Figure 4.1.

Afterwards, the X-ray eclipse time obtained by analysing the *RXTE* observations taken from 2011 November 15 to 30 (ObsId. P96344) was added. The same observation was analysed by Chou et al. (2016) using standard 2 data in the energy range 2-9 keV and inferring four eclipse arrival times. In order to make the analysis self-consistent, R. Iaria re-analysed these data using the X-ray light curves obtained from the standard 1 data products (Std1) of archival *RXTE* data, that is, the 2-40 keV background-subtracted light curves collected by the PCA with a time resolution of 0.125 s. He applied the barycentric correction to the events using the ftool `faxbary` and folded the light curve using as epoch $T_{\rm fold}$ = 55887 MJD and as period $P_{\rm fold}$ = 0.2321104 days. To estimate the orbital phase at which the eclipse occurred, he adopted the procedure reported by Burderi et al. (2010), finding that the eclipse

Table 4.1: Journal of available eclipse arrival times for source X 1822-371

Eclipse time (MJD, TDB)	Delays (s)	Cycle	Ref.	Satellite
43413.0272(46)	1416(397)	-29900	1	HEAO-1 Scan
43591.0521(46)	1145(397)	-29133	1	HEAO-1 Scan
43776.0459(12)	1359(104)	-28336	1	HEAO-1 Point
43777.9065(46)	1680(397)	-28328	1	HEAO-1 Scan
43968.9247(69)	991(596)	-27505	2	Einstein
44133.0277(30)	1124(259)	-26798	1	Einstein
45579.9932(5)	642(43)	-20564	1	EXOSAT
45614.80940(38)	622(33)	-20414	1	EXOSAT
45962.50914(33)	588(29)	-18916	1	EXOSAT
45962.74046(30)	520(26)	-18913	1	EXOSAT
45962.97254(54)	517(29)	-18912	1	EXOSAT
46191.13643(31)	533(27)	-17929	1	EXOSAT
46191.36768(33)	459(29)	-17928	1	EXOSAT
46191.60008(29)	484(25)	-17927	1	EXOSAT
47759.72810(30)	195(26)	-11171	1	Ginga
48692.34396(70)	83(60)	-7153	1	ROSAT
49267.50984(40)	-58(35)	-4677	3	ASCA
50352.85425(35)	-54(30)	-1	3	ASCA
50353.08728(23)	26(20)	0	3	RXTE
50701.0187(12)	46(104)	1499	3	BeppoSAX
50992.0858(23)	101(199)	2753	4	RXTE
51779.6317(19)	-61(164)	6146	4	Chandra
51975.06934(56)	59(48)	6988	4	XMM-Newton
51975.06935(31)	59(27)	6988	4	RXTE
52432.09458(30)	188(26)	8957	4	RXTE
52488.03300(38)	189(33)	9198	4	RXTE
52519.13569(85)	190(73)	9332	4	RXTE
52882.15470(37)	158(32)	10896	4	RXTE
54010.6730(9)	294(78)	15758	5	Suzaku
54607.19592(56)	408(48)	18328	4	Chandra
55887.05307(38)	838(33)	23842	6	RXTE
57818.44392(96)	1452(82)	32163	6	XMM-Newton

References:1) Hellier & Smale (1994), 2) Hellier & Mason (1989), 3) Parmar et al. (2000), 4) Burderi et al. (2010), 5) Iaria et al. (2011), 6) this work

arrival times are $T_{\rm ecl} = 57818.44392(96)$ MJD/TDB and $T_{\rm ecl} = 55887.05307(38)$ MJD/TDB for the *XMM-Newton/Epn* and *RXTE/PCA* observations, respectively. The associated errors are at 68% confidence level.

Table 4.2: Best-fit modelling parameters of eclipse time delays with different models, including quadratic, cubic, sinusoidal, and quadratic plus sinusoidal ephemeris.

Parameter	Quadratic Model	Cubic Model
a (s)	5 ± 15	-3 ± 14
b (10^{-4} s)	-5 ± 7	19 ± 16
c (10^{-6} s)	1.48 ± 0.05	1.52 ± 0.06
d (10^{-12} s)	–	-6 ± 4
$T_{0,\rm orb}$ (MJD/TDB)	50353.08733(16)	50353.08725(16)
$P_{0,\rm orb}$ (days)	0.2321095653(85)	0.232109593(18)
$\dot{P}_{\rm orb}$ (10^{-10} s s^{-1})	1.475(54)	1.514(55)
$\ddot{P}_{\rm orb}$ (10^{-19} s s^{-2})	–	$-0.91(55)$
χ^2/d.o.f.	42.3/29	37.4/28
Parameter	LS Model	LQS Model [1]
a (s)	8084 (fixed)	4 ± 13
b (10^{-4} s)	-873.9 (fixed)	-4 ± 7
c (10^{-6} s)	–	1.47 ± 0.05
A (s)	9290 ± 30	34 ± 12
$a_{\rm bin}/l$	–	1.1 ± 0.3
$\rm N_{MOD}$ ($\times 10^4$)	32.1 ± 0.5	0.5 ± 0.2
$\rm N_0$ ($\times 10^4$)	5.41 ± 0.06	-0.28 ± 0.03
$\rm P_{MOD}$ (yr)	204 ± 3	3.4 ± 1.2
$T_{0,\rm orb}$ (MJD/TDB)	50353.18085 (fixed)	50353.08733(15)
$P_{0,\rm orb}$ (days)	0.232108660 (fixed)	0.2321095661(81)
$\dot{P}_{\rm orb}$ (10^{-10} s s^{-1})	–	1.468(53)
χ^2/d.o.f.	37.8/29	31.2/26

To update the orbital ephemeris, the 2 eclipse arrival times shown above were included with those reported by Iaria et al. (2011); the 32 eclipse arrival times, the corresponding number of orbital cycles, and the delays are summarised in Table 4.1. The number of orbital cycles N and the delays associated with the eclipse arrival times were obtained by adopting a reference orbital period of $P_0 = 0.232109571$ days and a reference eclipse time $T_0 = 50353.08728$ MJD, estimated for the *RXTE* observation of the source performed in 1996 (Parmar et al. 2000).

I fitted the delays as function of cycles adopting the quadratic model $y = a + bN + cN^2$ and obtaining a $\chi^2(d.o.f.)$ of 42.3(29). The uncertainties associated with the best-fit parameters a, b, and c were scaled by a factor $(\chi^2_{\rm red})^{1/2}$ to take into account a $\chi^2_{\rm red}$ of the best-fit model larger than 1. The best-fit values of the parameters are shown in the second column of Table 4.2 (upper part); the best-fit quadratic curve (red) and the corresponding residuals in units of σ are shown in the

[1] The errors are at 68% confidence level.

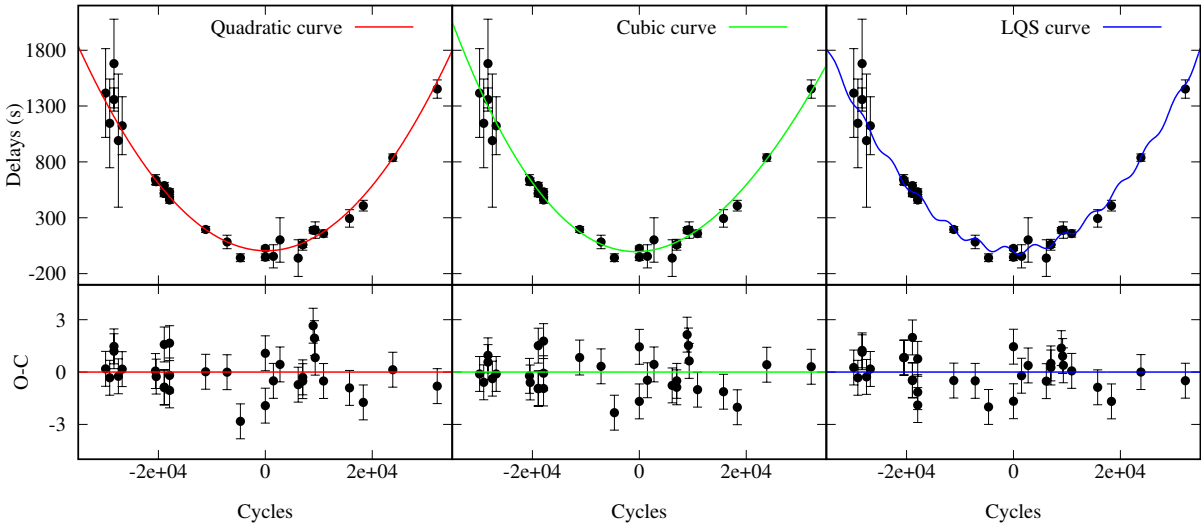

Figure 4.2: From left to right: delays vs. cycles for the quadratic (red), cubic (green), and LQS (blue) model. Residuals are in units of σ obtained by adopting the quadratic, cubic, and LQS model, respectively.

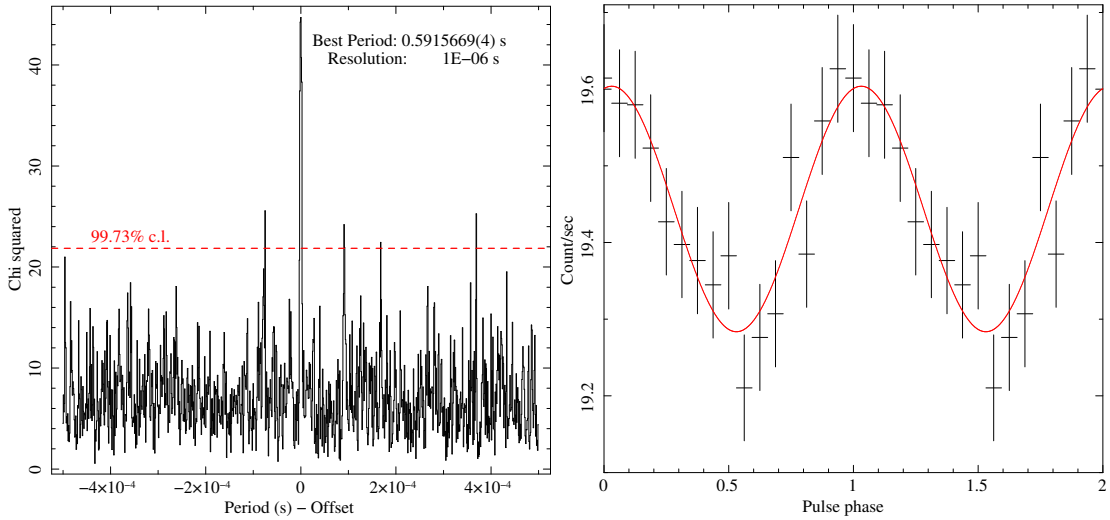

Figure 4.3: Left panel: Folding search for periodicity in the 5-12 keV *XMM-Newton/Epn* light curve. The horizontal dashed line indicates the χ^2 value of 21.85 at which it is found the 99.73% confidence level for a single trial, corresponding to a significance of 3 σ. Right panel: *XMM-Newton/Epn* folded light curves obtained by adopting the best period and using 16 phase bins per period.

left panel of Figure 4.2.

The updated orbital ephemerides are

$$T_{\rm ecl} = 50353.08733(16)\ {\rm MJD/TDB} + 0.2321095653(85)N + 1.711(63) \times 10^{-11} N^2, \quad (4.1)$$

where the first and the second term represent the new values of the reference epoch $T_{0,\rm orb}$ and orbital period $P_{0,\rm orb}$, respectively. The third term, equal to $\left(P_0 \dot{P}_{\rm orb}\right)/2$, allows us to estimate an orbital period derivative of $\dot{P}_{\rm orb} = 1.475(54) \times 10^{-10}$ s s^{-1}. Furthermore, I added a cubic term $d = \left(P_0^2 \ddot{P}_{\rm orb}\right)/6$ to the quadratic model in order to test the presence of a second derivative of the orbital period. The best-fit curve (green) and the corresponding residuals are shown in Figure 4.2 (central panel); the best-fit parameters are shown in the third column of Table 4.2 (upper part). The obtained $\chi^2(d.o.f.)$ is 37.4(28), with an F-test probability of chance improvement of 0.065, indicating that the cubic model improves the fitting at a confidence level lower than 2σ, meaning that the cubic term is not significantly required.

It was investigated also whether the quadratic term could mimic a sinusoidal modulation in the delays: the quadratic term was substituted with a sinusoidal one, using the model $y = a + bN + A\sin[2\pi(N - N_0)/N_{\rm MOD}]$ composed of a linear plus sinusoidal term (LS model, hereafter). Keeping the best-fit values of a and b fixed to 8084.33 s and -0.0873931 s to lead the fit to the convergence, the obtained $\chi^2(d.o.f.)$ is 37.8(29) with a $\Delta\chi^2$ of 4.9 with respect to the quadratic model, a modulation period $P_{\rm MOD} = N_{\rm MOD}\ P_0 = 204 \pm 3$ yr, and a semi-amplitude of the modulation $A = 9289(26)$ s. The best-fit values are shown in the second column of the lower part of Table 4.2. It was also verified a gravitational quadrupole coupling produced by tidal dissipation (Applegate & Shaham 1994) could be detectable in our data; to this aim, a quadratic term was added to the LS model. In the new model (hereafter LQS model), it was imposed $N_{\rm MOD} = 0.572\ c^{-1/2} A^{2/3} a_{\rm bin}/l$ (this relation will be discussed in section 4.3). The best-fit parameters are shown in the third column of the lower part in Table 4.2; the best-fit model (blue) and the corresponding residuals are shown in the right panel of Figure 4.2. The obtained $\chi^2(d.o.f.)$ is 31.2(26), and the F-test probability of chance improvement is 0.045 with respect to the quadratic model, indicating that the LQS model improves the fit at a confidence of about 2σ.

Finally, we searched for the X-ray pulsation of the source. Discovered by Jonker & van der Klis (2001), it can be used to determine orbital and spin parameters through the pulse arrival time delay technique (Chou et al. 2016): the events selected in a specific energy range are divided in

data segments of the same duration and the X-ray photon arrival times of each data segment were folded with a time-variable frequency, caused by the orbital Doppler effect of the circular orbit, to obtain the event phase, dependent on the orbital and spin period of the system (see Eq. 3 of Chou et al. 2016). Since it is equivalent to correcting the event times to the barycenter of the binary system and then folding with a constant frequency, here, the NS spin frequency has been searched in the *XMM-Newton/Epn* data by analysing the 5-12 keV events after applying the barycentric correction using the source coordinates. I corrected the data for the binary orbital motion using $a \sin i = 1.006(5)$ lt-s (Jonker & van der Klis 2001) and the value of the orbital period obtained from the quadratic ephemeris shown above. In order to search for the pulsation period, I applied the procedure described by Iaria et al. (2015b): I used the ftool `efsearch` of the XRONOS package (v 5.22), adopting as reference time the start time of the observation and a resolution of the period search of 10^{-6} s. I explored around a period $P_{\rm spin}$ of 0.591567 s, estimated using Eq. 6 in Chou et al. (2016), and subsequently, I fitted the peak of the corresponding χ^2 curve with a Gaussian function. I assumed that the centroid of the Gaussian was the best estimate of the spin period, and associated the 68% c. l. error obtained from the best fit with this. The inferred spin period is 0.5915669(4) s, the $\chi^2_{\rm peak}$ associated with the best period is 44.66 (see the left panel in Figure 4.3), and the probability of obtaining a χ^2 value greater than or equal to $\chi^2_{\rm peak}$ by chance, having seven degrees of freedom, is 1.58×10^{-7} for a single trial. Considering the 1000 trials in our research, almost 1.58×10^{-4} periods with a χ^2 value greater than or equal to $\chi^2_{\rm peak}$ is expected. This implies a detection significance at the 99.984% confidence level.

Furthermore, I folded the 5-12 keV *XMM-Newton/Epn* light curve by adopting the obtained $P_{\rm spin} = 0.5915669(4)$ s and the start time of the observation as reference epoch; I used 16 phase bins per period. I fitted the folded light curve with a constant plus a sinusoidal function with a period kept fixed to one, obtaining a $\chi^2(d.o.f)$ of 9.176(12), a constant value of 19.44(2) c/s and a sinusoidal amplitude $A = 0.16(2)$ c/s. The folded light curve and the best-fit curve are shown in the right panel of Figure 4.3. It was found the fractional amplitude of the pulsation to be $0.83 \pm 0.11\%$ for the estimated background count-rate of 0.15(1) c/s. This value is compatible with that reported by Jonker & van der Klis (2001) in the 5-12 keV energy band.

In the end, using the spin period values reported by Iaria et al. (2015b) in Table 2, the last value reported by Chou et al. (2016) in Table 4, and the spin-period obtained above, the estimated

spin period derivative is $-2.595(11) \times 10^{-12}$ s s^{-1} with

$$P_{\rm spin}(t) = 0.592758(3) \text{ s} - 2.595(11) \times 10^{-12} \ (t - 52500 \text{ MJD}) \times 86400 \tag{4.2}$$

(see also Jain et al. 2010).

4.3 Discussion

In the presented work, the orbital ephemeris of source X 1822-371 were updated by adding two eclipse arrival times obtained from the *RXTE/PCA* observations performed in 2011 and from the *XMM-Newton/Epn* observation performed in 2017. Our baseline covers almost 40 yr, from 1976 to 2017. The reference epoch of the ephemeris was moved to a more recent time, corresponding to 1996 September 27, which is close to the middle of the baseline. It was inferred $\dot{P}_{\rm orb}$ of $1.475(54) \times 10^{-10}$ s s^{-1}, compatible with the values in literature.The possibility that a cubic model could improve the fit of the delays was explored, as suggested by Chou et al. (2016); however, the addition of a cubic term to the quadratic model does not significantly improve the fit yet.

Several authors (Burderi et al. 2010; Bayless et al. 2010; Bak Nielsen et al. 2017) explained the high value of $\dot{P}_{\rm orb}$ as due to a super-Eddington non-conservative mass transfer rate. This 'quadratic model' seems the simplest explanation. Alternatively, the possibility that a large sinusoidal modulation could mimic the quadratic trend of the delays was investigated. A sinusoidal modulation of the delays could be associated with the gravitational quadrupole coupling (GQC) between the orbit and the changes of the quadrupole moment of the magnetically active companion star (Applegate 1992). The magnetic activity of the secondary generates a torque to the subsurface magnetic field of the companion star (CS); the torque induces a cyclic exchange of angular momentum between the inner and outer regions of the CS, changing its gravitational quadrupole moment, and consequently, the orbital period of the binary system. The necessary luminosity $L_{\rm GQC}$ to activate this mechanism was assmed to come from the nuclear luminosity $L_{\rm nuke}$ produced by the CS itself (Applegate 1992). Assuming the mass function $f = (2.03 \pm 0.03) \times 10^{-2} \ M_\odot$ (Jonker & van der Klis 2001) and the inclination angle 82.5 ± 1.5 deg (Heinz & Nowak 2001), then the estimated mass ratio is $q = M_2/M_1 = 0.27 \pm 0.02$ adopting a CS mass M_2 of $0.46 \pm 0.02 \ M_\odot$ and an NS mass M_1 of $1.69 \pm 0.13 \ M_\odot$ (Iaria et al. 2015b). Under

the reasonable hypothesis that the CS fills its Roche lobe, using Eq. 15 in Sanna et al. (2017),

$$L_{\rm GQC} = 3.35 \times 10^{32} m_1 q^{1/3} (1+q)^{4/3} P_{\rm orb,5h}^{-2/3} \frac{A^2}{P_{MOD,yr}^3} \ {\rm erg\ s^{-1}}, \tag{4.3}$$

where m_1 is the NS mass in units of $M_\odot$, A is the semiamplitude of the sinusoidal modulation in seconds, $P_{\rm MOD,yr}$ is the modulation period in yr, and $P_{\rm orb,5h}$ is the orbital period in units of 5 hr, it was found $L_{\rm GQC} = (2.14 \pm 0.22) \times 10^{33}$ erg s^{-1} when the best-fit values of A and $P_{\rm MOD,yr}$ obtained from the LS model are adopted. The nuclear luminosity of a star with mass $0.43\ M_\odot < M < 2\ M_\odot$ is given by $L_{\rm nuke}/L_\odot = m^4$, where m is the stellar mass in units of solar masses (Salaris & Cassisi 2005). Substituting to the latter expression the value of m_2, it is found $L_{\rm nuke} = (1.71 \pm 0.14) \times 10^{32}$ erg s^{-1}, implying that the nuclear luminosity is a factor of 13 lower than the luminosity needed to activate the GQC process. A large sinusoidal modulation in the delays therefore cannot be explained as results of an Applegate mechanism powered by the nuclear energy of the companion. It is more reasonable that the delays follow a quadratic trend caused by the high value of the orbital period derivative.

It could be possible, on the other hand, that the energy transferred to the CS to trigger the GQC process occurs through tidal dissipation (Applegate & Shaham 1994; Sanna et al. 2017, for a discussion). In this scenario, the magnetic field of the CS, interacting with the mass ejected from the system because of the irradiation from the accreting NS, could produce a torque that is able to slow down the rotation of the CS. The torque, then, holds the CS out of synchronous rotation, generating a tidal dissipation that could furnish the necessary energy to activate the GQC process. In this case, the CS should lose mass, and therefore an orbital period derivative should be observed. Combining Eqs. 17 and 18 of Sanna et al. (2017), the inferred mass transfer rate required to trigger the GQC process through tidal dissipation is

$$\dot{m}_T = 1.415 \times 10^{-8} \left(\frac{a_{\rm bin}}{l}\right)^2 m_1^{11/9} \frac{q^{7/9}}{(1+q)^{1/9}} \frac{A^{4/3}}{P_{MOD,yr}^2} \ {\rm M_\odot\ yr^{-1}}, \tag{4.4}$$

where $a_{\rm bin}/l$ represents the ratio between the binary separation and the lever arm of the mass transferred by the CS measured with respect to the centre of mass of the binary system. On the other hand, the mass transfer rate from the CS is linked to the $P_{\rm orb}$ and $\dot{P}_{\rm orb}$ values as reported in Eq. 4 of Burderi et al. (2010), that is,

$$\dot{m} = 0.39\ (1-3n)^{-1} m_2\ c\ P_{\rm orb,5h}^{-1}\ {\rm M_\odot\ yr^{-1}}, \tag{4.5}$$

where n is the mass-radius index of the CS, and c is the constant of the quadratic term in the model adopted to fit the delays. As reported by Burderi et al. (2010), $n = -1/3$ is assumed. Combining Eqs. 4.4 and 4.5, it is obtained $N_{\rm MOD} = 0.572\ c^{-1/2} A^{2/3} a_{\rm bin}/l$, which is used to constrain the best-fit model (see Section 2). The best-fit values obtained from this LQS model suggest that the GQC process is possible through tidal interaction if the mass transfer rate is $(9.4 \pm 0.3) \times 10^{-8}$ $M_\odot$ y^{-1}, that is, a factor of 6 higher than the Eddington mass accretion rate.

Chapter 5

A broadband spectral analysis of 4U 1702-429 using XMM-Newton/INTEGRAL and BeppoSAX data

S.M. Mazzola, R. Iaria, T. Di Salvo, M. Del Santo, A. Sanna, A.F. Gambino, A. Riggio, A. Segreto, L. Burderi, A. Santangelo and N. D'Amico (2019, A&A, 621, A89)

5.1 Introduction

In this work, a broad-band spectral analysis of the X-ray source 4U 1702-429 was reported. The source, known also as Ara X-1, was detected as a burster with *OSO 8* (Swank et al. 1976). Oosterbroek et al. (1991) classified 4U 1702-429 as an atoll source using *EXOSAT* data. Galloway et al. (2008), analysing the photospheric radius expansion of the observed type-I X-ray bursts, inferred a distance to the source of 4.19 ± 0.15 kpc and 5.46 ± 0.19 kpc for a pure hydrogen and pure helium companion star, respectively. Markwardt et al. (1999), using the data of the proportional counter array (PCA) onboard the *Rossi X-ray Timing Explorer (RXTE)* satellite, detected burst oscillations at 330 Hz that could be associated with the spin frequency of the NS.

Using *Einstein* data, Christian & Swank (1997) modelled the continuum emission adopting a cut-off power law with a photon index between 1.3 and 1.5 and a cut-off temperature between 8

and 16 keV. Markwardt et al. (1999), analysing *RXTE/PCA* data, adopted the same model and obtained a temperature between 3.5 and 4.6 keV. Using *XMM-Newton* and *INTEGRAL* spectra, Iaria et al. (2016) revealed the presence of a broad emission line at 6.7 keV. These authors fitted the spectra adopting a disc blackbody component plus Comptonisation and reflection component from the accretion disc. An inner disc temperature of 0.34 keV, an electron temperature of 2.3 keV, and a photon index of 1.7 - the latter two associated with the Comptonising cloud - have been obtained. The equivalent hydrogen column density associated with the interstellar medium was 2.5×10^{22} cm^{-2} and the ionisation parameter associated with the reflecting plasma was $\log \xi = 2.7$.

In order to compare recent observations with previous ones and explore different spectral states of the source (in particular, concerning the presence of the reflection component), the *XMM-Newton/INTEGRAL* spectrum of 4U 1702-429, already studied by Iaria et al. (2016), was re-analysed. The analysis of three 0.1-100 keV *BeppoSAX* spectra is also presented for the first time, showing that the addition of a reflection component is statistically required.

5.2 Observations and data reduction

The narrow field instruments (NFIs) on board the *BeppoSAX* satellite observed 4U 1702-429 three times between 1999 and 2000. The NFIs are four co-aligned instruments which cover three decades in energy, from 0.1 keV up to 200 keV. The Low-Energy Concentrator Spectrometer (LECS, Parmar et al. 1997) and the Medium-Energy Concentrator Spectrometer (MECS, Boella et al. 1997) have imaging capabilities with fields of view (FOV) of $20'$ and $30'$ radii, respectively. I selected data in circular regions - centred on the source - of $8'$ and $6'$ radii for LECS and MECS, respectively. The background events were extracted from circular regions with the same radii adopted for the source-event extractions and centred in a detector region far from the source. The High-Pressure Gas Scintillator Proportional Counter (HPGSPC, Manzo et al. 1997) and Phoswich Detector System (PDS, Frontera et al. 1997) are non-imaging instruments, with FOVs of $\sim 1^\circ$ FWHM delimited by collimators. The background subtraction for these instruments is obtained using the off-source data accumulated during the rocking of the collimators.

MECS is composed of three modules but only MECS2 and MECS3 were active during these observations. The event files of these two instruments are merged and they are indicated as MECS23. The first observation (obsid. 2069400100, hereafter observation A) was performed between 1999 February 27 17:34:34 UT and February 28 09:12:06 UT for a duration time of 58 ks, the second observation (obsid. 2122400100, hereafter observation B) was performed between 2000

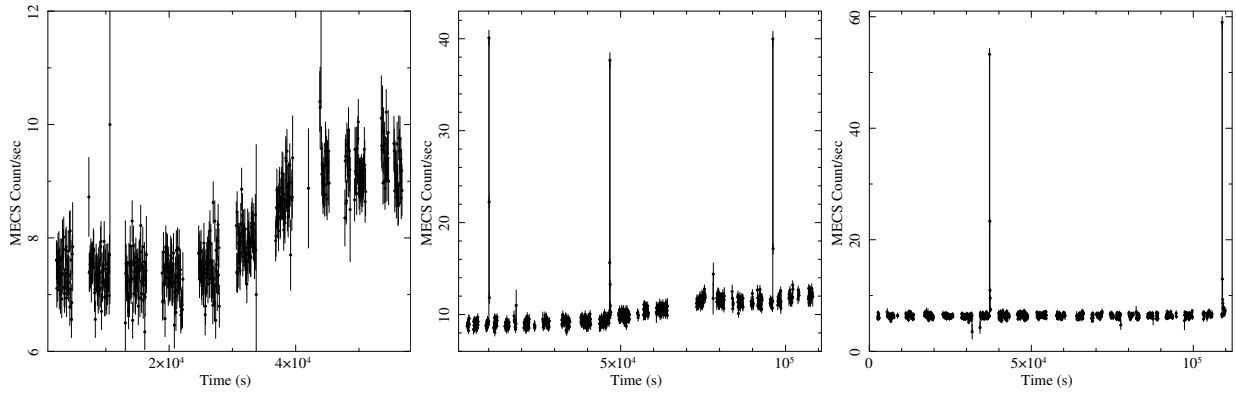

Figure 5.1: MECS23 light curves of the source 4U 1702-429 for the observations A, B, and C in the left, central, and right panels, respectively. The bin time is 64 s. Three and two type-I X-ray bursts occurred during observations B and C, respectively.

August 24 19:22:51 UT and August 26 01:04:01 UT for a duration time of 104 ks, and finally the third observation (obsid. 2122400200, hereafter observation C) was taken between 2000 September 23 22:41:50 UT and and September 25 04:30:29 UT for a duration of 107 ks. I used

Table 5.1: Observations of the source 4U 1702-429 presented in this work

Instrument		Observation time (dd-dd/mm/yyyy)			Exposure time (ks)		
XMM-Newton	RGS12	09-10/03/2010			37.0		
	MOS12				36		
	PN				36		
INTEGRAL	JEM-X2	10-11/03/2010			6.0		
	IBIS/ISGRI	5-15/03/2010			130.0		
		Obs. A	Obs. B	Obs. C	Obs. A	Obs. B	Obs. C
BeppoSAX	LECS	27-28/02/1999	24-26/08/2000	23-25/09/2000	7.1	19.1	16.3
	MECS23				27.5	40.4	46.8
	HPGSPC				28.3	40.1	41.8
	PDS				13.5	20.1	20.9

several tools of SAXDAS 2.3.3 and HEASOFT 6.20 to extract scientific products from clean event files downloaded from the Multi-Mission Interactive Archive at the ASI Space Science Data Center (SSDC). Initially, I extracted the MECS23 light curve in the 1.3-10 keV energy range for each observation. The three MECS light curves with a bin time of 64 s are shown in Figure 5.1. During observation A the count rate is constant at 8.5 c/s from the start time up to 35 ks, when the count rate increases up to 10 c/s (Figure 5.1, left panel). During observation B three type-I X-ray bursts are present at 6.6 ks, 43.3 ks, and 92.6 ks from the start time. The count rate at the peak of the bursts is 40 c/s, 35 c/s, and 40 c/s, respectively, whilst the count rate of the persistent emission gradually increases from 9.5 c/s to 11 c/s (Figure 5.1, middle panel). During observation

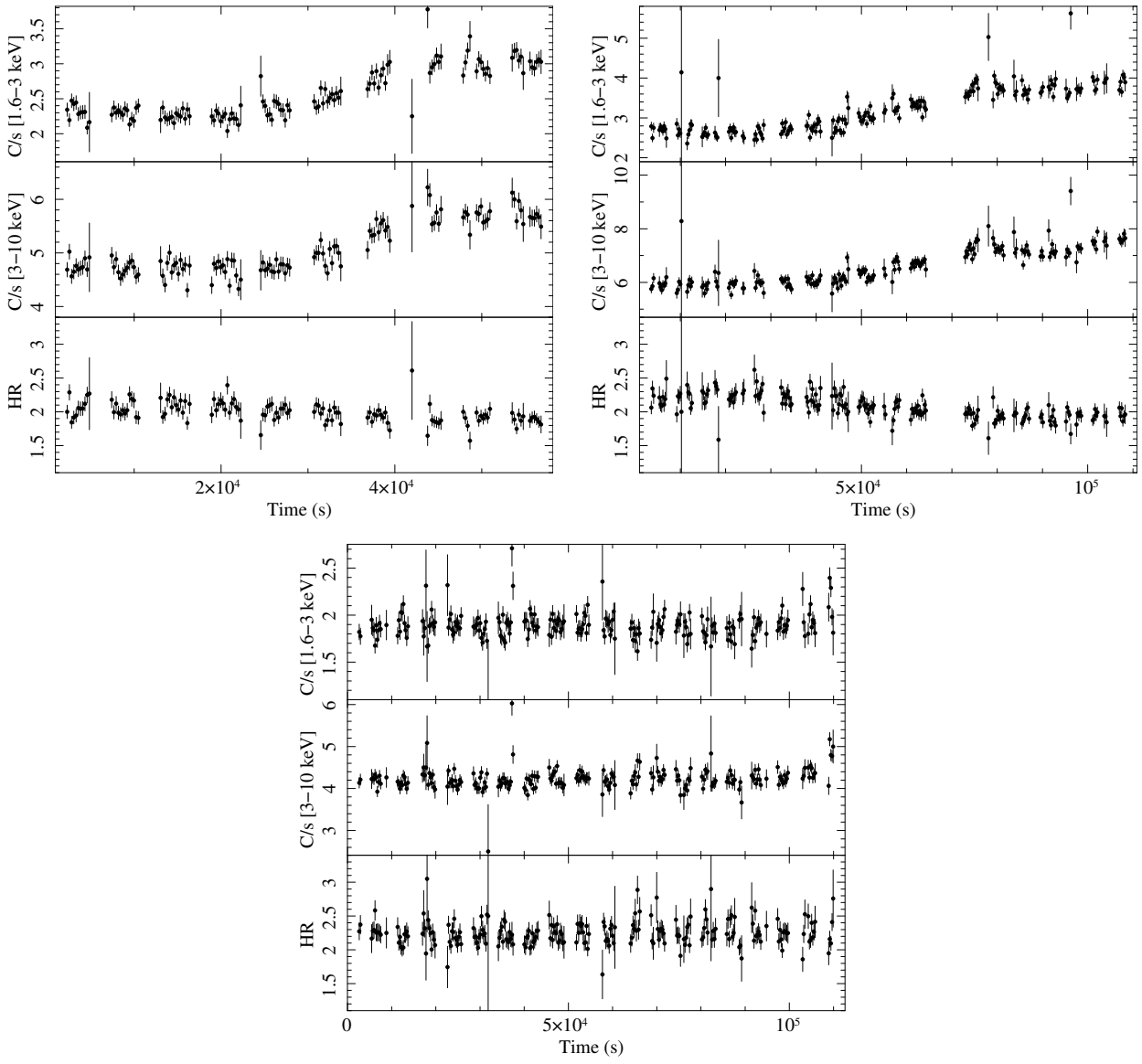

Figure 5.2: Upper left panel: MECS23 light curves and HR for observation A. Upper right panel: MECS23 light curves and HR for observation B. Bottom panel: MECS23 light curves and HR for observation C. In each panel, from the top to the bottom: MECS23 light curve in the energy band 1.6-3 keV, in the energy band 3-10 keV, and the corresponding hardness ratio.
The bin time is 256 s.

Table 5.2: Time intervals excluded for removing bursts

	Excluded temporal interval (in ks from the start time)	
Instrument	Observation B	Observation C
LECS	41.160 - 41.350	
MECS23	6.630 - 6.750	34.570 - 34.750
	43.250 -43.350	106.350 - 106.550
	92.680 - 92.760	
HPGSPC	6.800 - 7.000	34.430 - 34.560
	43.400 - 43.600	106.240 - 106.500
	92.800 - 93.100	
PDS	45.340 - 45.354	34.530 - 34.554
	94.767 - 94.780	106.316 - 106.334

C two type-I X-ray bursts are present at 34 ks and 106 ks from the start time. The count rate at the peak of the bursts is 52 c/s and 60 c/s, respectively. The count rate of the persistent emission is constant at 8 c/s (Figure 5.1, right panel).
LECS exposure times are 7.1 ks, 19.4 ks, and 12.3 ks for observation A, B, and C, respectively. LECS light curves corresponding to observations A and C do not show type-I X-ray bursts, while the LECS light curve corresponding to observation B shows only the first type-I X-ray burst observed in the MECS23 light curve of the same observation. The exposure times of each instrument for the three observations are shown in Table 5.1.

Since our aim is the study of the persistent emission of the source, I excluded the bursts detected from the light curves. Using the `XSELECT` tool, I determined the time intervals at which bursts occurred and excluded them (Table 5.2). The same operation was carried out on the background light curves to keep the same exposure time.

Once the time intervals of the bursts were excluded, I build the MECS23 hardness ratio (HR): I divided MECS data in the energy bands 1.6-3 keV and 3-10 keV and produced HR for each observation. The 1.6-3 keV light curves, the 3-10 keV light curves, and the corresponding HRs are shown in Figure 5.2 for observations A, B, and C. The HRs were relatively constant throughout the observations, and a spectrum of the persistent emission was extracted for each one of them.

I extracted MECS and LECS spectra using `XSELECT`, and grouped each one in order to have at least 25 photons for each energy channel. I used the `hpproducts` and `pdproducts` tools to obtain the HP and PDS background-subtracted spectra, cleaned of bursts. The PDS spectra were grouped adopting a logarithmic rebinning.

The XMM-Newton/INTEGRAL data studied have already been presented by Iaria et al. (2016).

The *XMM-Newton* observatory (Jansen et al. 2001) observed the source between 2010 March 09 14:11:26 UT and March 10 00:22:08 UT (OBSid 0604030101) for a total duration of 38 ks. During the observation, the two MOS charge-coupled devices (CCDs) (MOS1 and MOS2, Turner et al. 2001) were operating in Small window mode, while the pn CCD of the European Photon Imaging Camera (EPIC-pn, Strüder et al. 2001) was operating in Timing mode with medium filter. Concurrently, quasi-simultaneous *INTEGRAL* observations were selected in order to cover the highest energy and obtain a broadband spectrum of 4U 1702-429: 58 pointings (called Science Windows, SCWs) collected between 2010 March 5 and 15 for the IBIS/ISGRI instrument (Ubertini et al. 2003; Lebrun et al. 2003) and 3 SCWs obtained between 2010 March 10 and 11 for the JEM-X (Brandt et al. 2003; Lund et al. 2003) instrument (only the JEM-X2 module was active at the time of the observations). The combined *XMM-Newton* and *INTEGRAL* persistent spectrum of 4U 1702-429 used in this work was obtained as described by Iaria et al. (2016). The exposure times are 37 ks for the reflection grating spectrometers (RGS, den Herder et al. 2001), and 36 ks for the spectra collected by MOS1 and MOS2 instruments and by the EPIC-pn camera. The MOS1 and MOS2 spectra were combined, as were the RGS1 and RGS2 spectra. The exposure times of JEM-X2 and IBIS/ISGRI were 6 ks and 130 ks, respectively.

5.3 Spectral analysis

I used the `XSPEC` software package v12.9.1 to fit the spectra. For all observations, I fitted the continuum direct emission with a model composed of a multicolour disc blackbody emission (`diskbb` in `XSPEC`, Mitsuda et al. 1984; Makishima et al. 1986) plus a thermal Comptonisation (`nthComp` in `XSPEC`, Zdziarski et al. 1996b; Życki et al. 1999a), in which the `inp_type` parameter was set to 1, indicating that the seed photons were emitted by the accretion disc; both the components were multiplied by the `phabs` component, which takes into account the photoelectric absorption by neutral matter in the ISM. I set the abundances to the values found by Wilms et al. (2000) and the photoelectric absorption cross-sections were set to the values obtained by Verner et al. (1996).

Furthermore, in our analysis, a distance to the source of 5.5 kpc (Iaria et al. 2016) and a neutron star mass of 1.4 $M_{\odot}$ were assumed.

5.3.1 Re-analysis of the *XMM-Newton/INTEGRAL* spectrum

I re-analysed the *XMM-Newton/INTEGRAL* spectrum using the data in the energy ranges 0.6-2.0 keV for RGS12, 0.3-10 keV for MOS12, 2.4-10 keV for PN, 5-25 keV for JEM-X2, and 20-50 keV

for ISGRI.

I initially fitted the *XMM-Newton/INTEGRAL* data using the same self-consistent model used by Iaria et al. (2016), in which the continuum emission was described as reported above. The inner disc temperature kT_{bb} and the disc-blackbody normalisation were left free to vary, as well as the photon index Γ, the electron temperature kT_e, and the seed photon temperature kT_{seed}.

To fit the emission line in the Fe-K region, I adopted the self-consistent reflection model `rfxconv` (Kolehmainen et al. 2011a) in which I kept the iron abundance fixed to the solar one and left the ionisation parameter $\log \xi$ of the reflecting matter in the accretion disc and the reflection fraction rel_refl free to vary. To take into account the relativistic smearing effects in the inner region of the accretion disc, I used the multiplicative `rdblur` component, in which the outer radius was kept fixed at the value of 1000 gravitational radii ($R_g = GM/c^2$), while the inclination angle θ of the binary system, the inner radius R_{in} at which the reflection component originates, and the power-law dependence of emissivity `betor` were left free to vary. The incident emission onto the accretion disc is provided by the Comptonisation component. I obtained best-fit results consistent with the results reported by Iaria et al. (2016) with a χ^2(dof) of 2578(2247), but large residuals are still observed between 3 and 4 keV. To fit these residuals, I added two relativistically broad lines with a fixed energy of 3.32 keV and of 3.9 keV (corresponding to the emission line of Ar XVIII and Ca XIX ions), respectively. This model was called:

$$\texttt{Model 1}: \ \mathrm{edge} * \mathrm{edge} * \mathrm{phabs} * \{\mathrm{diskbb} + rdblur * (gauss + gauss + rfxconv * nthComp[inp\_type = 1])\},$$

and show the best-fit results in the second column of Table 5.3. From this model a χ^2(dof) of 2559(2245) and $\Delta\chi^2 = 19$ were obtained, with an F-test probability of chance improvement of 2.47×10^{-4} (corresponding to a significance of $\sim 3.8\sigma$) which suggests that the addition of both the lines is statistically significant. The significances of the two lines associated with Ar XVIII and Ca XIX are $\sim 4\sigma$ and $\sim 3\sigma$, respectively.

A variation was observed in all the parameters of the continuum. In particular, the obtained value of kT_{seed} was larger than kT_{bb} suggesting that the seed photons are not emitted by the accretion disc only but a possible contribution of photons emitted by the neutron star surface is present. For this reason, I fitted the data with

$$\texttt{Model 2}: \ \mathrm{phabs} * \{\mathrm{diskbb} + \mathrm{nthComp}[\mathrm{inp\_type} = 0]\},$$

in which the `inp_type` parameter set to 0 indicates seed photons emitted by NS, obtaining a χ^2(d.o.f.) of 2844(2252). Large residuals remain in the Fe-K region and between 3 and 4 keV; to fit those three `diskline` (Fabian et al. 1989) components were added to the model, keeping fixed the energies of two out of three lines at 3.32 and 3.9 keV, while the energy of the third one was left free to vary. For the two lines with fixed energy, the values of inclination angle, power law emissivity dependence, and blackbody radius were tied to those of the third one. The outer radius of the reflecting region was set to 1000 R_g for each line. Finally, the inner radius of the reflecting region was imposed to have the same value of the inner radius of the accretion disc. The best-fit results, obtained by adding the three disc lines, showed a χ^2(d.o.f.) of 2640(2246), with an F-test probability of chance improvement of 1.13×10^{-33}. Large residuals were still present at 0.8 keV and 8.8 keV, and for this reason two absorption edges were added, fixing the energy threshold at 0.871 keV and 8.828 keV, associated with the presence of O VIII and Fe XXVI ions, respectively. This model was called

$$\texttt{Model 3}: edge * edge * phabs * \{diskline + diskline + diskline + diskbb + nthComp[inp\_type = 0]\}.$$

A χ^2(d.o.f.) of 2523(2244) was obtained, with an F-test probability of chance improvement of 1×10^{-22} (corresponding to a significance much higher than 6σ) and a $\Delta\chi^2$ of 117 with respect to the previous model. A significance of 19σ, 4σ, and 6σ was obtained for the Ar XVIII, Ca XIX and Fe XXVI emission lines, respectively. The energy of the smeared emission line in the Fe-K region is 6.81 ± 0.07 keV, which is compatible within 3σ with the rest frame value. The best-fit results are shown in the third column of Table 5.3.

Although `Model 3` presented statistically good results, the data were fitted using also the self-consistent approach described above, which takes into account the reflection continuum. The outer radius in the `rdblur` component was kept fixed to the value of 1000 R_g and the power-law dependence of emissivity to the value of -2.5, consistent with the result of `Model 3`. In this case, the value of R_{in} was imposed to be the same as that of R_{disc}. Since the `rfxconv` model does not account for the emission lines associated to ionised Argon and Calcium, I added two Gaussian components with energies fixed at 3.32 and 3.9 keV, respectively. This model was called

$$\texttt{Model 4}: \text{edge} * \text{edge} * \text{phabs} * \{\text{diskbb} + rdblur * (gauss + gauss + rfxconv * nthComp[inp\_type = 0])\}.$$

Table 5.3: Best-fit values of the spectral models for XMM-Newton data

Component	Model 1	Model 3	Model 4
`Edge`			
$E_{O\,VIII}$ (keV)	0.871 (fixed)	0.871 (fixed)	0.871 (fixed)
$\tau_{O\,VIII}$	0.7 ± 0.1	0.7 ± 0.1	0.7 ± 0.1
`Edge`			
$E_{Fe\,XXVI}$ (keV)	8.828 (fixed)	8.828 (fixed)	8.828 (fixed)
$\tau_{Fe\,XXVI}$	0.05 ± 0.01	0.04 ± 0.01	0.04 ± 0.01
`phabs`			
nH(10^{22})	2.44 ± 0.04	2.40 ± 0.02	2.42 ± 0.04
`diskbb`			
kT_{in}(keV)	$0.43^{+0.02}_{-0.03}$	$0.48^{+0.04}_{-0.12}$	$0.46^{+0.03}_{-0.02}$
R_{disc} (km)	21^{+4}_{-2}	20^{+8}_{-3}	23^{+2}_{-3}
F_{bb} ($10^{-9} erg\ cm^{-2}\ s^{-}1$)			1.3
`nthComp`			
Γ	$1.80^{+0.12}_{-0.07}$	$1.73^{+0.12}_{-0.07}$	$1.79^{+0.03}_{-0.08}$
kT_e(keV)	$2.9^{+0.3}_{-0.2}$	$2.6^{+0.3}_{-0.1}$	$2.89^{+0.03}_{-0.02}$
kT_{seed}(keV)	$1.04^{+0.30}_{-0.20}$	$0.7^{+0.2}_{-0.4}$	0.7 ± 0.1
norm	$0.20^{+0.04}_{-0.02}$	0.08 ± 0.02	$0.09^{+0.02}_{-0.01}$
F_{Compt} ($10^{-9} erg\ cm^{-2}\ s^{-}1$)			2.4
`diskline`			
betor	-	$-2.5^{+0.2}_{-0.3}$	-
θ (deg)	-	35 ± 3	-
R_{in} (km)	-	20^{+8}_{-3}	-
$E_{Ar\,XVIII}$ (keV)	-	3.32 (fixed)	-
$N_{Ar\,XVIII}$ ($\times 10^{-4}$ photons/cm^{2}s^{-1})	-	4.1 ± 1.2	-
$E_{Ca\,XIX}$ (keV)	-	3.90 (fixed)	-
$N_{Ca\,XIX}$ ($\times 10^{-4}$ photons/cm^{2}s^{-1})	-	$2.6^{+0.8}_{-1.1}$	-
$E_{Fe\,XXV}$ (keV)	-	6.81 ± 0.07	-
$N_{Fe\,XXV}$ ($\times 10^{-4}$ photons/cm^{2}s^{-1})	-	5.7 ± 1.1	-
`rdblur`			
Betor10	-2.8 (fixed)	-	-2.5 (fixed)
R_{in} (km)	21^{+4}_{-2}	-	23^{+2}_{-3}
θ (deg)	36^{+2}_{-1}	-	38^{+7}_{-5}
`gauss`			
$E_{Ar\,XVIII}$ (keV)	3.32 (fixed)	-	3.32 (fixed)
$N_{Ar\,XVIII}$ ($\times 10^{-4}$ *photons*/cm^{2}s^{-1})	$3.9^{+1.1}_{-1.3}$	-	$3.3^{+1.1}_{-0.9}$
`gauss`			
$E_{Ca\,XIX}$ (keV)	3.90 (fixed)	-	3.90 (fixed)
$N_{Ca\,XIX}$ ($\times 10^{-4}$ photons/cm^{2}s^{-1})	$2.3^{+1.2}_{-1.4}$	-	$1.5^{+1.0}_{-0.8}$
`rfxconv`			
rel_refl	$0.09^{+0.03}_{-0.01}$	-	$0.05^{+0.03}_{-0.01}$
$\log \xi$	$2.72^{+0.2}_{-0.1}$	-	$3.0^{+0.1}_{-0.3}$
χ^2(dof)	2559(2245)	2523(2244)	2550(2245)

Uncertainties are reported at 90% confidence level. The spectral parameters are defined as in `XSPEC`.

F_{bb} and F_{Compt} represent the unabsorbed fluxes in the (0.1-100) keV energy range associated with the accretion disc and the Comptonisation component, respectively.

Using this self-consistent model, a χ^2(d.o.f.) of 2550(2245) was obtained, with a large improvement with respect to `Model 2` and a significance of 6σ for both Ar XVIII and Ca XIX emission lines. The comparison between the residuals obtained using `Model 2` and `Model 4` is shown in Figure 5.3; the best-fit values of the parameters are shown in the fourth column of Table 5.3.

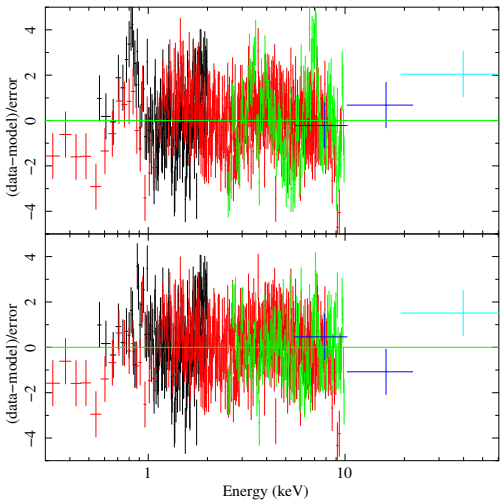

Figure 5.3: Comparison between residuals obtained adopting `Model 2` (top panel) and `Model 4` (lower panel). The RGS12, MOS12, PN, JEM-X2, and ISGRI data are shown in black, red, green, blue, and cyan colour, respectively.

Finally, the total unabsorbed flux is 3.8×10^{-9} erg cm^{-2} s^{-1} in the 0.1-100 keV energy range; and the corresponding luminosity is 1.5×10^{37} erg s^{-1}.

5.3.2 The *BeppoSAX* spectra

I adopted the 0.12-4 keV, 1.8-10 keV, 7-25 keV, and 15-100 keV energy range for LECS, MECS, HPGSP, and PDS spectra, respectively. Hereafter I refer to the spectra obtained from observations A, B, and C as spectra A, B, and C.

Initially, I fitted the continuum emission with `Model 2`. Assuming that N_H does not change with respect to *XMM-Newton/INTEGRAL* observations and considering the low statistics of the *BeppoSAX/LECS* data below 1 keV, I kept the value of equivalent hydrogen column associated with the interstellar matter fixed to 2.42×10^{22} cm^{-2}, as obtained from best-fit values of `Model 4` (see Table 5.3). Fitting the data, a χ^2(d.o.f.) of 472(477), 650(502), and 532(481) was obtained for spectra A, B, and C, respectively. The best-fit results are shown in the second, third, and fourth columns of Table 5.4.

Table 5.4: Best-fit values of the spectral models for BeppoSAX data

	Model 2			Model 5		
Component	Obs A	Obs B	Obs C	Obs A	Obs B	Obs C
`phabs`						
nH(10^{22})	2.42 (frozen)	2.42 (frozen)	2.42 (frozen)	2.42 (frozen)	2.42 (frozen)	2.42 (frozen)
`diskbb`						
kT_{in}(keV)	0.54 ± 0.02	0.54 ± 0.02	0.48 ± 0.06	0.51 ± 0.03	0.49 ± 0.02	0.4 ± 0.05
R_{disc} (km)	$9.8^{+0.08}_{-0.07}$	11.7 ± 0.7	8 ± 2	11^{+2}_{-1}	12 ± 1	14 ± 3
F_{bb} $(10^{-9} erg\ cm^{-2}\ s^{-1})$				0.5	0.4	0.2
`nthComp`						
Γ	$2.44^{+0.04}_{-0.08}$	2.24 ± 0.03	2.08 ± 0.04	2.3 ± 0.1	$2.40^{+0.09}_{-0.08}$	2.09 ± 0.04
kT_e(keV)	> 44	17 ± 2	34^{+13}_{-6}	> 40	28^{+20}_{-7}	45^{+34}_{-13}
kT_{seed}(keV)	$1.02^{+0.03}_{-0.05}$	0.98 ± 0.03	0.73 ± 0.06	0.96 ± 0.06	1.48 ± 0.07	0.63 ± 0.04
norm	$0.020^{+0.002}_{-0.001}$	0.026 ± 0.002	0.028 ± 0.004	0.018 ± 0.002	0.079 ± 0.003	$0.035^{+0.002}_{-0.004}$
F_{Compt} $(10^{-9} erg\ cm^{-2}\ s^{-1})$				0.95	1.4	1.0
`rdblur`						
Betor10	-	-	-	-2.5 (frozen)	-2.5 (frozen)	-2.5 (frozen)
R_{in} (km)	-	-	-	24 (frozen)	< 39	< 50
θ (deg)	-	-	-	38 (frozen)	38 (frozen)	38 (frozen)
`rfxconv`						
rel_refl	-	-	-	0.09 ± 0.04	0.4 ± 0.1	0.2 ± 0.1
$\log \xi$	-	-	-	3.14 (frozen)	2.32 ± 0.04	$2.38^{+0.33}_{-0.05}$
F_{bol} $(10^{-9} erg\ cm^{-2}\ s^{-1})$				1.5	2.1	1.3
χ^2(dof)	472(477)	650(502)	532(481)	449(476)	558(499)	482(478)

Uncertainties are reported at 90% confidence level. The spectral parameters are defined as in `XSPEC`. F_{bb}, F_{Compt} , and F_{bol} represent the unabsorbed fluxes in the (0.1-100) keV energy range associated with the accretion disc, the Comptonisation component, and the total emission, respectively.

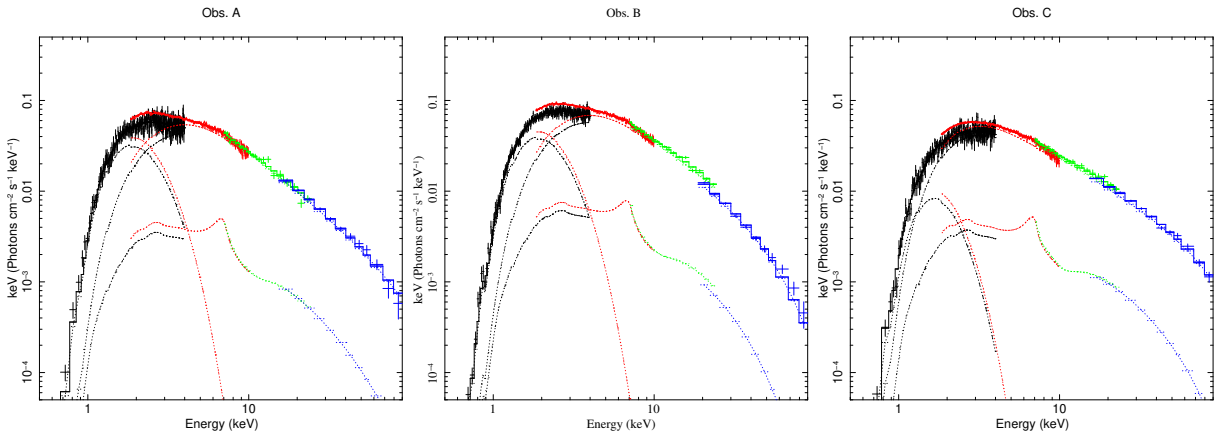

Figure 5.4: The unfolded spectra of the three *BeppoSAX* observations fitted adopting `Model 5`. The LECS, MECS23, HPGSP, and PDS spectra are shown in black, red, green, and blue, respectively.

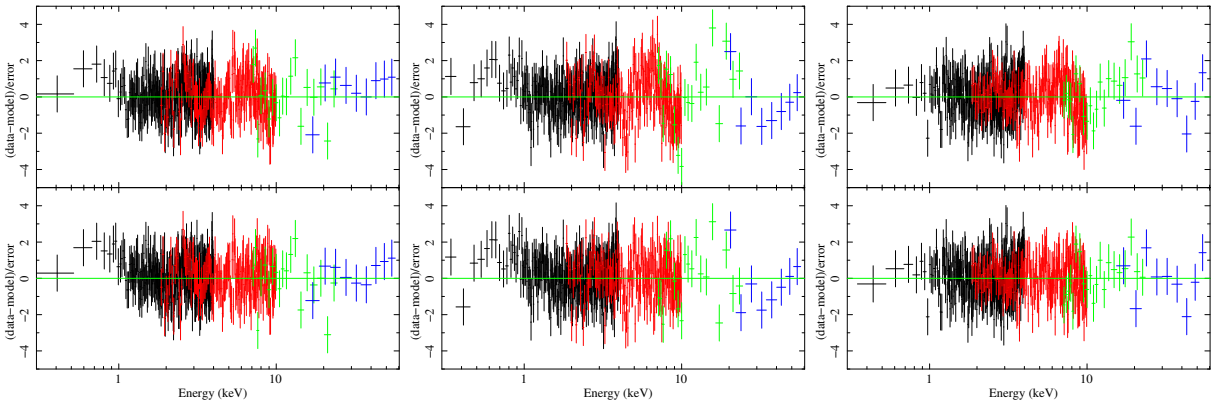

Figure 5.5: Comparison between residuals obtained adopting `Model 2` (top panels) and `Model 5` (bottom panels) for observation A (on the left), observation B (in the middle) and observation C (on the right). The black, red, green and blue points represent the LECS, MECS23, HPGSP, and PDS data, respectively.

It was observed that some residuals are present in the Fe-K region of the spectra A and C and these are slightly larger for spectrum B. For this reason, I added a smeared reflection component to `Model 2`. I adopted the Compton reflection model described for the analysis of the *XMM-Newton/INTEGRAL* spectrum. The inclination angle was kept fixed to 38° as obtained from `Model 4` (see Table 5.3). In this case, the inner radius R_{in}, the ionisation parameter $\log \xi$, and the reflection fraction rel_refl were left free to vary. This model was called

`Model 5` :

$$\text{phabs} * \{\text{diskbb} + \text{rdblur} * \text{rfxconv} * \text{nthComp}[\text{inp\_type} = 0]\}.$$

For observation B, I obtained a χ^2(d.o.f.) of 558(499), and found the F-test probability of chance improvement for the addition of the reflection component to be 2.0×10^{-16}. The Fe-K region of the spectrum does not show significant residuals anymore. The best-fit values of the parameters are shown in the sixth column of Table 5.4. The unfolded spectrum and the residuals are shown in the central panels of Figure 5.4 and Figure 5.5, respectively.

Subsequently, I adopted the `Model 5` to fit spectra A and C. For spectrum C, a χ^2(d.o.f.) of 482(478) was obtained with an F-test probability of chance improvement of 3.1×10^{-10} (significance higher than 6σ). The ionisation parameter $\log \xi$ and the relative reflection normalisation rel_refl are $2.38^{+0.33}_{-0.05}$ and 0.2 ± 0.1, respectively, and they are compatible within 90% c.l. with the values obtained for spectrum B. The best-fit values of the parameters for spectrum C are shown in the

seventh column of Table 5.4.

For spectrum A, I needed to fix the value of the ionisation parameter in order to lead the fit to convergence. The best value $\log\xi$ =3.14 obtained from the contour plot (shown in Figure 5.6) was chosen. This two-dimensional distribution of the χ^2 as a function of the ionisation and the reflection amplitude was obtained varying $\log\xi$ between 2.1 and 4 and rel_refl between -0.6 and -0.01 simultaneously through the `steppar` tool in `XSPEC`. Moreover, the inner radius of the reflection region was kept fixed to the value of 24 km because the χ^2 was insensitive to the variation of this parameter. The value of 24 km was obtained from `Model 5` leaving R_{in} free to vary and keeping all the other parameters fixed. A χ^2(d.o.f.) of 449(476)with an F-Test gives a probability of chance improvement of 1.1×10^{-6} was obtained, corresponding to a significance of $\sim 4.9\sigma$.

The best-fit values of the parameters for spectrum A are shown in the fifth column of Table 5.4. The unfolded spectrum and the residuals are shown in the left and right panels of Figure 5.4 and Figure 5.5 for spectra A and C, respectively. I found a total unabsorbed flux of 1.5×10^{-9} erg cm^{-2}

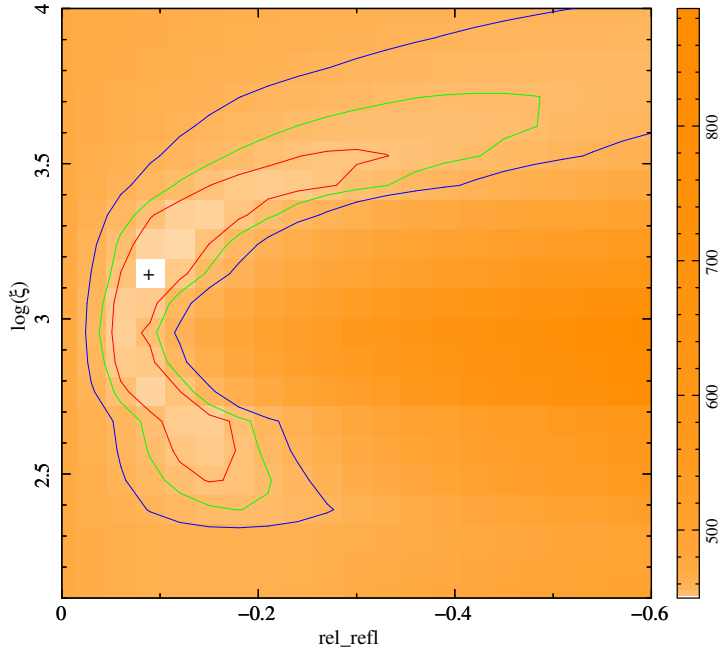

Figure 5.6: Contour plot of χ^2 changes for simultaneous variation of $\log\xi$ and rel_refl parameters for spectrum A. The red, green; and blue lines indicate the contours at 68, 90, and 99% confidence level, respectively. The black cross indicates the best-fit values of $\log\xi = 3.14$ and $rel\_refl = 0.1$. The orange-scale indicates the value of χ^2 changes in the grid.

s^{-1} for spectrum A, 2.1 $\times 10^{-9}$ erg cm^{-2} s^{-1} for spectrum B, and 1.3×10^{-9} erg cm^{-2} s^{-1} for

spectrum C. Finally, the corresponding luminosities are 5.5×10^{36} erg s^{-1}, 7.5×10^{36} erg s^{-1}, and 4.8×10^{36} erg s^{-1} , respectively.

5.3.3 Discussion and Results

The observations of the NS-LMXB 4U 1702-429 taken with *XMM-Newton/INTEGRAL* in March 2010 and three *BeppoSAX* observations performed in February 1999, August 2000 and September 2000 was studied. The broadband analysis indicates that the addition of a smeared reflection component to the spectral model is statistically significant in the case of the *XMM-Newton/INTEGRAL* observation and observations B and C, and is marginally significant for observation A.

The smeared reflection component allowed us to constrain the inclination angle θ of the source, which is 38^{+7}_{-5} degrees using the *XMM-Newton/INTEGRAL* spectrum.

The 0.1-100 keV unabsorbed luminosity is a factor of two to three larger during the *XMM-Newton/INTEGRAL* observation than that obtained from the three *BeppoSAX* observations (see previous section). Moreover, the electron temperature is $2.89^{+0.03}_{-0.02}$ keV for the *XMM-Newton/INTEGRAL* spectrum while it is 40^{+93}_{-14} keV, 28^{+20}_{-7} keV, and 45^{+34}_{-13} keV for spectra A, B, and C, respectively. This suggests that the source was in a SS during the *XMM-Newton/INTEGRAL* observation and in a HS during the three *BeppoSAX* observations.

From `Model 4` I obtain $R_{disc} = 23^{+2}_{-3}$ km for *XMM-Newton/INTEGRAL* spectrum, while R_{disc} is 11^{+2}_{-1} km, 12 ± 1 km, and 14 ± 3 km for spectra A, B, and C, respectively, adopting `Model 5`. I applied the correction factor to convert the inner radius R_{disc} values into the realistic inner radius r_{disc} values. The relation between these two radii is $r_{disc} \sim f^2 R_{disc}$, where the colour correction factor $f \simeq 1.7$ for a luminosity close to 10% of Eddington luminosity (Shimura & Takahara 1995a). I find that the r_{disc} values are 66^{+5}_{-9} km, 32^{+6}_{-3} km, 35 ± 3 km, and 40 ± 9 km for the *XMM-Newton/INTEGRAL* observation and for spectra A, B, and C, respectively. The r_{disc} values are compatible with each other within 90% c.l. for the three *BeppoSAX* spectra, while the value obtained from the *XMM-Newton/INTEGRAL* spectrum is larger by a factor of about two. The behaviour of the disc blackbody radius is similar to that obtained by Di Salvo et al. (2015) for the prototype atoll source 4U 1705-44. In that case the authors observed an inner radius of the blackbody component close to 11 km in the HS and about 33 km in the SS. Furthermore, the obtained values of r_{disc} also seem to suggest that the spectrum of 4U 1702-429 is in a SS during the *XMM-Newton/INTEGRAL* observation, while it is in a HS during the three *BeppoSAX*

observations.

This result could be explained assuming that the inner region of the accretion disc is occulted by an optically thick corona during the *XMM-Newton/INTEGRAL* observation. To verify the proposed scenario I estimated the optical depth τ of the Comptonising cloud using the relation provided by Zdziarski et al. (1996b):

$$\Gamma = \left[\frac{9}{4} + \frac{1}{\tau\left(1+\frac{\tau}{3}\right)\frac{kT_e}{m_e c^2}}\right]^{1/2} - \frac{1}{2}.$$

I found that $\tau = 11.9^{+0.2}_{-0.8}$ during the *XMM-Newton/INTEGRAL* observation while $\tau = 1.5^{+0.4}_{-0.9}$, $\tau = 1.8^{+0.3}_{-0.7}$, and $\tau = 1.7^{+0.5}_{-0.6}$ for spectra A, B, and C, respectively. Our results suggest that the corona is optically thick during the *XMM-Newton/INTEGRAL* observation, while the optical depth is much lower during the *BeppoSAX* observations. The obtained values of τ support the idea that the innermost region of the system is embedded in an optically thick corona in the SS, while the optically thin corona observed in the spectra A, B, and C allows us to look through at the innermost region.

Since the inner radius is between 30 and 50 km (for spectra A, B, and C) it is might supposed that the accretion disc is truncated and does not reach the NS surface. This hypothesis is endorsed by the general idea that in a HS the accretion disc is truncated and, in the region near the NS, the hot inner corona can be identified with the boundary layer, whose interactions with the colder accretion disc cause the emptying of the innermost region (Różańska & Czerny 2000). Then the flow and the boundary layer become optically thinner and the thermal emission can be dominated by the neutron star, as suggested by the smallest value of the inner radius of the accretion disc obtained in HS (Barret & Olive 2002).

The two observed spectral states are identified by changes in the electron corona: for the *XMM-Newton/INTEGRAL* spectrum the electron temperature kT_e is about ten times smaller. Since $\tau \propto N_e R$, where R is the size of the Comptonising region, an increase in the optical depth (τ is ten times larger during the *XMM-Newton/INTEGRAL* observation) can be associated with an increase in the electron density N_e of the corona. Therefore, an increase in the electron density entails an increase in the number of the electrons in the cloud, which is consistent with the observed increase in the flux associated with Comptonised component.

Assuming that the matter almost totally ionised in the accretion disc, I also estimated the electron density n_e of the reflecting skin using the relation $\xi = L_x/(n_e r^2)$, where L_x is the

unabsorbed incident luminosity between 0.1 and 100 keV, ξ is the ionisation parameter, and r is the inner radius of the disc where the reflection component originates. I find that for the *XMM-Newton/INTEGRAL* spectrum $n_e = (1.6^{+1.1}_{-0.5}) \times 10^{21}$ cm^{-3}; on the other hand, since only an upper limit was found for the reflecting radius for *BeppoSAX* observations, I obtain only a lower limit for the electron density: it is 1.7×10^{21} cm^{-3} for spectrum A, 1.6×10^{21} cm^{-3} for spectrum B, and 0.6×10^{21} cm^{-3} for spectrum C. Therefore, I estimated the seed-photon radius $R_{\rm seed}$ using the relation $R_{\rm seed} = 3 \times 10^4 d[F_{\rm Compt}/(1+y)]^{1/2}(kT_{\rm seed})^{-2}$ (in 't Zand et al. 1999), where d is the distance to the source in units of kpc, $y = 4kT_e\ max[\tau, \tau^2]/(m_e c^2)$ is the Compton parameter, $kT_{\rm seed}$ is the seed-photon temperature in units of keV, and $F_{\rm Compt}$ is the bolometric flux of the Comptonisation component. Using the best-fit values (reported in Table 5.3 and Table 5.4), I find that $R_{\rm seed}$ is 8 ± 2 km from the *XMM-Newton/INTEGRAL* spectrum, and it is $4.3^{+0.7}_{-0.6}$ km, $2.2^{-0.4}_{-0.3}$ km, and 10 ± 2 km from the *BeppoSAX* spectra A, B, and C, respectively. Although it can not be excluded that seed photons originate in the inner accretion disc, this suggests that during observations C and *XMM/INTEGRAL* the seed photons were mainly emitted from the NS surface, while the smallest values obtained from spectra A and B can be explained assuming that only an equatorial region of the NS surface injects photons in the electron corona.

Typical values of the reflection amplitude $\Omega/2\pi$ for NS-LMXB atoll sources are within 0.2-0.3 (Matranga et al. 2017b; Di Salvo et al. 2015; Egron et al. 2013; D'Aì et al. 2010). However, smaller reflection fractions are also observed for other systems, such as Ser X-1 (Matranga et al. 2017a; Cackett et al. 2010) and 4U 1820-30 (Cackett et al. 2010) and for AMSP SAX J1748.9-2021 (Pintore et al. 2016). I found typical values of $\Omega/2\pi$ for *BeppoSAX* observations B and C (0.4 ± 0.1 and 0.2 ± 0.1, respectively), whilst a reflection fraction of $0.05^{+0.03}_{-0.01}$ was obtained for *XMM-Newton/INTEGRAL* spectrum, which agrees with the value obtained by Iaria et al. (2016). Since this parameter is a measure of the solid angle subtended by the reflector as seen from the Comptonising corona, our results suggest a slightly different geometry of the electron cloud between SS and HS. In particular, the value obtained for *XMM-Newton/INTEGRAL* observation could indicate a small subtended angle due, for instance, to a less efficient interaction between the corona and the accretion disc or a different geometry of the cloud with respect to a central spherical corona contiguous to an outer accretion disc (which is a typical representation). Finally, I found that rel_refl$= 0.09 \pm 0.04$ for spectrum A, which is compatible with the value obtained for spectrum C, although the reflection component is unconstrained in this case and this does not represent a conclusive result.

In the case of this source the variation in the spectral state is likely caused by the changes occurring in the Comptonising corona, as suggested by Barret & Olive (2002) for 4U 1705-44. Indeed, the spectral component whose parameters show significant variation between the *XMM-Newton/INTEGRAL* analysis and the *BeppoSAX* analysis is the Comptonisation (see Table 5.3 and Table 5.4).

In conclusion, any emission lines and absorption edges are observed in the *BeppoSAX* spectra like those detected in the *XMM-Newton/INTEGRAL* spectrum because of the smaller effective area and poorer energy resolution of *BeppoSAX/MECS* with respect to the *XMM/EPIC-PN*.

Chapter 6

Fe Kα and Fe Kβ line detection in *NuSTAR* spectrum of ultra-bright Z-source Scorpius X-1

S. M. Mazzola, R. Iaria, T. Di Salvo, A. Sanna, A. F. Gambino, E. Bozzo, C. Ferrigno, A. Riggio and L. Burderi (submitted to A&A)

6.1 Introduction

In this work, it is shown the study of the spectral emission of Scorpius X-1 (hereafter Sco X-1), the brightest X-ray persistent source in the sky. Identified as the first X-ray extra-solar sources by Giacconi et al. (1962), Sco X-1 is a NS-LMXB system classified as Z-source (Hasinger & van der Klis 1989) in which the companion star is an M-type star with a mass of ~ 0.4 $M_{\odot}$ (Steeghs & Casares 2002). Sco X-1 was also the first X-ray binary found to exhibit radio emission (Andrew & Purton 1968) and, thanks to a monitoring campaign performed with the *Very Long Baseline Array*, Bradshaw et al. (1999) inferred a distance to the source of 2.8 ± 0.3 kpc, while Fomalont et al. (2001) determined an inclination angle $\theta = 46^{\circ} \pm 6^{\circ}$ of the system with respect to the line of sight.

Similarly to all Z-sources, Sco X-1 exhibits QPOs along all the branches of the Z-track: observed for the first time by Middleditch & Priedhorsky (1986), they can be distinguished, in general, between low (<10 Hz) and high (>10 Hz) frequency QPOs (Stella 1986) and they were extensively

studied. The horizontal branch oscillations (HBOs) in Sco X-1 were observed for the first time by van der Klis et al. (1996), with a peak of 45 Hz (and an harmonic near 90 Hz), then a *twin* kHz HBOs were also detected in the range 800-1100 Hz, shifting simultaneously in frequency with constant peak-to-peak separation (Zhang et al. 2006; Yin et al. 2007; Yin & Zhao 2007). The normal branch oscillations (NBOs) and the flaring branch oscillations (FBOs) were observed with peak frequencies in the range 4.5-7 Hz and 6-25 Hz, respectively, and seemed to be related to each other since the two peak frequencies converge when the source moves from NB to FB (see e.g. Casella et al. 2006; Yu 2007).

Because of the strong brightness of Sco X-1, which makes hard to collect high statistical data in the soft X-ray band without damaging the instruments, the study of the spectral emission of this source was mainly directed to the highest energies. Using several HEXTE (on-board *Rossi X-ray Timing Explorer* satellite, Rothschild et al. 1998) observations, D'Amico et al. (2001) searched for the hard tail in the spectra of Sco X-1, modelling the data with a thermal bremsstrahlung model. The authors found that the addition of a power-law was necessary to model the data in 5 out of the 16 analysed observations. Barnard et al. (2003) used both HEXTE and PCA instruments to study the broadband spectrum of this source, fitting the data with a model composed of a blackbody from the NS and a cut-off power-law interpreted as a Comptonised emission from an extended accretion disc corona (ADC, White & Holt 1982), plus a broad Gaussian line. Whilst, Bradshaw et al. (2003) applied a model composed of a blackbody emission plus a bulk motion Comptonisation and a broad Gaussian line to perform the analysis on PCA data in the range 2.5-18 keV. Di Salvo et al. (2006) exploited the monitoring carried out by *INTEGRAL* to follow the spectral evolution of the source along the Z-track. The authors analysed the data in the 20-200 keV energy range, collected by IBIS/ISGRI (Ubertini et al. 2003; Goldwurm et al. 2003) during two entire revolutions of the satellite ($\sim$ 300 ks each one), using a thermal Comptonisation model and observing that the spectra were dominated above 30 keV by a power-law of photon index $\Gamma \sim 3$, with intensity slightly decreasing from the HB along the other branches, becoming not significant in the FB. The absence of a cut-off detection at the highest energy suggested the non-thermal origin of this hard component. D'Aí et al. (2007) analysed 43 spectra collected by *RXTE* between 1997 and 2003, using a thermal and a hybrid Comptonisation model, plus a Gaussian and power-law component. The authors followed the spectral variation along the Z-pattern and obtained that, also in this case, the flux of the hard X-ray tail (with photon index between 1.9-3) was correlated with the position of the source in the CD and the contribution of this component to the total flux was anti-correlated to the mass accretion rate. Titarchuk et al. (2014) followed the evolution of Sco X-1 between the HB

and FB studying several *RXTE* observations collected between 1996 and 2002. The authors fitted the 3-250 keV spectra with a model consisting of two Comptonised component with different seed photons temperature and a broad iron line, observing a stability in the value of the photon index during the HB and NB until a slight decreasing in the FB. Finally, Revnivtsev et al. (2014) studied 4 Ms of data collected by SPI (Vedrenne et al. 2003) and IBIS instruments on-board *INTEGRAL* and related simultaneous *RXTE* observations, in order to have a coverage from 2 keV up to 10 MeV. The authors showed that the hard tail was well described by a power-law shape without cut-off up to 200-300 keV, proposing that it originates as a Compton up-scattering of soft seed photons on electrons with a non-thermal distribution.

Homan et al. (2018) partially analysed the *NuSTAR* observation of Sco X-1 reported here, in order to compare the results with those obtained in their study of the Z-source GX 5-1. Here, the analysis of *NuSTAR* data is extended, studying the 3-60 keV spectra extracted for NB and FB with two different classes of models which lead to the same physical description of the source.

6.2 Observations and data analysis

The Nuclear Spectroscopic Telescope Array satellite (*NuSTAR*, Harrison et al. 2013) observed Sco X-1 between 2014-10-08 06:46:07 UTC and 2014-10-08 16:16:07 UTC (ObsId 30001040002), for a total of $\sim$ 30 ks. The data were processed using the NuSTAR Data Analysis Software (NuSTARDAS) v1.9.3 for both the data sets collected by the two focal plane modules, FPMA and FPMB. The source events were extracted from a circular region with radius 250" and 200" for FPMA and FPMB, respectively, centred on the source coordinates. While for the background events, Iused a circular region with a radius of 120" far away from the source for both the instruments. Because of the extremely high count rate of the source, the `statusexpr` parameter in `nupipeline` was modified to avoid artificially vetoing events from the noise filter. The filtered events, the background-subtracted light curves, the spectra and the arf and rmf files were created using the `nuproducts` tool; live-time, point-spread-function, exposure, and vignetting corrections were applied.

The flaring activity of the source is observed in both the FPMA and FPMB light-curve, with a count rate between 5000 c/s and 12500 c/s. The 1.6-80 keV FPMA background-subtracted light curve is shown in Figure 6.1(left panel).

Furthermore, I build the CD of the source for the two instruments using the hardness ratio between the count-rate in the 6-10 keV and 3-6 keV energy bands and in the 10-20 keV and 6-10 keV energy bands to obtain the "soft colour" (SC) and "hard colour" (HC) light curves, respectively.

Comparing the obtained CD with what is reported in literature from *RXTE* data, it is found out whether the source was probably observed during the lower normal/flaring branch of its Z-track. I combined the CD of the two instruments and divided the two branches, performing a selection in HC and SC intervals in order to group the data. In particular, I selected the data between 0.58-0.62 SC and 0.22-0.25 HC, between 0.55-0.645 SC and 0.25-0.285 HC, and between 0.58-0.7 SC and 0.285-0.35 HC for NB (black points in Figure 6.1); for FB (red points in Figure 6.1) I selected the data in the following intervals: 0.62-0.66 SC and 0.22-0.25 HC, 0.66-0.74 SC and 0.225-0.228 HC and 0.74-0.82 SC and 0.25-0.33 HC. The grouped data are shown in Figure 6.1 using different colors.

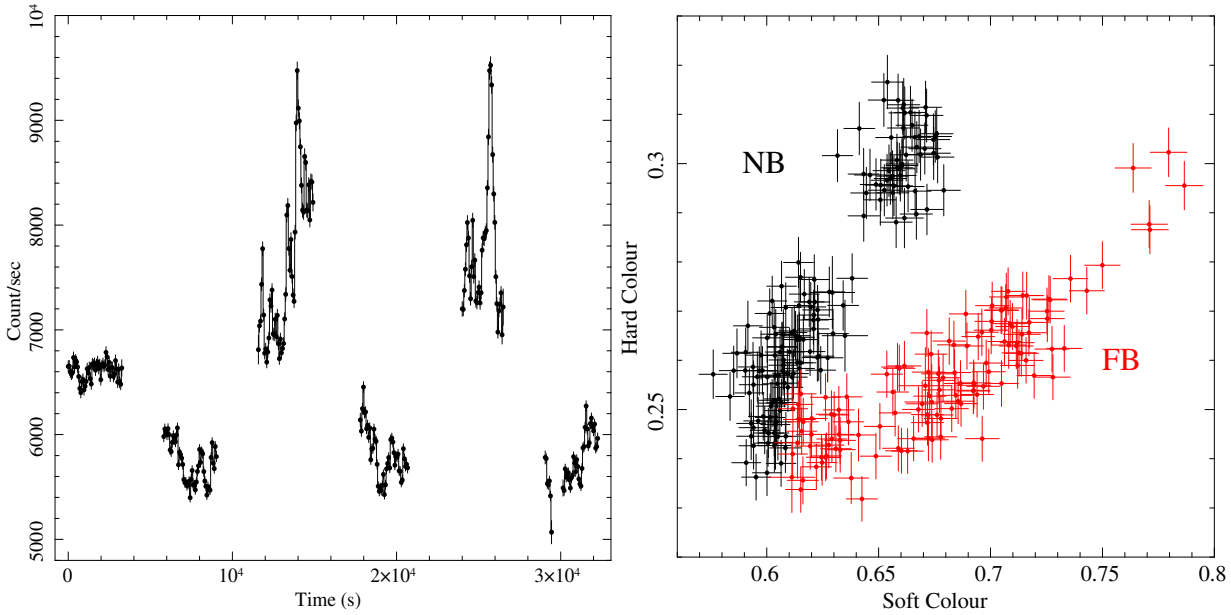

Figure 6.1: On the left: FPMA background-subtracted light curve of Sco X-1 in the 1.6-80 keV energy range, showing the flaring activity of the source. The bin time is 64 s. On the roght: colour-colour diagram of Sco X-1 from combined FPMA and FPMB data. The Soft Colour is the ratio between the count rate in the energy bands 6-10 keV and 3-6 keV, while the Hard Colour is the ratio between the count rate in the energy bands 10-20 keV and 6-10 keV. The bin time is 128 s.

Given the high count rate of the source, the possibility of pile-up effects in the data was explored. As reported by Grefenstette et al. (2016), a possible pile-up effect can occur in two different situations: when two photons arrive in the same pixel and they are counted as one, or when two photons arrive in adjacent pixels and they are then combined during the reprocessing stage of the data. For the first type of pile-up, Grefenstette et al. (2016) estimated for this

NuSTAR observation a pile-up fraction of 5.3×10^{-4} per pixel, that is a negligible contribution. For the second one, the same authors estimated a pile-up fraction of 8×10^{-4} per pixel, taking into account only the events with values of the `grades` parameter (that is a qualifier assigned to each event to identify the pattern of the detected photon on a 3×3 grid) between 21-24. As suggested by Grefenstette et al. (2016), I extracted the spectrum of the source using `grades=0-32` (total events), `grades=0` (single-photon events only) and `grades=1-32` (multiple-photons events only), but any variation in the counts per energy channel related to a possible pile-up was observed.

Using the standard `nuproducts` pipeline, I obtained a total spectrum with an exposure time around 800 s for both FPMA and FPMB, because of the dead-time correction factor due to the high count rate of the source. Finally, I extracted a NB spectrum of ∼500 s exposure time and a FB spectrum of ∼276 s exposure time, for both FPMA and FPMB.

Since the spectral shape for the two instruments turn out to be compatible above 3 keV, they were fitted simultaneously in the 3-60 keV energy range, in order to avoid the predominant contribution of the background at the highest energies; all the spectra were grouped to have a minimum of 25 counts per energy bin.

I used XSPEC v12.10.1q to perform the spectral fit; I set the abundances and the photoelectric absorption cross-sections to the values found by Wilms et al. (2000) and by Verner et al. (1996), respectively, for all the spectral models discussed in the following. I applied the same models to the NB and the FB spectra.

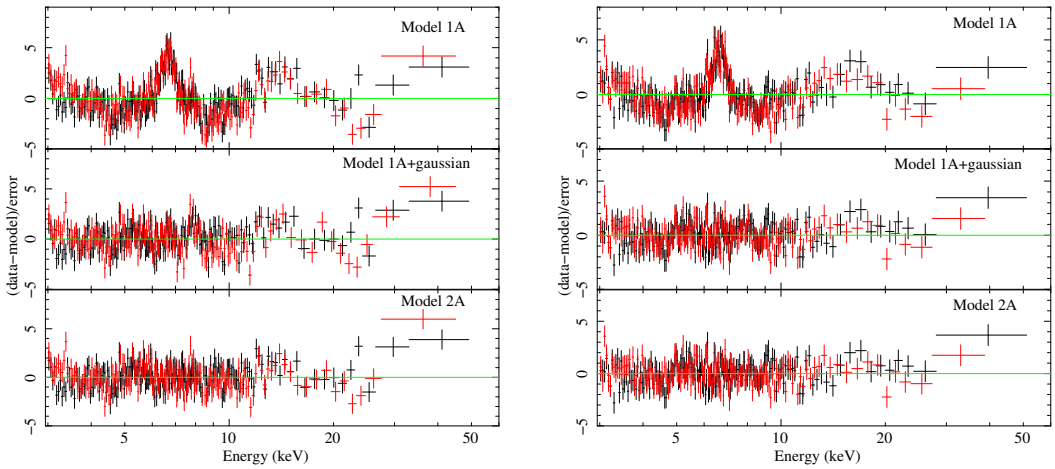

Figure 6.2: On the left: comparison between residuals obtained adopting Model 1A (top panel), Model 1A plus a Gaussian component (middle panel) and Model 2A (bottom panel) for NB. On the right: same comparison for FB. The FPMA and FPMB data are showed in black and red colour, respectively. The residuals are graphically re-binned in order to have at least 100σ per bin.

Table 6.1: Best-fit results

	NB				FB			
	Model 2A*	Model 2B$^\diamond$	Model 4A†	Model 4B‡	Model 2A*	Model 2B$^\diamond$	Model 4A†	Model 4B‡
Component								
TBABS								
nH(10^{22})	0.3 (frozen)	0.3 (frozen)	0.3 (frozen)	0.3 (frozen)	0.3 (frozen)	0.3 (frozen)	0.3 (frozen)	0.3 (frozen)
EXPABS								
LowECut(keV)			3 kT	kT_{bb}			3 kT	kT_{bb}
POWERLAW								
PhoIndex			3^{+2}_{-1}	2 ± 2			2 ± 2	2 ± 2
norm			> 0.04	< 17			< 32	< 123
F_{pow} ($\times 10^{-9}$ erg cm^{2}s^{-1})			2.85	1.06			0.78	1.77
GAUSSIAN								
$E_{line_{K\alpha}}$(keV)	6.62 ± 0.03	6.64 ± 0.03	$6.61^{+0.03}_{-0.04}$	6.64 ± 0.03	6.60 ± 0.03	6.63 ± 0.03	6.60 ± 0.03	6.63 ± 0.03
$\sigma_{K\alpha}$(keV)	$0.35^{+0.04}_{-0.05}$	$0.33^{+0.04}_{-0.03}$	$0.37^{+0.05}_{-0.04}$	0.35 ± 0.04	0.33 ± 0.04	0.28 ± 0.04	$0.34^{+0.05}_{-0.04}$	0.29 ± 0.04
norm	0.12 ± 0.01	0.12 ± 0.01	$0.13^{+0.02}_{-0.01}$	0.127 ± 0.008	0.16 ± 0.02	0.13 ± 0.02	$0.162^{+0.018}_{-0.009}$	0.13 ± 0.02
$EqW_{K\alpha}$ (eV)			56^{+6}_{-7}	54^{+7}_{-6}			52^{+5}_{-6}	41^{+6}_{-5}
GAUSSIAN								
$E_{line_{K\beta}}$	7.7 ± 0.1	7.75 ± 0.09	7.8 ± 0.1	7.77 ± 0.09	7.8 ± 0.2	7.8 ± 0.3	7.8 ± 0.2	7.9 ± 0.2
norm	0.022 ± 0.006	$0.026^{+0.007}_{-0.005}$	$0.026^{+0.006}_{-0.003}$	0.031 ± 0.004	0.016 ± 0.008	0.010 ± 0.005	0.018 ± 0.008	0.013 ± 008
$EqW_{K\beta}$ (eV)			17 ± 4	21 ± 5			9^{+4}_{-5}	6^{+5}_{-4}
BBODYRAD								
kT (keV)	1.29 ± 0.02		1.26 ± 0.02		1.51 ± 0.01		$1.50^{+0.02}_{-0.03}$	
R_{bb} (km)	13 ± 1		13 ± 2		13 ± 1		13 ± 1	
DISKBB								
kT_{in} (keV)		$0.46^{+0.02}_{-0.04}$		0.43 ± 0.03		0.62 ± 0.03		$0.60^{+0.04}_{-0.03}$
R_{disc} (km)		202^{+93}_{-40}		266^{+104}_{-83}		98^{+22}_{-16}		107 ± 21
F_{bb} (10^{-7} erg cm^{2}s^{-1})			0.61	4.21			1.19	2.76
NTHCOMP								
Γ	2.06 ± 0.01	$2.45^{+0.02}_{-0.04}$	$2.04^{+0.01}_{-0.02}$	$2.40^{+0.03}_{-0.01}$	$2.078^{+0.009}_{-0.018}$	$2.87^{+0.06}_{-0.08}$	$2.06^{+0.02}_{-0.01}$	$2.77^{+0.09}_{-0.07}$
kT_e(keV)	$2.96^{+0.02}_{-0.01}$	$3.19^{+0.01}_{-0.04}$	2.88 ± 0.04	$3.1^{+0.05}_{-0.03}$	2.99 ± 0.04	$3.34^{+0.08}_{-0.09}$	2.94 ± 0.06	$3.20^{+0.05}_{-0.10}$
kT_{bb}(keV)	< 0.33	$0.87^{+0.01}_{0.03}$	< 0.34	0.84 ± 0.02	< 0.38	$1.17^{+0.02}_{-0.03}$	< 0.37	$1.15^{+0.03}_{-0.02}$
norm	99^{+4}_{-20}	$13.0^{+0.9}_{-0.4}$	93^{+6}_{-16}	$14.0^{+0.6}_{-0.7}$	107^{+7}_{-23}	$8.9^{+0.4}_{-0.3}$	109^{+3}_{-7}	$9.2^{+0.2}_{-0.8}$
F_{Comp} (10^{-7} erg cm^{2}s^{-1})			5.55	3.21			6.8	3.67
τ			9.8 ± 0.2	7.58 ± 0.09			9.6 ± 0.2	6.2 ± 0.3
F_{bol} (10^{-7} erg cm^{2}s^{-1})			6.20	7.55			8.03	6.46
χ^2/dof	1395/1181	1339/1181	1336/1179	1307/1179	1181/1099	1154/1099	1167/1097	1146/1097

* Model 2A:TBabs*(Gaussian+Gaussian+bbodyrad+nthComp)

$^\diamond$ Model 2B:TBabs*(Gaussian+Gaussian+diskbb+nthComp)

† Model 4A: TBabs*(expabs*powerlaw+Gaussian+Gaussian+bbodyrad+nthComp)

‡ Model 4B: TBabs*(expabs*powerlaw+Gaussian+Gaussian+diskbb+nthComp)

The uncertainties are reported at 90% confidence level.

The spectral parameters are defined as in XSPEC.

Initially, I fitted the continuum direct emission with a model composed of a blackbody component (`bbodyrad` in XSPEC), which mimics a saturated Comptonisation associated with a boundary layer, plus a thermal Comptonisation (`nthComp`, Zdziarski et al. 1996a; Życki et al. 1999b), with the `inp_type` parameter set to 1, indicating that the seed photons have a disc-blackbody distribution. To take into account the photoelectric absorption by neutral matter in the ISM, I used the Tübingen-Boulder model (`TBabs` component), keeping the value of the equivalent hydrogen column associated with the interstellar matter fixed to 0.3×10^{22} cm^{-2} (D'Aí et al. 2007; Christian & Swank 1997) due to the lack of coverage below 3 keV. From this model, called Model 1A, a χ^2/d.o.f. of 2149/1186 and 1772/1104 was obtained for NB and FB, respectively, but large residuals are present around 6 keV, in the Fe-K region (top left and top right panels in Figure 6.2).

Then, a Gaussian component was added to the model, leaving all the line parameters free to vary. A significant improvement of the fit was obtained, with a χ^2/d.o.f. of 1428/1183 and 1190/1101 for NB and FB, respectively, and a significance of the line component (estimated as the ratio between the intensity of the line and the associated error calculated at 68% c.l.) of 13σ for NB spectrum and 15σ for FB spectrum. The emission line showed a centroid energy around 6.6 keV and a line width $\sigma \sim 0.3$ keV.

Looking at the residuals (central panels in Figure 6.2), some features are still observed in the Fe-K region, especially in the NB spectrum. Then, I added a second Gaussian component, keeping linked the width to the σ parameter of the first one, under the hypothesis that the two lines are associated to the emission from the same ion in the same region of the accretion flow, and so that their dispersion velocity is not dependent from the atomic weight of the element and they are affected by the same broadening effects. From this Model 2A, it results χ^2/d.o.f.= 1395/1181 with a significance of the new line component of 7.3σ for NB and χ^2/d.o.f.= 1181/1099 with a 3σ of significance for FB, implying that the detection of this feature is barely significant in the flaring branch spectrum. The centroid energy of this line is around 7.8 keV, suggesting an emission related to the Kβ transition of the Fe XXV ion. The best-fit results and residuals are shown in Table 6.1 (second and sixth columns for NB and FB, respectively) and Figure 6.2 (bottom panels).

As alternative description, I substituted the blackbody component with a multicolour disc-blackbody (`diskbb` in XSPEC, Mitsuda et al. 1984; Makishima et al. 1986), varying accordingly the `inp_type` value of `nthComp` to 0, indicating that the seed photons have a blackbody incoming spectrum; this modela was called Model 1B. Following the same steps described above for Model 1A, I added two Gaussian lines, obtaining our Model 2B:TBabs*(Gaussian+Gaussian+diskbb+nthComp).

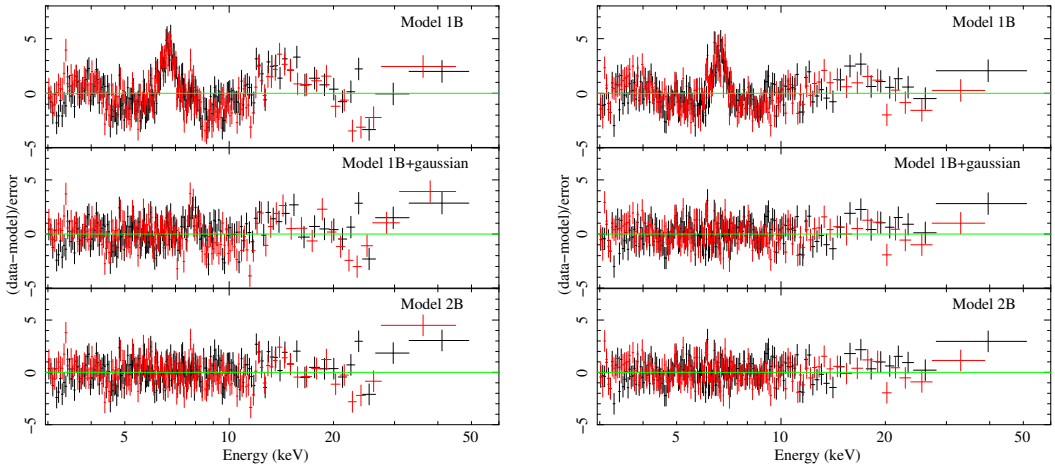

Figure 6.3: On the left: comparison between residuals obtained adopting Model 1B (top panel), Model 1B plus a Gaussian component (middle panel) and Model 2B (bottom panel) for NB. On the right: same comparison for FB. The FPMA and FPMB data are showed in black and red colour, respectively. The residuals are graphically re-binned in order to have at least 100σ per bin.

The Kα line has a significance of 12σ in both the branch spectra, while the Kβ has a significance of 8.7σ in NB and only 2σ in FB; the values of the lines parameters are compatible with those obtained from Model 2A. The best-fit results are shown in Table 6.1 (third and seventh columns for NB and FB, respectively); the residuals for each model step are presented in Figure 6.3.

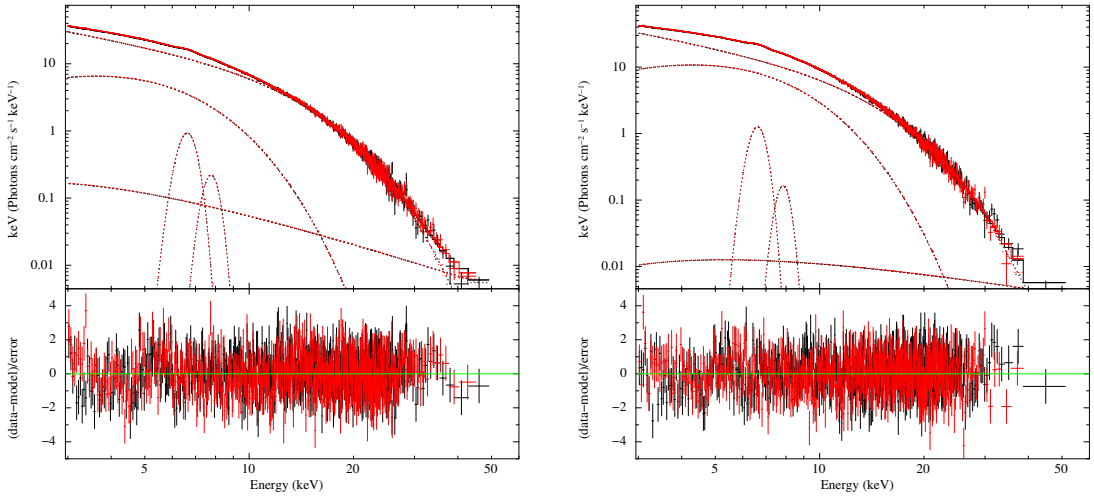

Figure 6.4: The unfolded spectrum and corresponding residuals obtained using Model 4A for NB (on the left) and FB (on the right). The FPMA and FPMB data are shown in black and red colour, respectively.

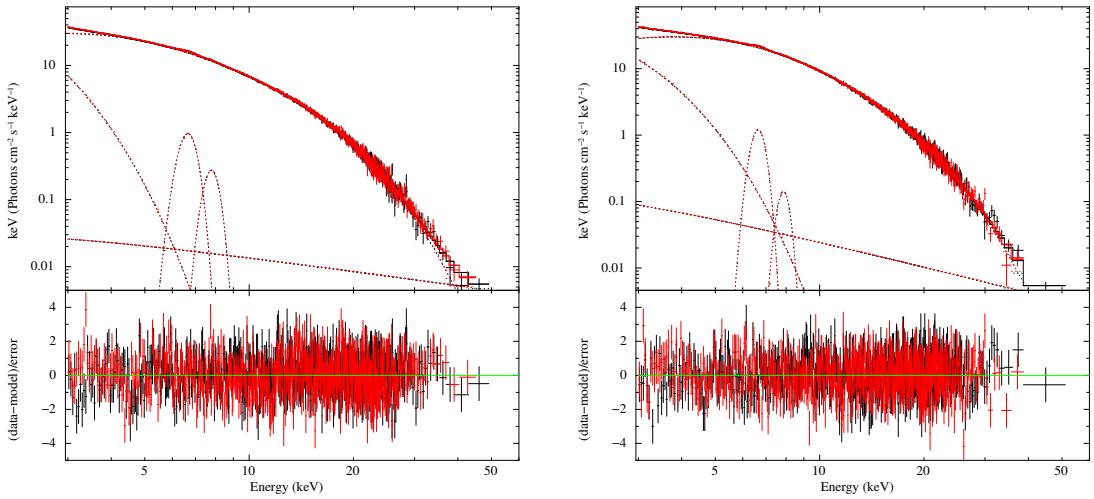

Figure 6.5: The unfolded spectrum and corresponding residuals obtained using Model 4B for NB (on the left) and FB (on the right). The FPMA and FPMB data are shown in black and red colour, respectively.

Since large residuals are still observed above 30 keV, I added to both Model 2A and 2B a `powerlaw` component to fit this hard excess, leaving the photon index and the normalisation free to vary; these ones are called Model 3A and 3B, respectively. From Model 3B, a χ^2/d.o.f.=1307/1179 was obtained for NB with an F-test probability of chance improvement of 6.7×10^{-7}, corresponding to a significance of $\sim 5\sigma$, which suggests that the addition of this component is statistically significant; while for FB it results χ^2/d.o.f.=1146/1097 with an F-test of 0.0156 (significance $< 2.8\sigma$), suggesting that the presence of the power-law is not significant. On the other hand, from Model 3A, χ^2/d.o.f.=1285/1179 and 1145/1097 for NB and FB, respectively, corresponding to a $\Delta\chi^2$ with respect to Model 2A of 110 and 36 (with 2 d.o.f. gap), which represent an improvement of the fits. Furthermore, an F-test probability of chance improvement of 8.8×10^{-22} for NB and of 4.6×10^{-8} for FB were obtained, corresponding to a significance larger than 6σ and about 5.7σ, respectively and suggesting that the power-law component is required in both the cases. A low-energy exponential roll-off was also added to the model, using the `expabs` component, in order to mimic a cutoff at the seed photon temperature, keeping fixed the low energy cut-off to a value equal to 3 times the blackbody peak temperature kT. This one was called Model 4A and returns a χ^2/d.o.f. of 1336/1179 with an F-test probability of chance improvement of 9×10^{-12} (significance $> 6\sigma$) with respect to the Model 3A for NB and χ^2/d.o.f.=1167/1097 with an F-test of 0.0018 (significance $\sim 3\sigma$) for FB. Also in this

case, the statistical weight of the power-law decreases in the flaring branch spectrum. The blackbody temperature is 1.26 ± 0.02 keV in NB and $1.50^{+0.02}_{-0.03}$ keV in FB, the electronic temperature and the photon index Γ related to the Comptonised component are 2.88 ± 0.05 keV and $2.04^{+0.01}_{-0.02}$, respectively, in NB and 2.94 ± 0.06 keV and $2.06^{+0.02}_{-0.01}$ in FB; whilst only an upper limit of 0.34 keV and 0.37 keV was obtained on the seed photons temperature $kT_{\rm bb}$ for NB and FB, respectively. The Fe Kα line has an energy $E_{\rm line_{K\alpha}} = 6.61^{+0.03}_{-0.04}$ keV and a width $\sigma_{K\alpha} = 0.37^{+0.05}_{-0.04}$ keV in NB, while $E_{\rm line_{K\alpha}} = 6.60 \pm 0.03$ keV and $\sigma_{K\alpha} = 0.34^{+0.05}_{-0.04}$ keV in FB. For the Fe-Kβ line, $E_{\rm line_{K\beta}} = 7.8 \pm 0.1$ keV in NB and $E_{\rm line_{K\beta}} = 7.8 \pm 0.2$ in FB. For the NB spectrum, a total unabsorbed flux $F_{\rm bol} = 6.20 \times 10^{-7}$ erg cm^{-2} s^{-1} in the 0.1-100 keV energy range is observed, corresponding to a luminosity of 5.79×10^{38} erg s^{-1} for a distance to the source of 2.8 ± 0.3 kpc (Bradshaw et al. 2003); the 0.1-100 keV bolometric flux associated to the power-law component is $F_{\rm pow} = 2.85 \times 10^{-9}$ erg cm^{-2} s^{-1}. While for the FB spectrum, the total unabsorbed flux in the 0.1-100 keV energy range is $F_{\rm bol} = 8.0 \times 10^{-7}$ erg cm^{-2} s^{-1} , corresponding to a luminosity of 7.5×10^{38} erg s^{-1}, and the bolometric flux associated to the power-law component is $F_{\rm pow} = 0.78 \times 10^{-9}$ erg cm^{-2} s^{-1}. The best-fit values of the parameters are shown in the fourth and eighth column of Table 6.1; the unfolded spectrum and the corresponding residuals are shown in Figure 6.4.

The addition of `expabs` to Model 3B is not required by the data. However, in order to perform a self-consistent analysis, I decided to take into account this component also in this case, keeping fixed the low energy cut-off to the seed photon temperature $kT_{\rm bb}$. The χ^2/d.o.f. value for Model 4B is the same obtained from Model 3B for both NB and FB spectrum. The inner disc-blackbody temperature is 0.43 ± 0.03 keV and $0.60^{+0.04}_{-0.03}$ keV in NB and FB, respectively. The electronic temperature kT_e and the seed photon temperature $kT_{\rm bb}$ are $3.20^{+0.05}_{-0.02}$ keV and $1.15^{+0.03}_{-0.02}$ keV, respectively, in NB and $kT_e = 3.20^{+0.05}_{-0.02}$ and $kT_{\rm bb} = 3.20^{+0.05}_{-0.02}$ in FB; the photon index Γ is $2.56^{+0.04}_{-0.03}$ and $2.77^{+0.09}_{-0.07}$ for NB and FB, respectively. For the iron emission lines,the Fe Kα line energy $E_{\rm line_{K\alpha}}$ is $6.64^{+0.03}_{-0.04}$ keV and the width $\sigma_{K\alpha} = 0.35 \pm 0.04$ keV and $E_{\rm line_{K\beta}} = 7.77 \pm 0.09$ keV for the Fe Kβ in NB, while $E_{\rm line_{K\alpha}} = 6.63 \pm 0.03$ keV, $\sigma_{K\alpha} = 0.29 \pm 0.04$ keV and $E_{\rm line_{K\beta}} = 7.9 \pm 0.2$ keV in FB. The total unabsorbed flux observed in the 0.1-100 keV energy range is $F_{\rm bol} = 7.55 \times 10^{-7}$ erg cm^{-2} s^{-1} , corresponding to a luminosity of 7.1×10^{38} erg s^{-1} for a distance to the source of 2.8 ± 0.3 kpc (Bradshaw et al. 2003), in NB and $F_{\rm bol} = 6.46 \times 10^{-7}$ erg cm^{-2} s^{-1} in FB, corresponding to a luminosity of 6.1×10^{38} erg s^{-1}. The 0.1-100 keV bolometric flux associated to the power-law component is $F_{\rm pow} = 1.06 \times 10^{-9}$ erg cm^{-2} s^{-1} and $F_{\rm pow} = 1.77 \times 10^{-9}$ erg cm^{-2} s^{-1} in NB and FB, respectively.

Table 6.2: Best-fit results from Model 6: TBabs*(expabs*powerlaw+diskbb+rfxconv*nthComp)

	NB	FB
Component		
TBABS		
nH(10^{22})	0.3 (frozen)	0.3 (frozen)
POWERLAW		
PhoIndex	2 (frozen)	2 (frozen)
norm	$0.086^{+0.022}_{-0.022}$	0.5 ± 0.3
RFXCONV		
Fe_abun	1 (frozen)	1 (frozen)
z	0 (frozen)	0 (frozen)
$\cos\theta$	0.6947 (frozen)	0.6947 (frozen)
rel_refl	0.20 ± 0.03	0.14 ± 0.02
logξ	$2.37^{+0.03}_{-0.02}$	$2.48^{+0.09}_{-0.05}$
DISKBB		
Tin(keV)	0.55 ± 0.03	0.64 ± 0.03
R_{disc} (km)	122 ± 27	89 ± 15
NTHCOMP		
Gamma	2.49 ± 0.03	$2.90^{+0.09}_{-0.07}$
kT_e(keV)	$3.14^{+0.04}_{-0.05}$	$3.29^{+0.11}_{-0.08}$
kT_{bb}(keV)	0.92 ± 0.02	$1.19^{+0.03}_{-0.02}$
norm	$10.9^{+0.5}_{-0.6}$	$8.3^{+0.3}_{-0.4}$
τ	7.2 ± 0.2	6.0 ± 0.3
R_{seed} (km)	39 ± 4	26 ± 3
χ^2/dof	1316/1183	1149/1101

The uncertainties were calculated at 90% c.l. The optical depth τ of the electron corona and the seed-photon emitting radius R_{seed} were estimated as described in Sec. 6.3.

The best-fit values of the parameters are shown in the fifth and ninth column of Table 6.1; the unfolded spectrum and the corresponding residuals are shown in Figure 6.5.

Moving forward, it was explored the hypothesis that the iron emission lines originates from a smeared reflection, thus I replaced the Gaussian components in Model 4B with a `diskline` (Fabian et al. 1989). I kept the outer radius of the reflection region $R_{\rm out}$ and the inclination angle θ of the binary system fixed to the value of 3000 gravitational radii ($Rg = GM/c^2$) and 46° (Fomalont et al. 2001), respectively, while the inner radius $R_{\rm in}$, the power-law dependence of emissivity `Betor` and the energy of the emission line were left free to vary. In order to lead the fit to convergence, I kept the photon index of the power-law component fixed to the value obtained from Model 4B for both NB and FB spectrum. From this Model 5, a χ^2/d.o.f. of 1374/1181 and 1155/1099 was obtained for NB and FB, respectively. The line energy is 6.65 ± 0.03 keV and the emissivity parameter is $-2.14^{+0.08}_{-0.13}$ for NB spectrum, while `LineE`= 6.64 ± 0.03 keV and `Betor`= $-2.5^{+0.5}_{-1.0}$ in FB. The inner radius is not well constrained: only un upper limit of 14 Rg was obtained in NB and $R_{\rm in} = 64^{+70}_{-53}$ Rg in FB; for the other components of the model, the best value

of the parameters are compatible at 90% c.l. with the results obtained from Model 4B. However, slightly large residuals are observed around 7.8 keV, especially for the NB spectrum (see central panels in Figure 6.6). Furthermore, it results a $\Delta\chi^2$ of 67 and 9 (2 d.o.f. apart) with respect to Model 4B for NB and FB spectrum, respectively. Thus, no improvement of the fit was produced.

Then, I replaced the `diskline` component with a self-consistent reflection model (`rfxconv`, Kolehmainen et al. 2011b), in order to fit the emission line in the Fe-K region and take also into account the reflection continuum. I kept the iron abundance fixed to the Solar one, the redshift parameter z fixed to 0 and the cosine of the inclination angle fixed to 0.6947, considering again $\theta = 46°$ (Fomalont et al. 2001), while I left the ionisation parameter $\log \xi$ of the reflecting matter in the accretion disc and the relative reflection normalisation rel_refl free to vary. The incident emission onto the accretion disc is provided by the Comptonisation component; this one was called Model 6. Also in this case, the photon index of the power-law component was kept fixed to the values obtained from Model 4B; the best-fit results are shown in Table 6.2. A χ^2/d.o.f. of 1316/1183 with a $\Delta\chi^2$ of 9 with respect to Model 4B was obtained for NB spectrum; while χ^2/d.o.f.=1145/1101 and $\Delta\chi^2$=3 for FB spectrum, suggesting that the reflection model does not provide an improvement of the fit.

To take into account the possible relativistic smearing effects in the inner region of the accretion disc, a multiplicative `rdblur` component was added to Model 6, in which the outer radius of the reflection region $R_{\rm out}$ was kept fixed to the value of 3000 gravitational radii ($Rg = GM/c^2$) and the inclination angle θ of the system to 46°, while leaving the power-law dependence of emissivity `Betor` free to vary. Since any constraints was obtained on the inner radius $\rm R_{in}$ at which the reflection component originates, in the hypothesis that the reflection occurs in a region of the disc where the relativistic effects are not predominant, the inner reflection radius was tied to the inner radius of the accretion disc, related to the normalisation of the disc-blackbody component by the relation $norm = R^2_{\rm disc}/D^2_{10}\ \cos\theta$, where D_{10} is the distance to the source in unit of 10 kpc and θ is the inclination angle of the source. Under this assumption, a constrain on the emissivity factor `Betor` was found, resulting $-2.0^{+0.5}_{-0.34}$ in NB and > -1.7 in FB. This model provides a χ^2/d.o.f. of 1305/1182 with an F-test probability of chance improvement of 0.0005, corresponding to a significance $\sim 3\sigma$ for NB spectrum and χ^2/d.o.f.=1146/1100 with an F-test value of 0.0698 (significance $< 2\sigma$) for FB spectrum. These results suggest that the addition of `rdblur` component is not significant, and then the iron emission line is probably not affected by relativistically smearing but only by Compton broadening.

Despite the best-fit values of the parameters are compatible at 90% c.l. with those obtained

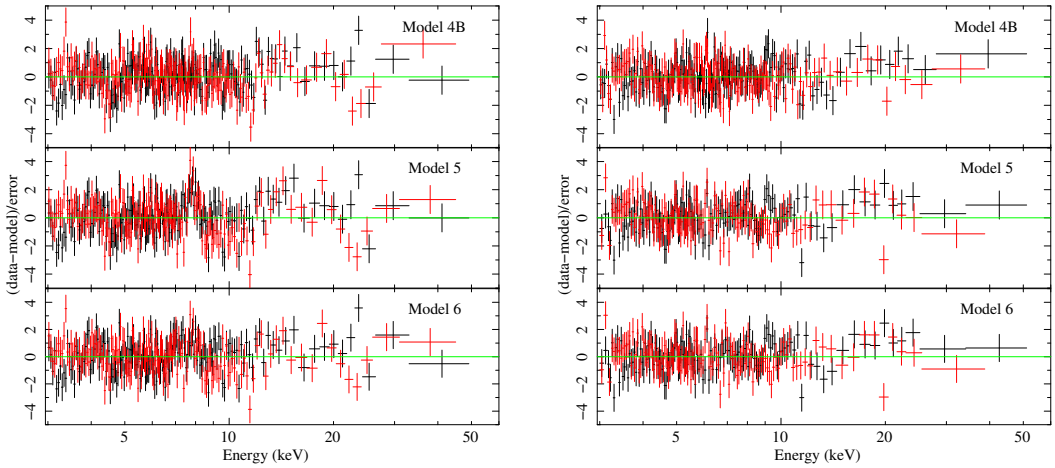

Figure 6.6: On the left: comparison between residuals obtained adopting Model 4B (top panel) and Model 5 (bottom panel) for NB. On the right: same comparison for FB. The FPMA and FPMB data are shown in black and red colour, respectively. The residuals are graphically re-binned in order to have at least 120σ per bin.

from Model 4B for both the branches, from Model slightly larger residuals are still observed around 7.8 keV, especially in NB spectrum (see the comparison in Figure 6.6). For this reason, together with the evidence that the reflection does not produce an improvement for the fit, the two Gaussian models (i.e. Model 4A and 4B) are taken into account as best-fit models. Hence, it can be supposed the Fe-K region of the spectrum is well-described by the presence of two Compton broadened iron emission line, related to the Kα and Kβ transition of the Fe XXV ions in the accretion disc.

In the end, I tested also the model used by Homan et al. (2018), composed of two thermal component, a power-law and a Gaussian component to fit the iron emission line at 6.6 keV, plus a `TBabs` component to take into account the absorption due to the interstellar medium. For the NB spectrum, a χ^2/d.o.f. of 1380/1184 was inferred, reproducing the same results obtained by Homan et al. (2018), but no improvement of the fit was attained with respect to Model 4A and 4B. For the FB spectrum, not analysed by Homan et al. (2018), I did not obtain a good fit using this model; a photon index of the power-law around 7 was inferred and some large residuals remain in the Fe-K region of the spectrum and above 20 keV.

6.3 Discussion

The first NuSTAR observation of the source Sco X-1, collected in October 2014, was analysed. From the obtained CD, it was pointed out that the observation covers the lower normal branch and the flaring branch of its Z-track; thus, an almost complete spectrum for NB and a partial spectrum for FB were extracted. For both the branches, the 3-60 keV spectrum is well fitted by a model composed of a thermal emission, a thermal Comptonisation and two Gaussian components corresponding to the Fe Kα and Fe Kβ emission line of the Fe XXV ion; a hard tail was detected above 20 keV and modelled by a power-law limited at low energies with a photon index value of 2. Two different description were adopted for the thermal emission: a blackbody component (Model 4A) and a multi-colour disc-blackbody (Model 4B).

From model 4A, assuming a distance to the source of 2.8 kpc and an inclination angle θ of 46°, I inferred a blackbody radius $\mathrm{R_{bb}} = 13 \pm 2$ km and 13 ± 1 km for NB and FB, respectively, according with the hypothesis that this emission generates in the innermost region of the system, generally identified with the NS surface and the so-called boundary layer. Furthermore, I estimated the radius of the seed-photon emitting region $\mathrm{R_{seed}}$ using the relation $R_{\mathrm{seed}} = 3 \times 10^4 d[F_{\mathrm{Compt}}/(1+y)]^{1/2}(kT_{\mathrm{seed}})^{-2}$ (in 't Zand et al. 1999), where d is the distance to the source in units of kpc, $y = 4kT_e\ max[\tau, \tau^2]/(m_e c^2)$ is the Compton parameter, $\mathrm{kT_{seed}}$ is the seed-photon temperature in units of keV, and F_{Compt} is the bolometric flux of the Comptonisation component. Using the best-fit values (fourth and seventh column in Table 6.1), I find $R_{\mathrm{seed}} = 303 \pm 2$ km and 286 ± 30 km for NB and FB spectrum, respectively. In this case, the seed photons is assumed coming from an equivalent spherical surface with radius $\mathrm{R_{seed}}$. Moving forward, I estimated the optical depth τ of the Comptonising cloud using the relation provided by Zdziarski et al. (1996a):

$$\Gamma = \left[\frac{9}{4} + \frac{1}{\tau\left(1+\frac{\tau}{3}\right)\frac{kT_e}{m_e c^2}}\right]^{1/2} - \frac{1}{2},$$

finding that $\tau = 9.8 \pm 0.2$ and $\tau = 9.6 \pm 0.02$ for NB and FB, respectively. The electron corona is then optically thick and it is likely responsible for the shielding of the emission coming from the innermost region of the system, as hypothesised for other NS-LMXBs (see e.g. Mazzola et al. 2019b; Iaria et al. 2019, and references therein). In both NB and FB spectrum, a broad emission line with energy $E_{\mathrm{line_{K\alpha}}}$ ~6.6 keV and width $\sigma_{\mathrm{K}\alpha}$ around 0.35 keV was detected; it corresponds to the fluorescence of the Fe XXV and it is compatible with the results obtained by D'Aí et al. (2007) for NB/FB spectra. An emission line was also observed around 7.8 keV, corresponding to the Kβ

transition of the Fe XXV ion. The inferred equivalent width is 56^{+6}_{-7} eV and 52^{+5}_{-6} eV for the Fe-Kα line in NB and FB, respectively; while the Fe-Kβ emission line shows an equivalent width of 17 ± 4 eV in NB and 9^{+4}_{-5} eV in FB. These features are two *intercombination* lines belonging to the He-like triplets of Fe XXV (see e.g. Iaria et al. 2005); the *forbidden* and *resonance* lines of the triplet were not detected, probably due to the spectral resolution of the *NuSTAR* instruments which do not allow to resolve them. From the ratio between the intensity of the triplet lines, it is possible perform a diagnostic on the plasma conditions and infer information about the temperature, the ionisation state of the matter and the electronic density (see e.g. Porquet et al. 2001; Kallman et al. 2004; Yaqoob et al. 2007, for detailed calculations). I estimated the branching ratio K_β/K_α between the intensity of the detected lines as the ratio between the normalisation values of the corresponding Gaussian components obtained from the best-fit parameters, finding that it is 0.20 ± 0.04 and 0.11 ± 0.04 in NB and FB, respectively; the uncertainties are calculated at 68% confidence level. These values are compatible each other within 3σ and with the theoretical value of 0.27 (expected for the resonance lines)[1], precisely within 2σ for the NB spectrum and within about 3σ for the FB spectrum, respectively. The difference between the K_β/K_α values in NB and FB is due to the reduced intensity of the K_β line in the flaring branch. This one might be related to the different statistics of the data between the two spectra; the total number of photons is indeed $\sim 3.6 \times 10^6$ and $\sim 2.51 \times 10^6$ for NB and FB, respectively. Unfortunately, no other information about the plasma diagnostic can be obtained due to the limited spectral resolution of the data for the emission lines. Further observations with higher spectral resolution in the Fe-K region of the spectrum are necessary to this purpose.

From model 4B, under the same assumption discussed above, the estimated inner radius of the accretion disc results $\mathrm{R_{disc}} = 266^{+104}_{-83}$ km and 107 ± 21 km for NB and FB, respectively. In order to convert this value into the realistic inner disc radius $r_{\rm disc}$, I used the relation $r_{\rm disc} \sim f^2 R_{\rm disc}$, where $f \sim 1.7$ is the colour correction factor and it depends on the mass accretion rate $\dot{M}$ (see Shimura & Takahara 1995b, for details). It is found that $r_{\rm disc} = 769^{+301}_{-240}$ km and 310 ± 61 km in NB and FB, respectively, which indicates it is not possible to observe the innermost region of the disc, and it is compatible with the results obtained from Model 4A. A possible explanation could be provided taking into account the high value of the mass accretion rate $\dot{M}$, that is around $\sim 2.5 \dot{M}_{\rm Edd}$ (for a NS with mass of 1.4 $\mathrm{M_\odot}$ and radius of 10 km). For such values of $\dot{M}$, the inner regions of the accretion disc are thermally unstable and they result radiation pressure dominated; this inflates the inner disc, generating an optically thick bulge of matter which may act as a shielding corona

[1]See the NIST Atomic Spectra Database Lines Data, `https://www.nist.gov/pml/atomic-spectra-database`

for the inner soft emission (Shakura & Sunyaev 1976; Sincell & Krolik 1997).

Furthermore, I estimated the optical depth τ of the Comptonising cloud using the relation described above, finding that $\tau = 7.58 \pm 0.09$ in NB and $\tau = 6.2 \pm 0.3$ in FB. Also in this case, the electron corona is optically thick and the value of τ is compatible with those obtained by Di Salvo et al. (2006) in FB and by D'Aí et al. (2007) in NB/FB. Under this scenario, I estimated also the average electron density N_e of the cloud using the relation $\tau = N_e \sigma_T R$, in which τ is the optical depth, σ_T is the Thomson cross-section and $R = r_{\rm disc} - R_{\rm NS}$ is the geometrical dimension of the Comptonising corona, assuming that it covers the innermost region of the system from the NS surface up to the inner radius of the accretion disc. Thus, $N_e = 1.48 \times 10^{17}$ cm^{-3} and $N_e = 3.01 \times 10^{17}$ cm^{-3} for $R_{\rm NS}$ =10 km, under the assumption that $r_{\rm disc}$ is the real inner radius of the accretion disc. Furthermore, I also estimated the radius $\rm R_{seed}$ from which the seed photons are emitted using the relation provided by in 't Zand et al. (1999), finding $R_{\rm seed} = 45 \pm 5$ km in NB and 23 ± 3 km in FB and suggesting the seed photons were mainly emitted from a region near the NS surface.

Lastly, also in this case, two broadened Gaussian lines in the Fe-K region of both NB and FB spectrum are observed around 6.6 keV and 7.8 keV, corresponding to the Fe-Kα and Fe-Kβ transition of the Fe XV, respectively. The inferred equivalent widths are 56^{+6}_{-7} eV and 52^{+5}_{-6} eV for the Fe-Kα line in NB and FB, respectively; while the Fe-Kβ emission line shows an equivalent width of 21 ± 5 eV in NB and 6^{+5}_{-4} eV in FB. The branching ration K_α / K_β is 0.24 ± 0.04 in NB and 0.10 ± 0.05 in FB, with uncertainties calculated at 68% c.l., and also in these case these values are compatible with each other within 3σ and with the theoretical value within 1σ for the NB spectrum and within 3σ for the FB spectrum. As mentioned in the previous section, the reflection component does not represent an improvement for the fit, as well as the smearing component is unnecessary to describe these features, suggesting that reflection occurs at such a distance from the NS surface that the relativistic and Doppler effect are not ruling. This hypothesis is endorsed by the larger value inferred from the diskbb model for the inner radius of the accretion disc, which would locate the radius at which the reflection originate at more than 250 km; besides, since the source is ultra-bright, it is possible that the inner region of the accretion disc are so ionised for the irradiation due to incident emission from NS/boundary layer to be mainly composed of neutral matter thus preventing the formation of discrete features in the reflection component, as suggested by Homan et al. (2018) for the Z-source GX 5-1. However, it is even possible that the lack of coverage of the data at the lower energy leads to an inefficiency of the self-consistent model into the description of the reflection continuum. Further investigations on a broader energy band are

required to shade light about these hypothesis.

In the end, a weak hard tail above 30 keV was detected; it contributes for less than 1% to the total unabsorbed luminosity in the 0.1-100 keV energy range, both in NB and FB, probably for the absence of coverage of data at the highest energies . Contribution of the power-law around 10%-12% of the total luminosity for this source was rather observed by Di Salvo et al. (2006); D'Aí et al. (2007); Revnivtsev et al. (2014) in the 2-200 keV energy range, who showed a correlation between the intensity of the power-law and the position of the source in CD. The lack of a high-energy cut-off suggest a non-thermal origin for the hard tail (see e.g. Di Salvo et al. 2006, and reference therein), which could be the result of synchrotron emission from energetic electrons (Riegler 1970) or a Comptonisation of the soft seed photons on non-thermal electrons (Revnivtsev et al. 2014) or a non-thermal Comptonisation due to a bulk motion in the nearest of the NS (Farinelli et al. 2008; Ding et al. 2020). In order to distinguish between these models and find the correlation between the X-ray hard tail and the other spectral components, broad band observations with good statistics along the complete Z-track of the source are needed, especially with simultaneous radio coverage to eventually correlate it with strong outflows or jets.

Chapter 7

Decade-long analysis of spectral state changes in NS-LMXBs with *INTEGRAL*

S.M. Mazzola, E. Bozzo, C. Ferrigno, R. Iaria, T. Di Salvo (in preparation)

7.1 Introduction

As discussed in Chapter 3, NS and BH LMXBs are known to undergo remarkable spectral-state changes over time, often accompanied by significant variations in luminosity and triggered by substantial alterations in the mass accretion rate and/or in the accretion flow geometry. Generally, we distinguish among a soft spectral state (SS), where the continuum spectrum can be described by a (predominant) blackbody or disc-blackbody component plus a harder saturated Comptonised component, and an hard state (HS), where the continuum spectrum can be described by a weak (hardly detectable at times) thermal emission plus a power law with a high energy cut-off. In both the SS and HS, the Comptonised component can be explained as due to inverse Compton scattering of soft photons in a hot electron corona placed above the accretion disk and surrounding the accreting NS. The physical conditions of the corona are the main indicators of the spectral state in which the source is observed: in general, if an optically thick corona with low temperature (a few tens of keV) is present, the source is typically in the SS. On the other hand, if an optically thin corona with a high temperature (up hundreds of keV) is observed, the source is in the HS. Between the SS and the HS, there are a number of intermediate states, which remained so far particularly elusive and difficult to detect/identify.

Spectral state changes in BH-LMXBs are far better understood and studied than in NS-LMXBs. This is because they display periods of enhanced X-ray emission ("outbursts") when the spectral state changes occur, that are far brighter and more extended in time than those displayed by NS-LMXBs. Exhaustive reviews of the spectral states of BH-LMXBs (see e.g. Done et al. 2007; Belloni et al. 2011) have definitively shown how these sources recurrently follow a q-shaped spectral evolution during outbursts moving from an initial HS to a SS and then going back into an HS before going back to quiescence (where the X-ray emission is not or hardly detectable at best). In the case of NS-LMXBs, the first attempt to an exhaustive review of the spectral state changes was provided by Muñoz-Darias et al. (2014) using *RXTE* data. Studying a sample of 50 NS-LMXBs, the authors observed a cyclical behaviour from their hardness-intensity diagram (HID): ten of these sources presented indeed hysteresis pattern for the spectral transitions, evolving from an initial HS to a later SS and returning during the past phases of the pattern toward an HS. They observed the same cyclical behaviour from the rms-intensity diagram of these sources. Intermediate states can be identified during the transitions from HR to SS and viceversa, displaying broad-band spectral properties that are not fully typical of either the HS or the SS.

Although the *RXTE* data span a large baseline covering roughly 15 years, the typical exposure time of each observation is rather short (typically a few ks). We thus planned to complement the *RXTE* study by adding all possible information that we can retrieve on the long-term spectral state changes in NS-LMXBs by exploiting the entire *INTEGRAL* archive, in collaboration with the *INTEGRAL* Science Data Center (*ISDC*).

With the aim to obtain all possible information about long-term spectral variability of NS-LMXB sources, almost the entire available *INTEGRAL* data archive will be studied, taking into account all the observations (the so-called Science Windows, hereafter SCWs) performed between the revolution 0047 and 1998 of the satellite. The stated goal is to widen the study about the spectral variation of these sources by adding to the identification of the different spectral states also a characterisation of these states through fits with physical models on to the corresponding broadband spectra. Indeed, the huge amount of *INTEGRAL* data (collected from 2002 to 2018) allows to perform stacking of mega-seconds of observations to each state and offers an excellent monitoring for the persistent sources, that are the subject of our analysis.

To reach this purpose, an analysis chain was developed, in which the main steps are:

- build mosaics in different energy bands for the IBIS/ISGRI (Lebrun et al. 2003; Gros et al. 2003) and the two JEM-X (Brandt et al. 2003; Westergaard et al. 2003) instruments in order

to verify the detection significance of each source and examine the statistics and quality of the available data;

- identify and filter out all the X-ray Type-I bursts detected by the two JEM-X instruments which could artificially affect the hardness/softness of the source X-ray emission;
- extract the light-curves from the two JEM-X and IBIS/ISGRI in different energy bands, cleaned from the type-I bursts, and built different HIDs by using different combinations of the energy-resolved JEM-X and IBIS/ISGRI light-curves to optimize the signal-to-noise ratio (S/N) and ease the identification of different spectral states;
- stack all data from the same spectral state to obtain the JEM-X and IBIS/ISGRI broadband spectra with the highest possible S/N and test different models for the spectral fit of the data, with the aim to achieve an unified description for all sources.

In the following, I presents the developed analysis set-up and its application onto a sample of 21 sources, up to the spectral analysis of the source GX 17+2.

7.2 Data reduction

In order to exploit the entire *INTEGRAL* data archive, it is needed to create a catalogue that included all the sources of interest. Taking advantage of a dedicated Python 3.7 code (see Appendix B.1), the general *INTEGRAL* catalogue was compared with the SIMBAD Astronomical Database[1], obtaining a list of all persistent LMXBs observed by the satellite since the beginning of the mission. Thanks to this code, it was possible to study also the position of these systems with respect to the field of view, building a plot as a function of the right ascension (RA) and declination (DEC) coordinates (Figure 7.1). Then, it was clear that most of them are located at a mutual distance such as to be simultaneously in the field of view of the instruments during most of the observations (Figure 7.1). Therefore, for these sources (hereafter called "bulge sources" and listed in Table 7.1), a comprehensive list of observations was created, combining both the common and the uncommon ones, in order to process them in a single step and not repeat the data extraction of the same pointing more than once.

A protocol for the automatic search of Type-I X-rays bursts observed by the JEM-X modules was also developed, integrating a Python 3.7 code with the `burstsearcher` tool of the *INTEGRAL*

[1] `https://simbad.u-strasbg.fr/simbad/`

Table 7.1: Sample of persistent NS-LMXBs observed by *INTEGRAL* belonging to the identified bulge

Source ID	RA (deg)	DEC (deg)	IBIS/ISGRI_scws	JEM-X_scws	JEM-X1_bursts	JEM-X2_bursts
1H 1746-370	267.552750	-37.052280	19506	762	3	-
3A 1728-169	262.934040	-16.961360	9725	114	1	-
4U 1722-30	261.888540	-30.802060	20915	3774	55	62
4U 1735-444	264.742900	-44.450000	7993	364	6	13
4U 1916-053	289.699463	-5.238081	4580	144	-	2
Ginga 1826-24	277.3675	-23.796944	14337	424	15	2
GX 3+1	266.983300	-26.563600	20981	7198	150	128
GX 5-1	270.290545	-25.078925	20810	3162	128	60
GX 9+1	270.384600	-20.528900	18396	1335	58	61
GX 13+1	273.631460	-17.157420	10342	1034	-	1
GX 17+2	274.005787	-14.036283	7821	1059	13	36
GX 349+2	256.435382	-36.423069	15942	1087	45	41
GX 354-0	262.990540	-33.834030	21286	2855	228	157
H 0614+091	94.280400	9.136900	1272	296	-	-
H 1624-490	247.023042	-49.211118	8297	1663	-	-
H 1636-536	250.23125	-53.751389	7293	657	19	13
H 1702-429	256.563808	-43.035747	9609	1507	25	33
H 1705-440	257.226958	-44.102042	9215	1369	-	20
H 1820-303	275.919040	-30.361280	18058	761	10	24
LMC X-2	80.116830	-71.964810	3824	1255	-	-
SLX 1735-269	264.571330	-26.994060	20812	7094	4	41

The SourceID is the same reported in the updated *INTEGRAL* Catalogue.
The number of available SCWs and of the Type-I bursts per instrument were obtained using the developed Python routines.

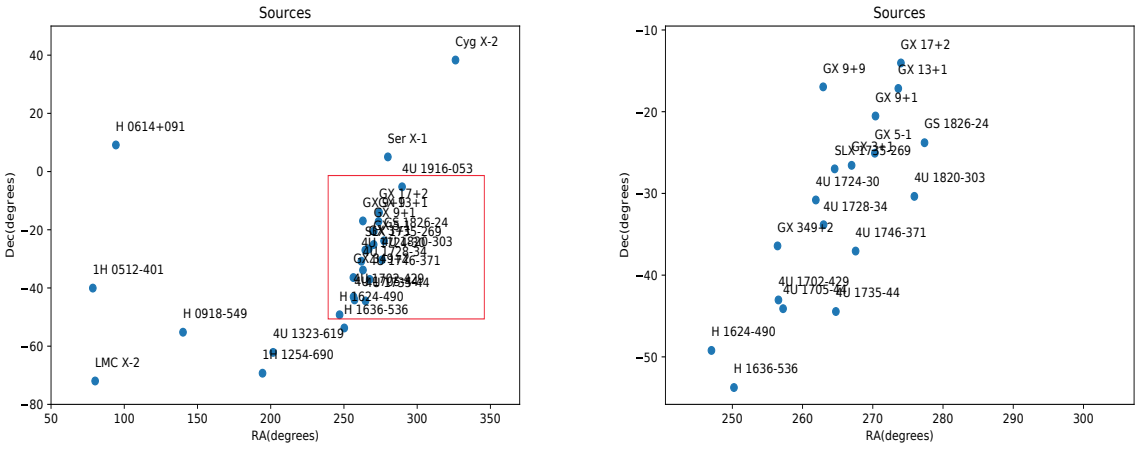

Figure 7.1: On the left: complete sample of persistent NS-LMXB sources observed by *INTEGRAL*. On the right: sample of sources for which the observations were grouped for the data extraction.

OSA 11.0 analysis software (Appendix B.2). Then, the information on the occurrence times of the bursts was obtained for each of the bulge sources and the corresponding good time interval (GTI) files was created, in order to exclude the time intervals at which each burst occurred from the analysis. The number of the bursts detected by JEM-X1 and JEM-X2 for each source is reported in Table 7.1. Subsequently, I used the `jemx_science_analysis` routine to extract the JEM-X data cleaned from bursts in the energy band 3-10 keV ("soft curve"), 10-20 keV ("hard curve") and 3-20 keV, adopting the `mosaic_spec` tool to estimate the flux and the associated error in the selected energy ranges and obtaining in the end the light-curves for each source.

In the same way, I extracted IBIS/ISGRI data using the `ibis_science_analysis` routine of the *INTEGRAL* OSA 10.2 release, deriving the value of the count rate in the energy range 25-40 keV ("soft"), 40-100 keV ("hard") and 25-100 keV from the imaging analysis level products obtained for each SCW (`isgri_sky_res.fits`, see Appendix B.3 and B.4), after checking out that `mosaic_spec` tool did not provide a correct value of the flux when the source was located at the edge of the field of view (FOV) of the instrument.

In order to check the calibration issues of the instruments, I performed the same analysis on the Crab data. I selected all the observation of Crab performed between the revolution 0046 and 1998 with a good observation time greater than 1000 s and within 12 and 3.0 degrees of off-axis for IBIS/ISGRI and JEX-X, respectively, avoiding the staring pointing. I extracted the long-term Crab light curves using a total of 1390 SCWs for IBIS/ISGRI and of 900 SCWs for both JEM-X modules,

respectively, and the same routines mentioned above. In the IBIS/ISGRI light curve (Figure 7.2, third panel), a decreasing in the count rate is observed after the revolution 1626 of the satellite, as expected (Savchenko et al. 2020). While, JEM-X data show a fairly large scatter, but the overall

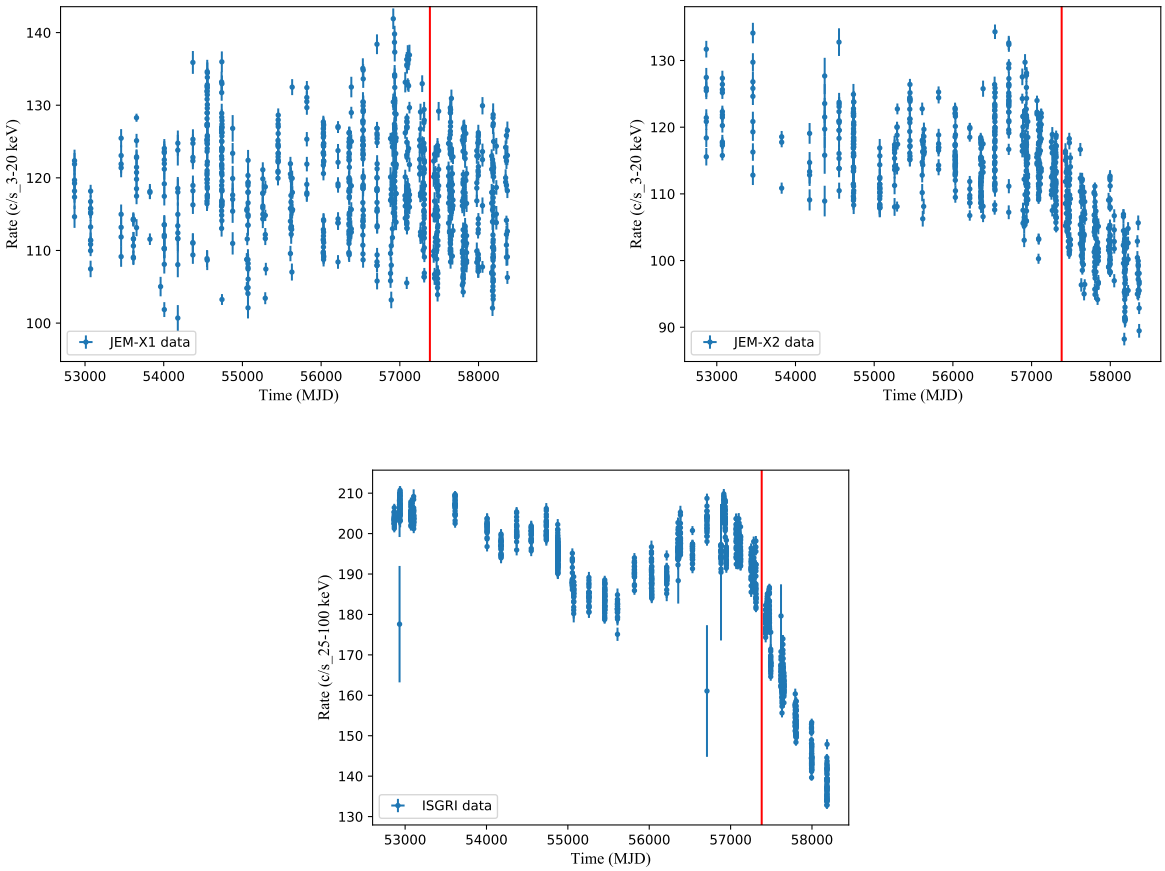

Figure 7.2: Crab light curves obtained in the 3-20 keV energy range for JEM-X1 and JEM-X2 data (first and second panel, respectively) and for IBIS/ISGRI data in the 25-100 keV energy range (third panel). Each point represents one SCW; the red line corresponds to the beginning of revolution 1626 of the satellite, corresponding to 57382 MJD.

trend is compatible with the intrinsic source variability; however, JEM-X2 light curve presents an anomalous decreasing trend after the revolution 1700 (second panel in Figure 7.2). For this reason, I built HIDs for both the JEM-X instruments and compared them, observing a large scattering of the points related to the SCWs collected after revolution 1700 for JEM-X2. Hence, these ones will be excluded from the analysis for all the sources, using only the observations performed before 57578 MJD which show a good agreement with the JEM-X1 data (see Figure 7.3).

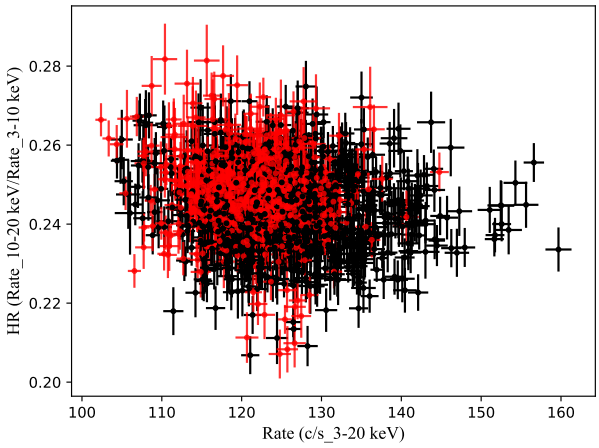

Figure 7.3: JEM-X combined HID of the source Crab obtained using a signal-to-noise rebinning factor of 50. The JEM-X2 data (red points) are related to the observations performed before revolution 1700 only; the JEM-X1 data are shown in black.

Moving forward, I built the HIDs of the sample of sources for each instrument, carrying out an adaptive rebinning on the light-curves in the soft and hard energy bands. The rebinning was performed using the tool developed by Dr. C. Ferrigno, called `timingsuite`, that builds a grid to rebin on the soft and hard curves and, then, plot the hardness ratio in function of the counts of the sum between the two curves. The main parameters on which the rebinning grid is calculated are

- the minimum signal-to-noise ratio (S/N) per channel: the program groups the data up to have a S/N ratio equal to at least this threshold;
- the maximum time interval (MTI) (in seconds) during which the data are grouped in order to reach the minimum S/N required. After that, if the S/N ratio obtained is lower than the threshold, the data collected up to that point are rejected;
- the minimum time binsize (in seconds) below which the data can not be accumulated (in this case it is always fixed at 0 s);
- the threshold GTI gap (TGG), i.e. maximum width (in seconds) of a time gap allowed to combine two consecutive data points. This parameter is used to manage the data gaps in the light curves (due, for example, to the satellite orbit) and to avoid the merging of data too far apart in time, that would result in a bin with a bad S/N. If during the collecting process

a gap greater than this threshold is encountered before the minimum S/N has been reached, the data grouped up to that point are rejected;

- the maximum noise-to-signal ratio allowed, useful to discard points with a bad S/N that would compromise the rebinning quality.

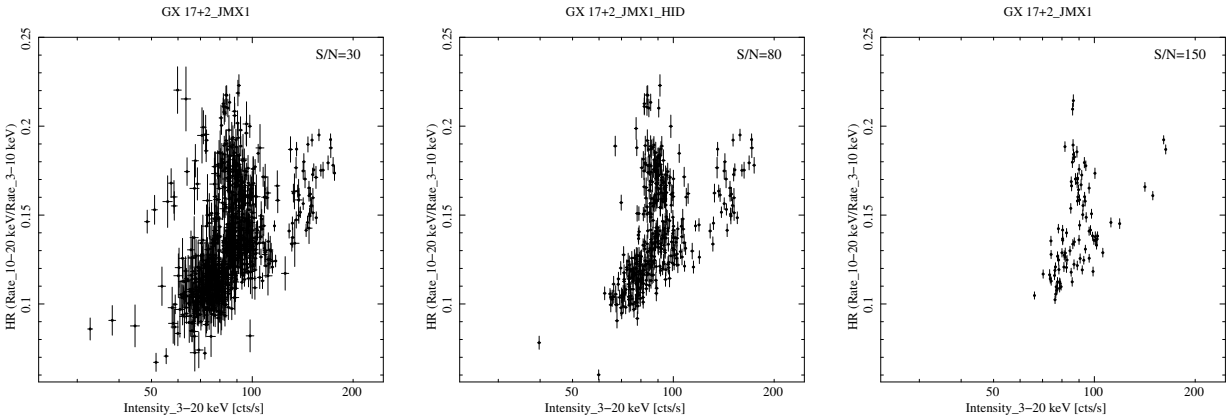

Figure 7.4: HID of the source GX 17+2 from JEM-X1 data obtained using signal-to-noise ratio values of 30 (left), 80 (central) and 150 (right) to rebin the light curves in the different energy bands.

These parameters have to be modified case to case, in order to obtain the best possible rebinning with the least data discarding for each source. The minimum S/N and the MTI, in particular, mainly influence the sampling. For example, to highlight low-flow data, it will generally be more useful to set a small S/N and a short sampling time (few hours); meanwhile, to distinguish (possible) groups of data relating to different spectral states, a high S/N may be useful (see e.g. Figure 7.4). Comparing the HID obtained using JEM-X and IBIS/ISGRI data, it can be noticed that the track shape is leaded by the former. This is pointed-out building the HID with combined JEM-X and IBIS/ISGRI data, suggesting that the sources show higher variability in the 3-20 keV energy range. To obtain this combined HID, I used the IBIS/ISGRI light-curve extracted in the 25-100 keV energy range as hard curve, and the JEM-X1 3-20 keV light-curve as soft curve, extracted from simultaneous observations (right panel in Figure 7.5). For this reason, the SCWs group selection will be performed on JEM-X data, using then the simultaneous IBIS/ISGRI observations for spectral extraction. Furthermore, I compared the HIDs obtained using the adaptive rebinning with those ones obtained using "raw" data, observing a good agreement between them for each source. This suggests us that the analysis is not particularly affected by the choice for the rebinning parameters.

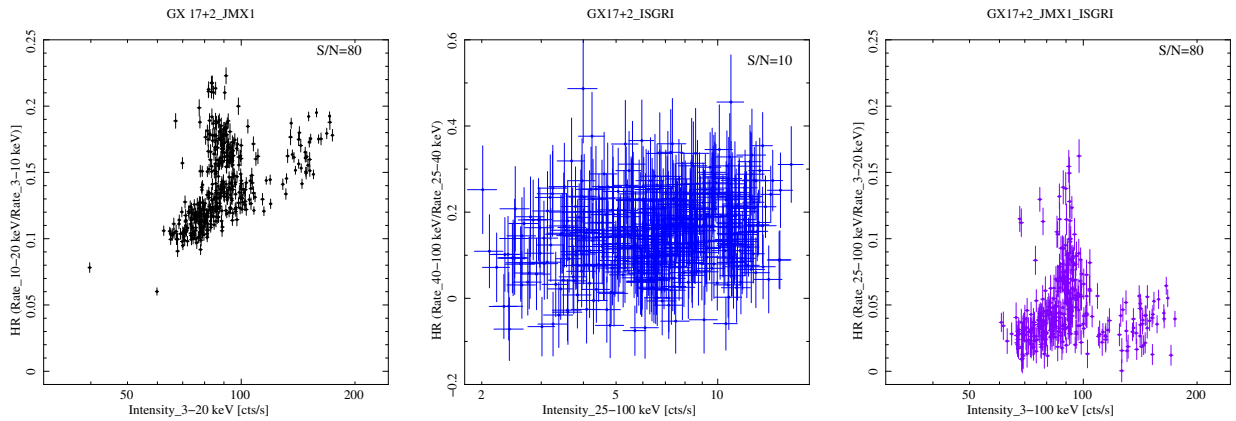

Figure 7.5: HID of the source GX 17+2 obtained from JEM-X1 (left panel) and IBIS/ISGRI (central panel) using a S/N rebinning factor of 80 and 10, respectively. The combined JEM-X1/ISGRI HID (right panel) was build using simultaneous observations of the two instruments.

Once built the HIDs, it is necessary to identify the groups of observations which can be combined for the spectral extraction. Relying on the idea that observations with similar HR and flux have similar spectral characteristics and shape (and then they are related to the same spectral state), I decided to use rectangular boxes to mark out the regions of the HIDs from which perform the data stacking. In order to avoid fluctuations due to calibration issues, a minimum size for the boxes was defined for each source, calculating the standard deviation of HR and intensity from the rebinned HIDs and re-scaling these values for those obtained from the HID of Crab produced using the same rebinning parameters chosen for the examined source. From the HID regions, it is possible to go up to the SCWs groups matching the rebinned light-curves with the non-rebinned ones, which contain the time information about the observations, and get the SCWs list for the spectra extraction (Appendix B.5).

7.3 Application: spectral analysis of the source GX 17+2

GX 17+2 is a bright Sco-like Z-source, that was discovered in the late sixties (Friedman et al. 1967). It exhibits Type-I X-ray bursts (Tawara et al. 1984; Sztajno et al. 1986), thanks to which Galloway et al. (2008) estimated a maximum distance of about 13 kpc. Using *EXOSAT* (Taylor et al. 1981) data, White et al. (1986) modelled the continuum of the spectrum with a blackbody at 1 keV and a power-law with a photon index $\Gamma \sim 0.6$ and a cut-off energy around 4.5 keV; a broad gaussian line at 6.5 keV was also detected. Hoshi & Asaoka (1993) studied the 1-20 keV

spectrum of the source observed in both the horizontal (HB) and normal branch (NB) with *Ginga* (Turner et al. 1989), noticing a decreasing of the blackbody temperature from the former to the latter. The first broadband spectral analysis was performed by Di Salvo et al. (2000), who analysed the 0.1-100 keV *BeppoSAX* (Boella et al. 1997) spectrum using a blackbody plus a Comptonisation component and discovering the presence of a transient hard tail with a non-thermal origin. Also Farinelli et al. (2005) exploited *BeppoSAX* observations to study the NB spectrum of the source, proposing two different models to explain the origin of the hard tail (a simple power-law and a hybrid thermal/non-thermal Comptonisation) which equally described the data. Meanwhile, Migliari et al. (2007a) showed a correlation between the radio emission and the presence of the hard tail using simultaneous radio/X-ray observations. Lin et al. (2012) analysed 68 *RXTE/PCA* (Jahoda et al. 1996) observations following the evolution of the accretion disc conditions along the Z-track. The authors fitted the data with a model composed of a blackbody and a disc-blackbody plus different semi-empirical models for the Comptonisation component, finding that a constant accretion rate over the three branches was in a good agreement with their results. Whilst Ding & Huang (2015) studied the transient hard tail by employing combined PCA and HEXTE (Rothschild et al. 1998) data, and pinpointed its origin to a possible bulk motion Comptonisation (see e.g. Paizis et al. 2006; Farinelli et al. 2007, 2008, 2009; Ding et al. 2011). In the end, Ludlam et al. (2017) analysed the NuSTAR (Harrison et al. 2013) spectrum of the source in its soft state, inferring a constraint on the inner radius of the accretion disc through spectral fits with several reflection models.

Here, I show the analysis performed on the all available *INTEGRAL* data of GX 17+2. Following the step-by-step method described above, I build the HID diagram for the two JEM-X and the IBIS/ISGRI instruments and carried-out the selection of the regions of the diagram used to perform the stacking of data for the spectral extraction. The combined JEM-X HID is shown in Figure 7.6, from which the same pattern of the Z-track obtained from *RXTE* data can be recognised (see e.g. Lin et al. 2012; Ding & Huang 2015); the data stacking regions are reported in the same figure, labelled from 1 (HB) to 10 (FB). I used the `jemx_science_analysis` and `ibis_science_analysis` routines until `SPE` analysis level to extract the spectrum of each SCW and then I applied the `spe_pick` tool to combine the spectra of the observations belonging to the same stacking region. The *INTEGRAL* OSA 11.0 release was employed for the spectra extraction of all JEM-X observations and IBIS/ISGRI observations collected after the revolution 1626 of the satellite, while the OSA 10.2 release was used for the former ones, as described in the instrument handbook (Savchenko et al. 2020).

The obtained JEM-X1, JEM-X2 and IBIS/ISGRI spectra were fitted simultaneously for each

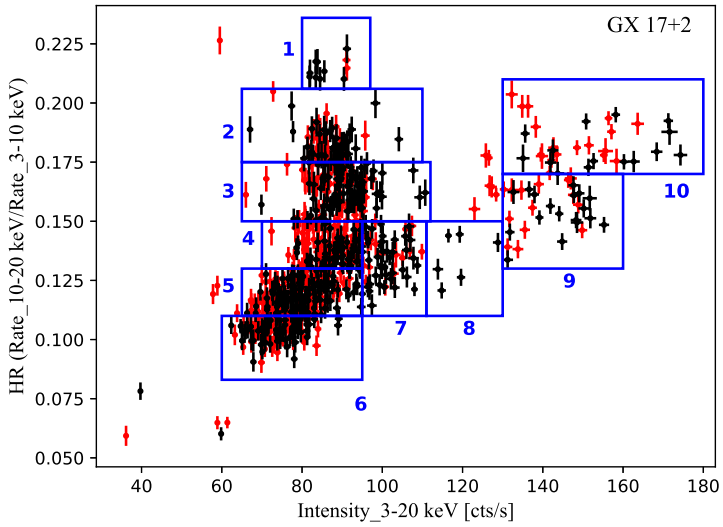

Figure 7.6: HID of GX 17+2 from combined JEM-X1 (black) and JEM-X2 (red) data obtained using a S/N=80 to rebin the JEM-X light curves of the source. The blue boxes identify the group of observations for the stacking; from each regions one spectrum for the data of each JEM-X module it is extracted, accordingly labelled.

region, using the 3-25 keV energy range for both JEM-X and the 20-100 keV energy range for IBIS/ISGRI. I used the XSPEC v12.9.1 to perform the spectral fits; the abundances and the photoelectric absorption cross-sections were set to the values found by Wilms et al. (2000) and by Verner et al. (1996), respectively, for all the spectra. Initially, I fitted the continuum direct emission of all spectra with a model composed of a blackbody component (BB, `bbodyrad` in XSPEC), a multi-colour disc-blackbody (MCD, `diskbb` in XSPEC) and a cut-off power-law (CPL) for the hard component, as reported by (Lin et al. 2012) . To take into account the photoelectric absorption by neutral matter in the ISM, I used the Tübingen-Boulder model (`TBabs` component); a gaussian line was added to fit the residuals around 6.6 keV. The line width was kept fixed to 0.4 keV (Lin et al. 2012; Ding & Huang 2015; Di Salvo et al. 2000), all the other spectral parameter were left free to vary. A systematic error between 2%-4% was applied to all the spectra.

However, the MCD is required only for the HB spectra (1 to 3) and the BB component is not significant for spectra 4, 5, 9 and 10 and results barely constrained in spectra 6 and 8. The best-fit models and results for each spectrum are reported in Table 7.2; the unfolded spectra and the corresponding residuals are shown in Figure 7.7.

Table 7.2: Best-fit results

		TBABS	GAUSSIAN		BBODYRAD		DISKBB		CUTOFFPL				
	N_spectrum	N_H $\times 10^{-22}$ cm^{-2}	E_{LINE} (keV)	$NORM_{LINE}$	kT_{BB} (keV)	$NORM_{BB}$	kT_{MCB} (keV)	$NORM_{MCB}$	Γ_{CPL}	E_{CPL} (keV)	$NORM_{CPL}$	F_{tot} ($\times 10^{-8}$ erg cm^{-2} s^{-1})	χ^2/d.o.f
HB	1	3.5 (frozen)	6.7 ± 0.4	0.015 ± 0.007	$2.89^{+0.14}_{-0.13}$	12 ± 3	1.7 ± 0.2	68^{+56}_{-29}	$2.3^{+0.5}_{-0.7}$	27^{+50}_{-12}	3 ± 2	2.01	40/48
	2	3.3 (frozen)	6.6 ± 0.2	0.021 ± 0.005	$2.87^{+0.8}_{-0.7}$	11 ± 2	1.8 ± 0.1	62^{+21}_{-15}	2.8 ± 0.3	49^{+146}_{-22}	5 ± 2	2.04	51/48
	3	3^{+2}_{-1}	6.4 ± 0.2	0.021 ± 0.005	2.82 ± 0.05	10 ± 1	$1.84^{+0.10}_{-0.08}$	68^{+18}_{-11}	$2.9^{+0.4}_{-1.0}$	> 21	4^{+6}_{-4}	2.05	73/49
NB	4	3.3 ± 0.5	6.4 ± 0.2	0.016 ± 0.005	-	-	-	-	1.21 ± 0.05	5.3 ± 0.1	5.3 ± 0.4	1.91	56/45
	5	4.0 ± 0.8	6.4 ± 02	0.028 ± 0.007	-	-	-	-	$1.19^{+0.07}_{-0.08}$	4.7 ± 0.1	5.6 ± 0.7	1.72	50/51
	6	3 ± 1	6.3 ± 0.1	$0.026^{+0.005}_{-0.002}$	$1.27^{+0.14}_{-0.08}$	84^{+78}_{-50}	-	-	$1.3^{+0.2}_{-0.3}$	5.0 ± 0.3	5 ± 2	1.60	78/49
	7	6 ± 1	6.8 ± 0.3	0.020 ± 0.007	$2.1^{+0.1}_{-0.2}$	12 ± 4	-	-	$1.7^{+0.3}_{-0.2}$	$6.5^{+0.8}_{-0.6}$	10^{+4}_{-3}	2.03	64/49
FB	8	3 ± 1	6.6 ± 0.4	$0.021^{-0.010}_{-0.009}$	3.1 frozen)	$3.4^{+0.5}_{-0.7}$	-	-	0.2 ± 0.4	$2.7^{+0.5}_{-0.3}$	3 ± 1	2.33	63/50
	9	3 ± 1	6.5 ± 0.3	$0.05^{+0.02}_{-0.01}$	-	-	-	-	0.5 ± 0.1	4.0 ± 0.1	3.6 ± 0.6	2.94	40/51
	10	2.3 ± 0.8	6.5 ± 0.3	0.04 ± 0.01	-	-	-	-	$0.40^{+0.08}_{-0.09}$	4.1 ± 0.1	3.0 ± 0.4	3.34	63/51

The uncertainties are reported at 68% confidence level.
F_{tot} is the observed total flux of the source in the 0.1-200 keV energy range.
A systematic error of 2% was applied for spectra 1,2,3,4,6 and 8, and of 3% for spectra 7, 9 and 10 and of 4% for spectrum 9.

The equivalent hydrogen column density N_H associated to the interstellar matter was kept fixed to the best-fit value for spectra 1 and 2 to led the fit to the convergence, while it was left free to vary in the other case, returning values compatible within each other and with results reported in literature within at least 2σ (see e.g. Di Salvo et al. 2000; Farinelli et al. 2005; Ding & Huang 2015).

A broad emission line associated with the fluorescence of ionised iron is also observed, with a centroid energy between 6.4-6.7 keV, as observed by Di Salvo et al. (2000); Ding & Huang (2015). Ludlam et al. (2016) interpreted this feature as the result of a reflection above an ionised accretion disc (see Brenneman & Reynolds 2006; Dauser et al. 2010, 2013, 2014; García et al. 2014, for the models discussed by the authors). Unfortunately, the spectral resolution of the JEM-X instruments does not allow a diagnostic of the line nor an estimation of the equivalent width.

The blackbody component is required in the HB spectra and for spectrum 7 (NB), whilst it represents only an upper limit for spectrum 8 (FB). In spectrum 6 (NB), it is unconstrained and its addition to the model is not significant (the F-test probability of chance improvement is 0.0688, corresponding to a significance less than 2σ). However, the presence of the component is necessary to well-fit the residuals below 10 keV and constrain the value of the hydrogen column density, hence I decided to include it in the best-fit model also in this case. Since the blackbody temperature in spectrum 6 is smaller almost by a factor of 2 with respect to those obtained for the other data sets, I explored the possibility the thermal component can be due to the accretion disc emission.

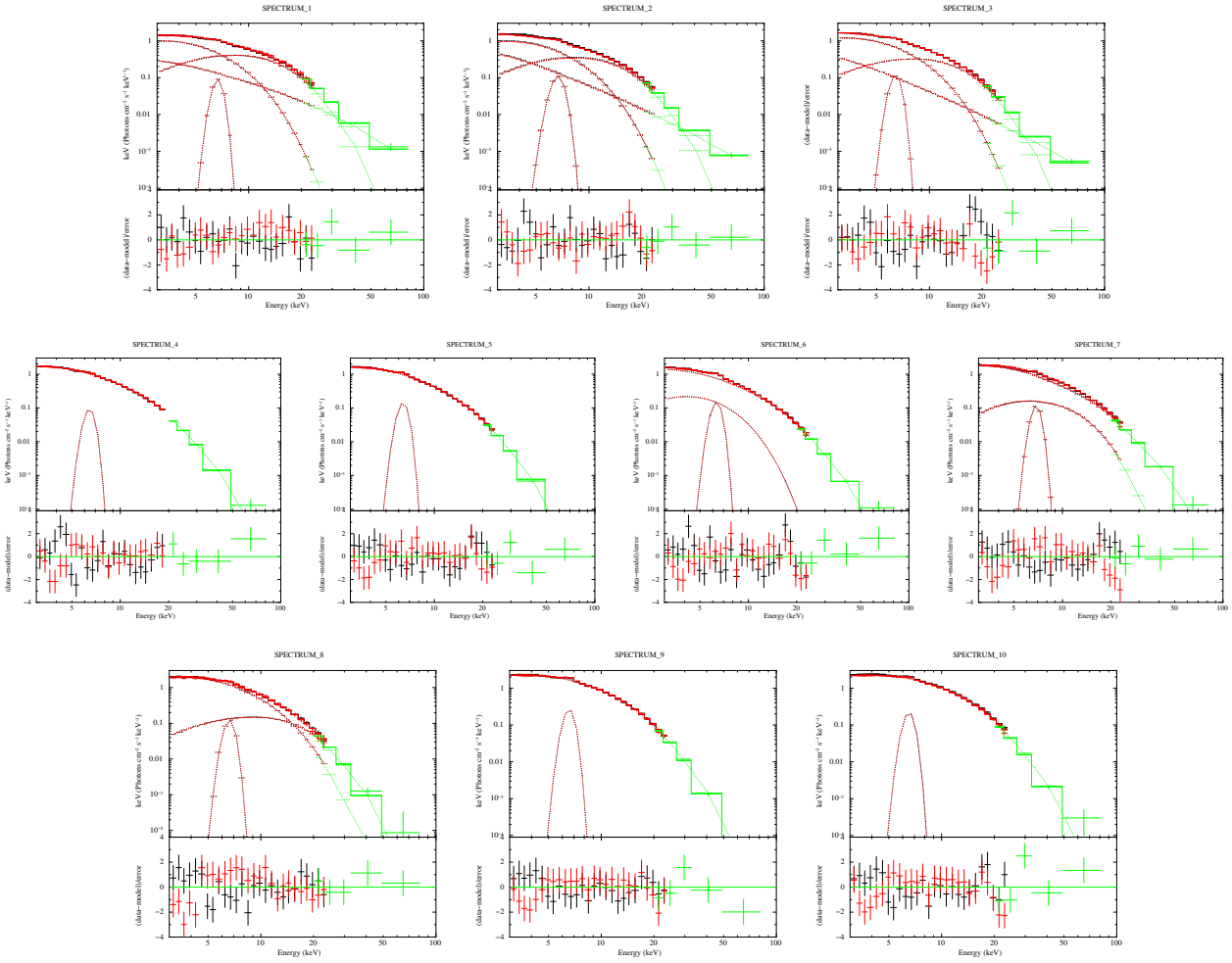

Figure 7.7: Unfolded spectra and corresponding residuals for HB (three top panels), NB (four central panels) and FB (three bottom panels). The JEM-X1, JEM-X2 and IBIS/ISGRI data are showed in black, red and green colour, respectively.

I substituted the BB component with a MCD, obtaining a temperature $kT_{\rm MCD} = 1.7^{+0.2}_{-0.1}$ and a normalisation parameter of 33^{+31}_{-21}, but any changes were not observed in the value of the $\chi^2/d.o.f.$ (79/48) nor in the values of the other best-fit parameters, suggesting that it is not possible to distinguish between this two components. The blackbody radius was estimated for all the spectra assuming a distance to the source of 12.6 kpc (Ding & Huang 2015; Galloway et al. 2008). Using the best fit parameters, it is obtained $R_{\rm BB} = 4.3 \pm 0.6$ km for spectrym 1, 4.1 ± 0.4 km for spectrum 2, 4.0 ± 0.3 km for spectrum 3, 11 ± 2 km for spectrum 6, 4.4 ± 0.7 km for spectrum 7 and $R_{\rm BB} < 2.3$ km for spectrum 8. In the other cases (spectra 4,5,9 and 10), an upper limit on this radius was evaluated adding a BB component to the fit model with temperature kept fixed to 2.8 keV, accordingly with those obtained from HB spectra and assuming it reaches compatible values along the Z-track (Lin et al. 2012; Ding & Huang 2015); it is found $R_{\rm BB} < 1.4$ km. For the HB

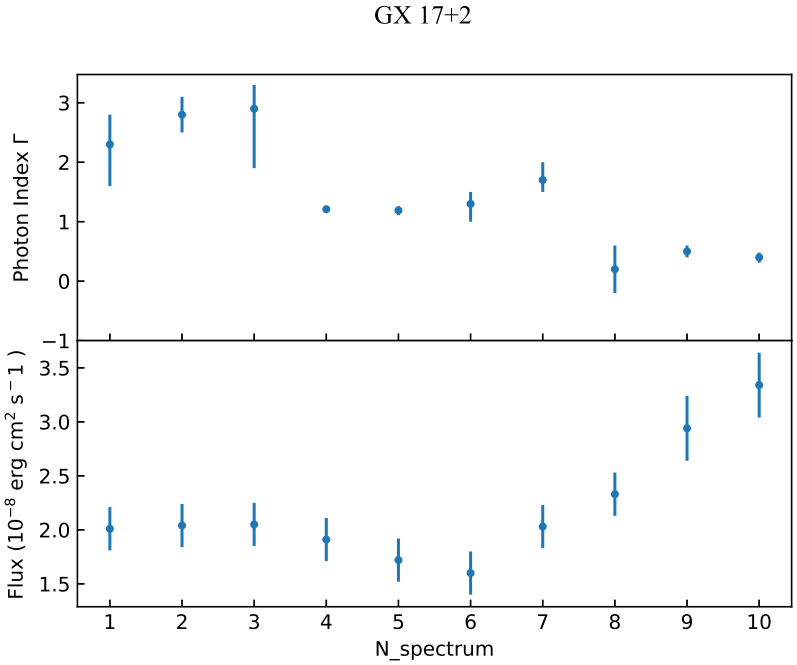

Figure 7.8: Variation of the photon index Γ (top panel) and the 0.1-200 keV observed flux (lower panel) along the Z-track. A 10% error was associated to the flux values. On the x-axis the labels of the group spectra are reported.

spectra, the inner disc radius was estimated also, using the relation with the normalisation of MCD component $NORM_{\rm MCD} = (R_{\rm MCD}/D_{10})^2 \cos\theta$, where D_{10} is the distance to the source in units of 10 kpc and θ is the inclination angle of the system with respect to the line of sight. Assuming

again $D = 12.6$ kpc and $\theta = 30°$ (Ludlam et al. 2017; Cackett et al. 2010, 2012), $R_{\rm MCD}$ results 11^{+5}_{-2} km for spectrum 1, 11^{+1}_{-2} km for spectrum 2 and 11 ± 1 km for spectrum 3, in agreement to those obtained by Ludlam et al. (2017).

It can be noticed that the photon index Γ associated to the hard component decrease along the Z-track fron HB to FB (see Figure 7.8), in which assumes values much lower than 1, as observed by Ding & Huang (2015). The cut-off energy $E_{\rm CPL}$ obtained for NB and FB spectra is compatible within 3σ to those reported by Ding & Huang (2015), following a downward trend; meanwhile the highest values inferred for the HB spectra suggest the presence of a hard tail with a possible non-thermal origin, as proposed by Di Salvo et al. (2000). Hence, I substituted the CPL component in spectra 1, 2 and 3 with a simple power-law (PL), adding a roll-off through the `expabs` component, in order to mimic a cutoff at the lower energy, keeping fixed the low energy cut-off to the MCD temperature $kT_{\rm MCD}$. It returns equivalent results for the best fit parameters and the residuals, with a contribution of the PL flux to the total flux of the source in the 0.1-200 keV energy band between 20%-25%, in accordance with the results of Ding & Huang (2015). Therefore, it can be conclude that CPL and PL are exchangeable and provide a description in agreement with the hypothesis of a hard component of non-thermal origin predominant in the HB, as observed for other Z-sources (see e.g. Di Salvo et al. 2000; Psaltis 2001; Iaria et al. 2001a; Di Salvo et al. 2001; Farinelli et al. 2005; Di Salvo et al. 2006; Paizis et al. 2006; D'Aí et al. 2007; Revnivtsev et al. 2014; Reig & Kylafis 2016).

In the end, the performed analysis allowed to follow the source along the Z-track. The spectra extracted from the different region of the HID show the same characteristics expected from the literature in all the branches, suggesting that the data stacking, even collected 15 years apart, provide a good description of the spectral evolution of the source.

Hardness-Intensity Diagrams

Figure 7.9: HIDs of bulge sources sample from combined JEM-X1 (black) and JEM-X2 (red) data. The S/N value used for the rebinnining is reported for each source.

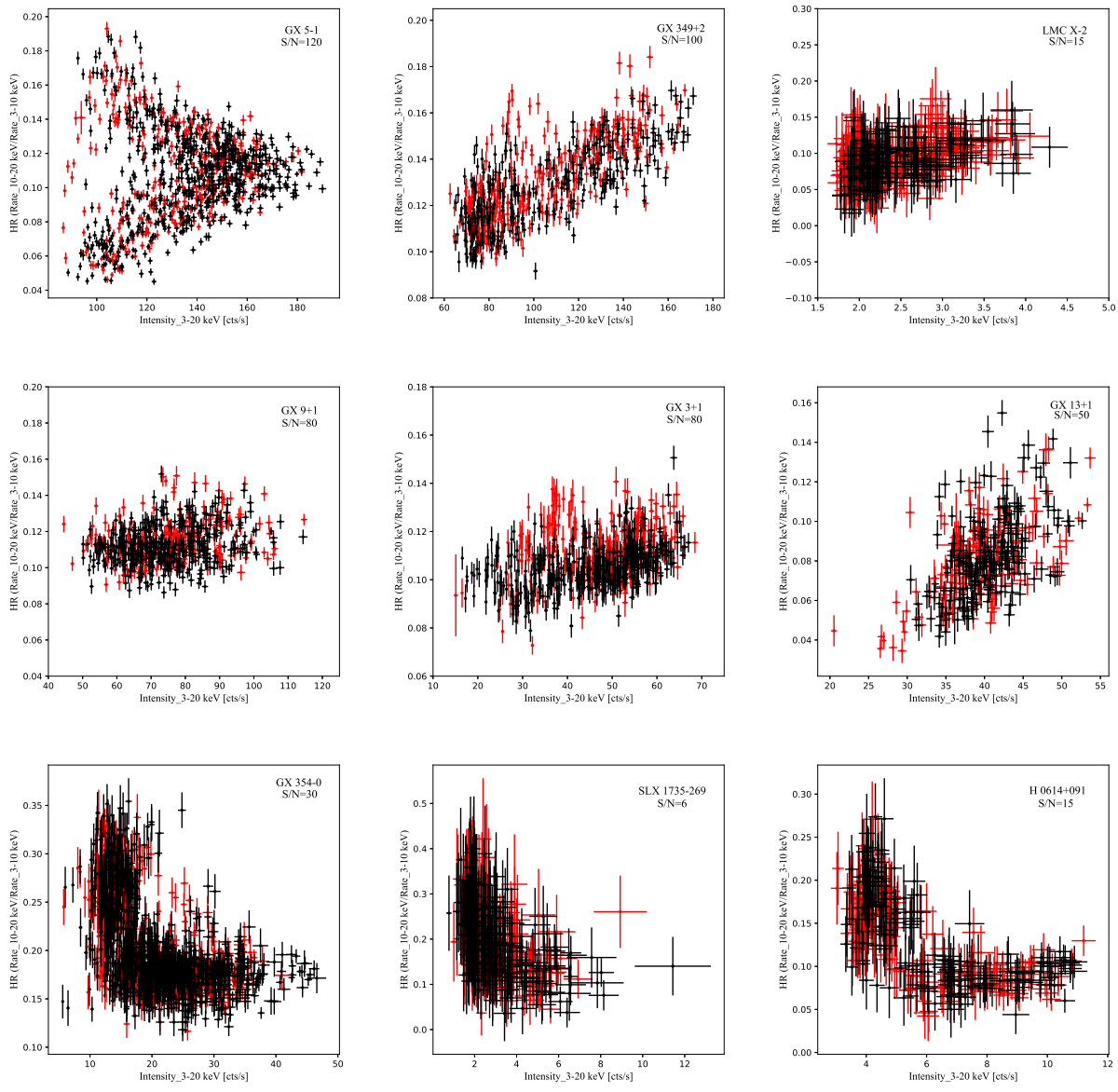

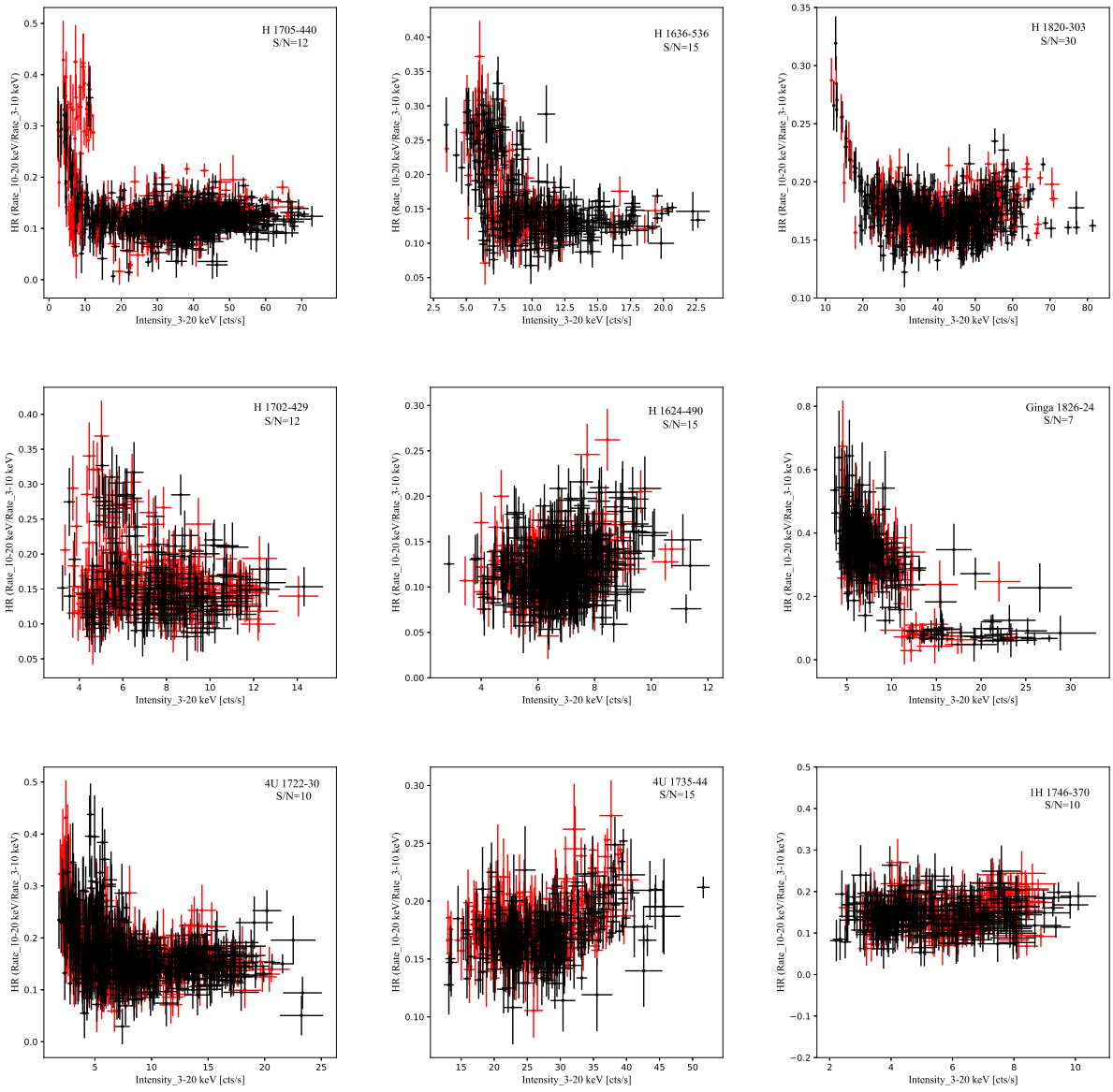
H 1705-440
S/N=12
H 1636-536
S/N=15
H 1820-303
S/N=30
H 1702-429
S/N=12
H 1624-490
S/N=15
Ginga 1826-24
S/N=7
4U 1722-30
S/N=10
4U 1735-44
S/N=15
1H 1746-370
S/N=10
HR (Rate_10-20 keV/Rate_3-10 keV)
Intensity_3-20 keV [cts/s]

Conclusion

The subject of this thesis is the study of the spectral and timing properties of several LMXB systems hosting a weakly magnetised neutron star. The orbital timing analysis of the eclipsing source XB 1822-371 and the spectral analysis of the atoll source 4U 1702-429 and of the Z-source Sco X-1 were presented. The results, summarised in the following, added some useful pieces to understand the complex puzzling scenario of these sources.

The analysis of the compact eclipsing binary X 1822-371 allowed to updated the orbital ephemeris of the source, by adding two eclipse arrival times obtained from the *RXTE/PCA* observations performed in 2011 and from the *XMM-Newton/Epn* observation performed in 2017, covering a baseline of almost 40 year. Fitting the delays with a quadratic model, an orbital period $\dot{P}_{\rm orb}$=1.475(54) $\times$ 10^{-10} s s^{-1} and a $\dot{P}_{\rm orb}$ value of 1.475(54) $\times$ 10^{-10} s s^{-1} have been estimated, accordingly with the values found in literature. We explored also the possibility that a cubic model could improve the fit of the delays, but the addition of a cubic term to the quadratic model is not significant. Alternatively, the possibility that a large sinusoidal modulation, associated to the gravitational quadrupole coupling (GQC) between the orbit and the changes of the quadrupole moment of the magnetically active companion star (Applegate 1992), could mimic the quadratic trend of the delays was investigated. The obtained results seemed to exclude that this coupling between the orbit and the changes in the oblateness of the companion is triggered by the luminosity of the companion star itself. However, the GQC mechanism via tidal interaction (Applegate & Shaham 1994) also predicts a parabolic trend of the delays over which a small modulation with a period of 3.4 $\pm$ 1.2 yr and an amplitude of 34 $\pm$ 12 s is superimposed. In other words, both the quadratic model and the GQC mechanism via tidal interaction require a large outflow of mass, several times the Eddington limit, from the system. This confirm the scenario of a super-Eddington mass transfer rate for X 1822-371, where most of the transferred mass is expelled from the system by the X-ray radiation pressure and only a fraction of it accretes onto the neutron star (see e.g.

Iaria et al. 2013).

A detailed broadband spectral analysis of the source 4U 1702-429 was performed in the 0.3-60 keV energy range using an *XMM-Newton/INTEGRAL* observation and studying separately the data of three observations collected by *BeppoSAX* in the 0.1-100 keV energy range. Using a self-consistent reflection model, it was found that the reflection fraction and the ionisation parameter of the reflection component are incompatible between the *XMM-Newton/INTEGRAL* spectrum and the *BeppoSAX* observations. Furthermore, an optically thin electron cloud with an electron temperature larger than 30 keV was observed in the *BeppoSAX* spectra , while a colder ($\sim$3 keV) optically thick corona is present in the *XMM-Newton/INTEGRAL* spectrum. In addition, the total unabsorbed bolometric flux is only twice larger in the case of the *XMM-Newton/INTEGRAL* observation with respect to *BeppoSAX* observations.

In the *XMM-Newton/INTEGRAL* spectrum the presence of three emission lines due to the fluorescence emission from Ar XVIII, Ca XIX, and Fe XXV, and two absorption edges due to the presence of O VIII and Fe XXVI in the accretion disc were detected. In conclusion, the best-fit parameters describe a physical scenario of a source in a hard state (HS) for the *BeppoSAX* observations, whilst the *XMM-Newton/INTEGRAL* spectrum could be associated with a soft state (SS). The inner radius of the accretion disc seems to be smaller in the HS (i.e. the disc is closer to the NS surface). This is probably due to the presence of an optically thinner corona than in the HS case, which allows to observe the emission from the innermost region of the system. In particular, a higher contribution from the boundary layer near the NS surface can be observed in HS, and it is shielded instead from the optically thicker corona during SS. This suggests that the thermal component in SS is probably well-fitted by a multi-colour disc-blackbody, while two blackbody components might be a better description of the soft component in HS: the first one to describe the accretion disc emission and the second one for the boundary layer emission (see e.g. Armas Padilla et al. 2017).

In order to study the spectral emission of the ultra-bright Z-source Sco X-1, the 3-60 keV spectrum collected by *NUSTAR* in 2014 was analysed. From the colour-colour diagram of this observation, the spectrum of the normal branch and the flaring branch of the track were separated. Both the spectra were fitted using a model composed of a blackbody component, a thermal Comptonisation and a power-law component, absorbed by the ISM at the lower energies. It is observed a blackbody temperature of 1.26 ± 0.02 keV and $1.50^{+0.02}_{-0.03}$ keV in NB and FB, respectively, and a Comptonising corona with and electron temperature $kT_{\rm e} = 2.88 \pm 0.04$ keV and optical depth $\tau = 9.8 \pm 0.2$ in NB, and $kT_{\rm e} = 2.94 \pm 0.06$ keV and $\tau = 9.6 \pm 0.2$ in FB. For the seed photons temperature $kT_{\rm bb}$ an

upper limit of 0.35 keV in NB and of 0.37 keV in FB was obtained. Alternatively, a good fit was represented by a model in which the thermal component is provided by a multi-colour blackbody. From this one, a disc-blackbody temperature $kT_{\rm in}$ of 0.43 ± 0.03 keV and of $0.60^{+0.04}_{-0.03}$ keV in NB and FB, respectively, was inferred and a seed photons temperature $kT_{\rm bb} = 0.84 \pm 0.02$ keV in NB and equal to $1.15^{+0.03}_{-0.02}$ keV in FB is found. For the NB spectrum the electron temperature $kT_{\rm e}$ is $3.1^{+0.05}_{-0.03}$ keV and $\tau = 7.58 \pm 0.09$; while in FB $kT_{\rm e} = 3.20^{+0.05}_{-0.10}$ keV and $\tau = 6.2 \pm 0.3$.

In both the cases, two Compton broadened emission lines were detected at 6.6 keV and 7.8 keV corresponding to the the Kα and Kβ transition of He-like Fe XXV ion. The detection of the Fe kα line is significant in both the CD branches, while the Fe Kβ line seems to be less important in the flaring branch. A reflection component seems to be not required to model these features. The presence of a power-law with a photon index between 2 and 3 is needed for both the models, despite the associated parameters are not well-constrained. The power-law is very weak and contributes to the total flux for $\lesssim$1% in both the branches.

To conclude, the two models depict equivalent physical scenarios for the source, with a softening of the spectrum between the normal and the flaring branch.

In the end, the analysis method developed for the long-decade study of the *INTEGRAL* data archive of persistent NS-LMXBs was presented. The created routines allowed to compile a catalogue of the interested sample of sources, to identify the Type-I X-ray in their light-curves and exclude them, and to build the hardness-intensity diagram (HID) of each source. A technique to select the group of observations from different region of the HID and perform the stacking of data to obtain the source spectra in different state was also set up during the work carried out in the writing of this thesis.

This allowed to follow the evolution of the Z-source GX 17+2 along its HID track, obtaining 10 different spectra which cover the horizontal, normal and flaring branches. The hard component of these spectra was modelled with a cut-off power-law, with a photon index value decreasing from the horizontal to the flaring branch. The presence of a hard tail with (possible) non-thermal origins was pointed-out in the spectra belonging to the horizontal branch. The obtained results are in agreement with the previous analysis of the source, suggesting that the data stacking of observations, even collected 15 years apart, is a powerful analysis method which provide a good description on the spectral characteristics of the source. It gives a clue that cyclical behaviour of these sources represents a good base scenario on which a unified picture of their spectral evolution can be drawn.

Appendix A

Instrumentation

A.1 BeppoSAX

The Italian-Dutch satellite *BeppoSAX* (Satellite per Astronomia X, named "Beppo" in honour of the Italian physicist Giuseppe Occhialini) was launched from Cape Canaveral on April 30, 1996 and ended the mission in 2002, after allowing to discover hundreds of X-ray sources.

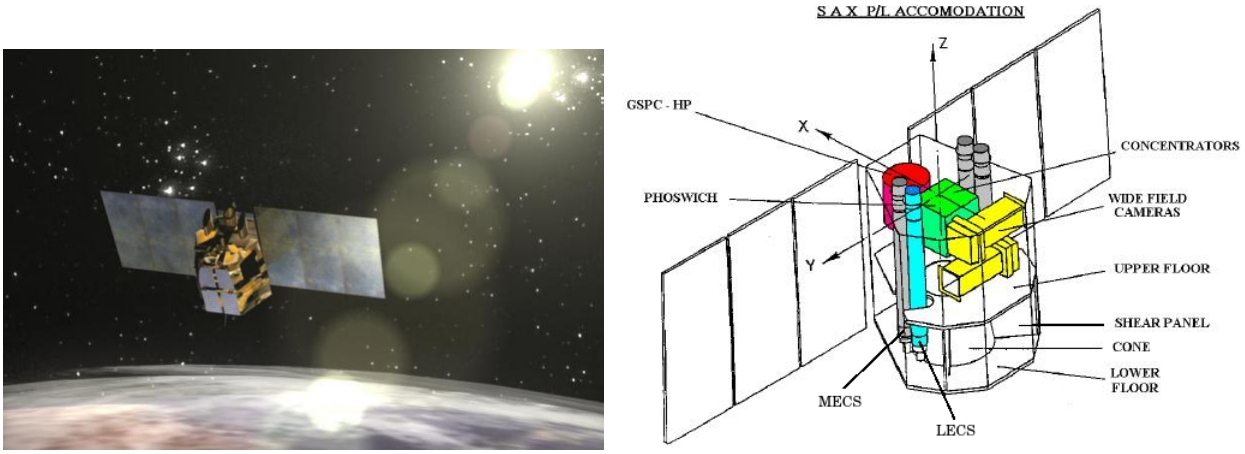

Figure A.1: On the left artistic representation of *BeppoSAX* satellite in orbit around the Earth (Orbiter 2016). On the right:*BeppoSAX* payload configuration (in 't Zand 1999).

It was the first X-ray satellite capable to observe a much wider energy range (0.1 - 200 keV), with a relatively large collection area, a good energy resolution and an imaging capability of $1'$ in the range 0.1-10 keV. A focusing telescope was mounted on the satellite: it was composed of four modules of 30 nested conic mirrors (realised with the replication technique using electroformed nickel) in an

approximation of Wolter-I geometry. It was equipped of 6 narrow fields instruments (NFIs) and two Wide Field Cameras (WFI) (Jager et al. 1989, 1997), i. e. coded mask proportional counters capable of monitoring large regions of the sky with a resolution of 5' in the range 2-30 keV and to detect transient X-ray phenomena.

NFIs were co-aligned on the axial plane of the satellite and pointed to the same object. The Low-Energy Concentrator Spectrometer (LECS, operating in the range 0.1-10 keV; Parmar et al. 1997) and the Medium-Energy Concentrator Spectrometer (MECS, 1.3-10 keV; Boella et al. 1997) were gas scintillator proportional counter, located on the focal plane of the telescope. They had imaging capabilities with fields of view (FOV) of $20'$ and $30'$ radii, respectively. While the High-Pressure Gas Scintillator Proportional Counter (HPGSPC, 7-60 keV; Manzo et al. 1997) and Phoswich Detector System (PDS, 13-200 keV; Frontera et al. 1997) were non-imaging instruments, with a FOVs of $\sim 1^{\circ}$ FWHM delimited by rotating collimators. The features of each NFI are summarised in Table A.1.

Table A.1: Characteristics of BeppoSAX NFI

Instrument	Energy Range keV	Pos. Res. arcmin	Eff. Area cm^2	Time Res. μs	Energy Res. $\%FWHM$
LECS	0.1 - 10	$1.6 \times (E/6)^{1/2}$	20 at 0.28 keV 38 at 1 keV 56 at 2 keV 50 at 6.4 keV 27 at 9 keV	>16	$8 \times (E/6)^{1/2}$
MECS	1.3 - 10	$1.4 \times (E/6)^{1/2}$	110 at 2 keV 150 at 6.4 keV 70 at 9 keV	16	$8 \times (E/6)^{1/2}$
HP-GSPC	3 - 120	collimated	200 at 6 keV 240 at 60 keV	15	$4 \times (E/60)^{1/2}$
PDS	15 - 300	collimated	600 at 20 keV 500 at 60 - 100 keV 140 at 200 keV	16	$16 \times (E/60)^{1/2}$

A.2 XMM-Newton

The X-ray Multi-Mirror satellite (*XMM-Newton*, Jansen et al. 2001) was launched on December 10, 1999 and it recently celebrated 21 years of activity. It follows a highly eccentric orbit, travelling out to nearly one third of the distance to the Moon (7×10^3 km at the peregree and 114×10^3 km at the apogee), allowing to make very long and uninterrupted observations.

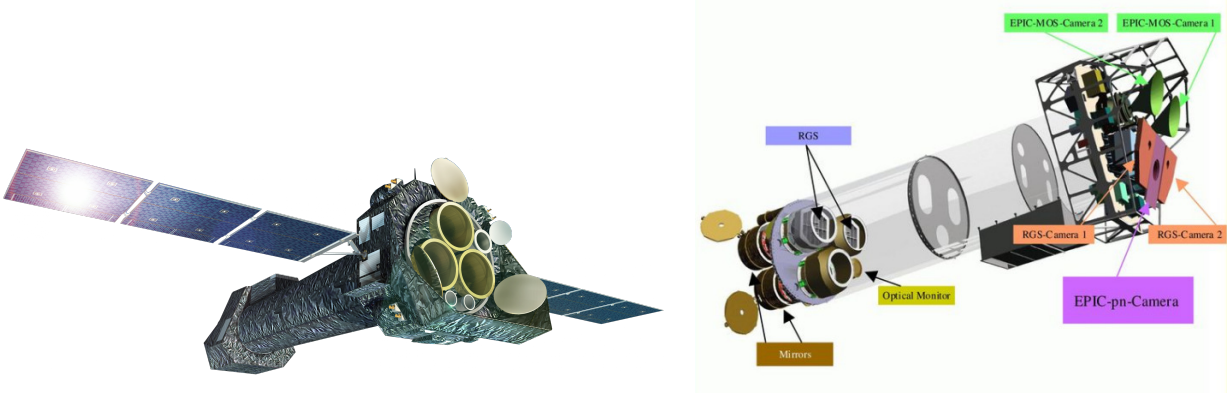

Figure A.2: On the left: artist's impression of the *XMM-Newton* spacecraft (credits: ESA). On the right: schematic payload of the *XMM-Newton* spacecraft (Kirsch 2006).

XMM-Newton carries three advanced X-ray telescopes, each one composed of 58 Wolter-I grazing-incidence mirrors nested in a coaxial and cofocal configuration to obtain the largest possible collecting area (13×10^3 cm^2 at 2 keV and 10×10^3 cm^2 at 6 keV, Lumb 2012).
The main focal plane instrument on-board *XMM-Newton* is the European Photon Imaging Camera (EPIC). It consists of three cameras, located at the prime focus of each telescope, which employ charge-coupled devices (CCDs) to perform imaging and spectroscopy over the 30 arcmin FoV in the 0.15-15 keV energy range, with spectral resolution $E/\Delta E \sim$ 20-50 and angular resolution about 6 arcsec FWHM (XMM-Newton Users Handbook, ESA: XMM-Newton SOC 2020). Two of the cameras use metal oxide semi-conductor CCDs (MOS Turner et al. 2001), consisting of seven silicon chips (600×600 pixels matrix each one) responsive to the soft part of the X-ray spectrum. Meanwhile, the third camera has pn detector (Epn Strüder et al. 2001) with a 36 cm^2 sensitive area (400×384 pixel matrix) and covers the upper part of X-ray spectrum. The EPIC cameras allow several modes of data acquisition:

- full frame, in which all pixels of the CCDs are read out and thus the full FoV is covered;
- partial window, in which two option are available: *small window* or *large window* mode; in

both the the cases only a part of the CCDs pixels is read out;

- timing, in this mode the imaging is made only in one dimension, along the column axis. The collapsing of the collected data into a one-dimensional row allows a high speed reading out, resulting in a time resolution of about 10^{-3} s for MOS and 3×10^{-5} s for Epn.

Furthermore, for the correct operation of the EPIC camera, the EPIC Radiation Monitor (ERM) has the task of detecting the solar flares in order to supply particle environment information.
The Reflection Grating Spectrometers (RGS, den Herder et al. 2001) are included on two of the three *XMM-Newton* X-ray telescopes. These consist of the Reflection Grating Arrays (RGAs), containing 182 identical gratings, located in the in-plane in which the incident and diffracted X-rays are perpendicular to the grating grooves, and the RGS Focal Cameras (RFCs), composed of nine back illuminated MOS chips which the dispersed spectrum is integrated on (Lumb 2012). RGS provides X-ray spectroscopy over the 0.35-2.5 keV energy range with spectral resolution $E/\Delta E$ from 200 to 800.
The third instrument aboard *XMM-Newton* is an optical/UV telescope, the Optical Monitor (OM, Mason et al. 2001). This 2-metre long telescope is mounted on the mirror support platform, alongside the X-ray mirror modules. Since it can observe simultaneously the same regions as the X-ray telescopes in the UV and blue part of the visible spectrum, this gives complementary data about the detected X-ray sources.

A.3 INTEGRAL

The Intrnational Gamma-Ray Astrophysics Laboratory (*INTEGRAL*) was launched on October 17, 2002 and it is still operational. It follows an elliptical orbit between 104 km and 150×10^3 km with an orbital period of ∼72 hrs. It was designed to produce a complete map of the sky in the hard X–ray/soft gamma–ray band and it is capable to perform simultaneous observations in different energy bands. The on-board instruments include two imaging detectors (which employ a coded mask telescope), a spectrometer and a monitoring camera.

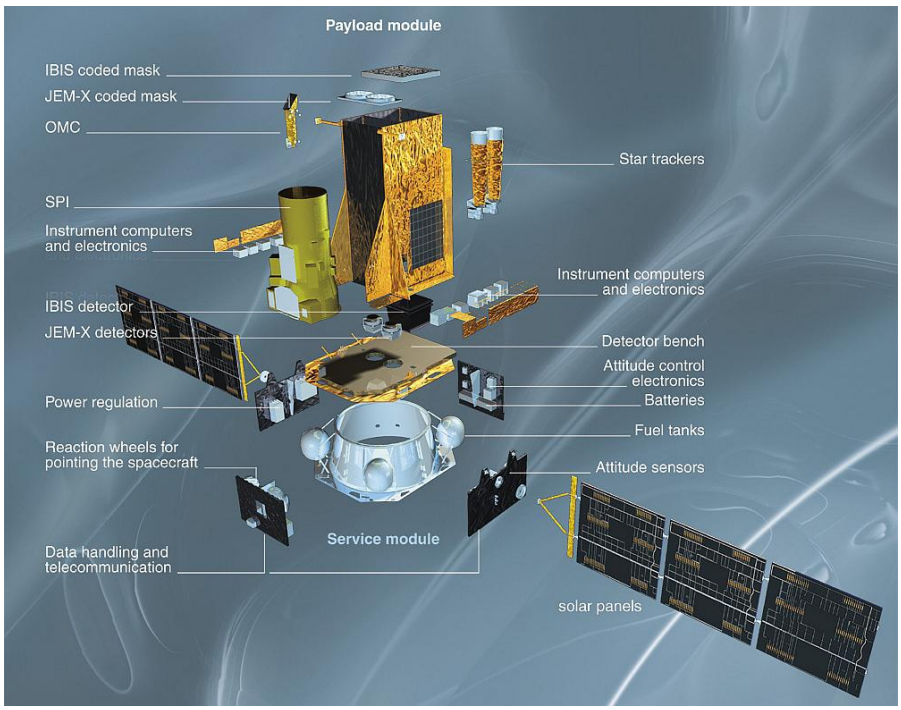

Figure A.3: *INTEGRAL* payload configuration (credits: ESA 2002).

The Imager on Board the *INTEGRAL* Satellite (IBIS, Ubertini et al. 2003) is a coded aperture mask telescope sensitive to the 15 keV - 10 MeV energy range. The detector assembly has two position-sensitive detection planes and a total FoV of $29.1^\circ \times 29.4^\circ$. On the front layer is located the IBIS Soft Gamma-Ray Imager (ISGRI, Lebrun et al. 2003; Gros et al. 2003), a solid-state detector, operating in the 20-500 keV energy range with an effective area of 2600 cm^2; while on the back layer, the Pixellated Imaging Caesium Iodide Telescope (PICsIT, Di Cocco et al. 2003) is composed of CsI(Tl) scintillator pixels with a 170 keV - 10 MeV pass-band. The separation between the two detecting planes is such that IBIS can also work as a Compton telescope; meanwhile an

anti-coincidence shield encases the detector. The coded mask is located 3.2 m above the collimated detection plane, providing an angular resolution of 12 arcmin, and it is responsible of the so-called indirect imaging. The coded mask, indeed, is composed of a grid of square elements, some of which are opaque to the incident radiation, according to a specific pattern (called MURA). Then, a shadowgram of the observed sources is created, which represents the bidimensional distribution of the emitting objects. In the end, thanks to a cross-correlation operation through a decoding mask specific for each MURA, an image of the sources in the FoV is obtained.

The Joint European X-Ray Monitor (JEM-X, Brandt et al. 2003; Westergaard et al. 2003) supplements the main INTEGRAL instruments providing the imaging for the soft X-ray sources. It is composed of two identical High Pressure Microstrip Chamber (HPMC) detectors and works in the 3-35 keV energy band with an angular resolution of ~ 3 arcmin. Each JEM-X module views the sky through its coded aperture mask located at a distance of approximately 3.2 m above the detection plane.

The Optical Monitoring Camera (OMC, Mas-Hesse et al. 2003) consists of a passively cooled CCD (1024 x 1024 pixels imaging area) located in the focal plane of a 50 mm diameter lens with a V-band filter. It is designed to support JEM-X observations in order to investigate the presence of an optical counterpart of the detected sources.

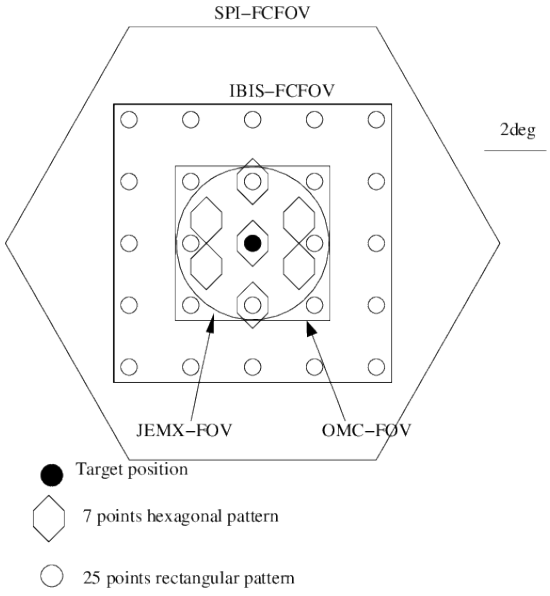

Figure A.4: Dither patterns for *INTEGRAL* (Courvoisier et al. 2003).

The Spectrometer on *INTEGRAL* (SPI, Vedrenne et al. 2003) consists of an hexagonal matrix array

of 19 cooled Germaniun photo-diodes detectors, surrounded by an active anti-coincidence shield. It operates in the 20 keV - 8 MeV energy band with an angular resolution of 2.5° (FWHM) in the 16° FoV. The Tungsten coded mask is circular with 127 hexagonal pixels, of which 63 are opaque. To further reduce the background, a plastic scintillator is located below the mask.
In order to suppress systematic effects on spatial and temporal background variations for SPI, a controlled and systematic spacecraft dithering manoeuvre is required. It consists of several off-pointings from the target in steps of 2.17 deg. Two different pointing patterns are used (see Courvoisier et al. 2003, for details): an hexagonal pattern around the nominal target location (*mode 1*: 1 source on-axis pointing, 6 off-source pointings) and a square pattern around the nominal target location (*mode 2*: 1 source on-axis pointing, 24 off-source pointings).
The data collected by INTEGRAL are grouped by satellite revolution and organised in storage directories called science windows (SCWs), which can be referred to a "proper" pointing or to a slew phase. The data analysis, performed using the Off-line Scientific Analysis software (OSA), is divided in Analysis Levels, which the main are:

- COR, data correction for instrumental effects, such as energy and position corrections
- GTI, good time handling (select, create and merge gti in a unique file)
- DEAD, computing the dead time of an instrument
- BIN_I, event binning for imaging
- CAT_I, catalogue source selection (selects a list of known sources, containing source location and expected flux values)
- IMA, image reconstruction (generates sky images and searches for significant sources)
- BIN_S, event binning for spectral analysis
- SPE, source spectra extraction and ARF creation
- BIN_T, event binning for light curves analysis
- LCR, source light curve extraction

A.4 NuSTAR

The Nuclear Spectroscopic Telescope Array (*NuSTAR*, Harrison et al. 2013) was launched on June 13, 2012 and it is still operational. It is the first satellite mission that makes use of focusing telescopes to image the sky in the 3-79 keV energy range.

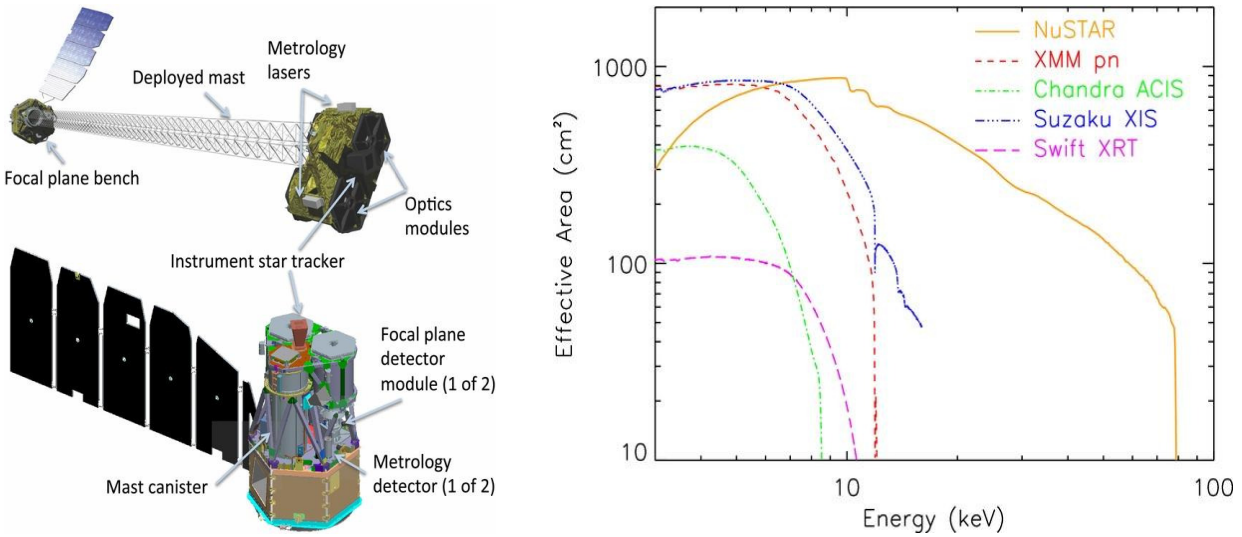

Figure A.5: On the left: diagram of the observatory in the stowed (bottom) and deployed (top) configurations. On the right: effective collecting area of NuSTAR compared to the CCD imagers on *Chandra*, *XMM-Newton*, *Suzaku* and *Swift/XRT* (Harrison et al. 2013).

Table A.2: NuSTAR performance parameters

Parameters	
Focal plane size	$12' \times 12'$
Max. flux meas. rate	10^4 counts s^{-1}
Energy range	3 - 78.4 keV
Angular resolution (FWHM)	$18''$
FoV	$10''$ at 10 keV $6''$ at 10 keV
Sensitivity (10^6 s, 3σ, $\Delta E/E = 0.5$)	(6 - 10 keV) 2×10^{-15} erg cm^{-2} s^{-1} (10-30 keV) 1×10^{-14} erg cm^{-2} s^{-1}
Energy resolution (FWHM)	400 eV at 10 keV 900 eV at 68 keV
Temporal resolution	2 μs
Dead time fraction	5% (at 2 keV energy treshold)

It consists of 2 co-aligned grazing incidence hard X-ray telescopes, focusing onto position sensitive detectors with 18″ FWHM angular resolution. Their focal length is 10.14 m, obtained with an extendable mast. Each optic module are composed of 133 nested shells in a conical approximation to a Wolter-I geometry; the special multi-layer coat of the optics increases the grazing angle with a significant reflectivity (Cavallari & Frontera 2017).
The performance parameters of the satellite are summarised in Table A.2.
The *NUSTAR* observatory provides a combination of sensitivity, spatial, and spectral resolution factors of 10 to 100 improved over previous missions that have operated at these X-ray energies.

Appendix B

Scripts Python codes

In the following, the main Python codes developed in collaboration with Dr. Carlo Ferrigno to perform the INTEGRAL analysis (described in Chapter 7) are reported.

B.1 Sample catalogue creation

It creates a catalogue of the source of our sample and collects the SCWs for each of them from the *INTEGRAL* data archive.

```
from astropy.table import Table
from astropy import units as u
from astropy.coordinates import SkyCoord
import numpy as np
get_ipython().run_line_magic('matplotlib', 'notebook')
import matplotlib.pylab as plt

#read the general INTEGRAL catalogue
index=Table.read('GNRL-SCWG-GRP-IDX.fits')

#example of source searching
ra_src=266.9833333333333
dec_src=-26.56361111111111
name="GX 3+1"
```

```
c_src=SkyCoord(ra_src*u.deg, dec_src*u.deg)

#select SCWs between revolution 46 and 1998 (included)
sw_type=index['SW_TYPE']
filter_pointing= sw_type == 'POINTING    ' #space is important !
filter_revol=np.logical_and(index['REVOL'] > 46, index['REVOL']<1999)
myfilter=np.logical_and(filter_pointing, filter_revol)
index_point=index[myfilter]

#select coordinates column
ra_x=index_point['RA_SCX']
dec_x=index_point['DEC_SCX']
sw_pointings=SkyCoord(ra_x, dec_x)

#select sources within 12deg of separation (example)
separation=sw_pointings.separation(c_src)
index_src=separation.deg <12
my_scw_list=index_point['SWID'][index_src]
filtered_sep=separation[index_src]

#filter list using deg separation
file_h=open('outputfile.txt', 'w')
for i in range(len(my_scw_list)):
    outstring="%s %.2f"%(my_scw_list[i], filtered_sep[i].deg)
    file_h.write(outstring+'\n')
file_h.close()

#select sources using Simbad (examples)
from astroquery.simbad import Simbad
my_src=Simbad.query_object('4U 1636-536')
my_src2=Simbad.query_object('GS 1826-24')

c_src=SkyCoord(my_src2['RA'].data[0], my_src2['DEC'].data[0],\\
```

```
file_h=open('sources_list.txt')  #file list containing names of the sources sample
src_names=file_h.readlines()
file_h.close()

#write SCWs list for each source
for nn in src_names:
    my_src2=Simbad.query_object(nn)
    c_src=SkyCoord(my_src2['RA'].data[0], my_src2['DEC'].data[0],
                   unit=[u.hourangle,u.deg])
    separation=sw_pointings.separation(c_src)
    index_src=separation.deg < 3.5
    my_scw_list=index_point['SWID'][index_src]
    short_nn=nn.strip().replace(' ','')
    print (short_nn, len(my_scw_list))
    file_h=open('list'+short_nn+'_jmx.txt','w')
    for ss in my_scw_list:
        file_h.write(ss+'\n')
    file_h.close()

#create file list with sources coordinates
all_ra=[]
all_dec=[]
for nn in src_names:
    my_src2=Simbad.query_object(nn)
    c_src=SkyCoord(my_src2['RA'].data[0], my_src2['DEC'].data[0],
                   unit=[u.hourangle,u.deg])
    print(nn.replace('\n','').replace(' ','').replace('+','p').replace('-','m'),
            c_src.ra.deg, c_src.dec.deg)
    all_ra.append(c_src.ra.deg)
    all_dec.append(c_src.dec.deg)

#plot FOV using RA and DEC
fi=plt.figure()
```

```
plt.scatter(all_ra,all_dec)
for i in range(len(src_names)):
    plt.text(all_ra[i],all_dec[i], src_names[i])

#read catalogues
local_cat=Table.read('mycatalog_finale.fits') #created catalogue
gnrl_cat=Table.read('gnrl_refr_cat_0041.fits') #INTEGRAL catalogue

#check sources coordinates
ra_c=local_cat['RA_OBJ']
dec_c=local_cat['DEC_OBJ']
cat_coord=SkyCoord(ra_c, dec_c)

for ra,dec,nn in zip(all_ra, all_dec, src_names):
    c_src=SkyCoord(ra*u.deg,dec*u.deg)
    separation=cat_coord.separation(c_src)
    ind = separation.arcmin < 3
    if ind.sum() > 0:
        print(nn.replace('\n',''),local_cat['NAME'][ind].data, separation.arcmin[ind])
    else:
        print(nn.replace('\n','')+' where is it?')

#check if all the sources of interest are present in the catalogue
cat_sources=local_cat['NAME']
cat_sources_good=[ss.strip() for ss in cat_sources.data]
not_present=[]
for ss in src_names:
    s=ss.replace('\n','').strip()
    if s in cat_sources_good:
        print(s+' is present')
    else:
        print(s+' is NOT present')
        not_present.append(s)
```

```
out_str=''
for i in not_present:
    out_str+='NAME == \''+ i + '\' || '
print(out_str)
```

B.2 Burst searcher

It performs an automatic search for Type-I bursts events exploiting the products of the `burstsearcher` tool of OSA 11.0.

```
from astropy.io import fits as pf
import numpy
from astropy.coordinates import SkyCoord
from astropy import units as u
from glob import glob

#point to directories containing JEM-X1 images and collect into a global variable
files=files=glob('jmx1_ima_*scw*/')
files.sort()

#source coordinates (example)
mycoord=SkyCoord(ra=264.57133333333326*u.deg, dec=-26.994055555555555*u.deg)
#write an outfile with SCWId, name and coordinates of the source
outfile_burst=open('burst_scw.txt','w')
outfile_burst.write('scw, name, ra, dec, flag\n')

#searching for FLAG=512 which indicates the detection of a Type-I burst event
for file in files:
    try:
        file_handler=pf.open(file+'/jmx1_srcl_res.fits') #try to open lightcurve file
    except:
        print('Failed '+file)
        continue
    data=file_handler[1].data
    for row in data:
        other=SkyCoord(ra=row['RA_OBJ']*u.deg, dec=row['DEC_OBJ']*u.deg)
        sep=mycoord.separation(other)
        flag=row['FLAG']
```

```
        #select only burst events of the interested source
        if sep.arcmin < 5 and flag == 512:
            outstring="%s, %s, %f, %f, %d\n"%(file, row['NAME'], row['RA_OBJ'],
                                              row['DEC_OBJ'], row['FLAG'])
            outfile_burst.write(outstring)
            print(outstring)
    file_handler.close()
outfile_burst.close()

#read text as table
import pandas as pd
aa=pd.read_csv('burst_scw.txt')

outfile_time=open('time_burst.txt','w')
outfile_burst=open('scw_time.txt', 'w')

#search for tstart and tstop of bursts and list them to file
rti=0
for file in aa['scw']:
    file_handler=pf.open(file+'/jmx1_sky_ima.fits')
    for ff in file_handler:
        try:
            rt1=ff.header['RTSTART']
            rt2=ff.header['RTSTOP']
            delta_t=(rt2-rt1)*86400
            outstring="%f %f\n"%(rt1,rt2)
            outstring_2="%s %f %f\n"%(file,rt1,rt2)
            if rt1!=rti and delta_t < 200:
                outfile_time.write(outstring)
                outfile_burst.write(outstring_2)
                print (outstring_2)
                rti=rt1
        except:
```

```
            pass
    file_handler.close()
outfile_time.close()
outfile_burst.close()
```

B.3 Light curve extraction

It collects all the information related to the light curves (as count rate, time, energy band, etc...) of all the sample sources into a single file. It is applied to IBIS/ISGRI data.

```
from astropy.io import fits as pf
import numpy as np
import sys

n=sys.argv[1]
list_1=("scw_isgri_file_"+n+".txt")
scw_str=np.loadtxt(list_1, type=str)
len(scw_str)

lc=("isgri_lc_total"+n+".txt")
outfile_lc=open(lc, 'w')
outfile_lc.write('SOURCE, BAND, TIME, TIME_ERR, FLUX, FLUX_ERR, DETSIG, SCWID\n')
outfile_fail1=open('fail_isgri_lc.txt', 'w')

#get all the information from isgri_sky_res files and point out process failed SCWs
sources=["H 1624-490","H 1636-536","GX 349+2","3A 1728-169","GX 3+1","GX 9+1",
        "GX 5-1", "GX 13+1","GX 17+2", "H 1705-440","4U 1722-30","GX 354-0",
        "4U 1735-444","1H 1746-370","H 1702-429","H 1820-303", "4U 1916-053",
        "Ginga 1826-24","SLX 1735-269"]

for scw in scw_str:
    try:
        file_name=scw+'.001/isgri_sky_res.fits.gz' #results of the image analysis level
        file_handler=pf.open(file_name)
    except:
        print('Failed '+scw)
        outfile_fail1.write(scw+"\n")
        continue
    t1=file_handler[1].header['TSTART']
```

```
    t2=file_handler[1].header['TSTOP']
    T=(((t1+t2)/2)+51544)*86400
    T_err=((t2-t1)/2)*86400
    for i in range(2,5):
        data=file_handler[i].data
        for source in sources:
            names=data['NAME']
            ind= names == source
            if np.count_nonzero(ind) > 0:
                outstring="%s, %d, %f, %f, %f, %f, %f, %s\n"%(source, i, T, T_err,
                                                data['FLUX'][ind],data['FLUX_ERR'][ind],
                                                data['DETSIG'][ind], scw)
                outfile_lc.write(outstring)
    file_handler.close()
outfile_lc.close()
outfile_fail1.close()

#display text file as table
import pandas as pd
colnames=['SOURCE', 'BAND', 'TIME', 'TIME_ERR', 'FLUX', 'FLUX_ERR', 'DETSIG', 'SCWID']
lc_fin=pd.read_csv('isgri_lc_total.txt', names=colnames)
lc_fin
```

B.4 Table converter

It converts pandas table file containing all light curves information into text file for each source and energy band. It is applied to IBIS/ISGRI data.

```
import csv
import pandas as pd
import numpy as np

sources=["H 1624-490","H 1636-536","GX 349+2","3A 1728-169","GX 3+1","GX 9+1",
        "GX 5-1", "GX 13+1","GX 17+2", "H 1705-440","4U 1722-30","GX 354-0",
        "4U 1735-444","1H 1746-370","H 1702-429","H 1820-303", "4U 1916-053",
        "Ginga 1826-24","SLX 1735-269"]

for src in sources:

    file_a=""+src+"_lc_total.txt"
    outfile=""+src+"_test.txt.bak"
    df = pd.read_csv(file_a, sep=',', names=["SOURCE", "BAND", "TIME", "TIME_ERR",
                    "FLUX", "FLUX_ERR", "DETSIG", "SCWID"], dtype={'SCWID':'str'})

    bands=[2,3,4]

    new_names=["SCWID", "TIME", "TIME_ERR", "FLUX_2", "FLUX_ERR_2", "DETSIG_2",
               "FLUX_3", "FLUX_ERR_3", "DETSIG_3", "FLUX_4", "FLUX_ERR_4",
               "DETSIG_4"]

    new_df_data=[]

    for scw in sorted(set(df['SCWID'])):

        ind_scw = df['SCWID'] == scw

        if np.count_nonzero(ind_scw) == 0:
```

```
            print("Something very wrong with scw %012d"%(scw))
            break

        rows = df[ind_scw]

        new_row=[rows[x].values[0] for x in new_names[0:3]]

        for i in bands:
            ind_band = rows['BAND'] == i
            if np.count_nonzero(ind_band) > 0:
                flux,err,det=rows['FLUX'].values[ind_band][0],
                             rows['FLUX_ERR'].values[ind_band][0],
                             rows['DETSIG'].values[ind_band][0]
            else:
                flux, err, det = -999,-999,-999

            new_row += [flux,err,det]

        new_df_data.append(new_row)

    new_df=pd.DataFrame(new_df_data, columns=new_names)

    newfile=new_df.to_numpy()
    np.savetxt(outfile, newfile, delimiter=',', fmt='%s %.15f %.15f %.12f %.12f %.12f
                                                    %.12f %.12f %.12f %.12f %.12f %.12f',
              header='SCWID TIME TIME_ERR FLUX_2 FLUX_ERR_2 DETSIG_2 FLUX_3
                        FLUX_ERR_3 DETSIG_3 FLUX_4 FLUX_ERR_4 DETSIG_4')
```

B.5 SCWs group selection from hardness-intensity diagram

It performs the selection of the SCWs Id to be grouped for spectral extraction from the HID.

```
import numpy as np
import itertools
import math

#here the minimum dimension of the box in HR and intesity is calculated
source="Crab"        #example
infile_0=(source+"_hid_reb.qdp") #rebinned HID
a=np.loadtxt(infile_0, skiprows=11, comments='!') #read HID file
hr=a[:,2]
flux=a[:,0]
dev_hr=np.std(hr)
dev_flux=np.std(flux)
wm=np.average(flux)



src_name="Crab"        #example
input_data_file=+src_name+"_JMX2_LC_data.txt" #not rebinned JEM-X2 light curve
input_rebinned_lc=src_name+"_jmx2_hratio.qdp" #rebinned JEM-X2 light curve
outlist_root=src_name+"_scwlist_jmx2"

#read the data
t,dt,r1,dr1,r2,dr2,r3,dr3,sw=np.loadtxt(input_data_file, unpack=True)
max_nsr=10.        #set the threshold on the maximun signal-to-noise allowed

ind=np.logical_and(np.logical_and(dr3/r3<max_nsr , dr2/r2 <max_nsr), dr1/r1 < max_nsr)

#skip 14 lines (standard timingsuite output)
tb, dtb, r1b, dr1b, r2b, dr2b, hr, dhr=np.loadtxt(input_rebinned_lc, skiprows=14,
                                                  unpack=True)
rtb=r1b+r2b
```

```
drtb=np.sqrt(dr1b**2+dr2b**2)
mjdref=0

#gets the offset time before time conversion
for line in open(input_rebinned_lc, 'r'):
    if "!lab x Time since" in line:
        time0=float(line.split(" ")[-1].replace("\n",""))
        break

#Input of rectangular regions for selection
boxes=src_name+"_boxes.txt"
ab=np.loadtxt(boxes, comments='!')
for i in ab:
    hr_min, hr_max, rate_min, rate_max=i
    outlist_name=outlist_root+'_hr_%.2f_%.2f_r_%.0f_%.0f.txt'%(hr_min,hr_max,rate_min,
                                                               rate_max)
    print(hr_min, hr_max, rate_min, rate_max, outlist_name)

    #do the selection
    ind_hr=np.logical_and(hr >= hr_min, hr <= hr_max)
    ind_rate=np.logical_and(rtb >= rate_min, rtb <= rate_max)
    ind=np.logical_and(ind_rate , ind_hr )

    scw_list=[]
    for i in range(len(ind)):
        if not ind[i] :
            continue

    #convert time and select tstart and tstop of each group of scw
        t_min=(tb[i]-dtb[i]+time0)/86400.0+mjdref
        t_max=(tb[i]+dtb[i]+time0)/86400.0+mjdref
```

```
        ind_t=np.logical_and(t>=t_min, t<=t_max)

    #write lists
        good_sw=sw[ind_t]
        scw_list.append(good_sw)
        merged_scw_list = list(itertools.chain.from_iterable(scw_list))
        ff=open(outlist_name, 'w')
        for i in merged_scw_list:
            ff.write("%0.12d\n"%(i))
        ff.close()
```

Bibliography

2007, Binary Stars as Critical Tools and Tests in Contemporary Astrophysics (IAU S240), Vol. 240

Abbassi, S., Ghanbari, J., & Najjar, S. 2008, MNRAS, 388, 663

Abramowicz, M. A., Chen, X., Kato, S., Lasota, J.-P., & Regev, O. 1995, ApJ, 438, L37

Abramowicz, M. A., Igumenshchev, I. V., & Lasota, J.-P. 1998, MNRAS, 293, 443

Alpar, M. A. & Shaham, J. 1985, Nature, 316, 239

Andrew, B. H. & Purton, C. R. 1968, Nature, 218, 855

Applegate, J. H. 1992, ApJ, 385, 621

Applegate, J. H. & Shaham, J. 1994, ApJ, 436, 312

Armas Padilla, M., Ueda, Y., Hori, T., Shidatsu, M., & Muñoz-Darias, T. 2017, MNRAS, 467, 290

Bak Nielsen, A.-S., Patruno, A., & D'Angelo, C. 2017, MNRAS, 468, 824

Balbus, S. A. & Hawley, J. F. 1991, ApJ, 376, 214

Barnard, R., Osborne, J. P., Kolb, U., & Borozdin, K. N. 2003, A&A, 405, 505

Barret, D. & Olive, J.-F. 2002, ApJ, 576, 391

Barret, D., Olive, J. F., Boirin, L., et al. 2000, ApJ, 533, 329

Bayless, A. J., Robinson, E. L., Hynes, R. I., Ashcraft, T. A., & Cornell, M. E. 2010, ApJ, 709, 251

Belloni, T., Parolin, I., Del Santo, M., et al. 2006, MNRAS, 367, 1113

Belloni, T. M. 2010, States and Transitions in Black Hole Binaries, ed. T. Belloni, Vol. 794, 53

Belloni, T. M., Motta, S. E., & Muñoz-Darias, T. 2011, Bulletin of the Astronomical Society of India, 39, 409

Bhattacharya, D. & van den Heuvel, E. P. J. 1991, Phys. Rep., 203, 1

Blumenthal, G. R. & Gould, R. J. 1970, Reviews of Modern Physics, 42, 237

Boella, G., Butler, R. C., Perola, G. C., et al. 1997, A&AS, 122

Boirin, L., Méndez, M., Díaz Trigo, M., Parmar, A. N., & Kaastra, J. S. 2005, A&A, 436, 195

Bradshaw, C. F., Fomalont, E. B., & Geldzahler, B. J. 1999, ApJ, 512, L121

Bradshaw, C. F., Geldzahler, B. J., & Fomalont, E. B. 2003, ApJ, 592, 486

Bradt, H. V. D. & McClintock, J. E. 1983, ARA&A, 21, 13

Brandt, S., Budtz-Jørgensen, C., Lund, N., et al. 2003, A&A, 411, L243

Brenneman, L. W. & Reynolds, C. S. 2006, ApJ, 652, 1028

Bruenn, S. W. 1973, ApJ, 186, 1157

Burderi, L., Di Salvo, T., Lavagetto, G., et al. 2007, ApJ, 657, 961

Burderi, L., Di Salvo, T., Menna, M. T., Riggio, A., & Papitto, A. 2006, ApJ, 653, L133

Burderi, L., Di Salvo, T., Riggio, A., et al. 2010, A&A, 515, A44

Burderi, L., Di Salvo, T., Robba, N. R., La Barbera, A., & Guainazzi, M. 2000, ApJ, 530, 429

Burderi, L., Di Salvo, T., Stella, L., et al. 2002, ApJ, 574, 930

Burderi, L., Possenti, A., D'Antona, F., et al. 2001, ApJ, 560, L71

Burderi, L., Riggio, A., di Salvo, T., et al. 2009, A&A, 496, L17

Burko, L. M. 2017, The Physics Teacher, 55, 288

Cackett, E. M., Altamirano, D., Patruno, A., et al. 2009, ApJ, 694, L21

Cackett, E. M. & Miller, J. M. 2013, ApJ, 777, 47

Cackett, E. M., Miller, J. M., Ballantyne, D. R., et al. 2010, ApJ, 720, 205

Cackett, E. M., Miller, J. M., Bhattacharyya, S., et al. 2008, ApJ, 674, 415

Cackett, E. M., Miller, J. M., Reis, R. C., Fabian, A. C., & Barret, D. 2012, ApJ, 755, 27

Campana, S., Gastaldello, F., Stella, L., et al. 2001, ApJ, 561, 924

Campana, S., Stella, L., Mereghetti, S., et al. 1998, ApJ, 499, L65

Campana, S., Stella, L., Mereghetti, S., & de Martino, D. 2018, A&A, 610, A46

Cannizzo, J. K. & Reiff, C. M. 1992, ApJ, 385, 87

Casella, P., Belloni, T., & Stella, L. 2006, A&A, 446, 579

Cavallari, E. & Frontera, F. 2017, Space Sci. Rev., 212, 429

Chen, X., Abramowicz, M. A., Lasota, J.-P., Narayan, R., & Yi, I. 1995, ApJ, 443, L61

Chiang, C.-Y., Cackett, E. M., Miller, J. M., et al. 2016, ApJ, 821, 105

Chou, Y., Hsieh, H.-E., Hu, C.-P., Yang, T.-C., & Su, Y.-H. 2016, ApJ, 831, 29

Christian, D. J. & Swank, J. H. 1997, ApJS, 109, 177

Courvoisier, T., Walter, R., Beckmann, V., et al. 2003, A&A, 411

D'Aì, A., di Salvo, T., Ballantyne, D., et al. 2010, A&A, 516, A36

D'Aí, A., Życki, P., Di Salvo, T., et al. 2007, ApJ, 667, 411

D'Amico, F., Heindl, W. A., Rothschild, R. E., & Gruber, D. E. 2001, ApJ, 547, L147

Dauser, T., Garcia, J., Parker, M. L., Fabian, A. C., & Wilms, J. 2014, MNRAS, 444, L100

Dauser, T., Garcia, J., Wilms, J., et al. 2013, MNRAS, 430, 1694

Dauser, T., Wilms, J., Reynolds, C. S., & Brenneman, L. W. 2010, MNRAS, 409, 1534

Degenaar, N., Ballantyne, D. R., Belloni, T., et al. 2018, Space Sci. Rev., 214, 15

Degenaar, N. & Wijnands, R. 2012, MNRAS, 422, 581

Del Santo, M., Malzac, J., Jourdain, E., Belloni, T., & Ubertini, P. 2008, MNRAS, 390, 227

den Herder, J. W., Brinkman, A. C., Kahn, S. M., et al. 2001, A&A, 365, L7

Di Cocco, G., Caroli, E., Celesti, E., et al. 2003, A&A, 411, L189

Di Salvo, T. 2001, PhD thesis, Dipartimento di Scienze Fisiche ed Astronomiche, Università degli Studi di Palermo, Via Archirafi 36, 90123, Palermo, Italy

di Salvo, T., Burderi, L., Riggio, A., Papitto, A., & Menna, M. T. 2008, MNRAS, 389, 1851

Di Salvo, T., D'Aí, A., Iaria, R., et al. 2009, MNRAS, 398, 2022

Di Salvo, T., Goldoni, P., Stella, L., et al. 2006, ApJ, 649, L91

Di Salvo, T., Iaria, R., Matranga, M., et al. 2015, MNRAS, 449, 2794

Di Salvo, T., Iaria, R., Méndez, M., et al. 2005, ApJ, 623, L121

Di Salvo, T., Robba, N. R., Iaria, R., et al. 2001, ApJ, 554, 49

Di Salvo, T., Stella, L., Robba, N. R., et al. 2000, ApJ, 544, L119

Díaz Trigo, M., Parmar, A. N., Boirin, L., et al. 2009, A&A, 493, 145

Díaz Trigo, M., Sidoli, L., Boirin, L., & Parmar, A. N. 2012, A&A, 543, A50

Ding, G. Q., Chen, T. T., & Qu, J. L. 2020, MNRAS

Ding, G. Q. & Huang, C. P. 2015, Journal of Astrophysics and Astronomy, 36, 335

Ding, G. Q., Zhang, S. N., Wang, N., Qu, J. L., & Yan, S. P. 2011, AJ, 142, 34

Done, C., Gierliński, M., & Kubota, A. 2007, A&A Rev., 15, 1

Dove, J. B., Wilms, J., & Begelman, M. C. 1997, ApJ, 487, 747

Eggleton, P. P. 1983, ApJ, 268, 368

Egron, E. 2013, PhD thesis, Dipartimento di Fisica, Università degli Studi di Cagliari, SP Monserrato-Sestu, KM 0.7, Monserrato, 09042 Italy

Egron, E., Di Salvo, T., Motta, S., et al. 2013, A&A, 550, A5

ESA. 2002, INTEGRAL: Mission Overview, `https://www.cosmos.esa.int/web/integral/mission-overview`

ESA: XMM-Newton SOC. 2020, XMM-Newton Users Handbook

Fabian, A. C., Iwasawa, K., Reynolds, C. S., & Young, A. J. 2000, PASP, 112, 1145

Fabian, A. C., Pringle, J. E., & Rees, M. J. 1975, MNRAS, 172, 15

Fabian, A. C., Rees, M. J., Stella, L., & White, N. E. 1989, MNRAS, 238, 729

Fabian, A. C., Zoghbi, A., Ross, R. R., et al. 2009, Nature, 459, 540

Farinelli, R., Frontera, F., Zdziarski, A. A., et al. 2005, A&A, 434, 25

Farinelli, R., Paizis, A., Landi, R., & Titarchuk, L. 2009, A&A, 498, 509

Farinelli, R., Titarchuk, L., & Frontera, F. 2007, ApJ, 662, 1167

Farinelli, R., Titarchuk, L., Paizis, A., & Frontera, F. 2008, ApJ, 680, 602

Fender, R. 2001, in American Institute of Physics Conference Series, Vol. 558, High Energy Gamma-Ray Astronomy: International Symposium, ed. F. A. Aharonian & H. J. Völk, 221–233

Fender, R., Wu, K., Johnston, H., et al. 2004a, Nature, 427, 222

Fender, R. P., Belloni, T. M., & Gallo, E. 2004b, MNRAS, 355, 1105

Fender, R. P., Homan, J., & Belloni, T. M. 2009, MNRAS, 396, 1370

Fomalont, E. B., Geldzahler, B. J., & Bradshaw, C. F. 2001, ApJ, 558, 283

Forman, W., Jones, C., Cominsky, L., et al. 1978, ApJS, 38, 357

Frank, J., King, A., & Raine, D. J. 2002, Accretion Power in Astrophysics: Third Edition, 398

Friedman, H., Byram, E. T., & Chubb, T. A. 1967, Science, 156, 374

Frontera, F., Costa, E., dal Fiume, D., et al. 1997, A&AS, 122, 357

Fukue, J. 2004a, PASJ, 56, 569

Fukue, J. 2004b, PASJ, 56, 181

Galloway, D. K., Muno, M. P., Hartman, J. M., Psaltis, D., & Chakrabarty, D. 2008, ApJS, 179, 360

Gambino, A. F., Iaria, R., Di Salvo, T., et al. 2016, A&A, 589, A34

Gambino, A. F., Iaria, R., Di Salvo, T., et al. 2017, Research in Astronomy and Astrophysics, 17, 108

Gambino, A. F., Iaria, R., Di Salvo, T., et al. 2019, A&A, 625, A92

Gammie, C. F. & Balbus, S. A. 1994, MNRAS, 270, 138

García, J., Dauser, T., Lohfink, A., et al. 2014, ApJ, 782, 76

Ghisellini, G. 2013, Radiative Processes in High Energy Astrophysics. Lecture Notes in Physics, Vol. 873 (Springer International Publishing Switzerland)

Ghosh, P. & Lamb, F. K. 1979, ApJ, 234, 296

Ghosh, P. & Lamb, F. K. 1991, in NATO Advanced Study Institute (ASI) Series C, Vol. 344, Neutron Stars, ed. J. Ventura & D. Pines, 363

Giacconi, R., Gursky, H., Kellogg, E., Schreier, E., & Tananbaum, H. 1971a, ApJ, 167, L67

Giacconi, R., Gursky, H., Paolini, F. R., & Rossi, B. B. 1962, Phys. Rev. Lett., 9, 439

Giacconi, R., Kellogg, E., Gorenstein, P., Gursky, H., & Tananbaum, H. 1971b, ApJ, 165, L27

Gilfanov, M. 2010, in Lecture Notes in Physics, Berlin Springer Verlag, ed. T. Belloni, Vol. 794, 17

Goldwurm, A., David, P., Foschini, L., et al. 2003, A&A, 411, L223

Grefenstette, B. W., Glesener, L., Krucker, S., et al. 2016, The Astrophysical Journal, 826, 20

Gros, A., Goldwurm, A., Cadolle-Bel, M., et al. 2003, A&A, 411, L179

Haardt, F. & Maraschi, L. 1991, ApJ, 380, L51

Haardt, F., Maraschi, L., & Ghisellini, G. 1994, ApJ, 432, L95

Hanke, M. 2011, PhD thesis, Dr. Karl Remeis-Sternwarte, Astronomisches Institut der Universität Erlangen-Nürnberg, Sternwartstr. 7, 96049 Bamberg, Germany

Harrison, F. A., Craig, W. W., Christensen, F. E., et al. 2013, ApJ, 770, 103

Hasinger, G. & van der Klis, M. 1989, A&A, 225, 79

Hasinger, G., van der Klis, M., Ebisawa, K., Dotani, T., & Mitsuda, K. 1990, A&A, 235, 131

Hawley, J. F. & Balbus, S. A. 1997, in Astronomical Society of the Pacific Conference Series, Vol. 121, IAU Colloq. 163: Accretion Phenomena and Related Outflows, ed. D. T. Wickramasinghe, G. V. Bicknell, & L. Ferrario, 179

Heinz, S. & Nowak, M. A. 2001, MNRAS, 320, 249

Heitler, W. 1954, The Quantum Theory of Radiation (Oxford University Press)

Hellier, C. & Mason, K. O. 1989, MNRAS, 239, 715

Hellier, C. & Smale, A. P. 1994, in American Institute of Physics Conference Series, Vol. 308, The Evolution of X-ray Binariese, ed. S. Holt & C. S. Day, 535

Hirayama, H. 2000, Lecture Note on Photon Interactions and Cross Sections

Homan, J., Steiner, J. F., Lin, D., et al. 2018, ApJ, 853, 157

Hoshi, R. & Asaoka, I. 1993, PASJ, 45, 567

Iaria, R., Burderi, L., Di Salvo, T., La Barbera, A., & Robba, N. R. 2001a, ApJ, 547, 412

Iaria, R., D'Aí, A., di Salvo, T., et al. 2009, A&A, 505, 1143

Iaria, R., di Salvo, T., Burderi, L., et al. 2011, A&A, 534, A85

Iaria, R., Di Salvo, T., Burderi, L., et al. 2014, A&A, 561, A99

Iaria, R., Di Salvo, T., Burderi, L., & Robba, N. R. 2001b, ApJ, 557, 24

Iaria, R., Di Salvo, T., D'Aì, A., et al. 2013, A&A, 549, A33

Iaria, R., Di Salvo, T., Del Santo, M., et al. 2016, A&A, 596, A21

Iaria, R., Di Salvo, T., Gambino, A. F., et al. 2015a, A&A, 582, A32

Iaria, R., Di Salvo, T., Matranga, M., et al. 2015b, A&A, 577, A63

Iaria, R., Di Salvo, T., Robba, N. R., et al. 2005, ApJ, 634, L161

Iaria, R., Gambino, A. F., Di Salvo, T., et al. 2018, MNRAS, 473, 3490

Iaria, R., Lavagetto, G., D'Aí, A., di Salvo, T., & Robba, N. R. 2007, A&A, 463, 289

Iaria, R., Mazzola, S. M., Bassi, T., et al. 2019, A&A, 630, A138

Ichimaru, S. 1977, ApJ, 214, 840

in 't Zand, J. J. M. 1999, BeppoSAX satellite, `https://personal.sron.nl/~jeanz/wfc/bepposax.html`

in 't Zand, J. J. M., Verbunt, F., Strohmayer, T. E., et al. 1999, A&A, 345, 100

Jager, R., in 't Zand, J. J. M., Schuurmans, J. J., Heise, J., & Mels, W. A. 1989, in Society of Photo-Optical Instrumentation Engineers (SPIE) Conference Series, Vol. 1159, EUV, X-Ray, and Gamma-Ray Instrumentation for Astronomy and Atomic Physics, ed. C. J. Hailey & O. H. W. Siegmund, 2–0

Jager, R., Mels, W. A., Brinkman, A. C., et al. 1997, A&AS, 125, 557

Jahoda, K., Swank, J. H., Giles, A. B., et al. 1996, in Society of Photo-Optical Instrumentation Engineers (SPIE) Conference Series, Vol. 2808, EUV, X-Ray, and Gamma-Ray Instrumentation for Astronomy VII, ed. O. H. Siegmund & M. A. Gummin, 59–70

Jain, C., Paul, B., & Dutta, A. 2010, MNRAS, 409, 755

Jansen, F., Lumb, D., Altieri, B., et al. 2001, A&A, 365, L1

Ji, L., Schulz, N. S., Nowak, M. A., & Canizares, C. R. 2011, ApJ, 729, 102

Jonker, P. G., Méndez, M., & van der Klis, M. 2000a, ApJ, 540, L29

Jonker, P. G. & van der Klis, M. 2001, ApJ, 553, L43

Jonker, P. G., van der Klis, M., & Groot, P. J. 2003, MNRAS, 339, 663

Jonker, P. G., van der Klis, M., Wijnands, R., et al. 2000b, ApJ, 537, 374

Kallman, T. R., Palmeri, P., Bautista, M. A., Mendoza, C., & Krolik, J. H. 2004, ApJS, 155, 675

Kalogera, V. 1998, ApJ, 493, 368

Kalogera, V., Kolb, U., & King, A. R. 1998, ApJ, 504, 967

Kalogera, V. & Webbink, R. F. 1998, ApJ, 493, 351

Kippenhahn, R., Weigert, A., & Weiss, A. 2012, Stellar Structure and Evolution

Kirsch, M. G. 2006, Health and cleanliness of the XMM-Newton science payload since launch, `https://slideplayer.com/slide/13249983/79/i`

Kolehmainen, M., Done, C., & Díaz Trigo, M. 2011a, MNRAS, 416, 311

Kolehmainen, M., Done, C., & Díaz Trigo, M. 2011b, MNRAS, 416, 311

Lamb, F. K., Shibazaki, N., Alpar, M. A., & Shaham, J. 1985, Nature, 317, 681

Laor, A. 1991, ApJ, 376, 90

Lebrun, F., Leray, J. P., Lavocat, P., et al. 2003, A&A, 411, L141

Lewin, W. H. G. & van der Klis, M. 2006, Compact Stellar X-ray Sources, Vol. 39

Lewin, W. H. G., van Paradijs, J., & Taam, R. E. 1993, Space Sci. Rev., 62, 223

Liang, E. P. T. & Price, R. H. 1977, ApJ, 218, 247

Lightman, A. P. & Eardley, D. M. 1974, ApJ, 187, L1

Lin, D., Remillard, R. A., & Homan, J. 2007, ApJ, 667, 1073

Lin, D., Remillard, R. A., Homan, J., & Barret, D. 2012, ApJ, 756, 34

Lin, D. N. C. & Papaloizou, J. 1979, MNRAS, 188, 191

Longair, M. S. 2011, High Energy Astrophysics (Cambridge University Press)

Lovelace, R. V. E., Romanova, M. M., & Bisnovatyi-Kogan, G. S. 1995, MNRAS, 275, 244

Ludlam, R., Miller, J. M., Cackett, E., et al. 2016, in AAS/High Energy Astrophysics Division, Vol. 15, AAS/High Energy Astrophysics Division #15, 120.14

Ludlam, R. M., Miller, J. M., Bachetti, M., et al. 2017, ApJ, 836, 140

Lumb, D. H. 2012, Optical Engineering, 51, 011009

Lund, N., Budtz-Jørgensen, C., Westergaard, N. J., et al. 2003, A&A, 411, L231

Ma, B. & Li, X.-D. 2009a, ApJ, 698, 1907

Ma, B. & Li, X.-D. 2009b, ApJ, 691, 1611

Makishima, K., Maejima, Y., Mitsuda, K., et al. 1986, ApJ, 308, 635

Malzac, J. & Jourdain, E. 1999, Astrophysical Letters and Communications, 38, 201

Manzo, G., Giarrusso, S., Santangelo, A., et al. 1997, A&AS, 122, 341

Marino, A., Del Santo, M., Cocchi, M., et al. 2019a, MNRAS, 490, 2300

Marino, A., Di Salvo, T., Burderi, L., et al. 2019b, A&A, 627, A125

Marino, A., Di Salvo, T., Gambino, A. F., et al. 2017, A&A, 603, A137

Markwardt, C. B., Strohmayer, T. E., & Swank, J. H. 1999, ApJ, 512, L125

Mas-Hesse, J. M., Giménez, A., Culhane, J. L., et al. 2003, A&A, 411, L261

Mason, K. O., Breeveld, A., Much, R., et al. 2001, A&A, 365, L36

Mason, K. O. & Cordova, F. A. 1982, ApJ, 262, 253

Matranga, M., Di Salvo, T., Iaria, R., et al. 2017a, A&A, 600, A24

Matranga, M., Papitto, A., Di Salvo, T., et al. 2017b, A&A, 603, A39

Matsuoka, M. & Asai, K. 2013, PASJ, 65, 26

Mazzola, S. M., Iaria, R., Di Salvo, T., et al. 2019a, A&A, 621, A89

Mazzola, S. M., Iaria, R., Di Salvo, T., et al. 2019b, A&A, 621, A89

Meyer, F. & Meyer-Hofmeister, E. 1994, A&A, 288, 175

Michaely, E. & Perets, H. B. 2016, MNRAS, 458, 4188

Middleditch, J. & Priedhorsky, W. C. 1986, ApJ, 306, 230

Migliari, S. & Fender, R. P. 2006, MNRAS, 366, 79

Migliari, S., Fender, R. P., Rupen, M., et al. 2004, MNRAS, 351, 186

Migliari, S., Miller-Jones, J. C. A., Fender, R. P., et al. 2007a, ApJ, 671, 706

Migliari, S., Miller-Jones, J. C. A., & Russell, D. M. 2011, MNRAS, 415, 2407

Migliari, S., Tomsick, J. A., Markoff, S., et al. 2007b, ApJ, 670, 610

Migliari, S., Tomsick, J. A., Miller-Jones, J. C. A., et al. 2010, ApJ, 710, 117

Miller, M. C., Lamb, F. K., & Cook, G. B. 1998, ApJ, 509, 793

Miller-Jones, J. C. A., Jonker, P. G., Maccarone, T. J., Nelemans, G., & Calvelo, D. E. 2011, ApJ, 739, L18

Miller-Jones, J. C. A., Sivakoff, G. R., Altamirano, D., et al. 2010, ApJ, 716, L109

Mitsuda, K., Inoue, H., Koyama, K., et al. 1984, PASJ, 36, 741

Muñoz-Darias, T., Fender, R. P., Motta, S. E., & Belloni, T. M. 2014, MNRAS, 443, 3270

Muñoz-Darias, T., Motta, S., & Belloni, T. M. 2011, MNRAS, 410, 679

Müller, A. 2004, PhD thesis, Combined Faculties for the Natural Sciences and for Mathematics of the University of Heidelberg, Germany

Narayan, R., Igumenshchev, I. V., & Abramowicz, M. A. 2000, ApJ, 539, 798

Narayan, R. & Yi, I. 1994, ApJ, 428, L13

Narayan, R. & Yi, I. 1995, ApJ, 452, 710

Neece, G. D. 1984, ApJ, 277, 738

Oosterbroek, T., Penninx, W., van der Klis, M., van Paradijs, J., & Lewin, W. H. G. 1991, A&A, 250, 389

Orbiter. 2016, BeppoSAX festeggia vent'anni, `https://orbiter.it/cms/bepposax-festeggia-ventanni/`

Paczyński, B. 1971, ARA&A, 9, 183

Paizis, A., Farinelli, R., Titarchuk, L., et al. 2006, A&A, 459, 187

Pandel, D., Kaaret, P., & Corbel, S. 2008, ApJ, 688, 1288

Papaloizou, J. & Pringle, J. E. 1977, MNRAS, 181, 441

Papitto, A., D'Aì, A., Di Salvo, T., et al. 2013, MNRAS, 429, 3411

Parikh, A. S. & Wijnands, R. 2017, MNRAS, 472, 2742

Parmar, A. N., Martin, D. D. E., Bavdaz, M., et al. 1997, A&AS, 122, 309

Parmar, A. N., Oosterbroek, T., Boirin, L., & Lumb, D. 2002, A&A, 386, 910

Parmar, A. N., Oosterbroek, T., Del Sordo, S., et al. 2000, A&A, 356, 175

Pintore, F., Di Salvo, T., Bozzo, E., et al. 2015, MNRAS, 450, 2016

Pintore, F., Sanna, A., Di Salvo, T., et al. 2016, MNRAS, 457, 2988

Piraino, S., Santangelo, A., di Salvo, T., et al. 2007, A&A, 471, L17

Piraino, S., Santangelo, A., Kaaret, P., et al. 2012, A&A, 542, L27

Ponti, G., Bianchi, S., De Marco, B., et al. 2019, MNRAS, 487, 858

Ponti, G., Bianchi, S., Muñoz-Darias, T., et al. 2018, MNRAS, 473, 2304

Porquet, D., Mewe, R., Dubau, J., Raassen, A. J. J., & Kaastra, J. S. 2001, A&A, 376, 1113

Poutanen, J. & Coppi, P. S. 1998, Physica Scripta Volume T, 77, 57

Pozdnyakov, L. A., Sobol, I. M., & Syunyaev, R. A. 1983, Astrophys. Space Phys. Res., 2, 189

Pringle, J. E. & Rees, M. J. 1972, A&A, 21, 1

Psaltis, D. 2001, ApJ, 555, 786

Rappaport, S., Verbunt, F., & Joss, P. C. 1983, ApJ, 275, 713

Reig, P. & Kylafis, N. 2016, A&A, 591, A24

Reis, R. C., Fabian, A. C., & Young, A. J. 2009, MNRAS, 399, L1

Revnivtsev, M. G., Tsygankov, S. S., Churazov, E. M., & Krivonos, R. A. 2014, MNRAS, 445, 1205

Reynolds, C. S. 1999, in Astronomical Society of the Pacific Conference Series, Vol. 161, High Energy Processes in Accreting Black Holes, ed. J. Poutanen & R. Svensson, 178

Reynolds, C. S. & Nowak, M. A. 2003, Phys. Rep., 377, 389

Riegler, G. R. 1970, Nature, 226, 1041

Rothschild, R. E., Blanco, P. R., Gruber, D. E., et al. 1998, ApJ, 496, 538

Różańska, A. & Czerny, B. 2000, MNRAS, 316, 473

Rybicki, G. B. & Lightman, A. P. 1979, Radiative processes in astrophysics (WILEY-VCH)

Salaris, M. & Cassisi, S. 2005, Evolution of stars and stellar populations (J. Wiley), 400

Sanna, A., Di Salvo, T., Burderi, L., et al. 2017, MNRAS, 471, 463

Sanna, A., Hiemstra, B., Méndez, M., et al. 2013, MNRAS, 432, 1144

Sanna, A., Pintore, F., Riggio, A., et al. 2018, MNRAS, 481, 1658

Savchenko, V., Chrnyakova, M., Paizis, A., et al. 2020, IBIS Analysis User Manual, 11th edn., INTEGRAL Science Data Centre, Chemin d'Ècogia , CH–1290, Versoix, Switzerland

Seifina, E., Titarchuk, L., Shrader, C., & Shaposhnikov, N. 2015, ApJ, 808, 142

Shakura, N. I. & Sunyaev, R. A. 1973, A&A, 500, 33

Shakura, N. I. & Sunyaev, R. A. 1976, MNRAS, 175, 613

Shaposhnikov, N., Titarchuk, L., & Laurent, P. 2009, ApJ, 699, 1223

Sharma, R., Jaleel, A., Jain, C., et al. 2018, MNRAS, 481, 5560

Shimura, T. & Takahara, F. 1995a, ApJ, 445, 780

Shimura, T. & Takahara, F. 1995b, ApJ, 445, 780

Shu, F., Najita, J., Ostriker, E., et al. 1994, ApJ, 429, 781

Sidoli, L., Oosterbroek, T., Parmar, A. N., Lumb, D., & Erd, C. 2001, A&A, 379, 540

Sincell, M. W. & Krolik, J. H. 1997, ApJ, 476, 605

Skumanich, A. 1972, ApJ, 171, 565

Smith, M. A. 1979, PASP, 91, 737

Steeghs, D. & Casares, J. 2002, ApJ, 568, 273

Steiner, J. F., Remillard, R. A., García, J. A., & McClintock, J. E. 2016, ApJ, 829, L22

Stella, L. 1986, in Plasma Penetration into Magnetospheres., ed. N. Kylafis, J. Papamastorakis, & J. Ventura (Crete University Press), 199–214

Stella, L., White, N. E., & Rosner, R. 1986, On the Long Term Activity of Pop. I Binary Systems Containing an X-ray Pulsar, ed. K. O. Mason, M. G. Watson, & N. E. White, Vol. 266, 77

Strohmayer, T. E., Zhang, W., Swank, J. H., et al. 1996, ApJ, 469, L9

Strüder, L., Briel, U., Dennerl, K., et al. 2001, A&A, 365, L18

Sunyaev, R. A. & Titarchuk, L. G. 1980, A&A, 500, 167

Swank, J. H., Becker, R. H., Pravdo, S. H., Saba, J. R., & Serlemitsos, P. J. 1976, IAU Circ., 3010

Sztajno, M., van Paradijs, J., Lewin, W. H. G., et al. 1986, MNRAS, 222, 499

Tailo, M., D'Antona, F., Burderi, L., et al. 2018, MNRAS, 479, 817

Tauris, T. M. & van den Heuvel, E. P. J. 2006, Formation and evolution of compact stellar X-ray sources, Vol. 39, 623–665

Tawara, Y., Hirano, T., Kii, T., Matsuoka, M., & Murakami, T. 1984, PASJ, 36, 861

Taylor, B. G., Andresen, R. D., Peacock, A., & Zobl, R. 1981, Space Sci. Rev., 30, 479

Thorne, K. S. 1983, The theory of gravitational radiation: an introductory review., Vol. 124, 1–57

Thorne, K. S. & Price, R. H. 1975, ApJ, 195, L101

Titarchuk, L., Kazanas, D., & Becker, P. A. 2003, ApJ, 598, 411

Titarchuk, L., Seifina, E., & Shrader, C. 2014, ApJ, 789, 98

Turner, M. J. L., Abbey, A., Arnaud, M., et al. 2001, A&A, 365, L27

Turner, M. J. L., Thomas, H. D., Patchett, B. E., et al. 1989, PASJ, 41, 345

Ubertini, P., Lebrun, F., Di Cocco, G., et al. 2003, A&A, 411, L131

Van, K. X., Ivanova, N., & Heinke, C. O. 2019, MNRAS, 483, 5595

van der Klis, M. 1989, ARA&A, 27, 517

van der Klis, M. 1995, in X-ray binaries., ed. W. H. G. Lewin, J. van Paradijs, & E. P. J. van den Heuvel, Vol. 26 (Cambridge Astrophysics Series), 252

van der Klis, M. 2000, ARA&A, 38, 717

van der Klis, M. 2006a, Advances in Space Research, 38, 2675

van der Klis, M. 2006b, in Compact stellar X-ray sources, ed. M. Lewin, Walter H.G.and Van der Klis, Vol. 39 (Cambridge Astrophysics Series), 39–112

van der Klis, M., Swank, J. H., Zhang, W., et al. 1996, ApJ, 469, L1

van Straaten, S., van der Klis, M., & Méndez, M. 2003, ApJ, 596, 1155

Vedrenne, G., Roques, J. P., Schönfelder, V., et al. 2003, A&A, 411, L63

Verbunt, F. 1993, ARA&A, 31, 93

Verbunt, F. & Lewin, W. H. G. 2006, Globular cluster X-ray sources, Vol. 39, 341–379

Verbunt, F. & Zwaan, C. 1981, A&A, 100, L7

Verner, D. A., Ferland, G. J., Korista, K. T., & Yakovlev, D. G. 1996, ApJ, 465, 487

Voss, R. & Gilfanov, M. 2007, A&A, 468, 49

Westergaard, N. J., Kretschmar, P., Oxborrow, C. A., et al. 2003, A&A, 411, L257

Whelan, J. & Iben, Icko, J. 1973, ApJ, 186, 1007

White, N. E. & Holt, S. S. 1982, ApJ, 257, 318

White, N. E., Peacock, A., Hasinger, G., et al. 1986, MNRAS, 218, 129

Wijnands, R. & van der Klis, M. 1998, Nature, 394, 344

Wilms, J., Allen, A., & McCray, R. 2000, ApJ, 542, 914

Yaqoob, T., Murphy, K. D., Griffiths, R. E., et al. 2007, PASJ, 59, 283

Yin, H. X., Zhang, C. M., Zhao, Y. H., et al. 2007, A&A, 471, 381

Yin, H. X. & Zhao, Y. H. 2007, Advances in Space Research, 40, 1522

Yu, W. 2007, ApJ, 659, L145

Zdziarski, A. 2002, in X-ray Binaries in the Chandra and XMM-Newton Era (with an emphasis on Targets of Opportunity), 54

Zdziarski, A. A. & Gierliński, M. 2004, Progress of Theoretical Physics Supplement, 155, 99

Zdziarski, A. A., Gierliński, M., Mikołajewska, J., et al. 2004, MNRAS, 351, 791

Zdziarski, A. A., Johnson, W. N., & Magdziarz, P. 1996a, MNRAS, 283, 193

Zdziarski, A. A., Johnson, W. N., & Magdziarz, P. 1996b, MNRAS, 283, 193

Zhang, C. M., Yin, H. X., Zhao, Y. H., Zhang, F., & Song, L. M. 2006, MNRAS, 366, 1373

Zhang, W., Strohmayer, T. E., & Swank, J. H. 1997, ApJ, 482, L167

Zhang, Z., Sakurai, S., Makishima, K., et al. 2016, ApJ, 823, 131

Zimmerman, M. E. 1980, PhD thesis, California Institute of Technology, Pasadena.

Życki, P. T., Done, C., & Smith, D. A. 1999a, MNRAS, 309, 561

Życki, P. T., Done, C., & Smith, D. A. 1999b, MNRAS, 309, 561

List of Journal Publications

- **S. M. Mazzola**, R. Iaria, T. Di Salvo, A. Sanna, A. F. Gambino, E. Bozzo, C. Ferrigno, A. Riggio and L. Burderi, "Fe Kα and Fe Kβ line detection in the NuSTAR spectrum of the ultra-bright Z-source Scorpius X-1", submitted for publication to A&A

- R. Iaria, A. Sanna, T. Di Salvo, A. F. Gambino, **S. M. Mazzola**, A. Riggio, A. Marino, L. Burderi, "Evidence of a non-conservative mass transfer in the ultra-compact X-ray source XB 1916-053", 2021, A&A, 646, A120
`https://ui.adsabs.harvard.edu/abs/2021A%26A...646A.120I/abstract`

- R. Iaria, **S. M. Mazzola**, T. Di Salvo, A. Marino, A. F. Gambino, A. Sanna, A. Riggio, L. Burderi, "Reflection component in the Bright Atoll Source GX 9+9", 2020, A&A, 635, A209
`https://ui.adsabs.harvard.edu/abs/2020A%26A...635A.209I/abstract`

- **S. M. Mazzola**, R. Iaria, A. F. Gambino, A. Marino, T. Di Salvo, T. Bassi, A. Sanna, A. Riggio, L. Burderi, "Broadband spectral analysis of MXB 1659-298 in its soft and hard state", 2019, Mem. SAIt, v. 90, p96, Proceedings of the 12th INTEGRAL conference and 1st AHEAD Gamma-ray Workshop, Geneva (Switzerland), 11-15 February 2019, Ed. C. Ferrigno, E. Bozzo, P. von Balmoos
`https://ui.adsabs.harvard.edu/abs/2019MmSAI..90...96M/abstract`

- N. M. Gorgone, C. Kouveliotou, H. Negoro, R. A. M. J. Wijers , E. Bozzo , S. Guiriec, P. Bult, D. Huppenkothen , E. Göğüs , A. Bahramian, J. Kennea, J. D. Linford, J. Miller-Jones, M. G. Baring, P. Beniamini, D. Chakrabarty, J. Granot, C. Hailey, F. A. Harrison, D. H. Hartmann, W. Iwakiri, L. Kaper, E. Kara, **S. M. Mazzola**, K. Murata, D. Stern, J. A. Tomsick, A. J. van der Horst, and G. A. Younes, "Discovery and identification of MAXI J1621-501 as a Type I X-ray Burster with a super-orbital period", 2019, ApJ, 884, 2, 168
(`https://ui.adsabs.harvard.edu/abs/2019ApJ...884..168G/abstract`)

- R. Iaria, **S. M. Mazzola**, T. Bassi, A. F. Gambino, A. Marino, T. Di Salvo, A. Sanna, A. Riggio, L. Burderi, and N. D'Amico, "Broadband spectral analysis of MXB 1659-298 in its soft and hard state", 2019, A&A, 630, A138
  https://ui.adsabs.harvard.edu/abs/2019A%26A...630A.138I/abstract

- A. Marino , T. Di Salvo , L. Burderi , A. Sanna , A. Riggio, A. Papitto, M. Del Santo, A. F. Gambino, R. Iaria, **S. M. Mazzola**, "Indications of non-conservative mass-transfer in AMXPs" , 2019, A&A, 627, A125, 11
  https://ui.adsabs.harvard.edu/abs/2019A%26A...627A.125M/abstract

- A. F. Gambino, R. Iaria, T. Di Salvo, **S. M. Mazzola**, A. Marino, L. Burderi, A. Riggio, A. Sanna, N. D'Amico , "Spectral analysis of the dipping LMXB system XB 1916-053", 2019, A&A, 625, A92, 12
  https://ui.adsabs.harvard.edu/abs/2019A%26A...625A..92G/abstract

- **S. M. Mazzola**, R. Iaria, T. Di Salvo, A. F. Gambino, A. Marino, L. Burderi, A. Sanna, A. Riggio and M. Tailo, "Updated orbital ephemeris of the ADC source X 1822-371: a stable orbital expansion over 40 years", 2019, A&A, 625, L12
  https://ui.adsabs.harvard.edu/abs/2019A%26A...625L..12M/abstract

- F. Coti-Zelati, A. Papitto, D. De Martino, D. Buckley, J. Li, T.D. Russell, E. Bozzo, **S. M. Mazzola**, D. Torres, C. Ferrigno, S. Campana, N. Rea, S. Migliari, "The prolonged sub-luminous state of the new transitional pulsar candidate CXOU J110926.4-650224", 2019, A&A, 622, A211
  https://ui.adsabs.harvard.edu/abs/2019A%26A...622A.211C/abstract

- **S. M. Mazzola**, R. Iaria, T. Di Salvo, M. Del Santo, A. Sanna, A. F. Gambino, A. Riggio, A. Segreto, L. Burderi, A. Santangelo, "A broadband spectral analysis of 4U 1702-429 using XMM-Newton and BeppoSAX data", 2019, A&A, 621, A89
  https://ui.adsabs.harvard.edu/abs/2019A%26A...621A..89M/abstract

- A. Sanna, F. Pintore, A. Riggio, **S. M. Mazzola**, E. Bozzo, T. Di Salvo, C. Ferrigno, A. F. Gambino, A. Papitto, R. Iaria and L. Burderi, 2018, "SWIFT J1756.9-2508: spectral and timing properties of its 2018 outburst", 2018, MNRAS, 481, 2, 1658
  https://ui.adsabs.harvard.edu/abs/2018MNRAS.481.1658S/abstract

- A. Sanna, E. Bozzo, A. Papitto, A. Riggio, C. Ferrigno, T. Di Salvo, R. Iaria, **S. M. Mazzola**, N. D'Amico and L. Burderi, 2018, "XMM-Newton detection of the 2.1 ms coherent pulsations from IGR J17379–3747", 2018, A&A, 616, L17, 5
  `https://ui.adsabs.harvard.edu/abs/2018A%26A...616L..17S/abstract`

- **S. M. Mazzola**, E. Bozzo, E. Kuulkers, C. Ferrigno, V. Savchenko, L. Ducci, ATel #11523, "INTEGRAL observation of SWIFT J1756.9-2508 in outburst."
  `https://ui.adsabs.harvard.edu/abs/2018ATel11523....1M/abstract`

In details: papers as second author

- R. Iaria, S. M. Mazzola et al., 2020, A&A, 635, A209

Abstract

GX 9+9 (4U 1728-16) is a low mass X-ray binary source harboring a neutron star. Although it belongs to the subclass of the bright Atoll sources together with GX 9+1, GX 3+1, and GX 13+1, its broadband spectrum is poorly studied and apparently does not show reflection features in the spectrum. To constrain the continuum well and verify whether a relativistic smeared reflection component is present, we analyze the broadband spectrum of GX 9+9 using BeppoSAX and XMM-Newton spectra covering the 0.3-40 keV energy band. We fit the spectrum adopting a model composed of a disk-blackbody plus a Comptonized component whose seed photons have a blackbody spectrum (Eastern Model). A statistically equivalent model is composed of a Comptonized component whose seed photons have a disk-blackbody distribution plus a blackbody that mimics a saturated Comptonization likely associated with a boundary layer (Western model). Other trials did not return a good fit. Results: The spectrum of GX 9+9 was observed in a soft state and its luminosity is 2.3×10^{37} erg s^{-1} assuming a distance to the source of 5 kpc. In the Eastern Model scenario, we find the seed-photon temperature and electron temperature of the Comptonized component to be $1.14^{+0.10}_{-0.07}$ keV and $2.80^{+0.09}_{-0.04}$ keV, respectively, while the optical depth of the Comptonizing corona is 8.9 ± 0.4. The color temperature of the inner accretion disk is $0.86^{+0.08}_{-0.02}$ keV and 0.82 ± 0.02 keV for the BeppoSAX and XMM-Newton spectrum, respectively. In the Western Model scenario, instead, we find that the seed-photon temperature is 0.87 ± 0.07 keV and 1.01 ± 0.08 keV for the BeppoSAX and XMM-Newton spectrum, respectively. The electron

temperature of the Comptonized component is 2.9 ± 0.2 keV, while the optical depth is $9.4^{+1.5}_{-1.1}$. The blackbody temperature is $1.79^{+0.09}_{-0.18}$ keV and $1.85^{+0.07}_{-0.15}$ keV for the BeppoSAX and XMM-Newton spectrum, respectively. The addition of a relativistic smeared reflection component improved the fit in both the scenarios, giving compatible values of the parameters, even though a significant broad emission line in the Fe-K region is not observed. From the reflection component we estimated an inclination angle of about 43^{+6}_{-4} deg and 51^{+9}_{-2} deg for the Eastern and Western Model, respectively. The value of the reflection fraction $\Omega/2\pi$ is 0.18 ± 0.04 and 0.21 ± 0.03 for the Eastern and Western Model, respectively, suggesting that the Comptonized corona should be compact and close to the innermost region of the system.

Part of contribution: *BeppoSAX* observations data reduction

The narrow field instruments (NFIs) on board the *BeppoSAX* satellite observed the source between 8 April 2000 13:28:08 UTC and 9 April 2000 17:53:28 UTC (ObsId. 2083600400). The NFIs consists of four co-aligned instruments which cover three decades in energy, from 0.1 keV to 200 keV. The Low-Energy Concentrator Spectrometer (LECS, operating in the range 0.1-10 keV; Parmar et al. 1997) and the Medium-Energy Concentrator Spectrometer (MECS, 1.3-10 keV; Boella et al. 1997) have imaging capability with a field of view (FOV) of deg ; 20; and deg ; 30; radii, respectively. The High-Pressure Gas Scintillator Proportional Counter (HPGSPC, 7-60 keV; Manzo et al. 1997) and the Phoswich Detector System (PDS, 13-200 keV; Frontera et al. 1997) are non-imaging instruments, and background rejection is obtained by using the off-source data accumulated during the rocking of the collimators. Of the three MECS modules, only MECS2 and MECS3 were active during the observation; the event files of these two instruments were merged and labelled as MECS23. Using the `XSELECT` tool, I extracted the MECS23 light curve and the LECS and MECS23 spectra from clean-event files downloaded from the Multi-Mission Interactive Archive at the ASI Space Science Data Center (SSDC). I selected the source events for LECS and MECS23 from a circular region of deg ; 6; radius, centred on the source. The background events were extracted from a circular region with the same radius adopted for the source-event extractions and centred in a detector region far from the source. The MECS23 light curves with a 64 s bin time shows a roughly constant count rate of 70 c s^{-1}. We used the HP and PDS spectra made available by SSDC. The exposure time of the LECS, MECS23, HP, and PDS spectra are 23 ks, 50 ks, 46 ks, and 22.5 ks, respectively. We grouped each spectrum to have a minimum of 25 counts

per energy bin.

- R. Iaria, S. M. Mazzola et al., 2019, A&A, 630, A138

Abstract

The X-ray transient eclipsing source MXB 1659-298 went into outburst in 1999 and 2015. During these two outbursts the source was observed by *XMM-Newton*, *NuSTAR* and *SWIFT*. Using these observations, we studied the broadband spectrum of the source to constrain the continuum components and to verify whether it had a reflection component, as is observed in other X-ray eclipsing transient sources. We combined the available spectra to study the soft and hard state of the source in the 0.45-55 keV energy range. We report a reflection component in the soft and hard state. The direct emission in the soft state can be modelled with a thermal component originating from the inner accretion disk plus a Comptonized component associated with an optically thick corona surrounding the neutron star. On the other hand, the direct emission in the hard state is described only by a Comptonized component with a temperature higher than 130 keV; this component is associated with an optically thin corona. We observed narrow absorption lines from highly ionized ions of oxygen, neon, and iron in the soft spectral state. We investigated where the narrow absorption lines form in the ionized absorber. The equivalent hydrogen column density associated with the absorber is close to 6×10^{23} cm^{-2} and 1.3×10^{23} cm^{-2} in the soft and hard state, respectively.

Part of contribution: *NuSTAR* observations data reduction

During the outburst that occurred between 2015 and 2017, MXB 1659-298 was observed twice by the Nuclear Spectroscopic Telescope Array satellite (*NuSTAR*, Harrison et al. 2013): the first observation (ObsId. 90101013002) was performed between 2015 September 28 21:51:08 UTC and September 30 00:56:08 UTC for an exposure time of 51.5 ks, the second observation (ObsId. 90201017002) was carried out between 2016 April 21 14:41:08 UTC and April 22 04:56:08 UTC for an exposure time of 26.8 ks. The analysis of the observation taken in 2015 was also reported by Sharma et al. (2018), and the observation taken in 2016 was reported by Sharma et al. (2018) and Ponti et al. (2019).

I processed the data using the *NuSTAR* Data Analysis Software (NuSTAR-DAS) v1.9.3 for the data sets taken by the focal plane modules, FPMA and FPMB, and for both observations.

The source events were extracted from a circular region centered on the source coordinates that had a radius of deg ; ; 110. The filtered events, the background-subtracted light curves, the spectra, and the arf and rmf files were created using `nuproducts` tool.

I identified two dips, two eclipses, and one type I X-ray burst in the light curve corresponding to the first observation, while in the second observation seven type I X-ray bursts, one eclipse, one almost complete dip at 25 ks after the start time, and part of two dips at the beginning and end of the observation were observed. The count rate during the persistent emission is close to 4 count s^{-1} and 20 count s^{-1} during the first and second observation, respectively.

To produce the FPMA and FPMB spectra associated with the persistent emission, I created, using `XSELECT` v2.4d, the good time intervals (gti) files to exclude the type I X-ray bursts, the eclipses, and the dips. Finally, after verifying the good agreement between the FPMA and FPMB spectra, I used the `addascaspec` task to obtain a single combined spectrum. The exposure times of the combined *NuSTAR* persistent spectrum are 92.8 ks and 44.3 ks for the first and the second observation, respectively. We adopted energy ranges of 3-35 keV and 3-55 keV for the spectra extracted from the observations taken in 2015 and 2016, respectively.

List of Figures

List of Tables

Acknowledgements/Ringraziamenti

Sono tantissime le persone a cui devo dire grazie, senza l'aiuto delle quali questa tesi non esisterebbe. Vorrei ringraziare in primo luogo il Prof. Tomaso Belloni e la Dott.ssa Elise Egron per l'attenta revisione del mio lavoro e i preziosi consigli, utili al miglioramento della presente tesi.
Voglio ringraziare il gruppo di Astrofisica delle Alte Energie di Palermo, in cui sono cresciuta, accademicamente e umanamente. Al Prof. Rosario Iaria, mio supervisor, per avermi guidata in un lungo percorso iniziato con la mia tesi triennale, grazie per aver sempre avuto una risposta alle mie domande, per i nostri dibattiti (più o meno pacifici) e per avermi insegnato, in sostanza, praticamente tutto quello che so. Grazie alla Prof.ssa Tiziana Di Salvo per essere stata sempre disponibile al dialogo, non solo scientifico ma anche umano; grazie per essere per me una continua fonte di ispirazione. Grazie al Dott. Angelo (Franck) Gambino per essere stato il mio "fratello maggiore" accademico e non avermi mai fatto mancare i suoi consigli, i suoi deliri da picco glicemico, e Ben Hur. Grazie al (neo) Dott. Alessio Marino per aver condiviso con me questo percorso ed essere stato un insostituibile compagno di scrivania e di chiacchere.
Ci tengo a ringraziare anche il gruppo dell'Università degli Studi di Cagliari, che è stata un po' la mia seconda casa: il Prof. Luciano Burderi per le conversazioni sempre illuminanti, il Prof. Alessandro Riggio e il Dott. Andrea Sanna per la continua, puntuale e fruttuosa collaborazione, iniziata ben prima del mio dottorato.
Un sentito ringraziamento va al Dott. Enrico Bozzo, per avermi accolta all'ISDC di Ginevra e avermi coinvolta in mille dei suoi progetti; grazie per il suo contagioso entusiasmo e la sua inesauribile pazienza. Grazie anche al Dott. Carlo Ferrigno, per avermi pazientemente guidata alla scoperta e conoscenza di INTEGRAL e per essere stato sempre disponibile ad aiutarmi anche fuori dall'università nelle piccole difficoltà quotidiane. Grazie ad entrambi per avermi insegnato, in pochissimo tempo, più di quanto avrei mai sognato.

Un amorevole ringraziamento va, ovviamente, alla mia famiglia.
Alla zia Cicci, per le sue lezioni di saggezze ed eleganza, per essere stata sempre entusiasta di tutti i miei traguardi e avermi spinto a cercare "la grandezza dei giganti".
Grazie a mio padre, per tutte le levatacce e gli arrivederci in aeroporto, per le valigie portate su e giù dalle scale, per i suoi silenzi pieni di mille parole. Grazie a mia madre, per la sua dolcezza, per la sua forza e la sua incrollabile fede nel domani, per le sue mille parole che coprono i silenzi rumorosi. Grazie ad entrambi, per aver appoggiato le mie scelte, anche quelle che forse non riuscivate a comprendere. Grazie perchè se so camminare da sola è anche merito di tutti i vostri insegnamenti e contraddizioni.
Grazie a coloro che sono per me gli amici più cari.
Ad Alessia, per aver affrontato con lucidità ogni ingarbugliata questione che le ponevo e aver ascolato i miei messaggi vocali lunghi come album musicali. A Marco, per essere stato la mia boa, per le ore al telefono ad ascoltare i miei deliranti soliloqui senza mai giudicarmi o farmi sentire in difetto. A Fabiana, per avermi sempre capita in modo profondo senza bisogno di troppe parole e per aspettarmi sempre a braccia aperte nella mia adorata Casteddu. A Marzia, per essere l'amica di una vita, per non aver mai lasciato che le difficoltà e le diversità ci allontanassero, e per non aver mai scordato i nostri tè pomeridiani con i biscotti.
Ed ancora una volta grazie a Dario. Sarebbe impossibile elencare tutti i perchè; su tutto, il non aver mai mollato e non aver permesso a me di farlo. Grazie per averci creduto insieme a me e per avermi spinta ad arrivare fino a qui. Grazie per avermi tenuta per mano quando il mondo, per noi prima così grande, è diventato all'improvviso così piccolo.
Alla fine di tutto ciò, guardando indietro, a tutte le difficoltà, a tutti i momenti no, specialmente in quest'ultimo anno, disastroso a livello globale, voglio essere soddisfatta di me, anche solo per un attimo, perchè alla fine ci sono riuscita. Alla fine ho mantenuto la mia promessa, Nonno; tutto questo è anche per te.